

# EGS Exploration Methodology Project

using the

## Dixie Valley Geothermal System, Nevada as a Calibration Site

### Baseline Conceptual Geothermal Model

15 May 2013

DOE Award: DE-EE0002778



## Table of Contents

EGS Exploration Methodology Project.....	i
using the .....	i
Dixie Valley Geothermal System, Nevada.....	i
Baseline Conceptual Geothermal Model .....	i
List of Figures* .....	vi
List of Appendices .....	ix
List of Acronyms .....	x
1.Introduction .....	1
1.1 Goals and Objectives.....	1
1.2 Report Basis .....	1
1.3 Background .....	3
1.3.1 Regional Setting .....	4
1.4 AltaRock Project Team .....	5
2. Geology.....	6
2.1 Stratigraphy.....	6
2.1.1 Basement Geology.....	7
Triassic marine sediments (Tr) .....	7
Jurassic shallow marine sedimentary rocks (Jbr).....	8
Jurassic mafic oceanic igneous rocks (Jz) .....	8
Cretaceous granodiorite (Kgr).....	8
Cenozoic silicic volcanic units, associated intrusives, (Tv) and Miocene basalts (Tmb) .....	9
2.1.2 Basin Lithology (Q-Tbf).....	10
2.2 Structure .....	10
2.2.1 Tectonic History .....	10
Late Jurassic thrust faulting .....	11
Basin & Range crustal extension.....	11
2.2.2 Structural Setting of the Dixie Valley Fault Zone .....	12
Dixie Valley Fault.....	14
Seismicity .....	14
Stillwater Seismic Gap (SSG) .....	15
2.2.3 Intra-basinal Faulting .....	15
2.2.4 Stress Modeling .....	17
3. Geophysics.....	18
3.1 Gravity.....	18
3.2 Aero Magnetics .....	20
3.2.1 Intrabasin faults .....	20
3.2.2 Magnetic Anomalies .....	21
Dixie Valley Faulting.....	23
3.3 Gravity and Magnetics .....	23
3.4 Magnetotelluric (MT) Surveys.....	28
3.5 Seismic .....	31

3.5.1. Faults.....	33
3.5.2 Previous Dixie Valley seismic experiments.....	33
Seismic Data Collection Experiments.....	33
3.5.3 Seismic Reflection Profiles.....	35
3.5.4 Seismic Events.....	36
2003 Seismic Sequence.....	37
3.5.5 Databases Compiled.....	38
3.5.6 Integrated Seismic Model in Dixie Valley.....	40
3.5.7 New Seismic Noise Derived Velocity Model.....	44
3.5.8 Crust-mantle Boundary (Moho) Discontinuity Constraints.....	44
3.5.9 Seismic Attenuation in Dixie Valley.....	45
3.5.10 Seismic Velocity Variations as a Function of Rock Composition and Temperature.....	46
3.6 Thermal.....	49
3.6.1 Background Conductive Heat Flow.....	49
3.6.2 Thermal Anomalies within Dixie Valley.....	50
Dixie Comstock Mine.....	50
Dixie Meadows.....	50
Hyder Hot Springs.....	50
New York Canyon.....	51
3.6.3 Numerical Modeling.....	51
Temperature Modeling Conclusions.....	51
4. Hydrology.....	53
4.1 Regional Setting.....	53
4.2 Groundwater.....	54
4.2.1 Buckbrush Fault System.....	55
4.3 Geothermal Waters.....	55
4.4 Hydrogeochemistry.....	56
5. Geochemistry.....	56
5.1 Introduction.....	56
5.2 Springs, fumaroles and shallow wells.....	58
5.2.1 Hot Springs and Fumaroles.....	59
Dixie Meadows.....	59
Hyder HS.....	59
Jersey HS.....	59
Lower Ranch HS.....	59
Section 10 (unnamed) fumaroles.....	59
Senator fumaroles.....	60
5.3 Deep Wells.....	61
5.3.1 Bolivan Artesian Well.....	62
5.3.2 Dixie Federal Well 45-14.....	62
5.3.3 Dixie Comstock Mine.....	62
5.3.4 Dixie Federal Well 66-21.....	62
5.3.5 Dixie Federal Well 62-21.....	63
5.4 Geothermal and Production Fluids.....	64
5.5 Helium Isotopic Data.....	64
5.6 Fluid-inclusion Gas Chemistry.....	66

5.7 Injection Studies.....	66
5.7.1 Tracer Test – Reservoir Connectivity .....	67
6. Dixie Valley Geothermal Wellfield .....	68
6.1 Structure .....	68
6.1.1 Stress Analysis.....	69
6.2 Geothermal Reservoir .....	72
6.3 Thermal Data.....	74
6.3.1 Shallow thermal regime.....	74
6.3.2 Deep thermal regime .....	75
6.4 Summary of Geothermal Wells.....	77
6.4.1 Geothermal Wells within the DVPF .....	77
Well 38-32 .....	78
Well 25-5 .....	80
Well 37-33 .....	80
Well 45-33 .....	80
7. Baseline Conceptual Geothermal Model .....	81
7.1 Introduction and Background .....	81
7.1.1 Public Domain Highlights .....	81
7.1.2 Introduction .....	82
7.1.3 Calibration of EGS Methodology.....	83
7.2 Geologic and Structural Interpretations .....	83
7.2.1 Re-Interpreted Structural Analysis .....	83
Zones of Compression and Dilatation .....	86
7.2.2 Re-Interpreted Stress Modeling .....	91
7.3 Qualitative Geoscience Correlations.....	95
7.3.1 Summary Description of Geoscience Data Sets .....	95
Geology .....	95
Thermal.....	96
Magnetotellurics .....	96
Geochemical Data .....	97
Gravity-Magnetics.....	97
Seismic Data .....	97
Seismic Reflection Profiles .....	98
Stress Data Sets.....	98
7.3.2 Wellfield Correlation of Geoscience Data Sets .....	98
Geologic Sections .....	99
Cross-Section C-C' .....	99
Cross-Section D-D' .....	102
Cross-Section E-E' .....	102
Cross-Section F-F' .....	103
Summary of Cross-Sectional Correlations.....	103
Correlation with Gravity-Magnetic Models .....	104
Correlation with Magneto-Telluric (MT) Resistivity Data .....	104
7.4 Quantitative Geoscience Correlations: Geostatistics.....	105
7.4.1 Database, Parameters Description, and Gridding .....	105
Constructing the Geostatistical Database.....	105
Description of Parameters .....	105

Gridding.....	107
7.4.2 Exploratory Data Analysis .....	107
Exploring the Temperature-Vp Relationship using well data .....	108
Residual and Multiple Regression Analyses.....	109
Sectional Data.....	111
Well Data .....	112
Precision of the Multiple Regression Results .....	112
Bootstrap Method .....	112
Cross Validation .....	114
Vp-Temperature Relationship: Effect of Density and Depth .....	118
Geologic Analysis.....	119
Effect of Lithology and Depth.....	119
Summary Assessment of the Vp-Temperature Relationship.....	123
Classification and Regression Tree Analysis (CART).....	123
Introduction.....	123
Explanation of CART .....	123
CART Methodology.....	124
Sectional Data.....	127
Predicting Temperature.....	127
Predicting Temperature from Vp.....	127
Predicting Lithology .....	127
Well Data .....	127
Predicting Temperature using Vp .....	128
Predicting Productive Wells.....	128
CART Sensitivity Analysis.....	129
Parameter Overview.....	131
Methodology .....	131
Results .....	131
Predicting Lithology using Section Data.....	132
Predicting Temperature using Section Data .....	132
Predicting Lithology using Well Data .....	132
Predicting Temperature using Well Data.....	133
Predicting Productive vs. Non-Productive Cells using Well Data.....	134
Predicting EGS Favorable Cells using Well Data .....	134
Implications .....	134
Summary of Exploratory Geostatistics and Geologic Significance.....	135
Correlation Analysis.....	135
Multiple Regression and Residual Analysis.....	135
Classification and Regression Tree Analysis .....	135
Assesment of the Vp-Temperature Relationship.....	136
7.5 Summary .....	136
7.5.1 Hydrothermal System .....	136
7.5.2 Engineered Geothermal System .....	138
8. EGS Favorability and Trust Mapping.....	139
8.1 Introduction .....	139
8.2 GIS Database .....	139
8.3 Description of Parameters .....	141
8.4 Gridding.....	141
8.5 Data Conversion.....	142
8.6 Integrated Geoscience Sections for EGS Favorability .....	145
8.6.1 Lithology.....	145
8.6.2 Temperature .....	145
8.6.3 Stress Parameter.....	145

Fault/Fracture Orientation.....	145
Coulomb Stress Modeling .....	145
Fault Present/Absent .....	146
Compression and Dilated Zones .....	146
8.7 Favorability Mapping Process .....	146
8.8 Trust Maps .....	147
8.9 Results Calibration / Verification .....	161
8.9.1 Averaged Favorability Values and Average Weights derived from the SMEs .....	161
8.9.2 Averaged Favorability Values derived from the SMEs with Equal Weights.....	162
9. References .....	163

## List of Figures\*

<a href="#">Figure 1. Dixie Valley Index Map.....</a>	<a href="#">4</a>
<a href="#">Figure 2. Location of shallow thermal anomalies.....</a>	<a href="#">5</a>
<a href="#">Figure 3. Regional map for Dixie Valley.....</a>	<a href="#">6</a>
<a href="#">Figure 4A. Seismicity Map of western Nevada.....</a>	<a href="#">7</a>
<a href="#">Figure 4B. East –West elevation cross section through the Basin and Range.....</a>	<a href="#">7</a>
<a href="#">Figure 5. Bedrock Geology Map modified from 1:1,000,00 NBMG map.....</a>	<a href="#">12</a>
<a href="#">Figure 6a. Map of area seismicity, faults, earthquake epicenters, and other features.....</a>	<a href="#">16</a>
<a href="#">Figure 6b. Simplified cross section of Dixie Valley Producing Field.....</a>	<a href="#">16</a>
<a href="#">Figure 7. Coulomb failure stress changes in the Stillwater Gap.....</a>	<a href="#">17</a>
<a href="#">Figure 8. Complete Bouguer anomaly (CBA) map of the region around Dixie Valley, NV.....</a>	<a href="#">18</a>
<a href="#">Figure 9A. CBA Total Horizontal Gradient of Dixie Valley.....</a>	<a href="#">19</a>
<a href="#">Figure 9B. Outline of geologic formations overlain on a total magnetic anomaly map of PACES data.....</a>	<a href="#">19</a>
<a href="#">Figure 10. Reduced-to-Pole (RTP) low-level high-resolution aeromagnetic map and mapped faults.....</a>	<a href="#">21</a>
<a href="#">Figure 11. Aeromagnetic survey and horizontal-gradient magnitude of pseudogravity map with faults.....</a>	<a href="#">22</a>
<a href="#">Figure 12. Detail of high resolution aeromagnetic map in the DVPP and DVPF areas.....</a>	<a href="#">23</a>
<a href="#">Figure 13. Horizontal gradient inferred faulting from gravity and magnetics.....</a>	<a href="#">24</a>
<a href="#">Figure 14. Structure of Dixie Valley (Smith et al. 2001).....</a>	<a href="#">25</a>
<a href="#">Figure 15A. Location of modeled lines A-A' through F-F' superimposed on the HELIMAG map.....</a>	<a href="#">26</a>
<a href="#">Figure 15B. Effects of removal of regional gravity trend on lines F-F' and E-E'.....</a>	<a href="#">27</a>
<a href="#">Figure 15C. Joint gravity and magnetic model of lines C-C' through F-F'.....</a>	<a href="#">29</a>
<a href="#">Figure 15D. Joint gravity and magnetic model of lines A-A' through B-B'.....</a>	<a href="#">30</a>
<a href="#">Figure 16A. Location of MT arrays on geologic map of the Dixie Valley-Stillwater Range area.....</a>	<a href="#">30</a>
<a href="#">Figure 16B. Electrical resistivity section for the northern (N) profile across Senator fumaroles.....</a>	<a href="#">31</a>
<a href="#">Figure 16C. Resistivity inversion section for the southern profile (S) across the Section 10-15 area.....</a>	<a href="#">32</a>
<a href="#">Figure 16D. Resistivity inversion section (C) across the Dixie Valley power producing field.....</a>	<a href="#">32</a>
<a href="#">Figure 16E. MT structures of the central Great Basin along WNW-WSW transect.....</a>	<a href="#">32</a>

<b>Figure 17A.</b>	Seismic Profile Index map of Dixie Valley Producing Field and DVPP areas.....	37
<b>Figure 17B.</b>	Okaya and Thompson (1985) interpretation of reflection profile SRC-3.....	38
<b>Figure 18.</b>	Dixie Valley basement configuration with valley fill removed.....	39
<b>Figure 19.</b>	Interpreted line drawings of stacked seismic sections for dip lines 102, 9, 104, and 6.....	40
<b>Figure 20.</b>	Natural and induced seismicity from 1900 to 2010 within 100km of the project area.....	41
<b>Figure 21.</b>	Waveforms recorded at station FPK from selected events.....	42
<b>Figure 22A.</b>	Relocated and catalog events of the January 2003 sequence in Dixie Valley.....	42
<b>Figure 22B.</b>	Focal mechanism of the largest earthquake from the January 2003 sequence.....	43
<b>Figure 23.</b>	Plan view map of relocated events shown in Figure 22.....	43
<b>Figure 24.</b>	COCORP seismic profile location from Catchings (1992).....	44
<b>Figure 25.</b>	UNR P-wave seismic velocity model in Dixie Valley from earthquake data.....	45
<b>Figure 26.</b>	The P-wave velocity model at 3km depth.....	47
<b>Figure 27.</b>	Newly extracted ambient noise results using ambient noise crosscorrelations.....	48
<b>Figure 28.</b>	Comparison of the Green's Functions (GF).....	48
<b>Figure 29.</b>	Lg coda Q @ 1 Hz for the western US as in Phillips and Stead (2008).....	49
<b>Figure 30.</b>	Thermal gradient and well locations in the Dixie Valley area.....	52
<b>Figure 31.</b>	Temperature-depth curves for wells in the Comstock Mine, Dixie Meadows and Hyder Hot Spring....	53
<b>Figure 32A.</b>	Extent of the ~13ka high stands of pluvial lakes Lahontan and Dixie.....	54
<b>Figure 32B.</b>	Extent of the Lake Dixie high stand map ~13 ka shorelines and intrabasin faults.....	54
<b>Figure 33.</b>	Map showing thermal features and location of geochemistry sites.....	57
<b>Figure 34.</b>	Deuterium versus oxygen-18 for Dixie Valley related.....	57
<b>Figure 35A.</b>	Distribution of Dixie Valley fluid types with sample locations.....	60
<b>Figure 35B.</b>	Variations in Dixie Valley fluid compositions: plot of BiCarbonate versus Chloride.....	61
<b>Figure 36.</b>	Plot of arsenic versus chloride for thermal and nonthermal waters.....	61
<b>Figure 37.</b>	Shaded relief sample location map of the B&R and surrounding areas for Helium ratios.....	65
<b>Figure 38.</b>	Non-atmospheric noble gases in selected Dixie Valley springs, fumaroles, and wells.....	66
<b>Figure 39.</b>	Cross Section showing tracer flow patterns of the producing field.....	67
<b>Figure 40A.</b>	Map showing the location of wells within the Dixie Valley Geothermal Wellfield (DVGW).....	69
<b>Figure 40B.</b>	Compilation Map showing lineaments, mapped faults, interpreted major fault zones, etc.....	70
<b>Figure 41.</b>	Map of the Dixie Valley Geothermal Field showing the orientation of $S_{hmin}$ .....	73
<b>Figure 42.</b>	Map of the geothermal producing field in reference to section number.....	74
<b>Figure 43.</b>	Temperature-depth curves for thermal gradient wells in the DVPP.....	75
<b>Figure 44.</b>	Map of deep wells and thermal gradient contours for the valley along the range front.....	76
<b>Figure 45A.</b>	Thermal model for the DVPP area based on temperature matching in the deep wells.....	76
<b>Figure 45B.</b>	Thermal model for the DVPF based on temperature matching in the deep wells.....	77

<b>Figure 46.</b>	<a href="#">Temperature-depth curves for wells within the Dixie Valley Geothermal Wellfield.....</a>	<a href="#">79</a>
<b>Figure 47.</b>	<a href="#">Cross-section of the Stillwater Range/Dixie Valley contact from Johnson and Hulen (2002).....</a>	<a href="#">81</a>
<b>Figure 48.</b>	<a href="#">The Dixie Valley Geothermal Wellfield and Calibration Area.....</a>	<a href="#">84</a>
<b>Figure 49A.</b>	<a href="#">Structure compilation map of the Dixie Valley EGS Project Area.....</a>	<a href="#">87</a>
<b>Figure 49B.</b>	<a href="#">Geologic Map of the Project Area.....</a>	<a href="#">88</a>
<b>Figure 49C.</b>	<a href="#">Interpreted Structural Map of the Project Area.....</a>	<a href="#">89</a>
<b>Figure 49D.</b>	<a href="#">Correlation of Shallow Thermal Anomalies, structural zones, and well type.....</a>	<a href="#">92</a>
<b>Figure 50.</b>	<a href="#">The expected CSC and strain (dilatation) from a realization of the Coulomb Stress Modeling.....</a>	<a href="#">94</a>
<b>Figure 51.</b>	<a href="#">Dixie Valley generalized geologic map showing the six major surface stratigraphic units.....</a>	<a href="#">100</a>
<b>Figure 52.</b>	<a href="#">Correlation of Geoscience Models along Section C-C'.....</a>	<a href="#">101</a>
<b>Figure 53.</b>	<a href="#">Correlation of Geoscience Models along Section E-E'.....</a>	<a href="#">103</a>
<b>Figure 54.</b>	<a href="#">Correlation plot of Vp vs. Temperature for all well data.....</a>	<a href="#">109</a>
<b>Figure 55.</b>	<a href="#">Correlation plot of Vp vs. Temperature using all well data except for surface data.....</a>	<a href="#">110</a>
<b>Figure 56.</b>	<a href="#">Correlation plot of Vp vs. Temperature using selected well data.....</a>	<a href="#">111</a>
<b>Figure 57.</b>	<a href="#">Linear Correlations of Key Variables vs. Elevation (Depth).....</a>	<a href="#">113</a>
<b>Figure 58.</b>	<a href="#">Bivariate Fit of Temperature, Vertical Stress and Vp-seismic by elevation.....</a>	<a href="#">116</a>
<b>Figure 59A.</b>	<a href="#">Linear Correlations of key variables vs. the residuals of Vertical Stress and Vp.....</a>	<a href="#">117</a>
<b>Figure 59B.</b>	<a href="#">Multiple Regression of Temperature vs. Residuals.....</a>	<a href="#">117</a>
<b>Figure 59C.</b>	<a href="#">Multiple Regression of Temperature vs. Key Variables.....</a>	<a href="#">117</a>
<b>Figure 60A.</b>	<a href="#">Regression Analysis for predicting depth vs. prediction from Resistivity (MT) and Vp.....</a>	<a href="#">118</a>
<b>Figure 60B.</b>	<a href="#">Regression Analysis for predicting Temperature vs. prediction using Lithology, Vp, and MT.....</a>	<a href="#">119</a>
<b>Figure 61A.</b>	<a href="#">Lithology-Vp-Temperature(°C)-Depth relationship in conductive vs. convective wells.....</a>	<a href="#">121</a>
<b>Figure 61B.</b>	<a href="#">Vp-Depth Relationship observed within the basin-filling sediments (QTbf).....</a>	<a href="#">121</a>
<b>Figure 62.</b>	<a href="#">Vp-Temperature relationship observed within the QTbf at the respective depths.....</a>	<a href="#">122</a>
<b>Figure 63.</b>	<a href="#">Relationship between Temperature (left) and T residuals (right) vs. Vp within the QTbf.....</a>	<a href="#">123</a>
<b>Figure 64.</b>	<a href="#">Idealization of vector (right) to raster (left) format conversion.....</a>	<a href="#">140</a>
<b>Figure 65.</b>	<a href="#">EXCEL spreadsheet representing plan view slice at 2.5km below sea level if thermal model.....</a>	<a href="#">143</a>
<b>Figure 66.</b>	<a href="#">Data Conversion Diagram: EXCEL to Coordinates to GIS to Raster.....</a>	<a href="#">144</a>
<b>Figure 67.</b>	<a href="#">EGS Favorability map (left) and associated trust map (right) at 1.0km asl.....</a>	<a href="#">149</a>
<b>Figure 68.</b>	<a href="#">EGS Favorability map (left) and associated trust map (right) at 0.5km asl.....</a>	<a href="#">150</a>
<b>Figure 69.</b>	<a href="#">EGS Favorability map (left) and associated trust map (right) at sea level (0km asl).....</a>	<a href="#">151</a>
<b>Figure 70.</b>	<a href="#">EGS Favorability map (left) and associated trust map (right) at -0.5km asl.....</a>	<a href="#">152</a>
<b>Figure 71.</b>	<a href="#">EGS Favorability map (left) and associated trust map (right) at -1.0km asl.....</a>	<a href="#">153</a>
<b>Figure 72.</b>	<a href="#">EGS Favorability map (left) and associated trust map (right) at -1.5km asl.....</a>	<a href="#">154</a>
<b>Figure 73.</b>	<a href="#">EGS Favorability map (left) and associated trust map (right) at -2.0km asl.....</a>	<a href="#">155</a>

<b>Figure 74.</b>	EGS Favorability map (left) and associated trust map (right) at -2.5km asl.....	156
<b>Figure 75.</b>	EGS Favorability map (left) and associated trust map (right) at -3.0km asl.....	157
<b>Figure 76.</b>	EGS Favorability map (left) and associated trust map (right) at -3.5km asl.....	158
<b>Figure 77.</b>	EGS Favorability map (left) and associated trust map (right) at -4.0km asl.....	159

## List of Tables\*

<b>Table 1.</b>	Generalized Dixie Valley and Stillwater Range Stratigraphy.....	9
<b>Table 2.</b>	Summary of Ages of Dixie Valley Spring Deposits.....	62
<b>Table 3.</b>	Well data outside of the producing field.....	78
<b>Table 4.</b>	Stress Information from deep wells penetrating the fault zone at at 2-3km depth.....	94
<b>Table 5.</b>	Correlation of the geology and MT data shown in Plate 1.....	105
<b>Table 6A.</b>	Results of the Weighting Analysis confidence interval determination using elevation.....	114
<b>Table 6B.</b>	Results of the Weighting Analysis confidence interval determination without elevation.....	114
<b>Table 7.</b>	Preliminary Summary of CART Analyses Conducted.....	126
<b>Table 8.</b>	CART Analyses in predicting temperature from P-wave velocity ( $V_p$ ) using well data.....	128
<b>Table 9.</b>	CART parametric sensitivity analysis results for predicting productive intervals.....	129
<b>Table 10.</b>	Identification of the Productive hydrothermal cells in the wells used in CART analyses.....	130
<b>Table 11.</b>	Summarized Results from the CART Sensitivity Analysis showing the range of $r^2$ -values.....	133
<b>Table 12.</b>	Preliminary weights and values used to test the generation of the favorability maps.....	147
<b>Table 13.</b>	Final favorability and weight values using averaged values and weights based on SME input.....	148
<b>Table 14.</b>	Scale used to assign trust values to existing data sets.....	148

## List of Appendices

<b>Appendix 1.</b>	Geologic Maps
<b>Appendix 2.</b>	Dixie Valley Seismic Data
<b>Appendix 3.</b>	Seismic Event Catalog
<b>Appendix 4.</b>	Seismic Indicators of Thermal and Rock Properties
<b>Appendix 5.</b>	Parameters with Influence on Seismic Velocity
<b>Appendix 6.</b>	Seismic Velocity and Rock Properties
<b>Appendix 7.</b>	Geochemical Data from Goff et al. (2002)
<b>Appendix 8.</b>	Summary of the Thermal Regime Data
<b>Appendix 9.</b>	Well Lithology Data
<b>Appendix 10.</b>	Project Area Lithology
<b>Appendix 11.</b>	Temperature Gradient Hole (TGH) and Well Temperature Data
<b>Appendix 12.</b>	Dixie Valley Wellfield Cross-Sections with Assumptions
<b>Appendix 13.</b>	Coulomb 3.1 Re-Interpreted Stress Modeling

- Appendix 14.** Cross-Section Correlation Table
- Appendix 15.** General Geoscience Data Parameters
- Appendix 16a.** Section data for Geostatistical Analysis
- Appendix 16b.** Well data for Geostatistical Analysis
- Appendix 17.** Correlation Analysis and Chi-Square Test Results
- Appendix 18.** Relationship between Temperature and P-wave Velocity: Effect of Depth and Density
- Appendix 19.** Classification and Regression Tree (CART) Analysis
- Appendix 20a.** Classification and Regression Tree (CART) sensitivity analysis predicting temperature using Section and Well data
- Appendix 20b.** Classification and Regression Tree (CART) sensitivity analysis predicting lithology temperature using Section and Well data
- Appendix 20c.** Classification and Regression Tree (CART) sensitivity analysis predicting productive vs. non-productive cells using Well data
- Appendix 20d.** Classification and Regression Tree (CART) sensitivity analysis predicting EGS favorable cells using well data
- Appendix 21.** EGS Favorability and Trust Maps using an Equal Weighting Scheme

\*Summarized captions are shown. Figure, table, and appendices are numbered consecutively from Section 1.

## List of Acronyms

Acronym	Description
AltaRock	AltaRock Energy Inc.
ARRA	American Recovery and Reinvestment Act
asl	Above seal level
B&R	Basin and Range
BHT	Bottom hole temperature
BHTV	Borehole Televiwer
BLM	U.S. Bureau of Land Management
CBA	Complete Bouguer Anomaly
CNSB	Central Nevada Seismic Belt
COCORP	Consortium for Crustal Reflection Profiling
CSC	Coulomb Stress Change
DOE	U.S. Department of Energy
DVF	Dixie Valley Fault
DVFZ	Dixie Valley Fault Zone
DVGS	Dixie Valley Geothermal System
DVGW	Dixie Valley Geothermal Wellfield
DVPF	Dixie Valley Producing Field
DVPP	Dixie Valley Power Partners
DVESA	Dixie Valley Extended Study Area

## List of Acronyms

Acronym	Description
DVSA	Dixie Valley Study Area
EGS	Engineered Geothermal System
EM	Electromagnetic
GDB	ESRI ArcGIS geodatabase
GIS	Geographic Information System
HS	Hot Spring
HTGF	High Temperature Geothermal Fluids
Jg	Jurassic rocks
Jgnm	Jurassic rock, non-magnetic
MT	Magnetotelluric
NV	Nevada
NBMG	Nevada Bureau of Mines and Geology
PASSCAL	Program for Array Seismic Studies of the Continental Lithosphere
QFFDB	Quaternary Fault and Fold Database
Qp	Attenuation of the P-wave
Qs	Attenuation of the S-wave
QTbf	Quaternary-Tertiary basin fill
RF	Receiver Fault
rho	Seismic inferred density
SF	Source Fault
SF	Stillwater Fault
SFZ	Stillwater Fault Zone
$S_{hmin}$	Horizontal minimum stress direction
SME	Subject Matter Expert/Expertise/Experience
Terra-Gen	Terra-Gen Power, LLC
TGH	Temperature Gradient Hole
USGS	United States Geological Survey
Vp	P-wave velocity in km/sec
Vs	S-wave velocity in km/sec

## 1.Introduction

### 1.1 Goals and Objectives

The U.S. Department of Energy (DOE) has contracted with AltaRock Energy Inc. (AltaRock) to develop a calibrated Engineered Geothermal System (EGS) exploration methodology (Award No. DE-EE0002778). This activity is jointly funded by AltaRock. To achieve the project goal, the following five technical tasks (objectives), with a description of what was done, were completed:

- **Task 1 – Collect and Assess Existing (baseline) Public Domain Geoscience Data**  
This task involves qualitatively assessing the geology, geophysics, geochemistry, hydrology, and well data in project area with particular emphasis on the existing Dixie Valley Geothermal Wellfield (DVGW).
- **Task 2 – Design and Populate a Geographic Information System (GIS) Database**  
Development of a GIS-database ensures that the project data can be easily stored and managed for retrieval, visualization, and data integration.
- **Task 3 – Develop Baseline (existing data) Geothermal Conceptual Model, Evaluate Geostatistical Relationships, and Generate Baseline EGS Favorability (and Trust) Maps**  
This task integrates the geoscientific data assessed; re-interpret data as required; conduct geostatistical exploratory data analysis to discern relationships among key geoscience parameters; and generate favorability/trust maps for the calibration area to identify EGS drilling targets at a scale of 5km x 5km at depths from +1km above sea level (asl) to -4km asl.
- **Task 4 – Collect New Field Data to Fill In Data Gaps and Improve Model Resolution (baseline and new data are combined to create an enhanced data set)**  
This task involves collecting new and interpreting the enhanced (1) gravity data to define the basin structure and subsurface faulting; (2) passive ambient seismic noise data to define the seismic parameters ( $V_p$ ,  $V_s$ ,  $\rho$ ,  $Q_s$ , and  $Q_p$ ) and potentially identify areas of seismic anisotropy; (3) Magnetotelluric (MT) data to define subsurface resistivity, pathway for fluid flow, potential subsurface structure, MT structural as well as developing a conductive MT-based subsurface thermal map; and (4) soil  $\text{CO}_2$  gas data for a focused investigation of zones of dilatation and compression. Additionally, develop 3-D conductive and convective thermal models.
- **Task 5 – Repeat Task 3 for the Enhanced Data Set**  
This task integrates the new results into the baseline geoscientific data assessment; re-interprets data as required; conducts geostatistical exploratory data analysis on the enhanced data set; and revises the calibration area favorability/trust maps for the enhanced data.

### 1.2 Report Basis

To date, there is no accepted, invasive or non-invasive exploratory methodology for “greenfield” EGS sites proven to be both technically feasible and cost effective. Although drilling slimholes provides direct data on the primary resource favorability criteria (i.e., temperature, rock composition and stress regime), widespread use is cost prohibitive necessitating selective use. Developing a cost effective and reliable exploration methodology is, therefore, essential for the economic viability of EGS in regions

beyond what has already been explored for hydrothermal resources. To determine whether an EGS exploration methodology can be calibrated using the Dixie Valley Geothermal System (DVGS, see [Figures 1 and 2](#) and [Section 1.3](#)) as a laboratory test case, AltaRock has designed a project consisting of the five technical tasks presented in [Section 1.1](#).

The Project Area consists of a 50km by 50km (31mi by 31mi) area roughly centered on the Dixie Valley Power Partners lease (DVPP, [Figure 1](#)). One of the key data sources for this study has been the extensive amount of information compiled and interpreted by Blackwell et al. (2005), the public domain in numerous DOE supported studies as well as non-DOE supported studies that have taken place over the past 40 to 50 years, and selected data released by Terra-Gen Power, LLC (Terra-Gen). This report does not attempt to re-interpret the bulk of the public domain data because we do not have access to the original data set. However, a re-interpretation of select data sets is presented where deemed appropriate. Original work by the authors is presented in the areas of gravity and magnetics, seismic, surface and subsurface structure, magneto-tellurics, cross-correlating these varied data sets, geostatistics, and in the development of the methodology.

Geothermal activity is present intermittently throughout Dixie Valley, over a distance of some 100km (62mi) in length ([Figure 2](#)). The overall study area for geological and geophysical regional setting purposes is a 50km<sup>2</sup> (19mi<sup>2</sup>) square block that includes a sizable portion of Dixie Valley and the Stillwater Range. The “calibration” area covers a much smaller area, the Dixie Valley geothermal wellfield (DVGW), which includes the geothermal production wells, as well as dry wells drilled in and around the production area (see below). This reduction of the detailed study area has been necessary, as this is where the greatest concentration of data is available, but has also resulted in biases within the conclusions that need to be appreciated by the casual reader. It is also critical for all readers to appreciate and accept that the analysis presented herein is not constructed to be used as an exploration guide to the DVGS. While parts of the analysis presented can be used in exploration work in the DVGS, the reader is cautioned that supplementary analysis and integration is required to use the work herein as an exploration guide. Rather this project was designed, and this report is presented as a methodology to evaluate potential EGS areas.

As indicated above, the focus of this investigation is the DVGW ([Figure 2](#)) which includes the Dixie Valley geothermal production field currently generating over 60 MWs of electrical power (DVPP in [Figure 1](#)), and the dry and sub-commercial wells primarily located to the southwest and northeast of the producing field. The DVGW was chosen because it provides the most extensive public-domain geothermal database in the Basin and Range Province (B&R) including but not limited to the substantial body of geological, geochemical and geophysical data available for portions of the valley and 30 geothermal wells. This project had access to lithologic data for 22 of 30 wells, bottomhole temperature data (BHTs) for 26 wells, temperature-depth profiles for 10 wells, and 9 temperature gradient holes (TGHs). The availability of downhole data, especially geothermal well data, provides the basis for calibrating the exploration methodology.

This effort is designed to test the value of a select variety of exploration tools in the identification of locations favorable for EGS development using the Dixie Valley Geothermal System (DVGS) as an evaluation site. Anomalous high temperatures in the near-surface (upper 3km [9800ft]) within the B&R are produced by long-lived hydrothermal cells. The continuous upwelling flow of hot water, over long periods of time, conductively heats adjacent lower permeability rock. These areas of conductively heated lower permeability rock are prime targets for EGS development. The first task in the identification of these favorable EGS sites is to understand where and why traditional hydrothermal cells are located. This study has identified and described basic structural conditions that are necessary for a geothermal cell to develop. This knowledge now provides the basis for identifying favorable EGS targets,

and for evaluating various exploration technologies for their abilities to assist in finding similar locations outside the study area.

This report covers the results of Tasks 1 to 3 described above. Sections 2 through 6 of this report provide a compilation of the geology, structure, geophysics (gravity, magnetics, magneto-tellurics, seismic, and thermal), hydrogeology, geochemistry, and the DVGW setting. New and re-interpreted data are introduced for the sake of clarity, where appropriate. Section 7 discusses the Baseline EGS Conceptual Geothermal Model. Presented therein are the results of qualitative and quantitative cross-correlation of the various data sets and their potential significance. Section 8 describes the generation of the Baseline EGS favorability and associated trust maps. Section 9 provides the references used in this investigation.

### 1.3 Background

The DVGW is an ideal region for this case study as it represents the largest and hottest B&R (deep circulation) hydrothermal system known and it has an extensive public domain database. The DVGW is part of a much larger DVGS which consists of a large number of potentially independent geothermal cells in Dixie Valley (Al Waibel, pers. comm., 2010) that lie along an active fault zone bounding the Stillwater Range in Dixie Valley, located in Churchill and Pershing Counties, Nevada ([Figures 1](#) and [2](#)). In addition to the geothermal systems along the east side of the Stillwater Range, others have been defined in the region, e.g., New York Canyon and Pirouette Mtn. ([Figure 2](#)), as well as a significant geothermal resource currently under development at Jersey Valley which lies just to the NE of the Project Area. Given the known and numerous potential geothermal systems present in this limited geographical region, the term Dixie Valley Geothermal District is used to reference all the geothermal systems present in the Dixie Valley region following the approach described by ITSI (2005), Waibel (1987), and well-established in the mining and oil/gas and mining industries.

The DVGW is considered for the purposes of this report as extending from the Dixie Comstock Mine and well 45-14 area to the southwest, to the Section 10 and Senator Fumarole Areas to well 76-28 to the northeast, and to well 62-21 to the southeast ([Figure 1](#)). It includes the area in and around the Dixie Valley Producing Field (DVPP) and Dixie Valley Power Partners lease (DVPP). The DVPP, lying south-southwest of the producing field, consists of at least four deep wells, one of which is the hottest geothermal well (285°C [545°F]) known in the B&R.

The DVGW has a complex structural setting and temperatures  $\gg 200^{\circ}\text{C}$  [ $\gg 392^{\circ}\text{F}$ ] over a large area at relatively shallow depth (2-3km [6400-9600ft]). Additionally a large amount of subsurface information such as deep well data, surface geophysical surveys, and hydrologic and geochemical investigations from published literature, DOE sponsored projects, and other data provided by Terra-Gen Power exceeds the publically available information basis for any other geothermal areas in the B&R. Geothermal electrical production from the producing field (62 Mw<sub>e</sub>) is significantly greater than that of any other geothermal system within the Great Basin.

The DVGS is considered a classic range-front fault system with production mainly from a complex structural setting involving brittle, permeable igneous units including a Jurassic mafic complex faulted against impermeable basement rocks. The producing field lies within a complex system of steep extensional faults which includes the well-known range-bounding fault and related subsurface structures, referred to in this report as the Dixie Valley Fault Zone (DVFZ), see [Section 2.2.2](#). There is no young volcanism (<8Ma) within 50km (31mi) of Dixie Valley, thus there is no upper crustal magmatic source for the elevated heat flow. The majority of existing studies conclude that the heat source for geothermal fluids results from deep circulation within a highly extended terrain (Benoit, 1999; Blackwell et al., 2000; 2002; 2005; 2007). Other studies include deep circulation with some degree of magmatic influence evidenced by geophysical and geochemical data. The supporting evidence for this alternate

interpretation includes helium enrichment showing a slight mantle component (Kennedy et al., 2005), magnetotelluric data imaging a potential deep feeder zone for geothermal fluids near the center of Dixie Valley (Wannamaker et al., 2007), and a small magmatic component for fluid-inclusion gases within veins from production wells (Lutz et al., 2002). While the majority of studies support the deep circulation model, these alternate hypothesis will also be discussed within the report.

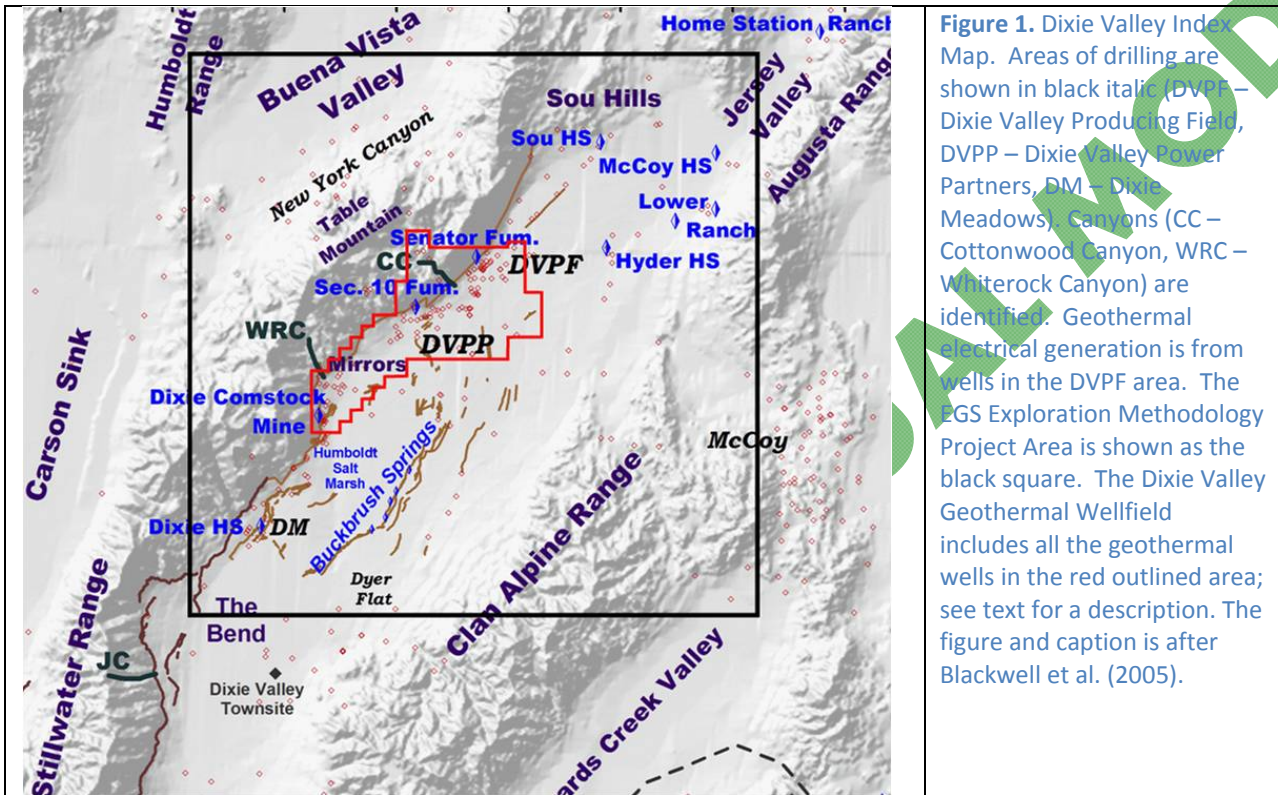
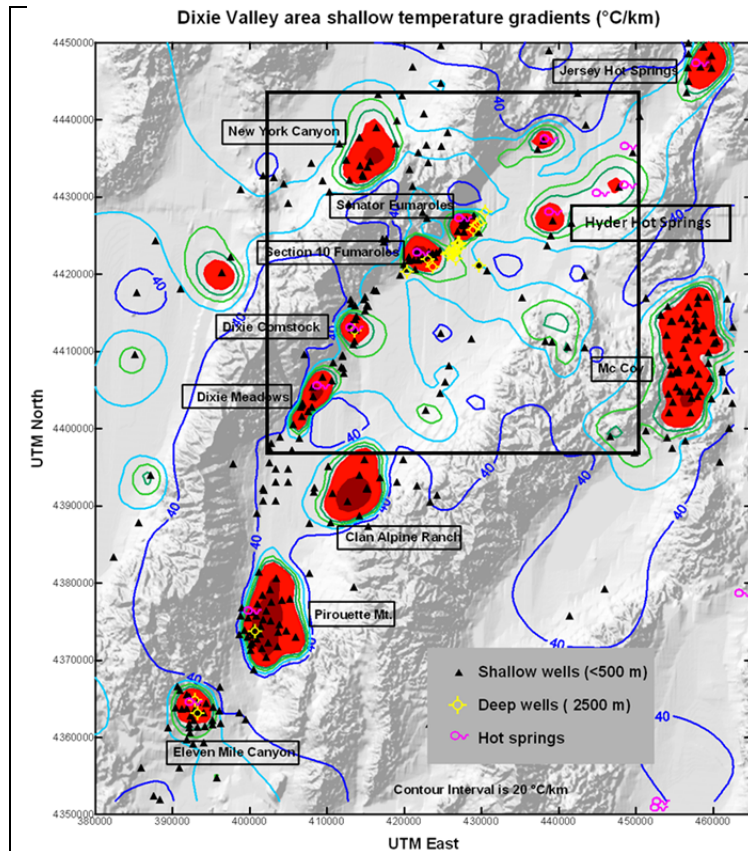


Figure 1. Dixie Valley Index Map. Areas of drilling are shown in black italic (DVPP – Dixie Valley Producing Field, DVPP – Dixie Valley Power Partners, DM – Dixie Meadows). Canyons (CC – Cottonwood Canyon, WRC – Whiterock Canyon) are identified. Geothermal electrical generation is from wells in the DVPP area. The EGS Exploration Methodology Project Area is shown as the black square. The Dixie Valley Geothermal Wellfield includes all the geothermal wells in the red outlined area; see text for a description. The figure and caption is after Blackwell et al. (2005).

### 1.3.1 Regional Setting

The DVGS lies within the northern part of the B&R and more specifically within the internally drained northern Great Basin (Figure 3). The highly extended terrain's topography is dominated by north to northeast trending ranges bounded by normal faults and separated by basins filled with Cenozoic sediments and volcanic deposits. Despite relatively thin crust typical of continental rift basins, surface elevations are relatively high, indicating underlying anomalously low mantle densities. Additional salient regional features of the DVGS are that it:

- Lies within the Central Nevada Seismic Belt (CNSB), Figure 4A, which is a zone of focused contemporary seismicity with a NNE trend extending from the Walker Lane into central Nevada and has had the largest earthquakes ( $M_w > 6-7$ ) recorded in Nevada over the last century;
- Occurs in the Greater Lahontan Basin (includes the Carson Sink and Dixie Valley) and forms the lowest topographical valleys in western Nevada (Figure 4B);
- Lies in the area of highest heat flow in the Great Basin, the Battle Mountain heat flow high; and
- Coincides with a major lithospheric boundary separating thinner crust and lower surface elevation to the west from thicker crust and higher surface elevation to the east. The  $^{87}\text{Sr}/^{86}\text{Sr}$  0.706 line, an isotopic variation line relating to the composition and age of basement rocks, divides the Precambrian cratonic rocks to the east from Paleozoic to Mesozoic accreted terrains to the west and passes directly through Dixie Valley (Figure 3).



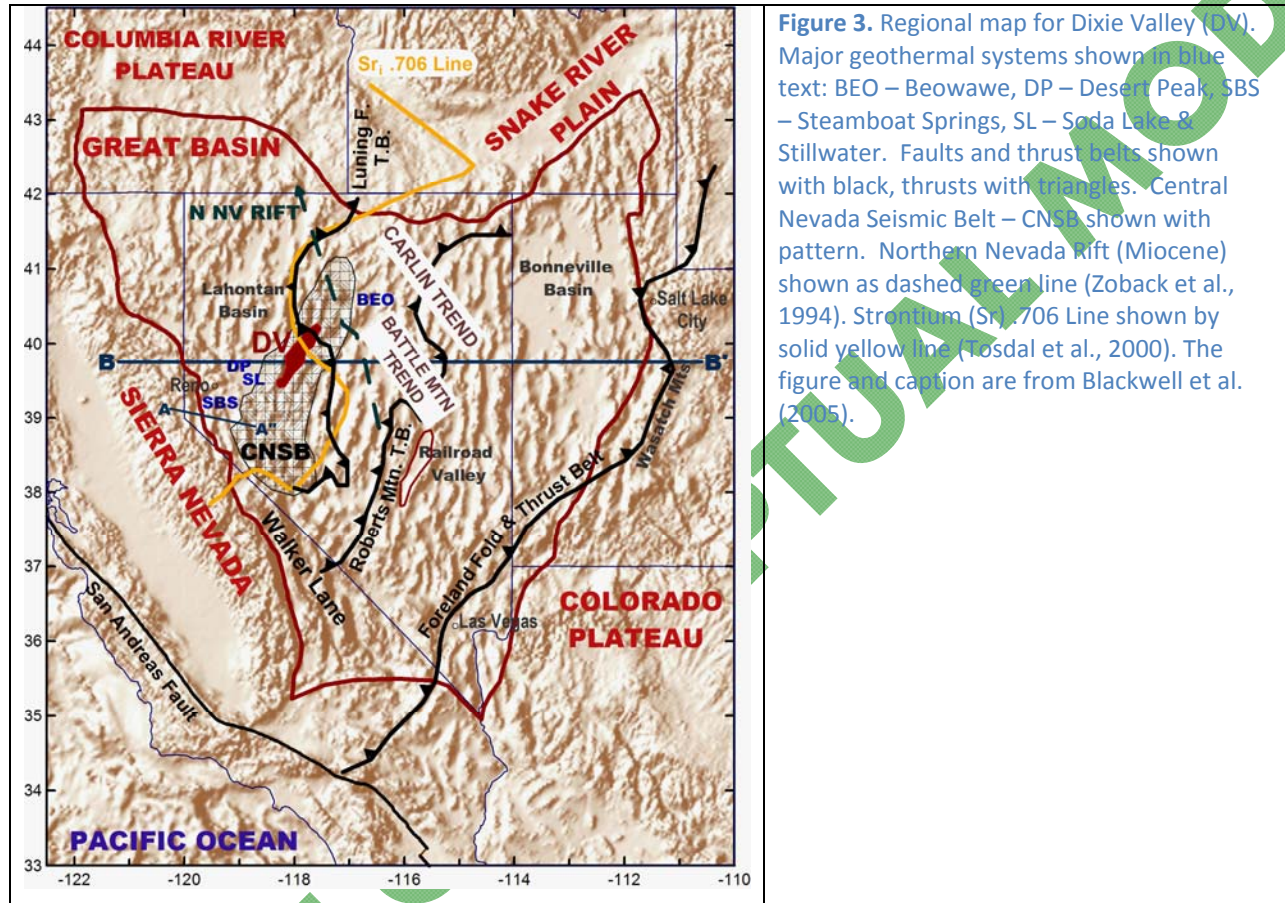
**Figure 2.** Shallow thermal anomalies and location of shallow thermal gradient holes and deep well locations in the Dixie Valley Geothermal District. Contour intervals are (20°C/km [1.5°F/100ft]). From 120 – 250 °C/km (8.75-18.5°F/100ft) the contours are a red fill and from 500°C/km (37°F/100ft) the contours are a dark red fill. Contours in the ranges are diagrammatic due to the lack of data. Well gradient locations are shown as black triangles for shallow wells (<500 meters [1640ft]) and as black circles for wells deeper than 500m. Black bounded box is the approximate boundary of the EGS Exploration Methodology Project Area. The figure and caption are after Blackwell et al. (2005).

### 1.4 AltaRock Project Team

The AltaRock team is comprised of a number of individuals with extensive expertise on the Dixie Valley Geothermal Resource in particular, as well as other geothermal systems in general. AltaRock Team members and their positions on the Team are:

- Dr. David Blackwell of Southern Methodist University, Thermal Task Leader;
- Dr. Philip Wannamaker of University of Utah, Earth Geosciences Institute, Magneto-tellurics Task Leader;
- Dr. B. M. Kennedy of Lawrence Berkeley National Laboratory, Geochemistry Task Leader;
- Dr. Trenton Cladouhos of AltaRock, Geology Task Leader;
- Dr. Ileana Tibuleac of University of Nevada Reno, Seismic Task Leader;
- Dr. Robert Karlin of University of Nevada Reno, Gravity and Magnetics Task Leader;
- Dr. Ed Isaaks of Isaaks & Co., Geostatistics Task Leader;
- Dr. Hank Ibser of University of California Berkeley, Geostatistical Consultant;
- Mr. Matthew Clyne, GIS Task Leader;
- Mr. Owen Callahan, AltaRock geologist;
- Ms. Maisie Nichols, AltaRock geologist/geophysicist;
- Mr. Mike Swyer, AltaRock geologist/engineer/GIS analyst
- Mr. Jon Sainsbury, AltaRock geologist;

- Mr. Al Waibel, Columbia Geoscience who contributed his geologic and geothermal expertise in the area and served on the Peer Review Committee;
- Ms. Susan Petty, AltaRock Energy who contributed her geothermal expertise in the area and served on the Peer Review Committee; and
- Mr. Joe Iovenitti of AltaRock, Principal Investigator.



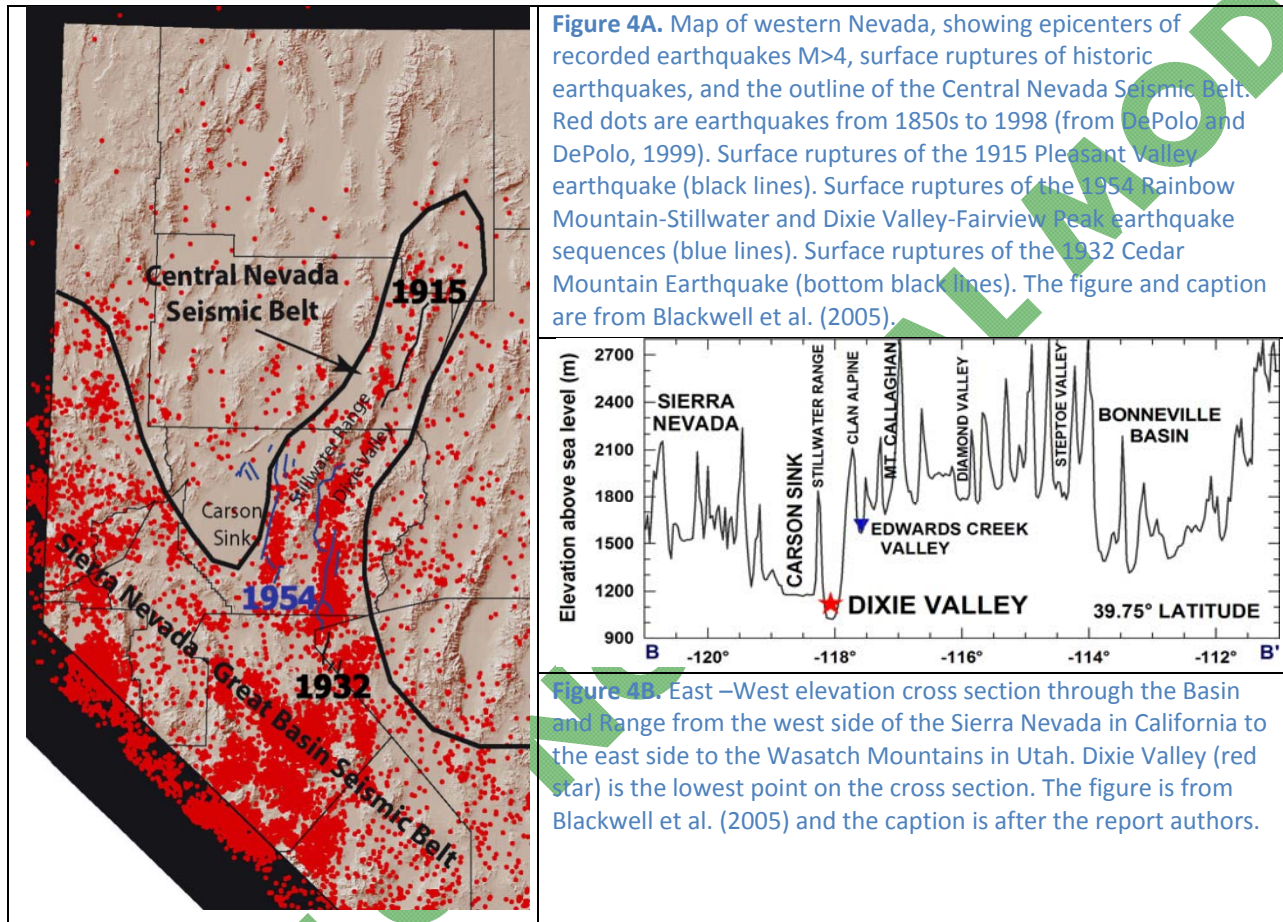
## 2. Geology

Physiographically, the Project area is comprised of from the northwest Buena Vista Valley, the Stillwater Range (more specifically Table Mountain), the northern portion of greater Dixie Valley, the Clan Alpine and Augusta Ranges and a small portion of Edwards Creek Valley to the southeast, and the Sou Hills and portion of Jersey Valley to the north (Figure 1). The general geology of the DVGW in northern Dixie Valley is described below.

### 2.1 Stratigraphy

The rocks exposed in the Stillwater Range are intersected at depth by the wells within the geothermal field. The generalized geologic map (Figure 5) highlights the exposed bedrock within the ranges surrounding Dixie Valley. A detailed geologic map of the Humboldt Lopolith from Speed (1976), centered in northern Dixie Valley is presented in Appendix 1. A preliminary geologic map of the Stillwater Range from the Nevada Bureau of Mines and Geology (NBMG) is also provided in Appendix 1. The Stillwater

Range consists of allochthonous thrust plates of Triassic and Jurassic oceanic sediments and Jurassic igneous rocks that were intruded by late Cretaceous to Tertiary granodiorite and overlain by mid-Cenozoic volcanic rocks. In Dixie Valley, the basement assemblage is overlain by late Cenozoic volcanics and basin-fill sediments, deposited during extensional events. It is noted that the discussion in this section is mostly from Waibel (1987). The generalized stratigraphy is summarized in [Table 1](#).



### 2.1.1 Basement Geology

Key features of the basement geology in the Project Area are presented from oldest to youngest. The notation for the major units as referenced in this report is also listed, e.g. (Tr) and described in [Section 7](#). A minor unit, a Paleozoic-derived section is present near the Sou Hills in the NE corner of the Project Area and is not discussed.

#### *Triassic marine sediments (Tr)*

- Deposited in a passive margin on the western continental shelf and slope;
- Interweaved tectonically with Jurassic sedimentary and igneous rocks;
- Consists of mostly meta-sediments with some interbedded volcanics;
- May be more likely to deform plastically rather than fracture when subjected to high differential stress;
- Consists of:
  - Winnemucca (Fm): feldspathic metasandstone to arkose; and

- Star Peak Group: slates, phyllites, and massive limestones which are the deepest layered rocks in northern Dixie Valley and have low permeability within faulted and sheared zones.

The majority of the Triassic meta-sediments exposed in the Project Area are derived from the Star Peak Group. While these meta-sediments are not expected have geothermal potential due to their low permeability and lack of fracturing, this formation possesses some possible localized EGS favorable characteristics within occasional zones of interbedded volcanics and intruding dioritic plutons. These intrusions are reported to contain open, but isolated faults and fractures and limited potential of hosting commercial geothermal hydrothermal production due to low permeability.

#### *Jurassic shallow marine sedimentary rocks (Jbr)*

- Boyer Ranch Formation (Jbr): mostly quartzite with some basal carbonate and minor conglomerates overlying, overridden and mechanically incorporated into the allochthonous oceanic crust;
- The quartz arenite portion is very well-indurated and fractured. It is associated with an injection zone within the northern producing field and the adjacent fumaroles, indicating that it is capable of hosting open fractures in permeable zones in association with fault planes. These characteristics and its connection with the hydrothermal system make the Boyer Ranch quartzites a suitable EGS target, while exposures are limited; and
- The Jbr is sufficiently exposed along the eastern edge of the Stillwater Range, adjacent to the producing zone including at the mouth of Cottonwood Canyon.

#### *Jurassic mafic oceanic igneous rocks (Jz)*

- Known as the Humboldt igneous complex, these rocks were originally interpreted as a locally intrusive "lopolith" by Speed (1967) but Waibel (1987) and others consider the unit to be an allochthonous fragment of oceanic crust with large blocks of ocean floor that have undergone low grade metamorphism containing spillite, keratophyre, trondhjemite-type rocks.
- Contains highly altered and fractured rocks within major fault zones;
- Tend to be very brittle and capable of maintaining good fracture permeability;
- Consists of a lower plutonic-derived section of mostly mafic crust overlain by a complex of mostly extrusive igneous rocks;
- Upper complex of igneous rocks (basalts, diorites, and gabbros) commonly occurs in thrust fault contact with the quartz arenite of the Boyer Ranch Fm (Lutz et al., 1997); and
- Overlying the plutonic rocks in the igneous complex (Lutz et al., 1997), and yielding an indicated K-Ar age of  $150 \pm 3$ Ma (Page, 1965) are sericitized and veined hornblende diorite or anorthosite, and andesitic to basaltic extrusives.

#### *Cretaceous granodiorite (Kgr)*

- Found in some of the deep wells in the geothermal field;
- Likely correlates with plutonic rocks outcropping on the western and eastern sides of the Stillwater Range in New York Canyon and Job Canyon, respectively;
- Observed in the wellfield within the footwall block of a major piedmont fault (see [Section 2.2.2](#)) in fault contact with Jurassic rocks; and
- Shows some evidence of fracturing under high differential stress as seen in bottom of well 36-14 (see [Section 6.3.2](#)); however lack of permeability and significant production in this unit in the DVGW indicates that fractures in this rock type may be prone to sealing or the existing wells

have not crossed a fault/fault zone where these rocks are fractured and these fractures are open. Thus, this unit is regarded as a strong EGS candidate.

**Table 1.** Generalized Dixie Valley and Stillwater Range Stratigraphy (compiled information from Waibel, 1987, 1999; Lutz et al., 1997; Denton et al., 1980).

Age	Lithology	Thickness
Pliocene to Recent	Basin-filling sediments composed of colluvial gravels, alluvial gravels, sands, and silts, eolian sands and silts, and lacustrine and playa silts and clays.	Up to 2,450m (8038ft)
Miocene 8-15 Ma	Basalt lava flows, agglutinates, scoria, and palagonite tuffs. Lava caps the range at elevations of up to 2500 meters and occurs in wells beneath 1830 to 2134 meters of basin-fill sediments.	90m (295ft) to > 580m (1902ft) in wells, up to 1000m (3280ft) in outcrops in Stillwater Range
	Lacustrine volcanoclastic sediments intercalated with carbonaceous siltstone; tuffaceous sediments	<152m (~500ft)
Oligocene	Silicic welded tuffs that crop out in the Clan Alpine and Stillwater Ranges, and are found below basin-fill sediments in wells.	1220m (~4000ft) in Clan Alpine Range, <300m (984ft) in Stillwater Range, <55m (180ft) in wells.
Cretaceous	Granodiorite, observed in deep wells in the geothermal field, and correlated with a pluton that outcrops on the west and east sides of the Stillwater Range.	N/A
Jurassic	Mafic complex – oceanic rocks: basalts, keratophyres, trondhjemites, albitites, plagiogranites, and gabbros.	Up to 760m (2493ft) in Stillwater Range
	Boyer Ranch Formation. Marine shelf and slope sediments - mostly quartzite, carbonates and minor conglomerate.	
Triassic	Winnemucca Formation: feldspathic metasandstone to arkose. Star Peak Group: marine sediments, carbonaceous shale, siltstone, silty carbonate rocks and massive, clean limestones.	≤3050 (10,004ft)
	Phyllite sequence, extensive black slates and shales.	>1000m? (3280ft?)

***Cenozoic silicic volcanic units, associated intrusives, (Tv) and Miocene basalts (Tmb)***

- Tilted and eroded silicic volcanic rocks overlie the Mesozoic basement rocks in the Stillwater and Clan Alpine Range (Figure 5) and are also found lying below valley-fill sediments in Dixie Valley;
- Show contemporaneous magmatism and extension with a close spatial and temporal relationship of eruption and tilting as evidenced by paleomagnetic data and K-Ar age dates (John, 1995);
- Contains Oligocene aged silicic volcanics (ash-flow tuffs and breccias) as well as interbedded volcanoclastics and occasional flows;
- Silicic volcanics exposed in the southern part of the Stillwater Range, south of the Dixie Meadows Hot Springs area and in White Rock Canyon (Figure 1), contains a tilted and eroded sequence of middle Cenozoic silicic ash flow tuffs, the associated caldera, and a subvolcanic granitic pluton (John, 1995). These silicic rocks comprise a large area of Tertiary volcanics (Tvl and Tvu in Figure 5) in the southern part of the range. This caldera may be the source of some or

all of the silicic volcanic rocks present in the Clan Alpine Range and Pirouette Mountain area, at depth in Dixie Valley, and above the Mesozoic rocks in the Northern Stillwater Range

- Within Dixie Valley, the silicic sequence present in the wellfield below the basin-fill is overlain by Miocene lake deposits, which is in turn overlain by Miocene-aged basalt; and
- Capping the Stillwater Range, the Miocene Table Mountain basalt (Lutz et al., 1997) is a nearly flat-lying (dips up to 5°N) resistant series of basaltic to andesitic flows overlying intermittent volcanoclastics, lacustrine sediments and basement. The Miocene basalt represents the youngest volcanic unit in the area and is also found at depth within the Dixie Valley wellfield.

### 2.1.2 Basin Lithology (Q-Tbf)

The Dixie Valley basin-fill is composed of moderately-to-poorly lithified sediments derived from the surrounding mountain ranges. The basin-fill is at least 2500m (8200ft) thick based on wells that reach the underlying volcanic rocks. These underlying volcanic rocks include Oligocene rhyolitic pyroclastic deposits (ash flow tuffs and air-fall deposits) which correlate to welded silicic tuffs that crop-out in the Clan Alpine and Stillwater Ranges. Miocene (8-15Ma) basalt flows and lacustrine volcanoclastic deposits overlie the Oligocene section. The overlying poorly lithified sediments include coarse colluvium and alluvial fan deposits, sandy and silty eolian deposits, and lacustrine and playa deposits. Lacustrine and playa sediments include fine-grained clays and silts in the deepest parts of the basin, and sands to gravels in shoreline beaches and bars developed at and near lake margins. A summary of the basin-fill within the producing area of the DVGW is as follows:

- ~2000m (6560ft) thick in the non-productive DVPP area ([Figure 1](#)) area; ~2500m (8200ft) thick to the northeast in the productive DVPP;
- Unsorted conglomerate, alluvial gravels, sands and silts, and coarse colluvial deposits;
  - Increase in tuffaceous better sorted sediments toward the lower section;
  - Clay matrix: contains abundant expandable smectite with some geothermal alteration to non-expandable illite;
- Miocene Basalt (8-15Ma) underlies the basin-filling sediments and is bounded by major NE-trending valley-bounding faults:
  - Thickness in wells range from ~90m (300ft) to more than 580m (1900ft);
  - Overlies Miocene lacustrine sediments; and
- Oligocene silicic welded tuffs as thick as 300m (980ft) in the Stillwater Range and overlying lacustrine, carbonaceous sediments underlie the basalt and the intermittent lacustrine sediments.

## 2.2 Structure

### 2.2.1 Tectonic History

The B&R has undergone a dynamic tectonic history beginning with a passive continental margin setting during the early Paleozoic that followed late Precambrian rifting. Accretionary events expressed by a series of orogenies, due in part to changing configurations of offshore plate boundaries included the Devonian-Mississippian Antler orogeny, the Triassic Sonoma orogeny and the Jurassic to Cretaceous Nevada Orogenies (Dickinson, 2006). In the Stillwater Range, the Boyer fault and Fencemaker thrust, are evidence of the last in this series of crustal shortening events. The B&R underwent an additional prolonged period of compressional thickening expressed by the Sevier and Laramide orogenies during the Mesozoic and early Cenozoic as the province was located in a retro-arc position. Waibel (1987) has described the structural history as exposed in Dixie Valley and identified three main phases of

deformation namely thrust faulting, early normal faulting, and current high angle normal faulting. The salient highlights of this work is outlined below.

### *Late Jurassic thrust faulting*

- Triassic shelf-related marine sediments are overridden by Jurassic oceanic crustal rocks and quartzite;
- Horizontal cataclasite zones and small scale mélangé-like features within localized shear zones are associated with the thrust faulting;
- Quartzite (Boyer Ranch Fm) associated with the Boyer Ranch Thrust lies over Upper Triassic slate and Lower Jurassic rocks. The structure, exposed in the Stillwater Range, is truncated by the range-front fault adjacent to the northern producing area and is possibly intersected by an injection well (38-32);
- Triassic to Jurassic marine siltstones, shales and volcanoclastic rocks are associated with the western originating Fencemaker Thrust overlying older rocks (Lutz et al., 1997). The low angle structure pinches out just north of the geothermal field and is likely encountered within the producing field (Lutz et al., 1997), see [Figure 16A](#).

The Dixie Valley region appears to be structurally quiet from the Cretaceous through the Oligocene. In other words, no deformation is evident in the Project Area during these time periods.

### *Basin & Range crustal extension*

- Series of early (pre-8 Ma) north-trending normal faults:
  - Exposed in the Stillwater and Clan Alpine Range as major north-trending structures;
  - Expressed as “early” narrow graben structures with north-striking trends continuing into Dixie Valley and buried beneath valley fill sediments based on geophysical data;
  - Show likely re-activation of some normal faults with a dextral strike-slip component under current stress regime;
  - Have been active before and after Oligocene silicic volcanism;
  - Shows evidence of rotation and listric faulting;
  - Contains N- to NNW-trending segments of the main range-bounding fault relating to early extension sealed under the current stress regime while NE-trending segments remain open (Lutz et al., 1997); and
  - Contain Miocene alteration, sericite (illite) and wairakite veins, events associated with N-NNW faulting and the intrusion of andesitic dikes during the initial stages of BR extension in northern Dixie Valley (Lutz et al., 1998).
- Northeast trending, late Cenozoic high angle normal faults:
  - Define the Stillwater Range and Dixie Valley physiographic features;
  - Truncate the older north-trending structures preserved in the ranges;
  - Uplift of the Stillwater Range occurred after eruption of the Miocene basalts;
  - Contain younger carbonate alteration along NE striking segments of the Stillwater Fault normal to the present day extension direction (Lutz et al., 1997);
  - Show WNW-ESE direction of extension superimposed on earlier E-W extension with the onset following late Miocene to early Pliocene basalt volcanism since about 8 Ma;
  - Exhibits a likely strike-slip component along older N-striking faults; and
  - Show localized zones of tension/compression due to combination of dip-slip (NNE faults) and strike-slip (N faults) movement.

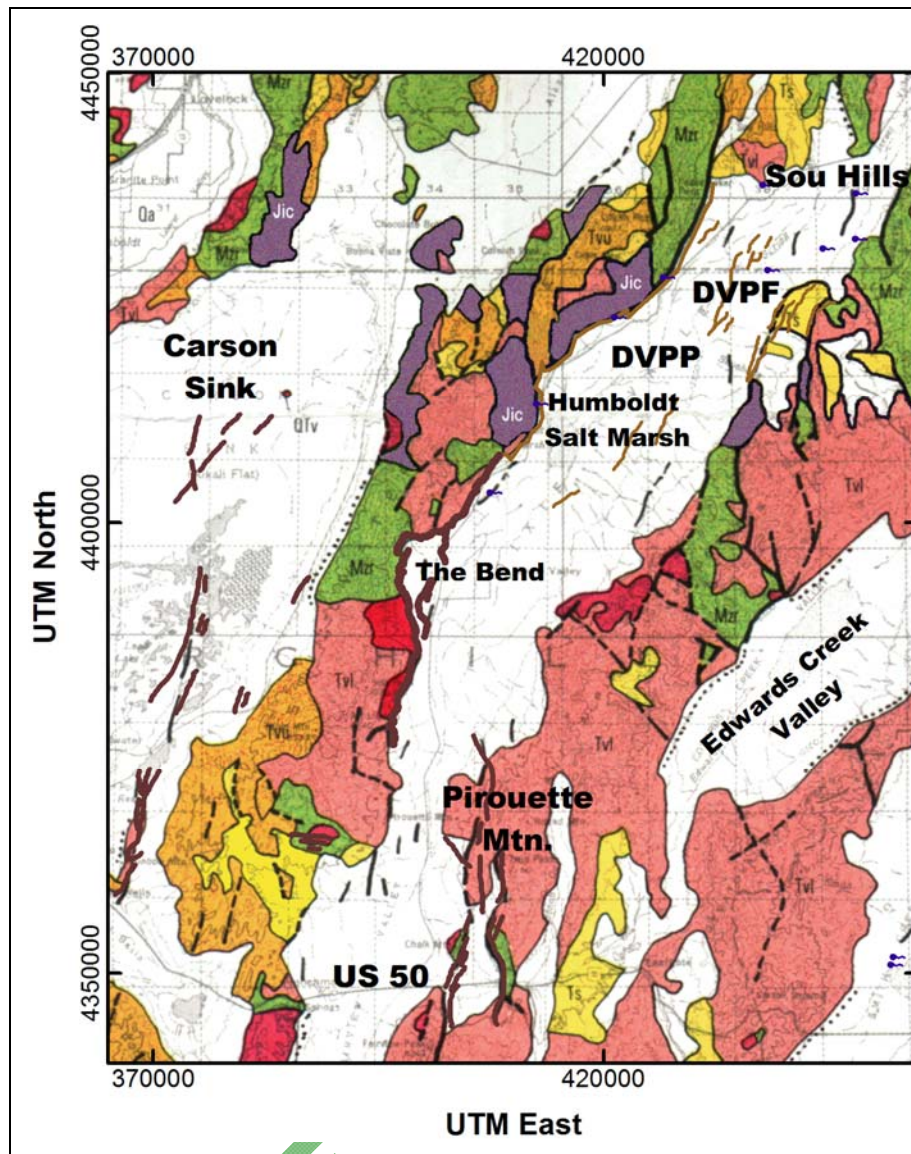


**Figure 5.** Bedrock Geology Map, modified from 1:1,000,000 Nevada Bureau of Mines and Geology map (Stewart and Carlson, 1977). Bright red denotes intrusive rocks; oranges are Cenozoic volcanics; yellow represents Cenozoic sediments; green represents Mesozoic sediments; purple represent the Jurassic section including the Humboldt igneous complex. Thick brown lines are 1954 fault breaks and thin light brown lines are other valley faults. The figure and caption are after Blackwell et al. (2005).

LEGEND	
Mz sediments	(Mzr)
Jz section/Humboldt igneous complex	(Jic)
Intrusives	(red)
Cz volcanics	(Tvl;Tvu)
Faults	(brown)

### 2.2.2 Structural Setting of the Dixie Valley Fault Zone

Early structural models for Dixie Valley (Okaya and Thompson, 1985; Benoit, 1999) identified a single, moderately east dipping ( $\sim 54^\circ$ ) normal fault bounding the Stillwater Range on its eastern side, referred to as the Dixie Valley Fault (DVF). The single fault model was based on surface fault measurements, initial interpretation of the seismic data (e.g. profile SRC-3 in [Section 3.5.1, Figure 17B](#)), and the assumption that the producing wells located a few kilometers basinward were connected to the surface scarp of the range-front fault. Blackwell et al. (2005) proposed a steeply dipping, more complex structural setting consisting of a range-front fault and a piedmont fault based on wellfield data (see [Sections 6.3.2 and 7](#)) and gravity and magnetic data (see [Section 3.1](#) through [3.5](#)). This complex fault zone is referred to as the DVFZ; see discussion below. In the DVGW, the evidence favors two or more steeply dipping faults for the DVFZ; however,  $>20\text{km}$  (12mi) to the south, at Dixie Meadows, seismic profiles have been interpreted by Abbott et al. (2001) to support the hypothesis that the range-front fault segment of the Dixie Valley Fault Zone (DVFZ) is a seismically active, low angle normal fault ([Figure 6a](#)). Because Dixie Meadows is in the southernmost portion of the project area, this apparent controversy is significant to this study.

The Dixie Meadows area is at the northern end of a NNE-striking DVFZ segment that produced the 1954 Fairview Peak-Dixie Valley seismic event (see [Section 2.2.2](#)). Based on two seismic lines in the area, Abbott et al. (2001) interpreted a 25-30°SE dip ~10km (6mi) south of Dixie Meadows. Based on this interpretation, Kennedy-Bowdoin et al. (2004) also showed the range front fault with a ~35°SE dip at Dixie Meadows. Geophysical data suggests a more complex multi-fault setting at this location. Well 45-14, 10km to the north and the southernmost well in the DVGW, lies adjacent to a major north-striking structure within DVFZ that didn't rupture during the latest seismic event and encountered lithologies that require steeply dipping faults, as it lies within a structural block between a north-trending segment of the range front fault and the piedmont fault; see [Section 5.3](#), [6.1.1](#) and [6.3.2](#) for a more detailed discussion.

There are two possible explanations for the interpreted change in dip from near vertical at 45-14 to low angle at Dixie Meadows and to the south:

1. The dip change over the 10km gap is accurate. The change in dip could have stopped the 1954 event rupture and may also be related to the change in fault strike from NE to N. This would also suggest that an accommodation zone between the intervening structures is present at Dixie Meadows as evidenced by numerous surface springs.
2. The seismically-inferred low angle fault could have been a mis-interpreted basalt reflector, a shallow dipping bedrock contact between the range front and piedmont fault, a buried landslide plane or a step-down zone of faulting that agrees with the general trend recognized along the DVFZ. Because our Project Area mostly coincides with the seismic gap (see [Figure 6a](#)) and not the 1954 earthquake segment, we do not need to decide between the two explanations here. However, a planned seismic survey in the area (under Task 4) may provide additional insight. The baseline conceptual model ([Section 7](#)) postulates a steeply dipping multi-fault model along the entire length of the DVFZ through the DVGW as required by the geologic, drilling, and geophysical evidence available within the Project Area.

The DVFZ is considered to be a series of step-down faults (complex system of subparallel steep dipping faults) including faults within the Stillwater Range, at the topographic break between the range and the valley (the range-front fault) and the piedmont faults east of the range front within Dixie Valley (Wallace and Whitney, 1984; Blackwell et al. 2005). Empirical evidence strongly suggests, and Blackwell et al. (2005) show that the DVFZ is complex fault zone, dominated, though not completely composed of, strands of steep normal faults. To the south of Hare Canyon (see [Figure 1](#) and [6a](#), adjacent to Dixie Hot Springs [HS]) the 1954 fault scarps suggest much longer strands of normal faults than are observed to the north, from between Hare Canyon and the northern end of Dixie Valley. A generalized cross section within the DVPF ([Figure 6b](#)) shows a set of steeply dipping structures representing the DVFZ bounds the western edge of Dixie Valley. Within the range young, brittle, steeply east dipping normal faults cut the bedrock just west of the DVPF. Blackwell and others (Waibel, pers. comm., 2010) suggest these intra-range faults possess thermal significance due to the exposed hydrothermal alteration and zones of fumarole activity as the structures are considered to play an important role in the range structure. A complex system of steeply dipping normal faults has been mapped (see [Figure 14](#)) adjacent to the DVPF that show evidence of recent alteration (Plank, 1998). Mapping efforts and cross-sections from Gabe Plank (GBC Workshop, 2002) show only one possible active intra-range fault in this area, and considers the other faults in the range to be inactive splays of the main fault, which is common in extensional areas.

Besides the main, well exposed range-front fault bounding the western edge of Dixie Valley, a major steep piedmont fault and other discontinuous strands of normal faults occur a few kilometers basinward. The term piedmont fault, used by Blackwell and others to define the zone of faulting

occurring parallel to the range-front within the pediment surface (alluvial slope derived from the range), applies to a blind fault/fault system that doesn't break the surface like the well-exposed range-front fault. Geophysical and drilling data (described in Sections [3.1](#), [3.2](#) and [6](#), respectively) provide evidence that this piedmont fault takes up the majority of the normal displacement along the structure and plays a crucial role in the producing field. The piedmont fault is buried by a thin cover of sediments and shows no surface expression. Within this report, the DVFZ refers to the 2-4km (1.2-2.5mi) wide zone of deformation bounding the northwest edge of Dixie Valley including the active intra-range faulting, the range-bounding fault, a major piedmont fault, and other associated faults and fracture zones.

### *Dixie Valley Fault*

The Dixie Valley Fault (DVF), also referred to as the Stillwater Fault (SF), occurs along the western side of Dixie Valley and represents the main surface-bearing and range-bounding component of the DVFZ. The fault separates the bedrock of the Stillwater Range from the late Cenozoic sediments that fill the basin. Where exposed at the surface, the fault is steeply dipping to the east. The fault is one of the most active faults in the B&R with the most recent activity occurring as the Dixie Valley-Fairview Peak earthquake in 1954. The long-lived structure (intermittent for several million years) is marked by historic, Holocene, and/or Pleistocene fault scarps that cut and mostly vertically offset late Pleistocene and early Holocene alluvial fans and pediment surfaces. The trace of the fault extends from the southwest side of the Sou Hills at the north end of Dixie Valley ([Figure 1](#)) to the south end of the valley about 10km (6mi) north of highway US 50, a distance of about 80km (50mi). Other implications of the DVF are listed below.

- The DVF is the primary range-bounding, normal fault, between the Stillwater Range and Dixie Valley;
- The maximum total vertical displacement between the Stillwater Range and bedrock beneath Dixie Valley sediments in this target study area is approximately 3000m (9800ft), since Late Miocene, based on the top of the elevation of Late Miocene basalt flows observed in the Stillwater Range, and the depth these basalts were intersected in some of the deep wells in the producing field; and
- Deep pull-apart zones occur along the western edge of Dixie Valley and are associated with the most recent extensional regime (WNW-ESE). These pull-apart structures show the greatest vertical off-set, including the 3000m off-set in the Miocene basalts mentioned above. This amount of normal fault off-set is not a continuous characteristic of the DVFZ.

### *Seismicity*

The DVF is part of a 250-km (154-mi) long system of faults in Nevada that have experienced historic surface rupturing earthquakes and that help to define the Central Nevada Seismic Belt - CNSB ([Figure 3](#)). The historical seismicity of Dixie Valley has been well-studied (see [Section 3.5](#)). Nearby earthquakes include the:

- 1915 Pleasant Valley earthquake to the north, which ruptured on a westward dipping fault system that extends into the northernmost Project Area;
- July 6 and August 23, 1954 Rainbow Mountain earthquakes to the southwest;
- December 16, 1954 Dixie Valley-Fairview Peak earthquakes to the south of Dixie Valley; and
- The Fairview Peak earthquake (Mw=7.0) was followed a few minutes later by the Dixie Valley earthquake (Mw =6.8) as the event propagated (south to north) into southern Dixie Valley. The northernmost ruptures terminated near Dixie Meadows.

Surface ruptures produced from these seismic events bound the western edge of Dixie Valley and include the 1954 break, 1915 ruptures within northern Dixie Valley and surface traces relating to a pre-historic “Bend Event” occurring during Holocene time (2.2 – 2.5 ka), [Figure 6a](#).

### *Stillwater Seismic Gap (SSG)*

The Dixie Valley geothermal system lies adjacent to a 45-km (28-mi) segment of the DVF, along which no evidence for recent surface-rupturing faulting has been found. This segment referred to as the Stillwater Seismic Gap, is between the 1915 Pleasant Valley and 1954 Dixie Valley earthquake rupture zones (Caskey and Wesnousky 2000). It was informally reported at the GBC Geothermal Workshop in 2002, that a vigorously spouting geyser briefly formed above the geothermal system during the 1954 seismic event. While this is based on unverified reports as the area was largely uninhabited at the time, this supports the opening of permeable pathways at depth within the Stillwater Gap during seismic events, regardless of if the rupturing produced a surface trace. Characteristics of the SSG include:

- No evidence of Holocene/historic surface ruptures has been found;
- Seismic creep may relieve stress and maintain fracture permeability or displacement is accommodated by a buried structure;
- Alternatively, faulting could have been confined to the range block where it would be more difficult to find and assign a date to; and
- The “Bend Event” (2.2-2.5 ka) likely propagated through this area, but is now eroded ([Figure 6a](#)).

### 2.2.3 Intra-basinal Faulting

Additionally, a number of intrabasin faults not directly associated with the DVFZ have also been recognized and assumed to play a role in accommodating extension within the valley. This includes the Buckbrush Springs fault system, a major surface-bearing system of intrabasin faults, located basinward to Dixie Meadows on the eastern edge of the Humboldt Salt Marsh and south of the producing area ([Figure 6a](#)). The majority of the intrabasin faults are northeast striking, show mostly eroded surface expressions, are often associated with springs, cut alluvial sediments, and are interpreted as both east dipping and antithetic (west dipping) with a down to the west displacement direction. Major west dipping intrabasin faults bound the southeastern edge of the valley-fill sediments and underlying volcanics in Dixie Valley. Additionally geophysical evidence and surface scarps show that the major north-trending structures present in the Stillwater Range also continue into Dixie Valley. A more detailed discussion on these intrabasin faults within Dixie Valley is in the following Geophysics section, as they are mostly recognized by geophysical methods.

This structural section has focused on pre-existing work and interpretations that represent the general consensus of the structural setting in Dixie Valley. Models have been introduced that are no longer relevant in order to complete the discussion of the public domain data. While most work has previously referred to the major structure as the DVF or SF, herein the authors have introduced and described a complex set of steeply dipping structures consisting of two or more faults and referred to as the DVFZ. A re-interpretation of the structural data will be presented within Section 7 of this document that represents recent analysis from the AltaRock Team. Additionally, major observations are noted that describe the interaction and significance of the presently-active northeast trending structures with the earlier set of north-trending structures. These interpretations are the first attempt to characterize the relationship between the intersection of major fault trends that produce zones of compression and dilation in the DVFZ, and the relation to the occurrence of geothermal cells in Dixie Valley.

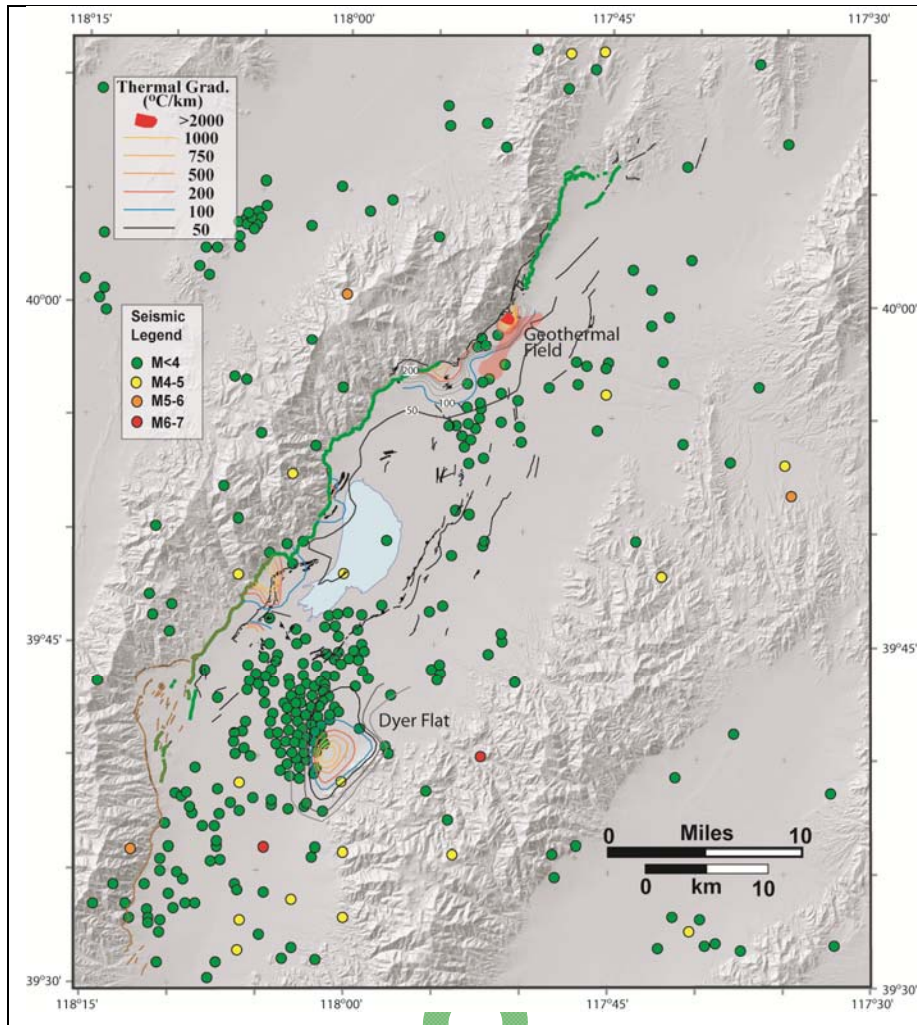


**Figure 6A.** Presented are the area seismicity, faults, earthquake epicenters, geothermal gradient, and range front fault scarp. Brown line represents northernmost surface ruptures of the 1954 Dixie Valley-Fairview Peak earthquake sequence; Green line represents the Bend Event (-2.5ka), which corresponds to the Stillwater Seismic Gap. Clusters of earthquake epicenters (dots) occur near the Dyer Flat thermal anomaly and south of the DVPF. Both are near where the intrabasin fault system joins the Dixie Valley fault system and an area of high geothermal gradients. The figure and caption are from Blackwell et al. (2005).

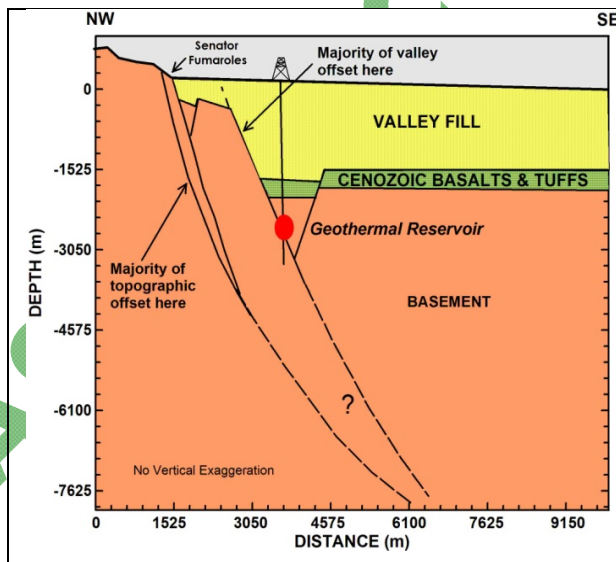


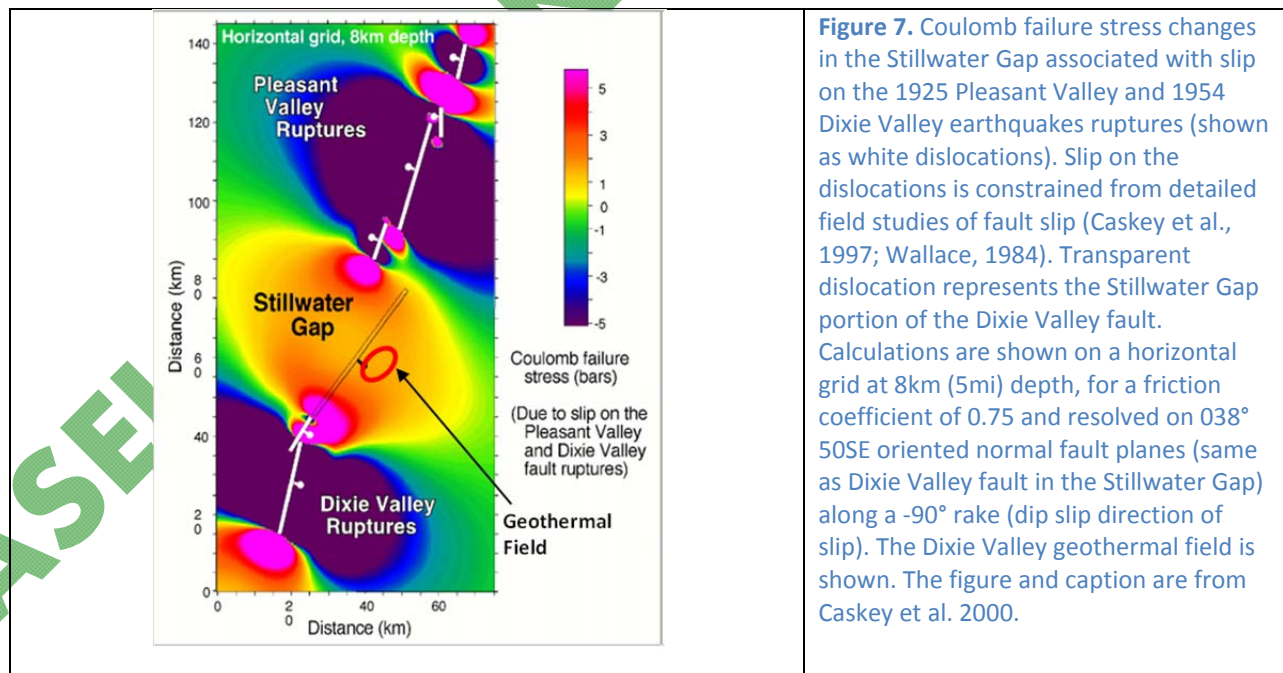
**Figure 6B.** Simplified cross section of Dixie Valley Producing Field showing valley fill sediments, Cenozoic volcanics deep in the section, basement and interpretation of fault structure (dashed lines). The figure and caption are from Blackwell et al. (2005).

### 2.2.4 Stress Modeling

Caskey et al. 2000 and Wesnousky et al. 2003 performed a detailed study on fault slip and the required stress conditions that would result from the 1915 Pleasant Valley ruptures and the 1954 ruptures and seismic activity on the Dixie Valley Fault (range-front fault segment), assuming that no slip occurred along the Stillwater Seismic Gap. The study assumes a single fault model with a 50° dip, although the majority of evidence presented herein agrees that extension is accommodated along several steeper dipping structures within the DVFZ. It is likely that slip occurred on piedmont faults within the Stillwater Gap segment of the DVFZ during the latest 1954 seismic event, which would significantly lower the expected accumulated stress in this area. The geothermal field is located within the central portion of the Stillwater Seismic Gap, where no surface rupturing has occurred from the last two major seismic events. Some main points from this analysis are described below and shown in [Figure 7](#).

- The analysis determined an increased failure stress on faults and fractures associated with the geothermal reservoirs with contributions from both increased shear stress and decreased fault-normal stress;
- Large increases in failure stress are concentrated between the Holocene rupture endpoints of the DVF, i.e. range-bounding fault segment of the DVFZ;
- Fault-parallel fractures within the DVFZ are critically stressed for failure and hydraulically conductive within the geothermal field;
- The larger stress changes occur at the north and south ends of the seismic gap near the rupture endpoints (>5 bars); and
- The DVFZ and parallel fractures in the vicinity of the DVGF have experienced large positive stress changes (>10 bars) and are most strongly affected by tensile stress changes.

A re-interpreted Stress Modeling analysis that builds on this model and assumes slip did occur within the SSG can be found in [Section 7.2.2](#).



### 3. Geophysics

A variety of geophysical data collected in the Dixie Valley area and specifically within the wellfield were detailed in the Blackwell et al. 2005 comprehensive report. These surveys included Gravity, Magnetics, Magnetotellurics and Seismic, Thermal Modeling, and a variety of remote sensing techniques. The important aspects and results are presented in this section.

#### 3.1 Gravity

Complete Bouguer gravity anomaly data was obtained from three public domain sources: (1) USGS Gravity Data of Nevada (Ponce, 1997); (2) UTEP PACES GEONET Gravity and magnetic data set repository - Gravity and magnetic data base of the United States <http://irpsrvgis00.utep.edu/repositorywebsite/>; and (3) gravity surveys compiled by David Blackwell at SMU (pers. comm., 2010). A complete Bouguer anomaly (CBA) map of the region ([Figure 8](#)); shows positive values within the ranges (bedrock) and negative values in the valleys (poorly consolidated sediments) arising from distinct density contrasts. Thus the regional gravity data defines the shape of the Dixie Valley basin and confirms that the basin is asymmetrical. There appears to be little evidence of a distinct regional trend.

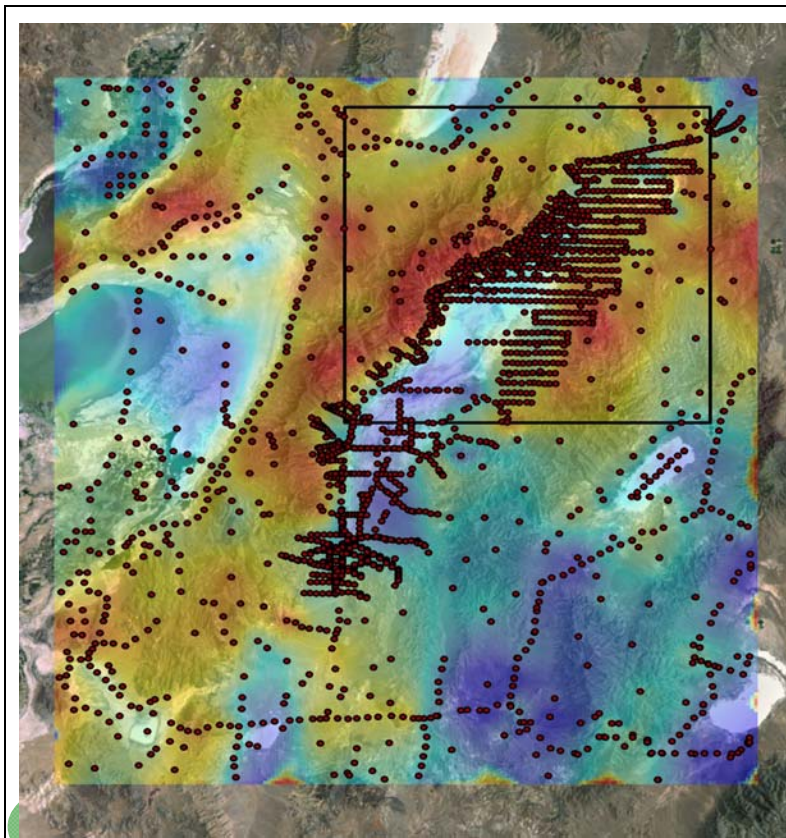


**Figure 8.** Complete Bouguer anomaly map of the region around Dixie Valley, NV. Highs (warm colors) correspond to the bedrock in the ranges, while lows (cool colors) represent loosely consolidated basin fill sediments. The color scale ranges from -129 to 0233 mgal. The Project Boundary is shown in black. The location of gravity stations are shown as red dots.

The horizontal gradient of the gravity field is particularly useful in locating contacts of greatest density contrast, with a high peak shown over sharp, vertical edges, which are presumably buried faults. A map detailing the maximum horizontal gradient shows the regions of gradient maximas (warm colors) occur along intrabasin faults as well as along the main range front fault ([Figure 9A](#)). The maximum horizontal gradient map is compared to the total magnetic anomaly map in [Figure 9B](#).

A continuous gravity gradient occurs on the west side of the valley parallel and basinward to the range front fault and defines the main structural offset between the basement and valley fill. The location coincides with segments of the fault imaged by the aero-magnetic data (see [section 3.2](#) and [Figure 11](#)) and strongly implies that the major piedmont faults within the valley accommodate most of the displacement between the range front and the valley bottom. The east side of the basin does not have a clearly defined gravity gradient maxima due to a number of potential factors including higher rates of subsidence, widely spaced displacement faults described as a zone of step-faulting (Wallace and Whitney, 1985; Blackwell et al. (2002; 2005), and the occurrence of large bodies of mafic rock beneath shallow basin-fill sediments that control much of the gravity signature. Salient features of the gravity data are:

- Emphasizes the asymmetry of the basin and confirms that the western side of Dixie Valley is fault controlled along a steeply dipping structure;
- Location of the maximum gravity slope is generally offset (1-3km [0.6-1.9mi]) into the valley from the range-valley contact and main range front fault;
- Major piedmont faults parallel to the trace of the range-front fault accommodates most of the displacement along the structure. These faults are where most of the geothermal producing wells are found; and
- While the principal fault trend is NE-SW, a gradient high in the south-central valley shows a more northerly trend, perhaps representing an earlier rifting episode when maximum stresses were oriented N-S ([Figure 9A](#)).

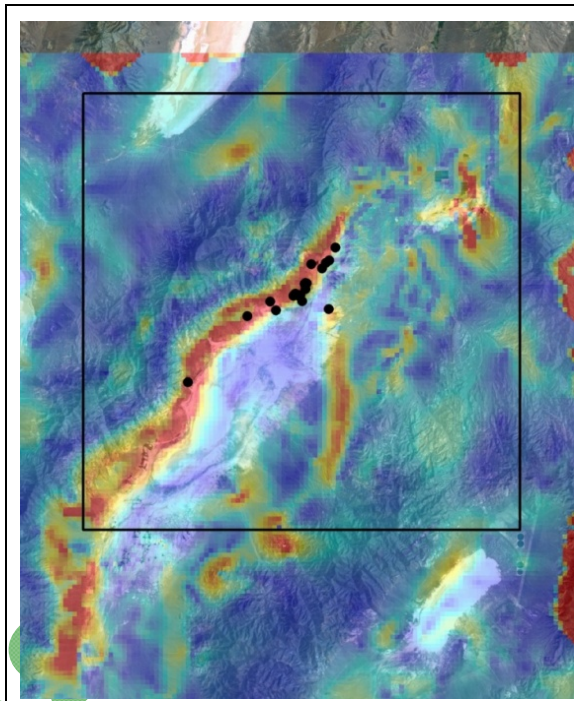


**Figure 9A.** CBA Total Horizontal Gradient of Dixie Valley. Well locations are shown by black dots, within the EGS ExplorMetodology Project Area area (black outline) superimposed. Warm colors represent areas of dense horizontal gradients.

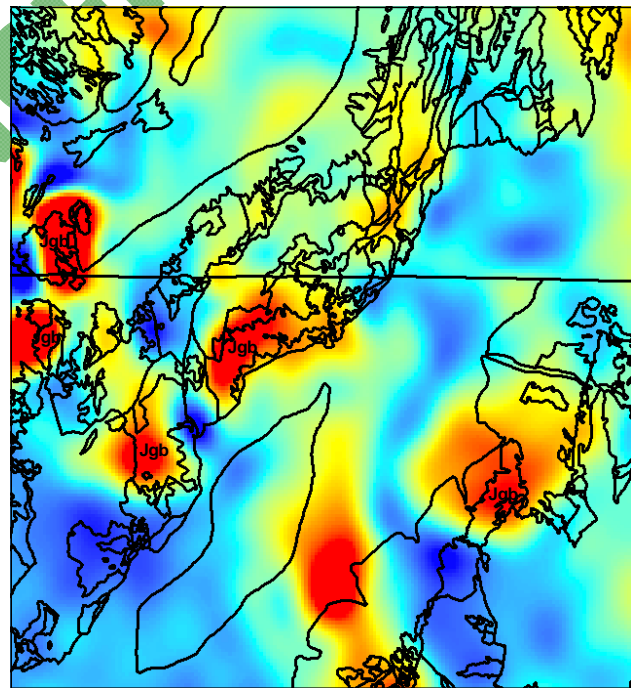


**Figure 9B.** Outline of geologic formations overlain on a total magnetic anomaly map of PACES data. Magnetic highs are primarily associated with exposed Jurassic igneous rocks (Jgb) in the Stillwater and Clan Alpine ranges.

## 3.2 Aero Magnetics

Aeromagnetic data were obtained from four sources: (1) The USGS magnetic database of North America (here referred to as the PACES) which was continued to a 300m (980ft) elevation (UTEP PACES GEONET <http://irpsrvgis00.utep.edu/repositorywebsite/>, 2011); (2) a USGS-sponsored helicopter survey of Dixie Valley (here referred to as HELIMAG) flown at 120m (390ft) (Graugh; 2002; <http://pubs.usgs.gov/of/2002/ofr-02-0374/>); and older aeromagnetic surveys flown by fixed wing aircraft at 1680 and 2290m (5500 and 7500ft) (Blackwell, pers. comm., 2010).

The total field anomaly map of the region shows discrete sub-circular magnetic highs (Figure 9B). The mafic Jurassic volcanics appear to be the only strongly magnetized units in the Dixie Valley area. In the Stillwater and Clan Alpine Ranges, the magnetic highs are almost exclusively associated with the Jurassic volcanic units, especially gabbros. The shape and intensity of the highs suggests that the volcanic units are positively magnetized which is consistent with their emplacement during the normally magnetized Jurassic Quiet Zone period. A number of magnetic highs are observed in Dixie Valley which presumably are associated with buried Jurassic igneous rocks. The distribution of Tertiary volcanics shows only a weak spatial correlation to the anomalies except in one case, while the widely distributed Tertiary rhyolites and limited Cretaceous granite exposures show no spatial association.

Graugh (2002 a,b), Smith et al. (2002), and Blackwell et al. (2007) analyzed the high resolution HELIMAG data within Dixie Valley to delineate intra-basin faults which may provide permeable conduits for geothermal fluids (Figure 10). The horizontal gradient method when applied to the data reveals steep magnetic gradients over near-vertical contacts (faults), shown on the horizontal gradient map as long narrow ridges (Figure 11A). Some of the shallow faults imaged in aero-magnetic data directly correlate to the surface traces of mapped faults (Figure 11B). The position and distribution of faults indicated by the magnetic data and mapped surface faults are consistent with a dominant northeast trending fault pattern (Figure 11C). The set of faults defined by magnetic anomalies at shallow depths must be very young, late Pleistocene or Holocene, and thus must be part of the presently active B&R system of extensional faulting. While the aero-magnetic data does locate a number of intra-basin faults, it does not extensively image a large piedmont fault on the west side of the valley as expected by the gravity and well data (Blackwell et al., 2005).

### 3.2.1 Intrabasin faults

Conclusions of the HELIMAG aeromagnetic data in relation to intra-basin faulting are:

- Northeast trending, steeply dipping and sub-parallel to the range-front fault;
- Show curved and branching shapes;
- Turn to a more easterly strike in northern Dixie Valley (including range-front) indicating a change in fault geometry at the northern end;
- Terminate south of the survey area as motion and displacement is transferred to nearby faults (to the west or east); and
- A north-trending structure occurs on the eastern bounding edge of Dixie Valley and projects near well 62-21 (Figure 9A). It likely intersects the main Dixie Valley western-bounding structure within the northern producing zone and coincides with known surface faults. The total field magnetic data indicates that the magnetic highs correspond to the Jurassic igneous suite.
- The Humboldt Salt Marsh is the deepest part of the valley (surface) down-dropped by faulting within the basin;
- Faults broaden and branch into a classic “horsetail” shape at the southern strands of the Humboldt Salt Marsh; and

- The Marsh lies at the southern end of a deep structural block bounded by fault systems that are projected to merge near the geothermal field at its most northern end.

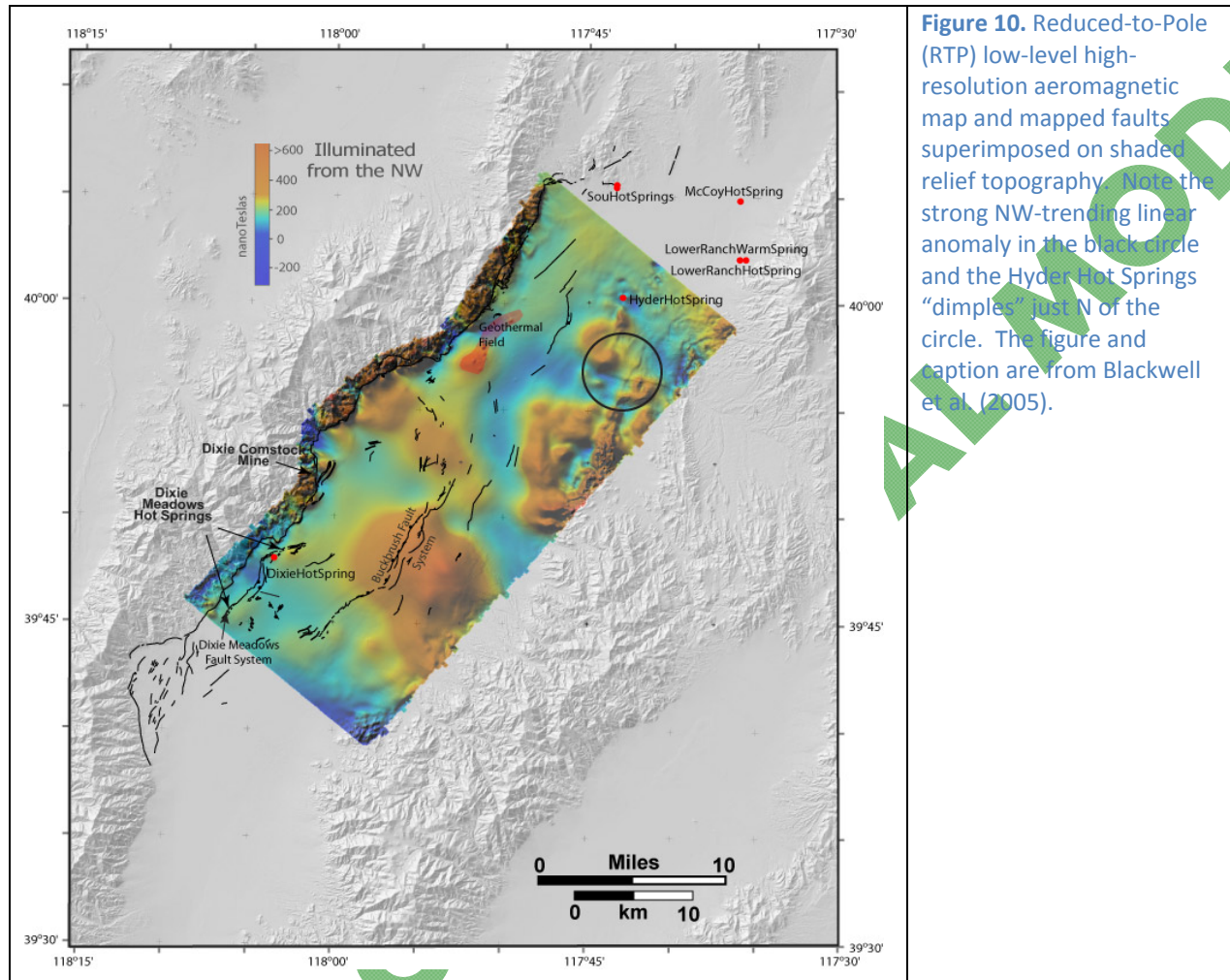


**Figure 10.** Reduced-to-Pole (RTP) low-level high-resolution aeromagnetic map and mapped faults superimposed on shaded relief topography. Note the strong NW-trending linear anomaly in the black circle and the Hyder Hot Springs “dimples” just N of the circle. The figure and caption are from Blackwell et al. (2005).

### 3.2.2 Magnetic Anomalies

Aero-magnetic mapping has the ability to image magnetic anomalies within the subsurface. Negative anomalies may result from the alteration of magnetic minerals along the walls of geothermal fluid channel pathways that transect mafic dominated sediments. Alternatively, they can also be linked to a high titanium (Ti) content in the mafic minerals making the mineral weakly magnetic and/or reversely magnetized rocks. Negative anomalies are present near Hyder HS in the northern valley and near Dixie Meadow HS (Figure 10). The smaller anomaly near Hyder HS suggests limited interaction of hot waters with magnetic wall rocks. The second area near Dixie Meadows lies within a higher geothermal gradient just southwest of the DVPF and suggests a higher degree and longer-lived geothermal system that has removed a large volume of magnetic minerals. The high-resolution aero-magnetic map (Figure 12) is focused within the DVPF and DVPP and salient features identified are:

- A large positive anomaly near the southern part of the geothermal field likely reflects strongly magnetic mafic rocks beneath the valley fill (occurring in the range directly to the west);
- A large negative anomaly (northern part of geothermal field) due to:
  - weakly magnetic sediments, reversely magnetized rocks; and/or

- o destruction of magnetism by high temperature alteration of magnetic mineral.

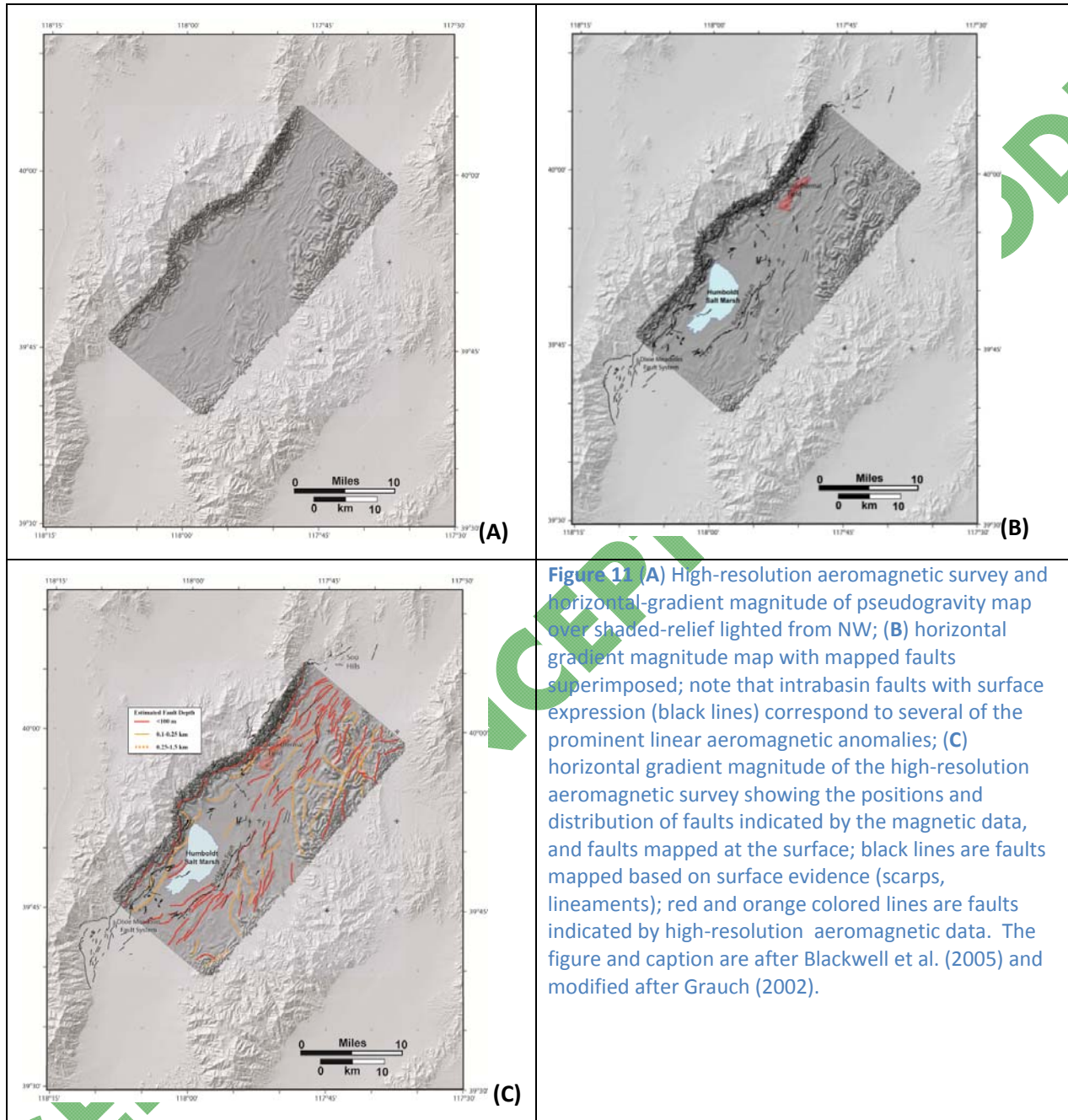


**Figure 11** (A) High-resolution aeromagnetic survey and horizontal-gradient magnitude of pseudogravity map over shaded-relief lighted from NW; (B) horizontal gradient magnitude map with mapped faults superimposed; note that intrabasin faults with surface expression (black lines) correspond to several of the prominent linear aeromagnetic anomalies; (C) horizontal gradient magnitude of the high-resolution aeromagnetic survey showing the positions and distribution of faults indicated by the magnetic data, and faults mapped at the surface; black lines are faults mapped based on surface evidence (scarps, lineaments); red and orange colored lines are faults indicated by high-resolution aeromagnetic data. The figure and caption are after Blackwell et al. (2005) and modified after Grauch (2002).

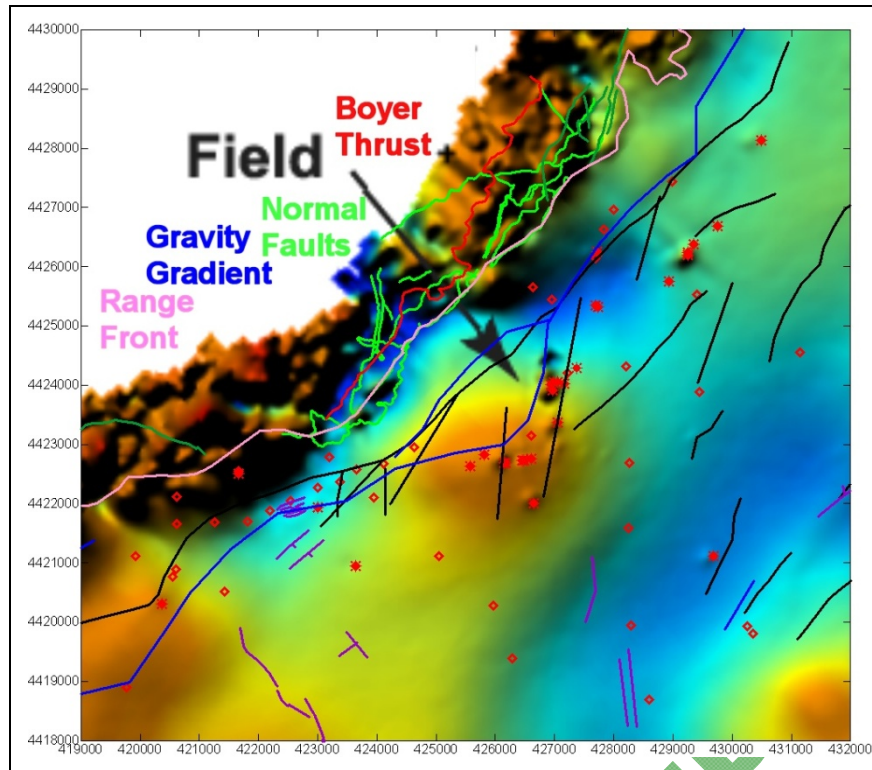


**Figure 12.** Detail of high resolution aeromagnetic map in the DVPP and DVPF areas (Figure 1) enlarged from Figure 10 and overlain with color-coded structures. Non-labeled features include: black lines are geophysical-inferred structures, purple lines are surface faults, red diamonds are temperature gradient holes (TGHs), and red stars are wells. The figure and caption are after Blackwell et al. (2005).

### *Dixie Valley Faulting*

The combined horizontal gradients from both the gravity and magnetic data provide a detailed picture of the structure of Dixie Valley (Figure 13). The horizontal gravity gradient maximums show both north and north-east trends and coincide with surface faulting and the position of the horizontal gradients for the HELIMAG data. Smith and Blackwell (2001) have constructed a structure compilation map of Dixie Valley that shows the interpreted major structures indicated by the areas of dense gravity and magnetic horizontal gradients, seismic profiles and the surface geology (Figure 14). The faulting has been broken up into two dominant trends, north-east striking steep normal faulting reflecting the current stress regime superimposed over an earlier episode of north-south faulting. The importance of these two dominant fault trends and the significance of their associated intersections will be discussed in more detail in Section 7.2.1.

### *3.3 Gravity and Magnetics*

The CBA gravity data and the HELIMAG aeromagnetic total field anomaly data representing the baseline gravity and magnetic data set were jointly modeled in along five lines labeled A-A' to F-F' in the geothermal area to create a 2½ D geophysical model consistent with the surface geology and well data (Figure 15A). The modeling was performed along pre-existing geologic cross-sections through the wellfield, with lines C-C' through F-F' lying perpendicular to the strike of the Stillwater Range and the Dixie Valley range-bounding fault and lines A-A' and B-B' parallel to the range. It was not possible to model the magnetics of the range-parallel line B-B' because of 3-D effects due to the extensive Jurassic section exposed in the southeastern part of the range.

The modeling was performed by Dr. Bob Karlin, the Gravity and Magnetics Task Leader using a compilation of pre-existing data. Gravity modeling was done using the GM-Sys module of the Oasis Montaj program from Geosoft Inc. Measured gravity models of unknown shape were forward modeled by trial and error adjustment of density and polygon vertices. Once the fit was considered close, XZ

positions were optimized using inverse methods. The objective was to minimize the RMS error between observed and computed values. A fit was considered acceptable if the misfit  $F$  was less than 1% ( $F=100 \times \text{RMS error}/\text{profile gravity data range}$ ). As described in the GM-Sys manual, 2-D models may be visualized as a number of tabular prisms with their axes perpendicular to the profile; blocks and surfaces are presumed to extend to infinity in the strike direction. 2½-D modeling, as implemented in GM-SYS, allows the prisms to be truncated at some distance in the plus and minus strike directions ( $\pm Y$ ). It also allows the strike direction to be skewed relative to the profile azimuth.

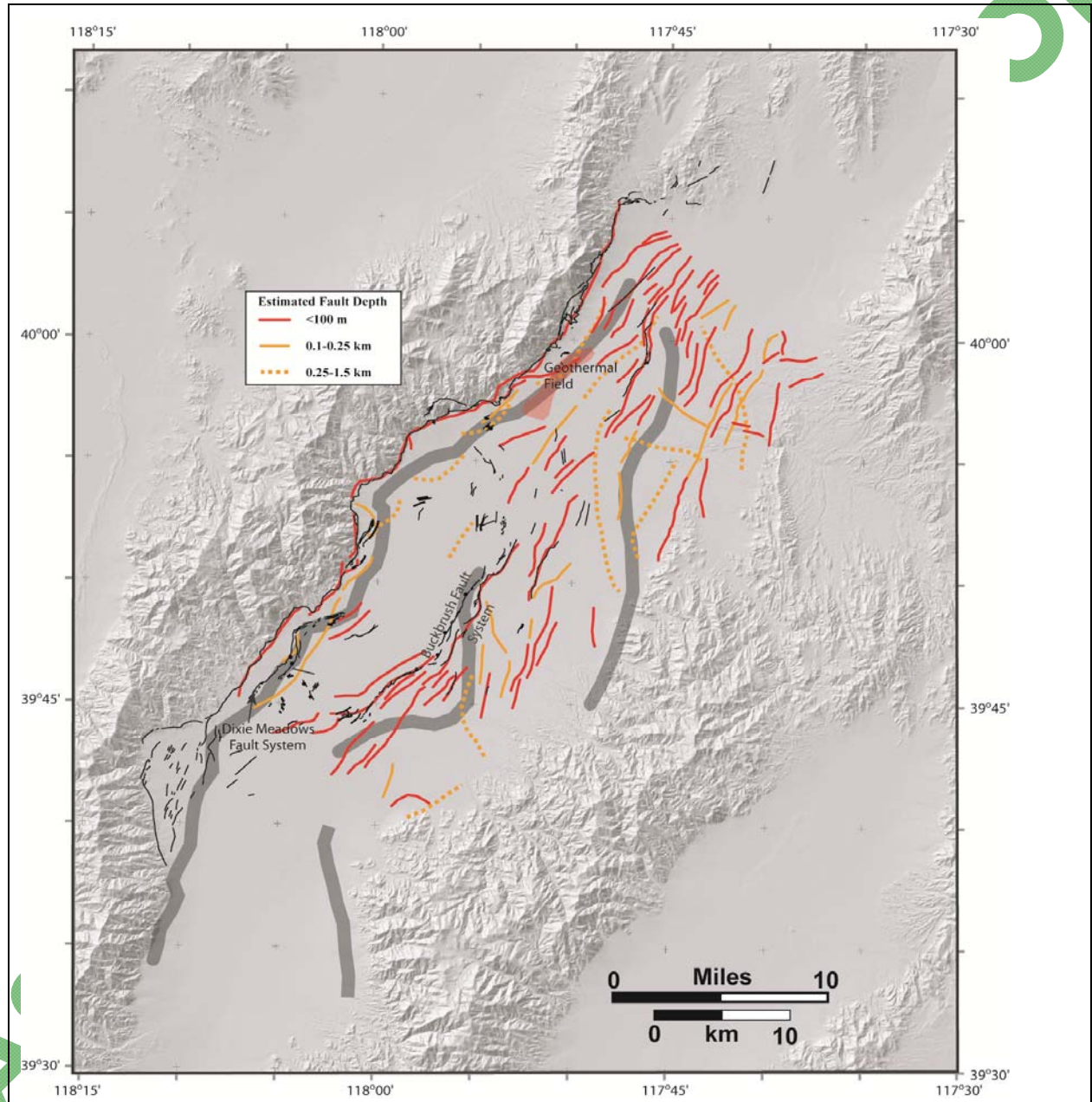


**Figure 13.** Horizontal gravity gradient maxima (wide gray lines) and faults from the surface geology (black lines) and from the horizontal gradient of the HELIMAG data (red lines) on a topographic background. Surface evidence of rampart faults & intrabasin faults occurs on or near gravity gradient maxima. The figure and caption are from Blackwell et al. (2005).

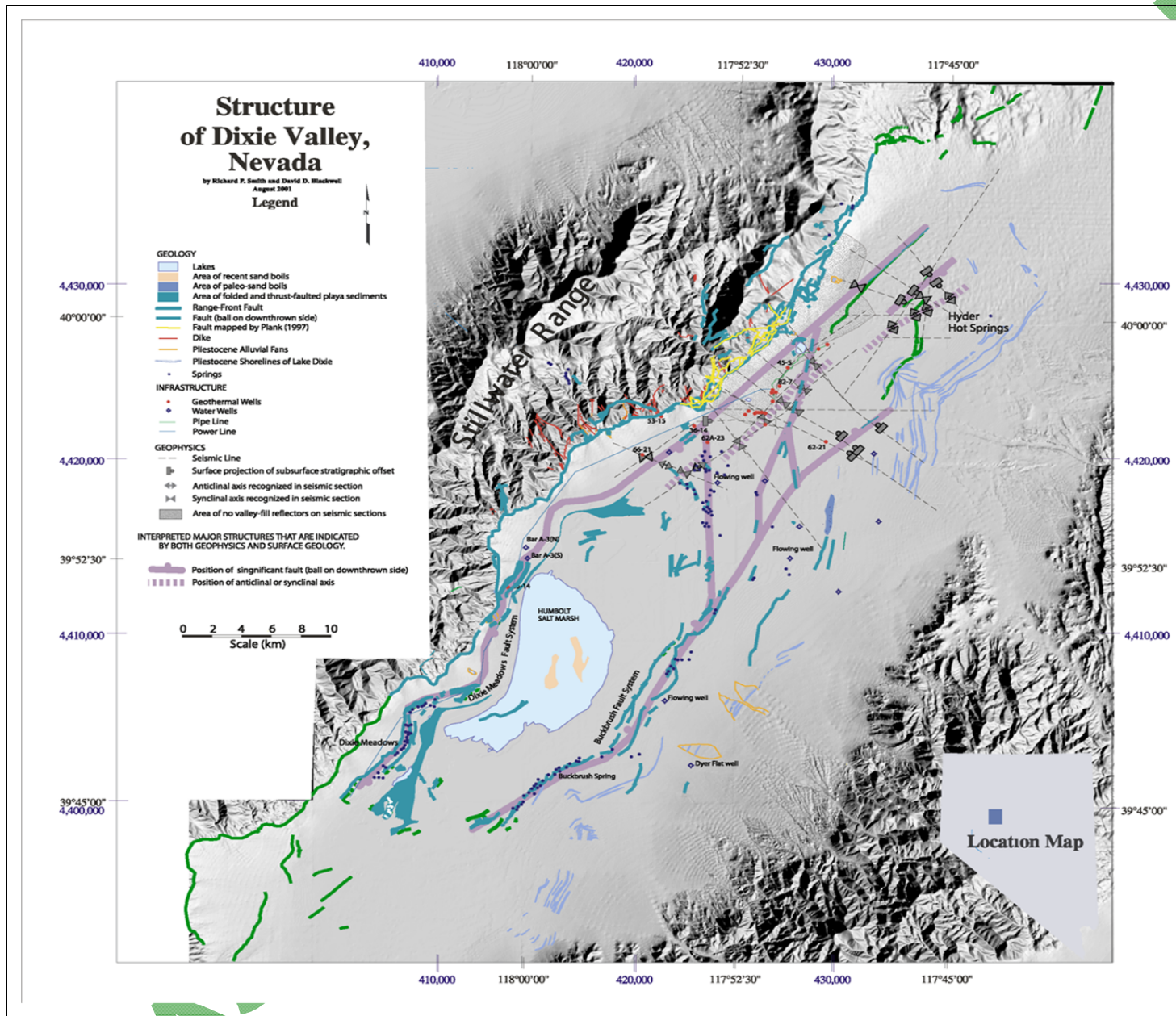
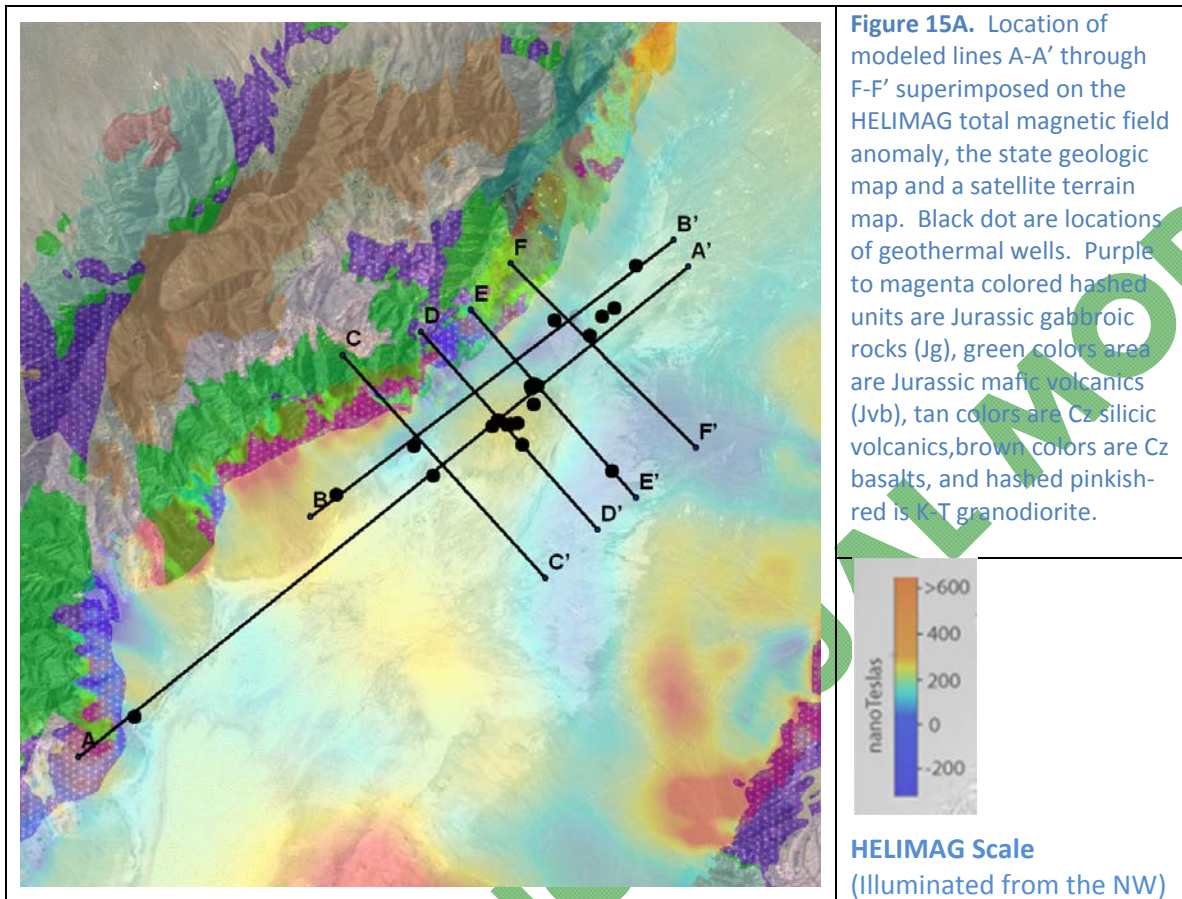


**Figure 14.** Structure of Dixie Valley (Smith and Blackwell 2001). Thick purple lines indicate the positions of interpreted major intrabasin faults based on geophysical data and surface geology. The figure and caption are from Blackwell et al. (2005).



The methods used to calculate the gravity and magnetic model response are based on the methods of Talwani et al., 1959, and Talwani and Heirtzler, 1964, and make use of the algorithms described in Won and Bevis, 1987. Two-and-a-half dimensional calculations are based on Rasmussen and Pedersen, 1979. The GM-SYS inversion routine utilizes a Marqardt inversion algorithm to linearize and invert the calculations (Marqardt, 1963). Gravity and magnetics models are non-unique, i.e., several model families can be created to match the data. It is up to the interpreter to assess whether the model(s) are geologically reasonable.

The principles of successful modeling are to create the simplest models with the fewest number of densities, blocks and vertices. In the Dixie Valley area, a few constraints were available from well lithologies which defined basin depth. It is important to note that density contrasts, not absolute values are what control the gravity signature. Complete Bouguer gravity values were calculated with a background reduction density of 2.67 gm/cc. Models with basin fill densities ranging from 1.4 to 2.6 gm/cc were tested and only those with densities of 2.2 gm/cc or greater provided the requisite minimum basin thickness. The final basin fill density of 2.445 gm/cc was selected based on fitting the model to the observed basin fill depth in well 62-21 on line E-E'. Independent fits of lines D-D' and F-F' show basin fill depths are consistent with other wells in the area. In some of the lines, it was necessary to introduce a surficial (<100m [330ft]) low density layer of D ~1.5-1.8 gm/cc to account for very short wavelength gravity variations. This might represent the vadose zone or alternatively, lake and playa sediments.

Bedrock density values were determined by modeling the outcropping bedrock on the eastern flanks of the Stillwater Range. Geologic units in the Stillwater Range are varied and complex,

ranging from gabbros to basalts to rhyolites to quartz arenites. The most dominant geologic units in the range in the study area are the Jurassic gabbros and Tertiary basalts. Line F-F' is the only profile where the gabbros unambiguously are the only outcropping bedrock unit. The gravity signature of the Stillwater bedrock along line F-F' was modeled using density values ranging from 2.6 to 3.0 gm/cc. A density of  $D=2.876$  gm/cc. was found to provide the optimal fit to the slope of the CBA, and this value, which is typical of mafic volcanic rock was adopted for the rest of the lines. A slightly reduced density of 2.4 to 2.5 gm/cc proven necessary to model some near surface rocks in the Stillwater Range that are classified as rhyolites or mixed clay/limestone/arenites.

The effects of removing a slight NW/SE regional trend was tested on the gravity models (Figure 15B). The net effect was to slightly deepen the basins, but no significant changes were observed to the locations of the basin walls or the positions of postulated faulting.

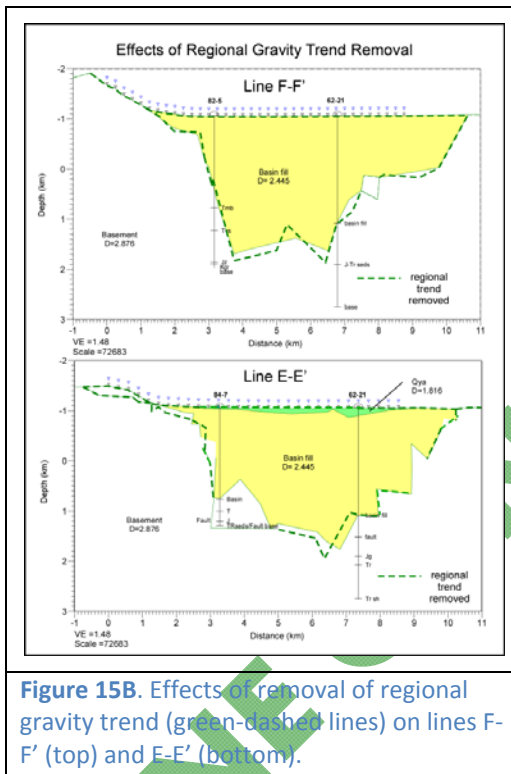


Figure 15B. Effects of removal of regional gravity trend (green-dashed lines) on lines F-F' (top) and E-E' (bottom).

Magnetization values were varied from  $M=0.001$  to  $M=0.008$  emu/cc. Values of  $M < 0.003$  and  $M > 0.005$  emu/cc did not yield acceptable fits. Values  $< 0.003$  emu/cc required magnetized volumes in excess of 700m (2300ft) thick, which seems unrealistic. Models with magnetizations of  $M=0.003$  to  $M=0.005$  emu/cc yielded acceptable fits. Increasing the magnetization above  $M=0.004$  emu/cc somewhat decreases the volume of the magnetized bodies and to a lesser extent changes their relative positions. A series of modeling experiments were done to determine whether the Jurassic rocks were positively or negatively magnetized. Although some fits in the eastern part of the Dixie Valley basin allowed negatively magnetized units, the signature of the rocks in the Stillwater range required positively magnetized bodies. The prominent subsurface magnetic anomalies are positive highs implying buried normally magnetized bodies. Finally, the dominant magnetic field during most of the Jurassic was normal (i.e., positive), had very few reversals, and is known as the Jurassic Quiet Zone

(Tivey et al. (2006)). Thus, for simplicity and consistency positively magnetized units were assumed in the modeling.

Ambient field directions of inclination =  $64^\circ$  and declination = 0 were used in the modeling. Field observations suggest that the units are extensively deformed and structurally complex and at times are steeply dipping to near vertical at the surface. The subsurface magnetizations are, of course, impossible to know. Changing the magnetic field directions could significantly alter the model fits, but for lack of knowledge we are left with little choice but to make the simplistic assumption that the Jurassic volcanics reflect modern values, implying that susceptibility rather than remanence controls the magnetization.

After a number of trials, a value of  $M=0.004$  emu/cc was found to be optimal in modeling the magnetic signature of the Jurassic volcanics in all of the profiles. This is equivalent to using a susceptibility of  $.S=00079$  cgs units using the ambient magnetic field of  $B= 51290.46$  gammas

found in the HELIMAG survey (Graugh et al., 2002) with an inclination of 64° and a declination of 0°. The final joint gravity/magnetics models with their data fits are shown for perpendicular lines C-C' through F-F' and A-A' to B-B' are shown in Figures 15C and 15D, respectively. The following observations can be made:

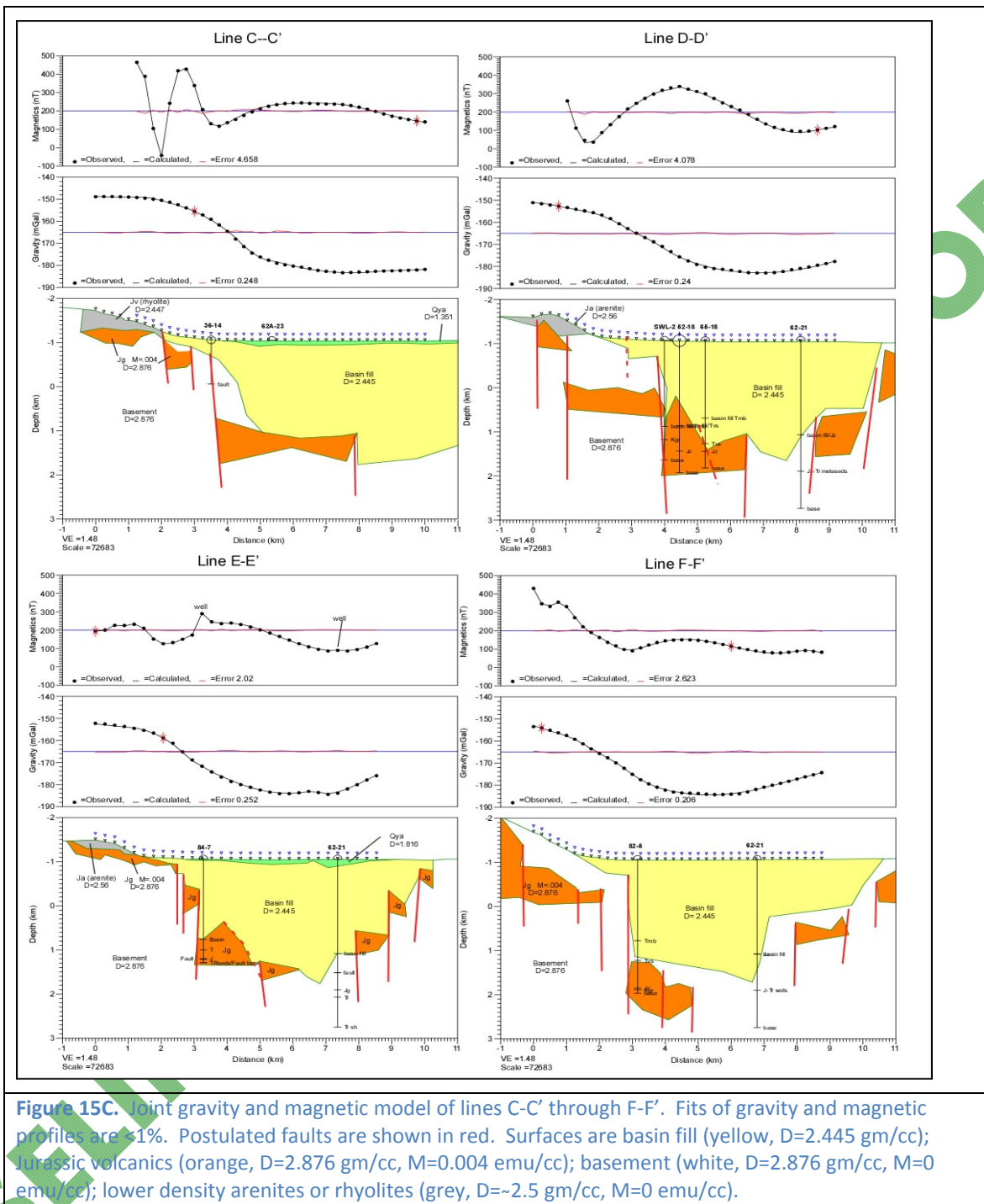
- The basin is 1.0 to 1.3km (0.6-0.8mi) thick and is wider in the vicinity of Line C-C'. Line A-A' suggests that the basin may be divided into two subbasins going from south to north;
- The magnetic anomaly data can be successfully modeled with a single magnetic Jurassic mafic rock unit. The magnetic modeling and thus the fault locations and dip are very sensitive to the shape and location of the individual blocks as well as the interaction between blocks;
- The basin walls appear to be fault controlled and indicate a complex, steeply dipping to near vertical, multi-fault structural geometry for the DVFZ. The step-down fault zone indicates the majority of the normal-sensed displacement occurs on multiple piedmont faults. This interpretation replaces the original range-bounding, moderately dipping, single fault model; and
- All the wells (producing zone) occur within the block faulting zone and more specifically on the major piedmont structures.

### 3.4 Magnetotelluric (MT) Surveys

Electromagnetic (EM) and MT surveys within Dixie Valley have been used to image the structural resistivity as bedrock and unconsolidated sediments show sharp resistivity contrasts. In addition, increased fluid content due to fracturing as well as the development of conductive alteration minerals (clays) can show electrical resistivity contrasts. Thus, EM can also be used for finding blind geothermal systems, defining the extent of geothermal reservoirs and controlling structures, and locating/characterizing permeable fracture zones.

While these methods can be subject to limited resolution and other variables, a new generation MT-array system has been applied to three profiles over the Dixie Valley thermal area (Figure 16A). This study described in Wannamaker et al. (2007) is defined as state-of-the-art MT array measurements in contiguous bipole deployments across the Dixie Valley thermal area that have been integrated with regional MT transect data and other evidence. The purpose was to (1) resolve the complex structural setting; (2) delineate fault zones which have experience fluid flux as indicated by low resistivity; (3) infer ultimate heat and fluid sources for the thermal area; and (4) investigate the capability of well-sampled electrical data for resolving subsurface structure.

The northern profile (Figures 16A and 16B) and central profile (Figure 16D) show that shallow basement rocks extend for a considerable distance (1-2km [3280-6560ft]) SE from the topographic scarp of the Stillwater Range before plunging steeply down the main strand (major displacement along piedmont fault) of the DVFZ. The southern profile (Figure 16C) images a more steady dip likely suggesting a localized step-down zone. The findings reported in Wannamaker et al. (2003) supports a multi fault-step model, infers that an unknown amount of slide-block material may exist over the main DV range-front fault which complicates the structural framework, and images a low resistivity zone flanking the interpreted main offsetting fault that could be due to alteration from geothermal fluid outflow/upflow. A highly altered section of silicified alluvium near the surface encountered in well 38-32 likely supports this interpretation.



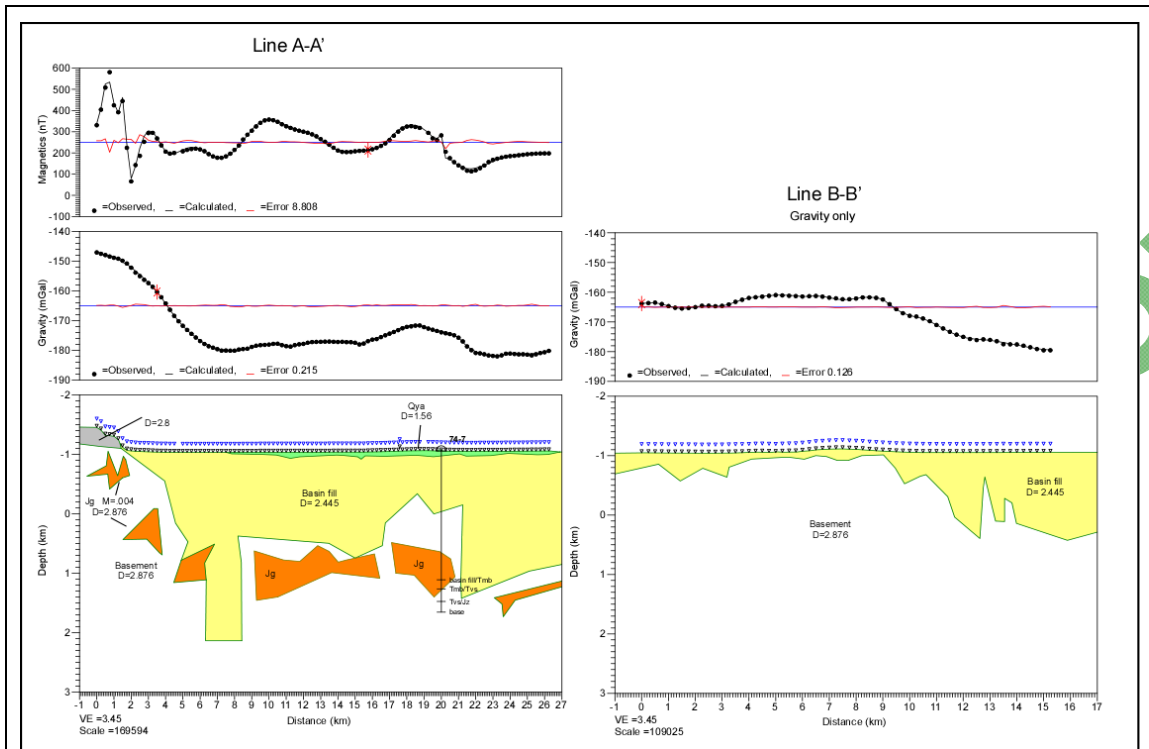


Figure 15D. Joint gravity and magnetic model of lines A-A' through B-B'.

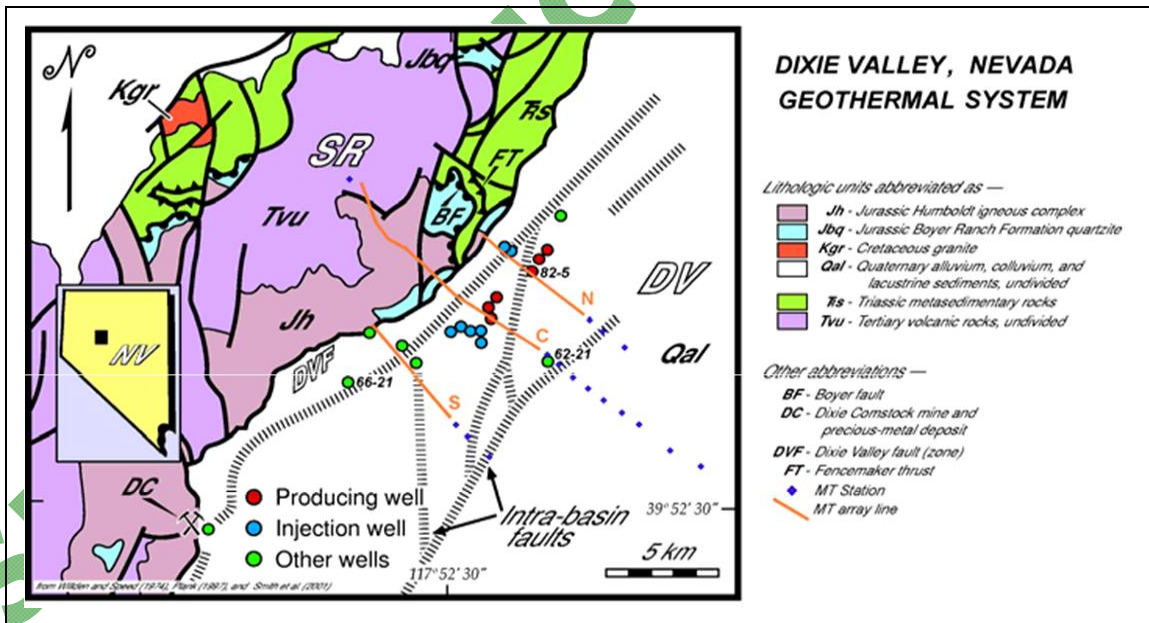
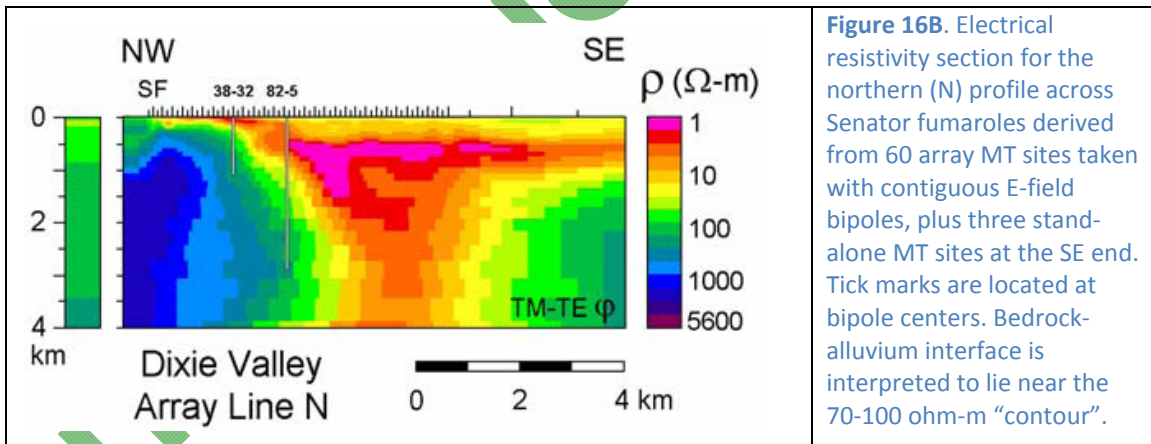


Figure 16A. Simplified geologic map of the Dixie Valley (DV)-Stillwater Range (SR) area surrounding the Dixie Valley thermal field. Orange-brown lines are the MT profiles lines (see text) Lines are labeled N (north), C (central), and S (southern). Blue diamonds are five-channel MT stations added to extend profiles across the valley. Original figure courtesy of Jeff Hulen. The figure and captions are after Wannamaker et al. (2007).

In a more recent analysis (Wannamaker et al., 2007) resolved the structural setting and supported a multi-fault steeply dipping structural model. The transition from low to high resistivity ( ~100 ohm-m) represents the basement interface within the resistivity models which is supported by drilling results. A large scale, very high resistivity domain is present below the approximate central portion of the Stillwater Range which could likely be attributed to the presence of Cretaceous aged intrusive bodies. In addition, all three inverted profiles show a low resistivity deep feeder zone for high temperatures fluids rising into central Dixie Valley (Figures 16B-D). This broad, subvertical conductor connecting from depth (greater than 10km [6.2mi], see Figure 16E) along the eastern base of DV has been interpreted as a presently inactive, large-scale faulting damage zone with fluidization and alteration (Wannamaker, pers. comm., 2010), and alternatively as a less significant alteration structure due to localized change in mineralogy (Waibel, pers. comm., 2010). It provides the possibility that the N-trending structures inferred by the geophysical data within the intrabasin are thermal-bearing structures (Figure 12) which merge with the NE trending active system of faults within the DVFZ in the vicinity of the geothermal field. This potential feeder zone is also imaged in the regional MT transect inversion (Wannamaker et al., 2006) that appears to connect to a pronounced low resistivity zone in the deep crust below the Humboldt Range (Figure 16E). This low resistivity zone has been interpreted as a region of magmatic underplating which would be a direct source for the active thermal fluids upwelling in Dixie Valley. If the resistivity models are correct, then it would imply some sort of magmatic input to the Dixie Valley geothermal system. However, one of the deepest wells in the DVGW, well 66-21, lies just to the east of this low resistivity zone and is relatively cold with respect to the producing wells and wells in the DVPP. A more detailed MT study will take place under Task 4 of the EGS Exploration Methodology Project. One objective will be to further resolve this low resistivity structure within central Dixie Valley.



**Figure 16B.** Electrical resistivity section for the northern (N) profile across Senator fumaroles derived from 60 array MT sites taken with contiguous E-field bipoles, plus three stand-alone MT sites at the SE end. Tick marks are located at bipole centers. Bedrock-alluvium interface is interpreted to lie near the 70-100 ohm-m “contour”.

### 3.5 Seismic

Dixie Valley is a structurally asymmetric basin bounded by a complex zone of faulting on the northwest and by step faulting to the southeast (Okaya and Thompson, 1985; Blackwell et al, 2005). The Dixie Valley Study Area (DVSA) extends from 39.7°N to 40.2°N and from 117.5°W to 118.2°W (Figure 1) and encompasses ~787mi<sup>2</sup> (2025km<sup>2</sup>). To avoid boundary effects, we plan to estimate tomographic models over a much larger region than the project area in future planned work. As such, we have collected seismicity and ambient noise information within 200km (124mi) of DVSA. This extended study area, from 38.7°N to 41°N, and from 117°W to 119°W, is referred to as the Dixie Valley Extended Study Area (DVESA).

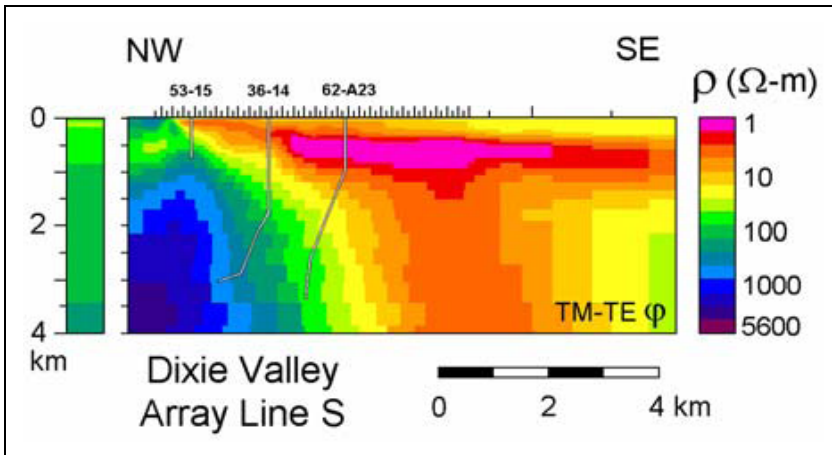


**Figure 16C.** Resistivity inversion section for the southern profile (S) across the Section 10-15 area for the dense MT array line S plus three stand-alone MT sites to the SE. The figure and caption are from Wannamaker et al. (2007).

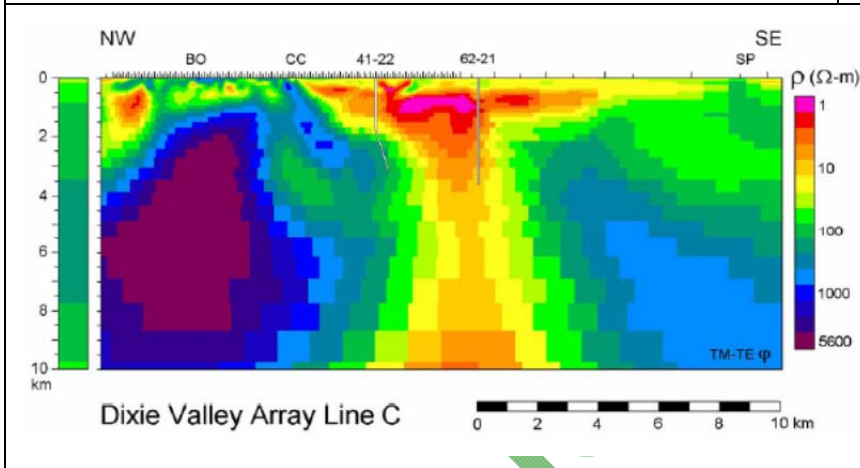


**Figure 16D.** Resistivity inversion section (C) across the Dixie Valley power producing field from 120 dense MT array measurements and 13 appended wideband MT soundings. The figure and caption are from Wannamaker et al., (2007).

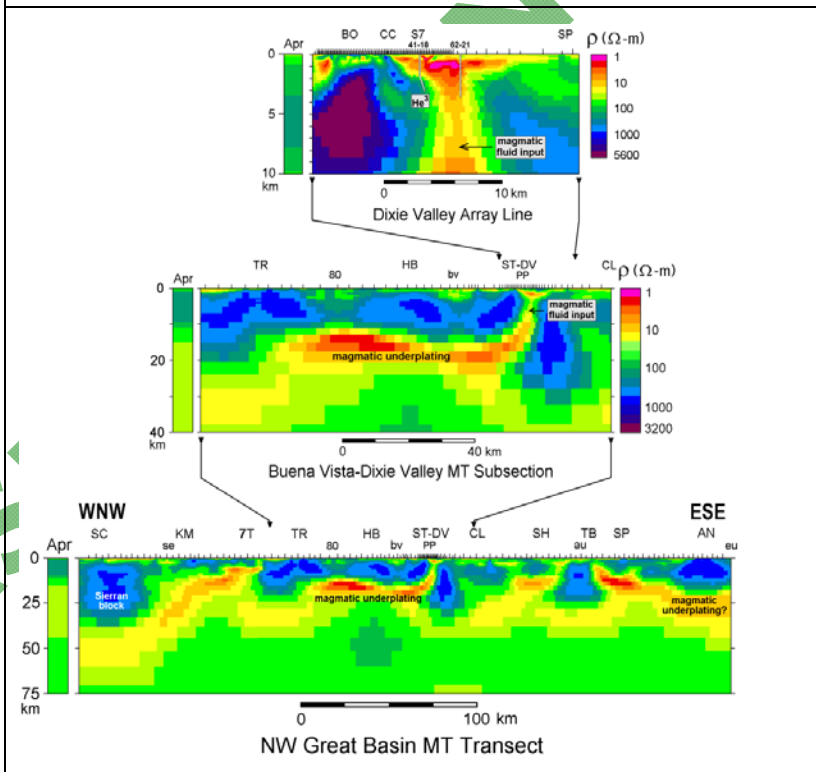


**Figure 16E.** MT structures of the central Great Basin show multi-scale magmatic-hydrothermal residence zones and pathways to the upper crust and geothermal systems. The figure and caption are after Wannamaker et al. (2006).

We expect our study will also address, directly or indirectly, several of the unresolved seismic issues in Dixie Valley. In this area, geophysical data interpretations in terms of fault parameters are controversial. For example, it is still debated whether the Dixie Valley earthquake in 1954 ( $M=6.8$ ) was the first large, low-angle normal earthquake on land recorded historically. Seismic studies conducted by Abbott et al., 2001 at Dixie Hot Springs, inferred that the range front fault dips  $25-30^\circ$  to the southeast at this location (see [Section 2.2.2](#) for additional discussion). Also, while most of the authors agree that the fault system penetrates deep into the crust, it is still debated whether there is a second order magmatic connection of the deep circulation system in Dixie Valley (McKenna and Blackwell, 2004; Wisian and Blackwell, 2004; Wannamaker et al., 2006). In addition, the nature of the seismic gap located on the Stillwater Range in northern Dixie Valley is yet to be resolved. The seismic gap (see [Section 2.2.2](#) and [6.1.1](#) for additional discussion) lies between the 1954 Dixie Valley earthquake ruptures to the south and the 1915 Pleasant Valley ruptures to the north. The geothermal field is located between the endpoints of the 1954 and 1915 surface ruptures (Slemmons, 1956) within the seismic gap. The Stillwater seismic gap (Wallace and Whitney, 1984) falls within a major tilt domain boundary or transverse zone between the east-tilted Tobin range to the north and the west-tilted Stillwater Range. Fault slip rates in this area suggest that the gap may be simply a manifestation of the fact that major slip has not occurred in recent times.

### 3.5.1. Faults

Dixie Valley is the location of a complex fault system (Caskey et al., 1996). The Dixie Valley rupture zone does not fit a simple segmentation model. It is instead a complex interaction of separate fault zones (Bell, 1990). Due to the lack of systematic seismic studies, the depth and angle to which these fault zones penetrate the crust is still under debate. Several main faults have been distinguished, such as the Stillwater Fault (SF), a normal fault which bounds the Dixie Valley basin to the northwest and dips  $52-54^\circ$ , while the dip of this segment is debatable (see [Section 2.2.2](#)). This fault is estimated to be planar from the surface to a depth of at least 3km (9850ft). The SF is the producing reservoir for a 62 MW geothermal electric power plant originally built and operated by Oxbow Geothermal Corporation and currently owned and operated by Terra-Gen Power, LLC. There are well-documented lateral variations in productivity along the fault that are not fully understood. Work by Blackwell et al. (2005) and the current authors has shown that in the DVSA the Stillwater Range is bounded by a complex multi-fault system referred to as the DVFZ consisting of at a minimum a range-front fault and a piedmont fault; [see Section 2.2.2](#). Based on the baseline data presented herein, the current Dixie Valley producing reservoir is located in the piedmont fault section of the DVFZ.

### 3.5.2 Previous Dixie Valley seismic experiments

#### *Seismic Data Collection Experiments*

**1964.** Studies of microearthquakes were carried out in the Fairview Peak Region, southwest of the DVSA, the earliest of which involved a network of five portable seismographs distributed in an area of about  $2500\text{km}^2$  ( $965\text{mi}^2$ ) to the east of Fallon, Nevada (Oliver et al., 1966).

**1965.** A similar study of microearthquakes near Fairview Peak was carried out in 1965, using a small local network of four portable seismographs (Westphal and Lange, 1967). Three recording periods were covered in this study, totaling 129 days. The first was a period of low seismic activity during January and February, and the others followed the occurrence of magnitude 4.6 earthquakes in April and June. Results of the study deal primarily with the determination of

focal coordinates for 244 events, based on a standard four-station location procedure, with the assumption of a uniform 5.0 km/sec P-wave velocity for the Fairview Peak area.

**1965.** The Lamont Geological Observatory and the University of Nevada undertook a cooperative microearthquake survey of selected areas in Nevada, using seismographs of high sensitivity (Oliver et al., 1966). The main purpose of this study was to compare short-term (i.e., daily) rates of occurrence of microearthquakes in seismically active areas with regional seismicity determined from the occurrence of large earthquakes over periods as long as several decades. Ten sites in western Nevada were monitored for periods from a few hours to several days, and the results of the study indicated that microearthquake activity was generally higher in areas of recent faulting, and lower in areas where large earthquakes had not occurred for 50 years or more.

**1966.** A small tripartite array (Stauder and Ryall, 1967) was established at the southern extremity of the surface faulting of the Fairview Peak earthquake of 1954. Over a period of six weeks an average 31 earthquakes per day were detected. Foci were found to concentrate between 10 and 15km (6.2 and 9.3mi) and to cluster toward the end of the surface faulting of the 1954 earthquake. The foci were also found to lie along two planar zones. The first was parallel to the fault plane solution (strike N 11° W, dip 62° E) of the 1954 Fairview Peak earthquake and terminated at the southern extremity of the surface fracture. The second began at this point and extended to the southwest, with loci distributed about a plane striking N 50° E and dipping 50° to the southeast. The latter zone apparently marked the southern terminus of the 1954 faulting.

**1967.** During the course of geothermal exploration in northern Dixie Valley, Thompson et al. (1967) reported that Southland Royalty Co. obtained 28km (17mi) of high-resolution seismic reflection data. The four seismic lines, recorded by Petroleum Geophysical Co. and processed by Western Geophysical Co., represented a detailed cross section of the northwestern side of northern Dixie Valley. Two of the four seismic lines were parallel to the Stillwater Range. The remaining two lines were oblique to nearly perpendicular to the range-front. Of these lines, SRC-3 was discussed by Okaya and Thompson in 1985. This seismic data is described by Blackwell et al. (2007) as difficult to interpret because "reflection data are only two dimensional and are thus of limited use in interpreting structures in Dixie Valley because of the three-dimensional velocity setting. There are many off-the-line reflection features in the data that complicate the interpretation, and even if the data were of modern vintage, the two dimensionality would still be a problem." The profiles have been reinterpreted by Optim LLC (Optim) in 1997 and reported in Anonymous (1998). A total of 34km (21mi) of 2-D seismic reflection data from the Dixie Valley geothermal field, were re-processed. The results revealed a completely different model for the geothermal field. This study used data recorded along nine seismic lines (Figure 17A, Appendix 2-Table 1.3), covering an area of approximately 160km<sup>2</sup> (62mi<sup>2</sup>). A detailed discussion on seismic reflection line interpretation is provided below.

**1984.** Hague et al. (1987) reported on deep crustal profiles across the western B&R acquired by the Consortium for Crustal Reflection Profiling (COCORP). Uncorrelated field data were collected using a 96-channel off-end spread at 100m (328ft) group intervals, an 8-32Hz (2.0 octave bandwidth), 30s upswep with an additional 20s listen time (50s record time).

**1985.** A reflection-spread "piggyback" data set was collected in Dixie Valley during the PASSCAL (Program for Array Seismic Studies of the Continental Lithosphere) northwestern Nevada seismic experiment. Catchings et al. (1986) reported that this experiment used explosive sources of up to 2700kg (5401lbs) recorded into receivers offset to 300km (186mi). The piggyback

receiver array used five multichannel recording units to record 384 channels in two adjacent deployments. Middle crustal and very strong Moho (10s) reflections were identified.

**2002.** A crustal refraction profile was collected by Louie et al. (2004) from Battle Mountain, Nevada across western Nevada, the Reno area, Lake Tahoe, and the northern Sierra Nevada Mountains to Auburn, CA (Appendix 2-Table 3). Mine blasts and earthquakes were recorded by 199 Texan instruments extending across this 450km (280mi) long transect. Reftek RT-125 recorders were linked to 4.5Hz single geophones with an average inter-station distance of 4.5km (2.8mi).

### 3.5.3 Seismic Reflection Profiles

**A closer look at seismic reflection profile interpretation in Dixie Valley in terms of fault structure:** We are presenting herein more detailed results of an extensive suite of seismic reflection profiles in the Dixie Valley area, as interpreted by Blackwell et al. 2005. Problems with interpretations of these profiles are due to steeply dipping structures, variable lithologies, and degrees of lithification of the valley-fill sediments. As mentioned above, seismic data was collected in the late 1970s to early 1980s, with reprocessing performed in the 1990s. The profiles were concentrated within the DVPF and the DVPP ([Figure 1](#)) coinciding with the area of highest geothermal gradient ([Figure 17a](#)).

The seismic reflection interpretation most commonly cited (seismic line [SRC-3]) emphasized a 54° dip of the Stillwater Range bounding fault, with a broken up reflection pattern SE of the fault presumed to be due to scattering within a coarse alluvial fan along the down thrown edge of the hanging wall block ([Figure 17b](#)). Recent interpretation including analysis from thermal and drilling data revealed that, near the range front, the area is composed of massive bedrock on the footwall of a steeply dipping buried fault zone defined by the gravity gradient maximum (see [Section 2.2.2](#) and [Figure 11](#)). In addition, seismic profiles reveal several intra-basin faults that show correlation to faults mapped on the surface. The seismic reflection profiles are generally in two predominant orientations, parallel to the dip "dip lines" or to the strike "strike lines" of the fault. The dip lines trend NE-SW (approximately perpendicular to the range-front and to the strike of major normal faults) while the strike lines trend NW-SE (parallel to the range front).

**Strike Lines:** The strike lines are supportive for imaging the depth to the basement ([Figure 18](#)), position and depth to basalt reflectors, and any cross-valley (NW-SE) structures including transfer zones between normal faults. Line 101 images a "flower" structure in correlation with the cross-valley transfer zones and shows the valley fill thickening to the north. SRC-1S images a basement high underlying the DVPP with accompanied "flower" structure. SRC-1N runs through the northern producing field and contains a lack of reflectors within the center due to the proximity of the piedmont fault. Line 5 running at an angle between the strike and dip lines (E-W) images several step faults towards the western line and shows the basalt thickens towards the valley depression. Interpreted line drawings of the majority of the seismic lines discussed are given in the seismic appendices in Blackwell et al. (2005).

**Dip Lines:** The majority of the seismic profiles cut roughly perpendicular to the DVFZ and the associated NNE to NE trending major structures. Specifically, 102, 9, 104, and 6 ([Figure 17a](#)) are shown with interpreted line drawings ([Figure 19](#)). Seismic lines SRC-3 & 102 run through the DVPF near the section 33 production wells and is regarded as the most well known and cited seismic reflection line in the B&R. It images the major range bounding fault as a more complex structure between wells 38-32 and 82-5. Within the eastern side of the valley, steeply NW

dipping (antithetic) faults offset the basement and the overlying Miocene basalt reflector. Seismic lines 104 and 9 run just south of Cottonwood canyon between the producing field and the DVPP lease, and cuts through the Lamb Ranch injectors (section 18). The most important feature of this line is that it shows the structure of the deep, early, N-S oriented graben underlying the deepest part of the valley. The termination of valley reflectors coincides with the location of the maximum gravity gradient and images the main strand of the DVFZ just west of well SWL-3 ([Figure 19](#)). A steeply west dipping fault that bounds the eastern graben is supported by the seismic data and the structure is likely encountered by well 62-21, which lies near the center of Dixie Valley. This line also correlates with the geophysical data that the largest fault displacement along the seismic profile lies about 3km (2mi) basinward of the range-front fault. Seismic line 6 is the longest profile available extending from 1km (3280ft) east of Stillwater to 2km (6560ft) west of Clan Alpine and lying just north of lines 104 and 9. The line positions the main valley-bounding fault at the peak of gravity gradient ([Figure 13A](#)), and also locates several faults within the eastern valley ([Figure 11](#)).

In summary, the interpretation of seismic reflection lines from Blackwell et al. (2005) are:

- Piedmont faults are the main valley-bounding faults, are located by both the gravity and seismic data in the same location and often correlated with geologic mapping from air photos (e.g., fault scarps, small grabens);
- The deepest part of the valley underneath the producing field is an early N-S oriented graben that formed prior to the still active extensional phase expressed by NE-trending normal faults;
- A correlation exists between of the termination of the reflector points and the axis of the maximum gravity gradient; and
- In the central cross-section ([Figure 19](#)) the deep graben's shape appears to synclinal. The axis of this syncline within the basin-fill sediments is shown in [Figure 14](#) and either supports sedimentation within a graben dominated structure, or could be a velocity pulldown feature due to lower velocity lacustrine dominated sediments in the lower section.

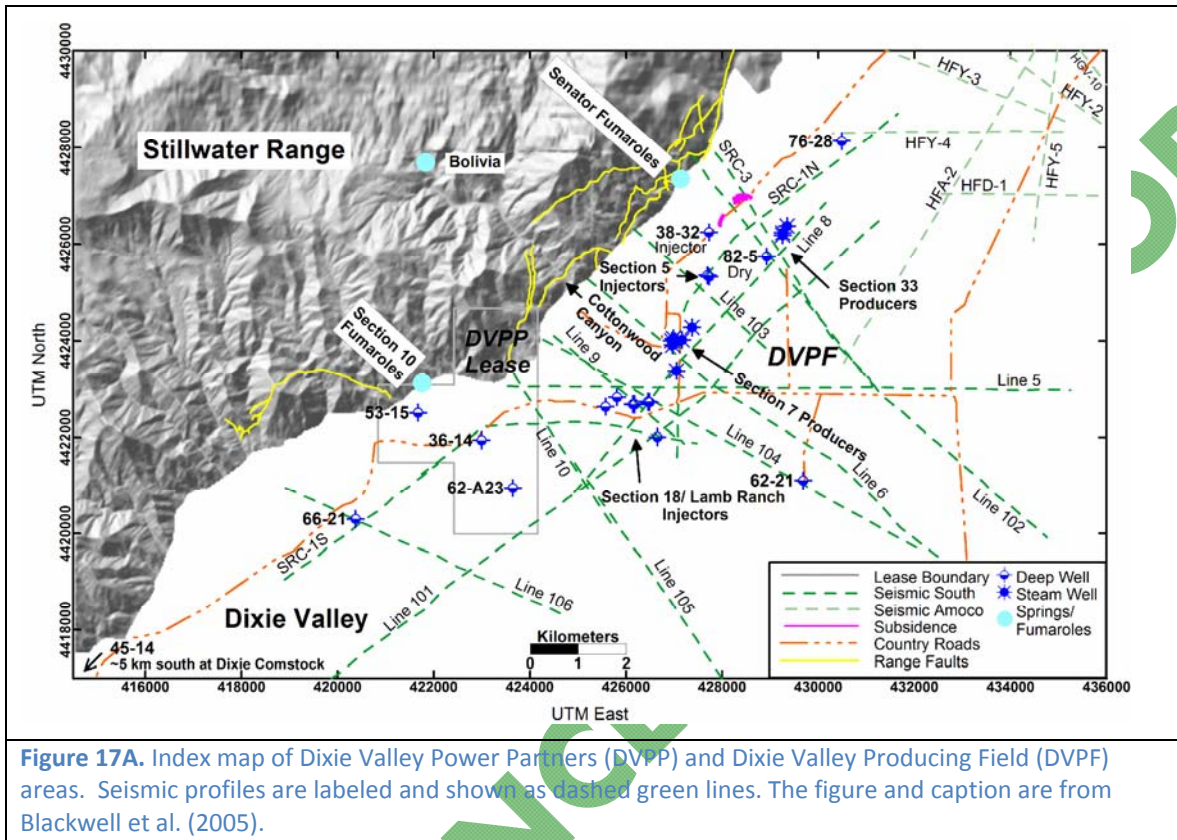
Limitations to the seismic reflection line data are:

- A simple model for basement and valley fill (density/velocity) was used, that doesn't include the Miocene and Oligocene volcanics (discussed in [Section 2.1.1](#));
- Geophysical logs (sonic, gamma ray, etc.) often used in conjunction with seismic data are available for some of the wells, but the intervals and types vary; and
- Inability to clearly image (seismic) in the vicinity of the fault zone due to steeply dipping and complicated structures and shallow valley-fill above the basement wedge between the range-front and piedmont fault.

### 3.5.4 Seismic Events

A catalog of seismic events (earthquakes and quarry blasts) that occurred in DVESA from 2000 to 2010 and were located by the Nevada Seismological Laboratory was extracted from the UNR database (Appendix 3 and [Figure 20](#)). These events were recorded by seismic stations in and around Dixie Valley (Appendix 2-Table 1). Some of these seismic events were relocated and reinterpreted catalog of seismic events. Due to poor station coverage, however, location errors are on the order of 5 to 10km ( 3.1-6.2mi). The seismicity and the proposed array configuration

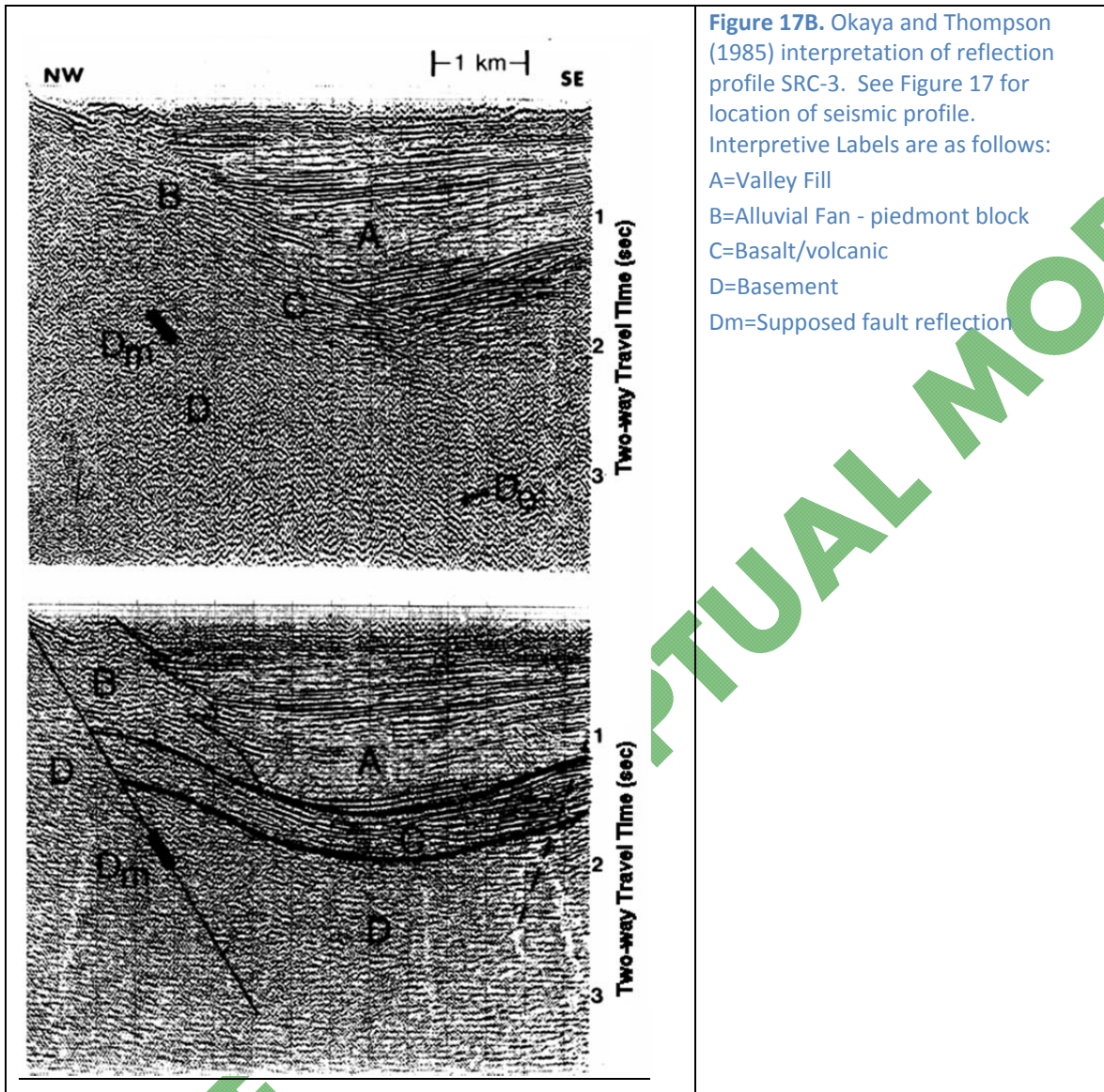
proposed to be conducted in Task 4 indicate that there might be enough information for a Dixie Valley earthquake-based tomographic model.



Historical seismicity in Dixie Valley (Blackwell et al., 2007) available from the United States Geological Survey (USGS) was added to the catalog and includes the July 6 ( $M_L$  6.8) and August 23, 1954 ( $M_L$  6.8) Rainbow Mountain earthquakes to the west of Dixie Valley, and the December 16, 1954 Dixie Valley ( $M_L$  7.1)-Fairview Peak ( $M_L$  7.2) earthquakes in and to the south of Dixie Valley.

### 2003 Seismic Sequence

A sequence of events (Appendix 2-Table 2; [Figure 21](#)) occurred in Dixie Valley in January 2003, about 26km (16mi) northeast of station DIX (Appendix 2-Table 1). The largest event and majority of the activity occurred from 6-13km (3.7-8.1mi). Using HYPODD (Waldhauser and Elsworth, 2000), the events were relocated ([Figure 22a](#)) in a cluster centered at 39.948°N, 117.863°W and depth 8.4km (5.2mi). The mechanism of the largest earthquake in this sequence is shown in [Figure 22b](#). It shows normal faulting on dipping plane of approximately 45°SE assuming that all the events lie along a single structure. It is also possible that the swarms occurs along several faults as suggested in [Figure 23](#). It is estimated that the other, smaller events, with similar waveforms ([Figure 21](#)), also had similar mechanism. Solving for the mechanism of these events is important to resolve the controversy on fault geometry in the DVSA.

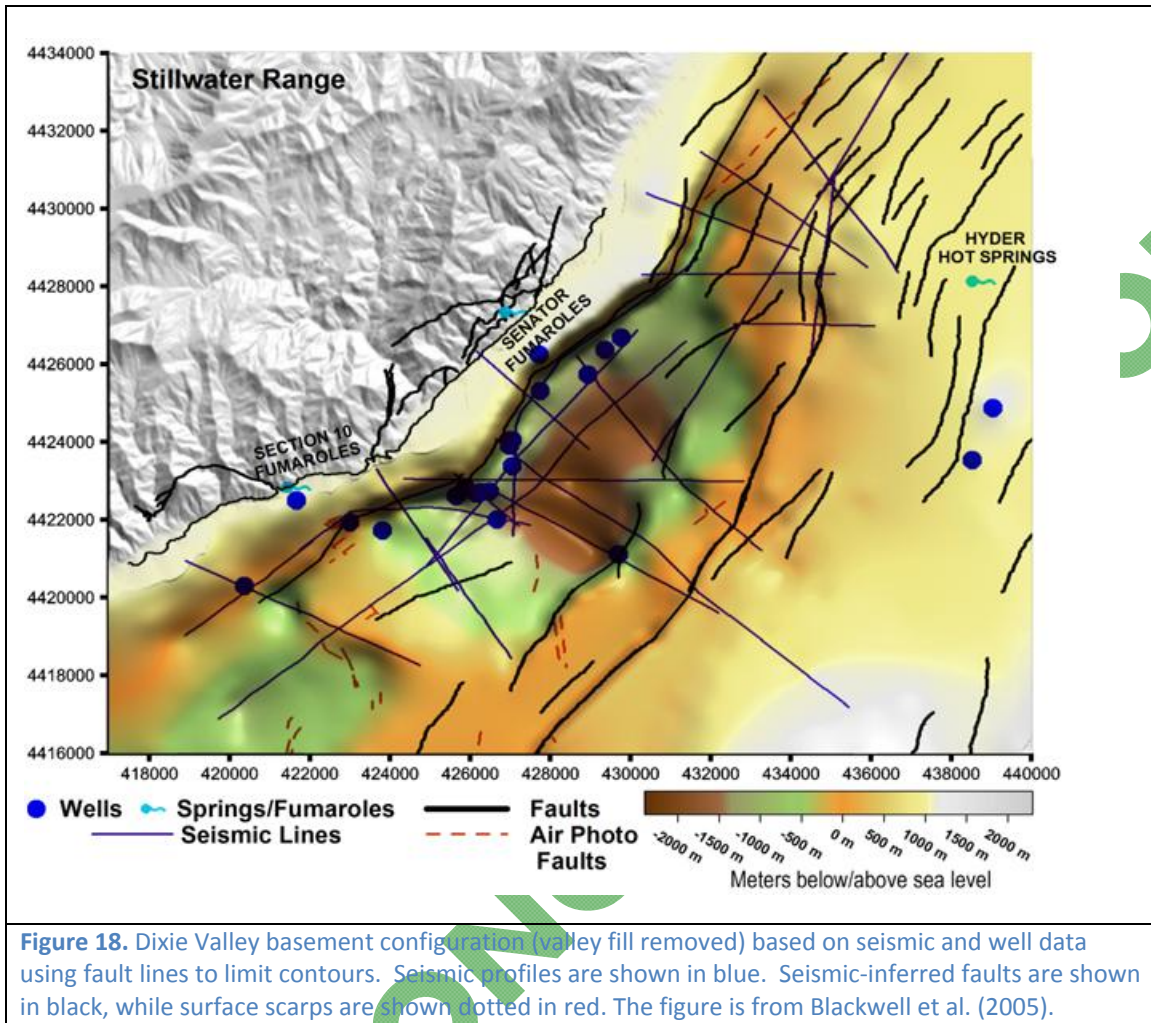


### 3.5.5 Databases Compiled

We have acquired or compiled the following databases, including waveforms from the seismic experiments listed above:

- An Antelope (Datascope) database of earthquake and explosion waveforms available at UNR from 1984 to August 2010. These events occurred in an area from 38.7°N to 41°N and 117°W to 119°W. Four days of continuous waveforms from the 2003 earthquake sequence which occurred in Dixie Valley have been added to this database.
- Data from the 2002 Walker Lane experiment through the northern part of Dixie Valley was acquired from IRIS; and

A new database of ambient-noise extracted Green's functions, a key component of the initial velocity model estimation in DVESA 3.5.5.



### Seismic Velocity Models

We have acquired the following crustal seismic velocity models (Appendix 4-Tables 3 and 4) in and around Dixie Valley.

#### Global and regional models

- CRUST 5.1, a global crustal model with 240km (149mi) resolution (<http://mahi.ucsd.edu/Gabi/rem.html>), (Basin et al., 2000; Mooney et al., 1998);
- Model AK135, a global Earth model;
- CU\_SDT1.0, a shear wave velocity model obtained from diffraction tomography over North America (Ritzwoller et al., 2002) which has 200km (124mi) resolution; and
- A shear wave velocity model for the Basin and Range by Priestley and Brune (1978).

#### Location-specific models

- The COCORP -derived model (Catchings, 1992) in a region shown in [Figure 24](#);
- The UNR-estimated P and S-velocity model (Preston, 2010) from earthquakes ([Figure 25](#));
- The re-processed seismic lines in Dixie Valley (Anonymous, 1998); and
- The Louie et al. (2004) Walker-Lane model.

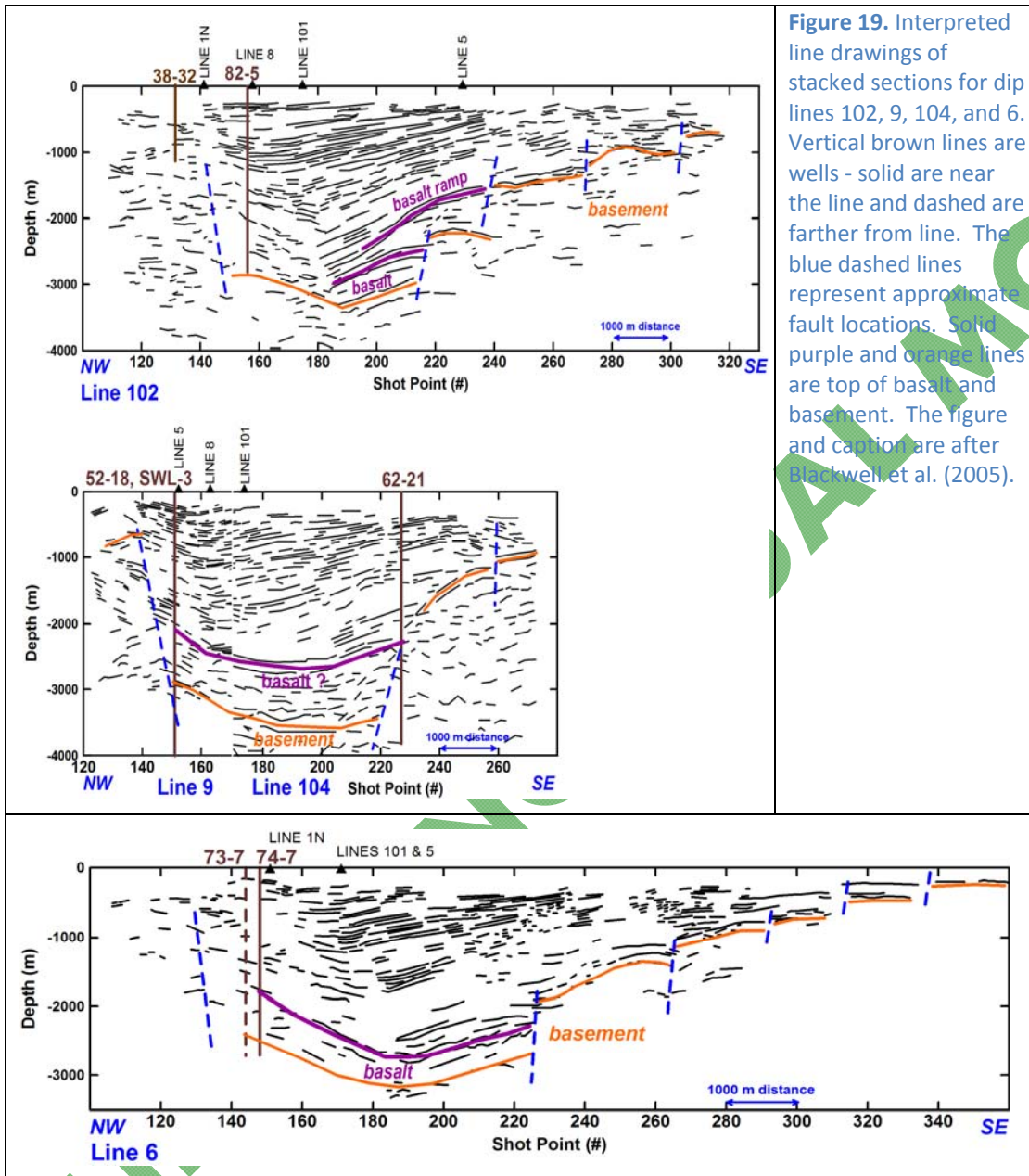


**Figure 19.** Interpreted line drawings of stacked sections for dip lines 102, 9, 104, and 6. Vertical brown lines are wells - solid are near the line and dashed are farther from line. The blue dashed lines represent approximate fault locations. Solid purple and orange lines are top of basalt and basement. The figure and caption are after Blackwell et al. (2005).

### 3.5.6 Integrated Seismic Model in Dixie Valley

The models in Appendix 4-Tables 3 and 4 were used to create an integrated model for the Project Area using algorithms written in Matlab. A set of depths of interest were chosen for all models. Each model is stored into a Matlab structure. The structure includes the model reference, the model area (which is a square oriented North-South, East-West), and the parameter model. The parameter model matrix consists of seven columns: depth, P-wave velocity in km/s, S-wave velocity in km/s, density ( $\text{g/cm}^3$ ), P and S attenuation factors  $Q_p$  and  $Q_s$  and a "trust" factor, described below. "No information" is marked by the parameter value set to -99. The "trust" factor ranges from 0 to 1 and is, for example, set by the analyst up to 0.9 for

reflection/refraction lines and is set to 0.01 for general (non-local) models. Using the "trust" parameter, seismic lines and local data are given higher weights than the general model

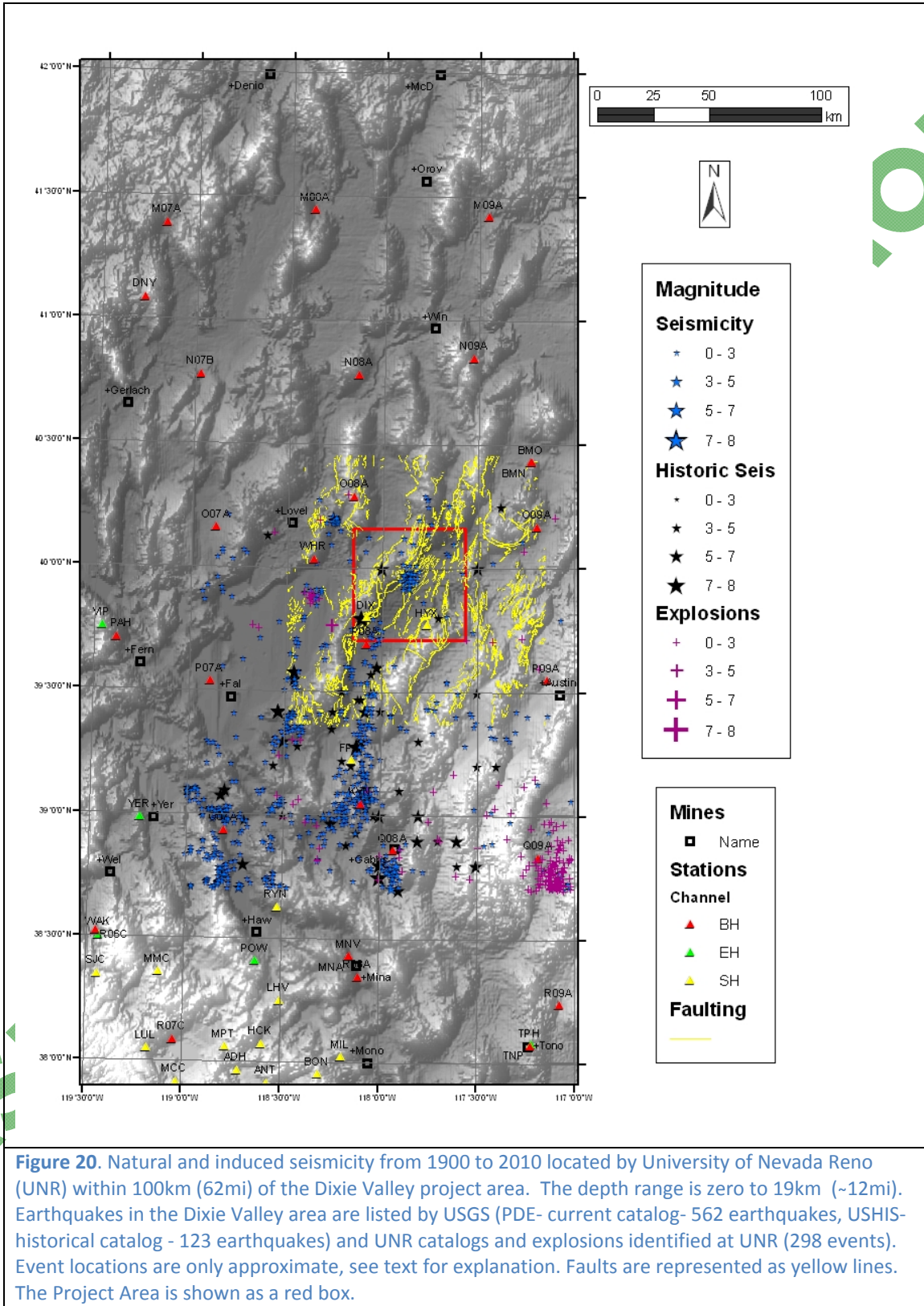


**Figure 20.** Natural and induced seismicity from 1900 to 2010 located by University of Nevada Reno (UNR) within 100km (62mi) of the Dixie Valley project area. The depth range is zero to 19km (~12mi). Earthquakes in the Dixie Valley area are listed by USGS (PDE- current catalog- 562 earthquakes, USHIS- historical catalog - 123 earthquakes) and UNR catalogs and explosions identified at UNR (298 events). Event locations are only approximate, see text for explanation. Faults are represented as yellow lines. The Project Area is shown as a red box.

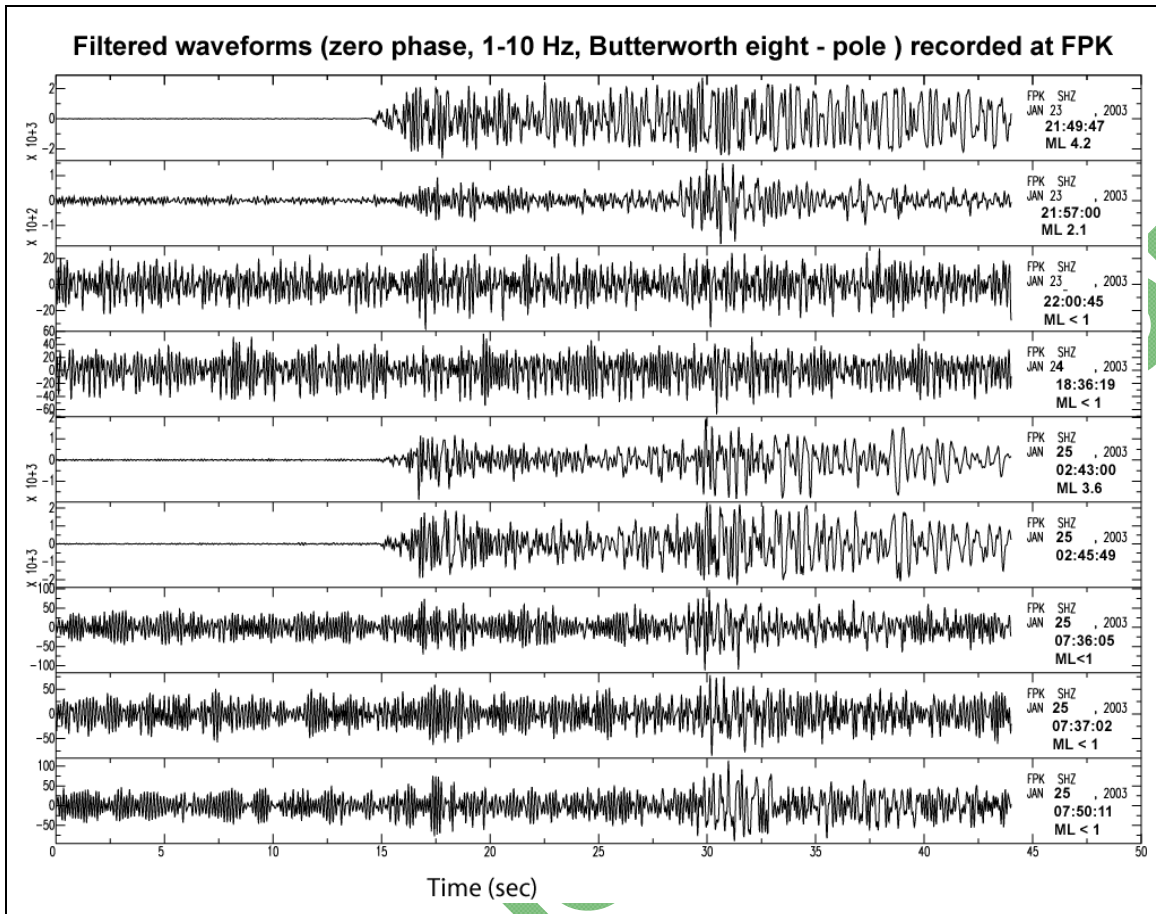


Figure 21. Waveforms recorded at station FPK from selected events in Appendix 2-Table 1.2.

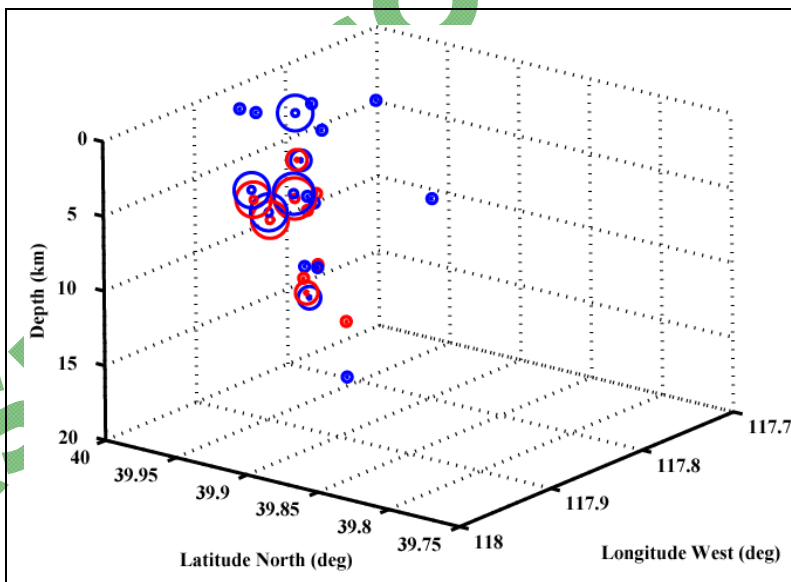
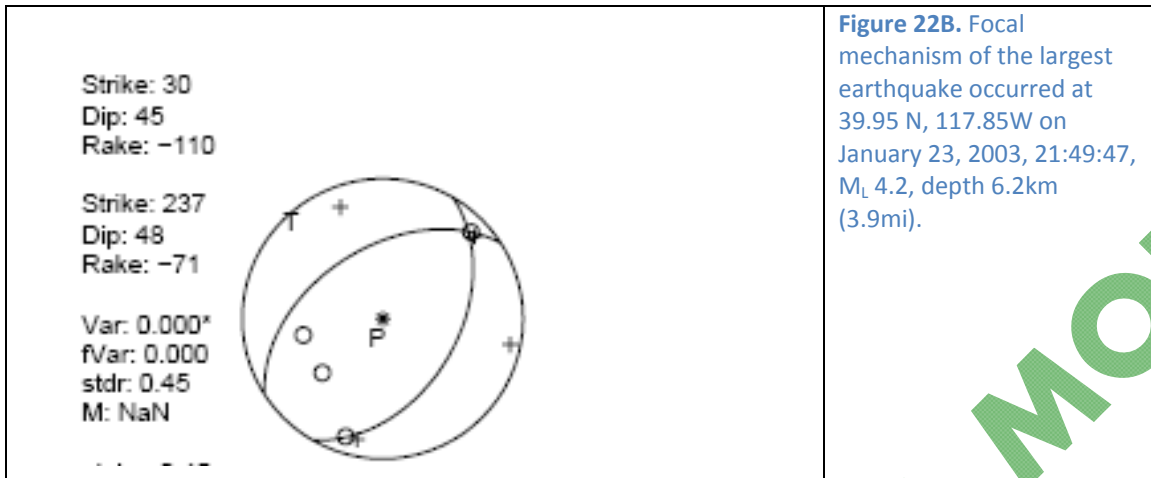
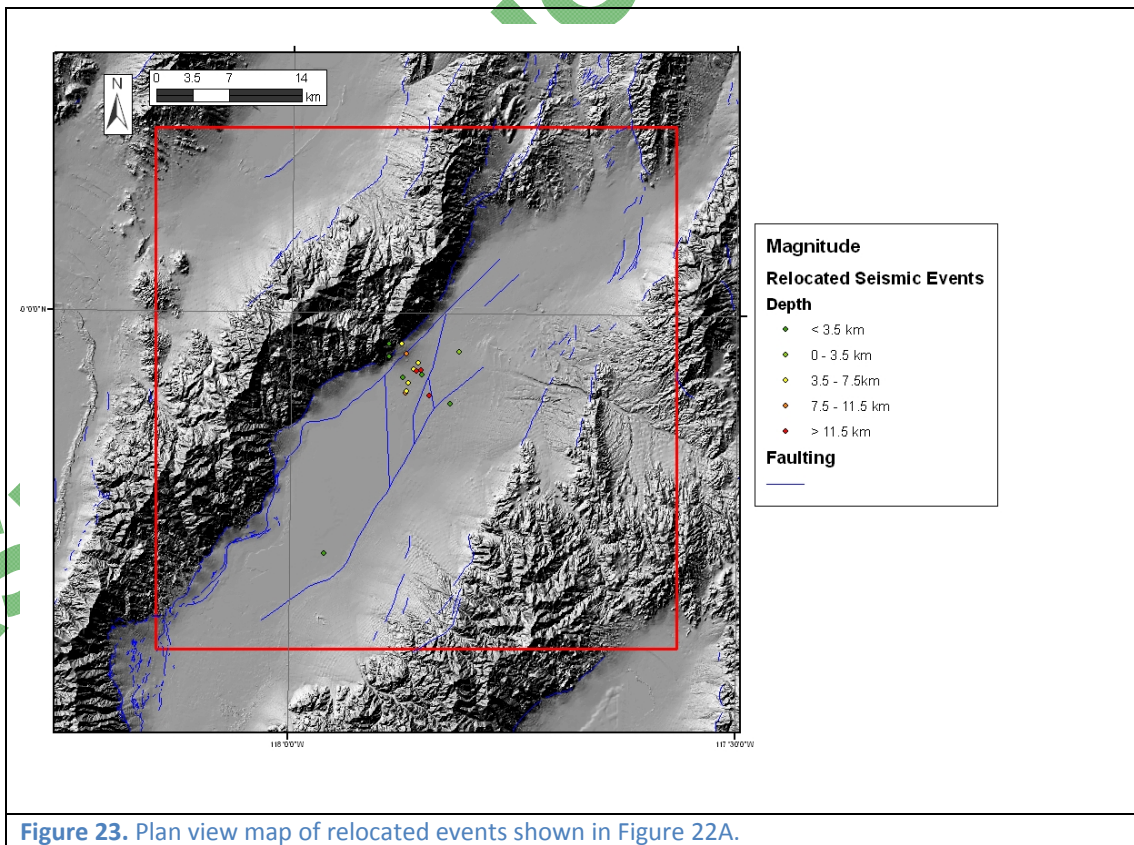


Figure 22A. Relocated events (red) and catalog events (blue) of the January 2003 sequence in Dixie Valley (Appendix 2-Table 2). All the events are represented by circles, proportional to magnitude. The largest earthquake was ML 4.2 and the smallest was ML < 2 (or less). The smallest earthquake magnitudes were not estimated because they were not recorded by enough stations.



weights. A "slack" factor for each model represents a chosen extension of the model area. When, for example, the P-velocity model at a point characterized by latitude and longitude is requested by the user, the program finds all the models including the respective point and collects all the P-velocity values, together with their "trust" values. The resulting P-velocity at the respective point is a "trust" - parameter weighted mean, after the "-99" estimates are discarded. Sixty-four models are currently used for the integrated model, including all the information in the study area collected so far.

The P-velocity integrated model at 3km (9600ft) depth with the planned seismic deployment stations is shown in [Figure 26](#).



**Figure 23.** Plan view map of relocated events shown in Figure 22A.

### 3.5.7 New Seismic Noise Derived Velocity Model

We have extracted more than 2000 new Green's Functions (GF's), [Figures 27](#) and [28](#) from cross-correlations of ambient noise at 61 stations within 200km (124mi) of Dixie Valley, with the objective to obtain higher resolution shear-wave velocity model than the current UNR model. To avoid model edge effects and due to the station distribution ([Figure 20](#)), Rayleigh group velocity maps need to be estimated in a larger area than the DVSA and this will be done in Task 4. Good correspondence of the GF extracted from ambient noise between Dixie Valley stations DIX ("SH"- analog short period sensor) and WHR ("BH" digital broadband sensor) with waveforms recorded at WHR ([Appendix 2-Table 1](#)) from an earthquake that occurred at 6km (3.7mi) depth 26km (16mi) northeast of the seismic station DIX is shown in [Figure 28](#).

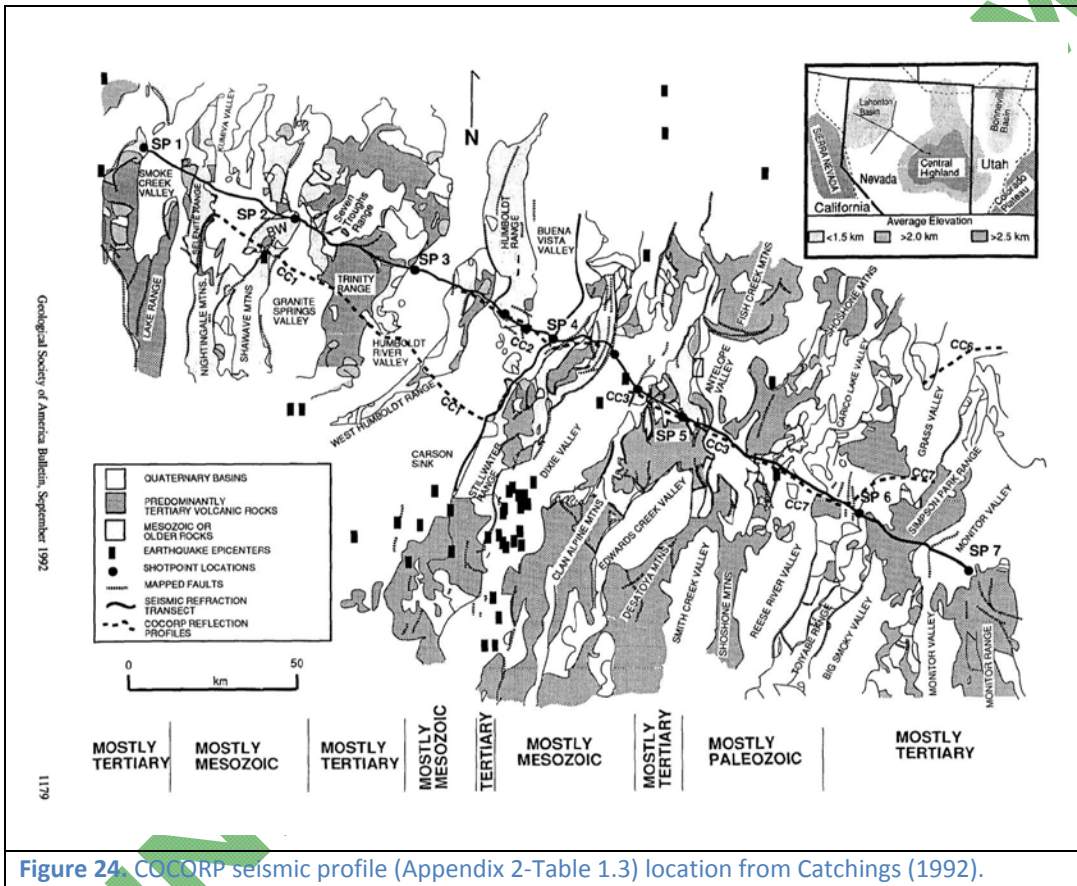


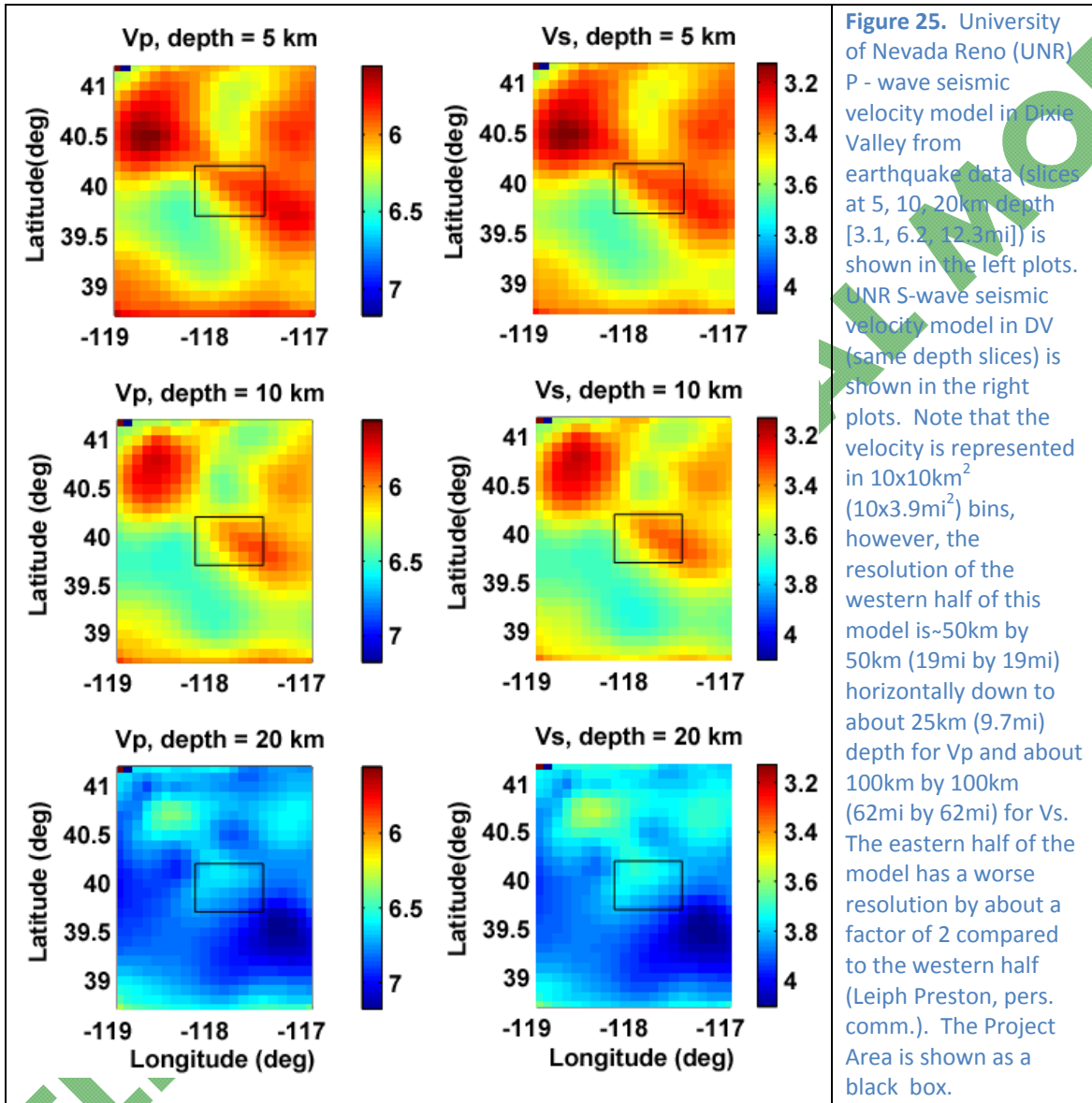
Figure 24. COCORP seismic profile ([Appendix 2-Table 1.3](#)) location from [Catchings \(1992\)](#).

### 3.5.8 Crust-mantle Boundary (Moho) Discontinuity Constraints

The depth of the crust-mantle boundary discontinuity (Mohorovicic or Moho) in DVESA is an important constraint on the tomographic model inversion.

Moho velocity and depth in Dixie Valley has been estimated by [Catchings and Mooney \(1991\)](#) as a 7.8km/s discontinuity at 30km (18.6mi) depth. In their studies in the northern part of Dixie Valley [Louie et al. \(2004\)](#), did not find a clear Moho signature. Northeast of Dixie Valley, at Battle Mountain, Nevada, the same authors observed anomalously thin crust over a limited region perhaps only 150km (93mi) wide, interpreted as a Moho depth of 19 to 23km (11.8-14.3mi). This area of thin crust is the part of a feature known as the "Humboldt Lineament" (or "Battle Mountain Heat Flow High") just west of Battle Mountain, which shows a high rate of extension normal to the trends of mapped faults in GPS analyses ([Blewitt et al., 2002](#)). The area of high

extension rate is roughly 100km (62mi) in diameter. In Dixie Valley, Hauge et al. (1986) observed Moho reflections at 9-10s. Receiver functions (Appendix 2-Table 4) within 200km (124mi) from Dixie Valley are continuously estimated by the EarthScope Automated Receiver Survey (EARS), Crotwell and Owens (2005), however, the results in Dixie Valley have large errors.



### 3.5.9 Seismic Attenuation in Dixie Valley

Physicists can measure the 'quality factor' of materials, i.e., the efficiency of the material to pass energy at a particular frequency. The quality factor,  $Q$ , is defined as the ratio of stored to dissipated energy in material as seismic waves propagate through. Attenuation is defined as the reciprocal of  $Q$  and represents a measure of the absorption or loss of energy in the seismic waves as they pass through intervening material.  $Q$ -values range typically from 10 to 100 in laboratory measurements on sandstones and 100–1000 in igneous and metamorphic rocks (Johnston et al., 1979). These measurements are performed on small, simple samples and do not take into account large scale structures, fractures, and mixtures. Attenuation usually comes

in two forms: intrinsic and scattering. Intrinsic attenuation relates to losses associated with heat and friction. Scattering attenuation is due to losses from waves reflected and refracted throughout the medium as they propagate from source to receiver. This implies that 3D Q- variations can be interpreted as being related to intrinsic physical properties of the rocks such as lithology, temperature, and porosity

Lees (2007) argues that attenuation is a relatively sensitive indicator of rock temperature in the upper 5km (3.1mi) of the crust. Seismic attenuation structure interpreted jointly with seismic velocity structure has the potential to strengthen the interpretation made on velocity structure alone. The attenuation image can also add independent information to the interpretation. For example, if a low velocity body beneath a caldera (such as at Medicine Lake volcano in northern California) is interpreted as a magma chamber, the interpretation is strengthened if the low velocity zone is also a high attenuation zone (Evans and Zucca, 1988). However, using P wave attenuation tomography Zucca and Evans, (1990), found that, beneath the Newberry volcano, low velocity and high attenuation were correlated in shallower layers, however, not correlated in deeper layers. According to Nakajima and Hasegawa (2003), consideration of attenuation, together with the  $V_p$ ,  $V_s$  and  $V_p/V_s$  values may resolve fluid-related low-velocity zones consistent with highly conductive zones detected in MT surveys.

As a result of the Lg coda being composed of waves scattered in the upper crust, coda Q is a suitable expression of attenuation. The variations in Lg coda Q at 1Hz attenuation for the western US are shown in [Figure 29](#) (Phillips and Stead, 2008) and are valid to a depth of around 3km (1.9mi). Low Q is correlated to volcanic areas (Cascades, Yellowstone, San Francisco field, and others surrounding the Colorado Plateau). The Lg Q values at 1Hz in the DVESA grid in [Figure 29](#) are shown in Appendix 2-Table 5.

### 3.5.10 Seismic Velocity Variations as a Function of Rock Composition and Temperature

We have collected physical property relationships based on literature and relevant exploration analogs (Appendices 4, 5 and 6). Our investigations are summarized below.

Estimation of elastic rock parameters using seismic methods is inherently a remote method. Measurements are made on arriving wave travel time at the surface (P or S waves with velocity  $V_p$  or  $V_s$ ) and on surface waves (Rayleigh) and used to infer properties deep within the earth. Variations of rock lithology or other physical parameters are estimated from the P- and S-wave velocity variations. This process leads to non-unique solutions because many rocks with differing physical states have similar seismic velocities and because inverting for subsurface properties from surface observations is poorly-constrained.

Seismic velocity depends on:

- Phase state (i.e., the presence or absence of partial melt);
- Composition (lithology, mineralogy and chemistry);
- Density;
- Temperature;
- Rock porosity; and
- Pressure.

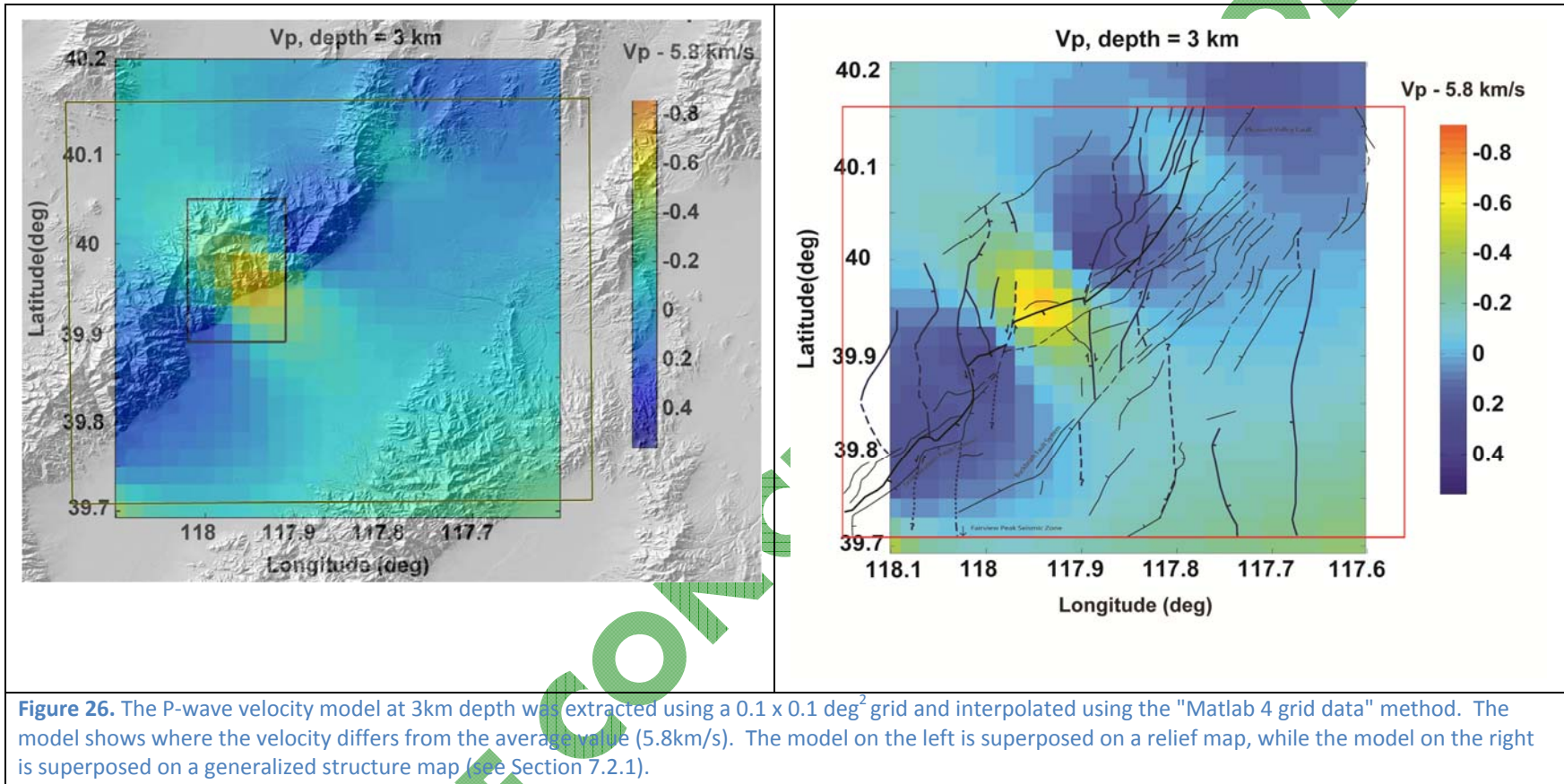


**Figure 26.** The P-wave velocity model at 3km depth was extracted using a  $0.1 \times 0.1 \text{ deg}^2$  grid and interpolated using the "Matlab 4 grid data" method. The model shows where the velocity differs from the average value (5.8km/s). The model on the left is superposed on a relief map, while the model on the right is superposed on a generalized structure map (see Section 7.2.1).

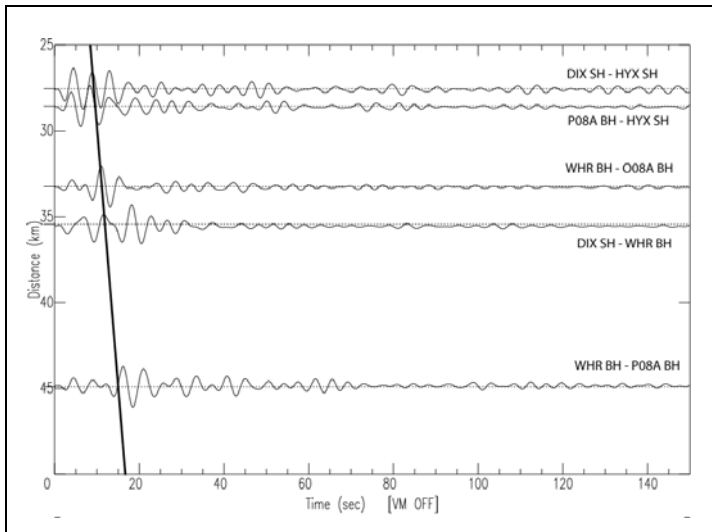


**Figure 27.** Newly extracted ambient noise results in Dixie Valley and vicinity using ambient noise crosscorrelations. Data was filtered with a 3 pole, zero phase ButterE in marworth filter from 0.15Hz to 0.3Hz (3 to 6 sec period). A 3km/s arrival time is represented by a black line in the plot. The Rayleigh component of the Green's Functions is clearly visible.

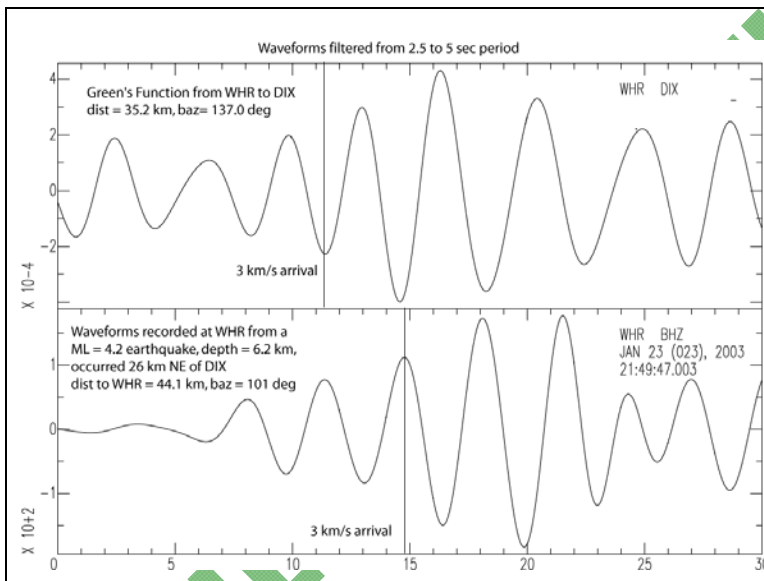


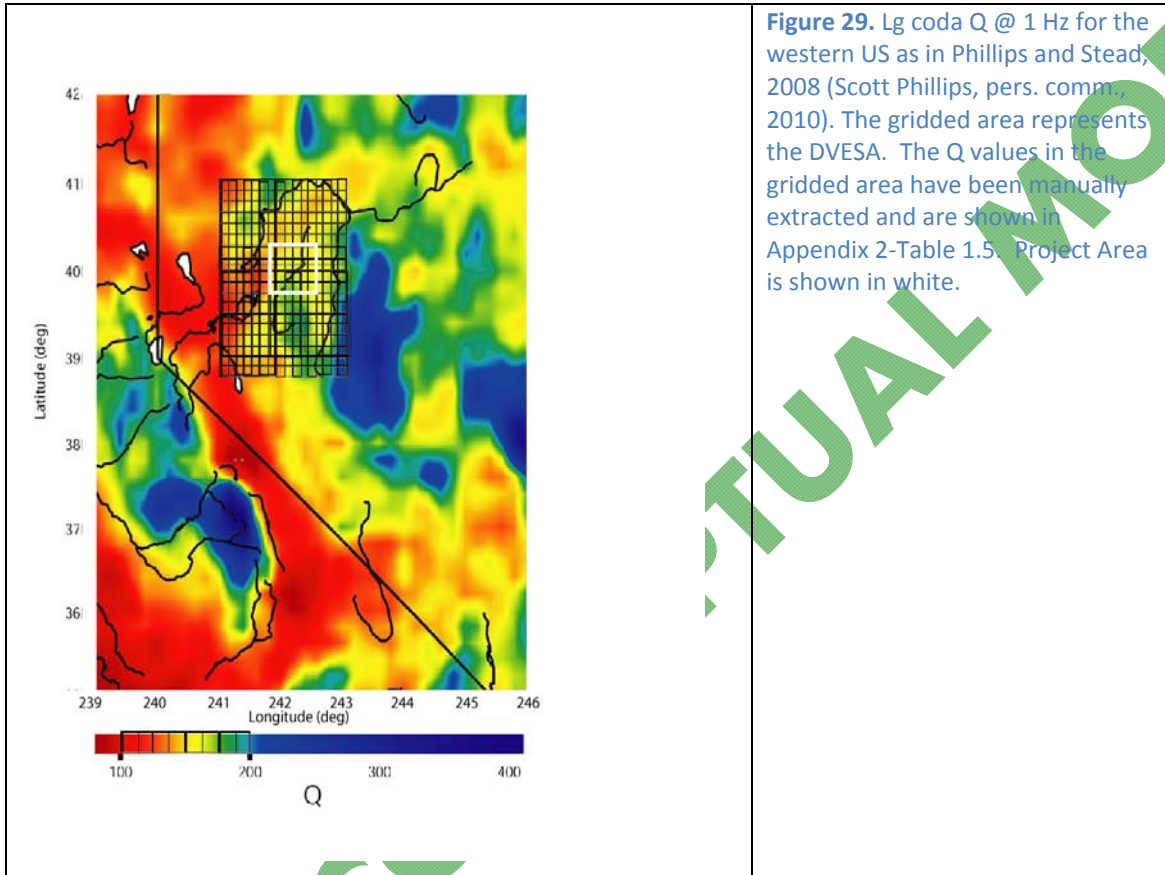
**Figure 28.** Shows a comparison of the GF extracted from ambient noise between stations DIX (SH - analog short period ) and WHR (BH broadband ) and waveforms recorded at WHR from an earthquake that occurred at a 6 km depth, 26km (16mi) northeast of DIX. Station DIX (Appendix 2- Table 1) is located in Dixie Valley. The plots show velocity in counts. The waveforms were filtered from 0.2 to 0.4Hz using a zero phase, six pole Butterworth filter.

For the majority of tomography studies, the seismic parameters under investigation include only four derived properties: velocity and attenuation of P- and S-waves, ( $V_p$ ,  $V_s$ ,  $Q_p$ ,  $Q_s$ ), and their respective ratios. These are the only properties that can be directly inverted for with seismic data. Reducing a myriad of geological and physical processes to four simple seismic observations is non-unique. Converting seismic field results to three-dimensional variations of rock states is tenuous, because a comprehensive data base of field based seismic properties related to rock physics laboratory studies is currently not available. Furthermore, most laboratory studies are performed in conditions significantly different from real earth situations and at frequencies substantially higher than typical seismic recordings (Kern, 1982).

Given these uncertainties, interpretation of tomographic images will be done using more geophysical information (i.e., geology, M, geochemistry, heat flow and gravity/magnetic investigations) than a simple velocity–density–temperature correlation. When coupled with experimental data on seismic properties of continental rocks at pertinent temperatures and

pressures, the geological and geophysical data can be used to correlate measurements of seismic velocities with mineralogic composition at depth.

The utility of the seismic information as a thermal and rock property indicator is discussed in Appendix 4.



### 3.6 Thermal

#### 3.6.1 Background Conductive Heat Flow

A shallow temperature gradient map, shown initially as [Figure 2](#) and also included as [Figure 30](#), uses a number of constraints to assess the background heat flow in Dixie Valley. To analyze the conductive heat flow only, wells that were influenced by geothermal water circulation were not used. This includes most of the wells within the Senator fumaroles and the DVPP area.

Additional constraints are:

- The total temperature dataset includes 25 TGHs within bedrock and 157 TGHs in the valley;
- While the temperature data used in this model includes only 13 holes within the ranges and 78 holes in the valley;
- Higher thermal conductivity of the bedrock in ranges compared to the valley fill;
- Gradient values at depths less than ~500m (1640ft) were used for contouring; and
- Temperature inputs from the range and valley were calculated separately due to topography and elevation.

### 3.6.2 Thermal Anomalies within Dixie Valley

There are around ten areas that have relatively dense thermal gradients within the Dixie Valley area ([Figure 30](#)). Four of these are located along the DVFZ and around six occur within the DVSA. The dense thermal gradient areas along the DVFZ include from north to south: (1) the Senator Fumaroles just northwest of DVPF; (2) the section 10 fumaroles within the DVPP; (3) the Dixie Comstock Mine; and (4) the Dixie Meadow anomalies. The anomalies occurring away from the DVFZ are located near Hyder HS (northeast of producing field) and near New York Canyon within Buena Vista Valley. Temperature-depth profiles of the Dixie Comstock Mine, Dixie Meadows, and Hyder Hot Springs are shown in [Figure 31](#). These anomalies are described below. Two additional prominent anomalies in the Dixie Valley area include the McCoy and Clan Alpine Ranch anomalies, which lie primarily outside the Project Area, and are not directly discussed in this report.

#### *Dixie Comstock Mine*

- Stable isotope analyses of mineralized quartz breccia show that the ore fluid was 180°C (356°F), near-boiling meteoric water, possibly related to the present-day hydrothermal activity in Dixie Valley (Vikre, 1994).
- One deep well (45-14) has a maximum temperature of 196°C (385°F) at 2750m (9022ft) with an upper gradient of (52°C/km [3.9°F/100ft]) within the upper 1200m (3900ft) of the hole and lower gradient of (12°C/km [0.9°F/100ft]) with the section below 1200m;
- Curves in intermediate depth TGHs (SR-2, SR-2A) shows evidence of lateral flow at shallow depth; and
- “Hot” rock faces are observed within the mine and the area shows significant surface alteration.

#### *Dixie Meadows*

- Most TGHs have “normal” background gradients indicative of the area (58°C/km [4.3°F/100ft]);
- TGHs (8G1 and 8G2) have high initial gradients (600+°C/km [44.5°F/100ft]) that become isothermal by about 15m (50ft);
- Three anomalous temperature curves (8g1, 8g2, 8g3) indicate lateral flow of warm water (~75-125°C [167-257°F]) at very shallow depth;
- Extensive fluid flow at the hot springs and a weak fumarole at the range front ~1km (3280ft) west of the hot spring area imply lateral flow from the range front; and
- Hot springs are coincident with the sharp horizontal gravity gradient in this area suggesting possible vertical up-flow along the piedmont fault.

#### *Hyder Hot Springs*

- Located ENE of the producing field near the center of the valley ([Figure 14](#));
- Occurs near a strong positive aeromagnetic anomaly related to a body of gabbroic rocks in the basement beneath the valley fill and at the intersection of two faults ([Figure 10](#))
- Lies within an suggested accommodation zone between the east-dipping Dixie Valley Fault and the west-dipping Pleasant Valley structures (Drakos et al. 2011); and

- Intermediate depth TGHs (EDV-1, EDV-2, EDV-3) have gradients that change only at conductivity breaks from valley fill to basement indicating the background conditions for the valley in that area.

### *New York Canyon*

- Thermal anomaly located west of the Stillwater Range in the Buena Vista Valley;
- May infer a large area of elevated heat flow beneath the Stillwater Range that could possibly connect to the thermal anomalies in Dixie Valley based on the suggested elevated thermal conditions under the Stillwater Range; and
- Occurs adjacent to a major north-trending structure and the range-bounding fault that bounds the western edge of the Stillwater Range, referred to as the Stillwater Fault.

### **3.6.3 Numerical Modeling**

The general consensus of geothermal systems in the B&R assumes no magmatic component and that meteoric water enters the system via the ranges or valley-fill, heats up during deep circulation, and ascends along the permeable pathway, usually an active range-bounding fault. In the case of Dixie Valley, the geothermal system is unusually hot as temperatures in excess of 280°C (536°F) have been encountered at ~3km (9840 ft) depths.

Wisian and Blackwell (2004) and McKenna and Blackwell (2004) have numerically examined the conditions necessary for a reservoir temperature near 280°C (536°F) to be generated and sustained in the Dixie Valley geothermal system. Parameters used were the measured temperature along the producing fault and the predicted surface heat flow. Drilling indicates temperatures >190°C (374°F) at a 2.5 to 3.0km (8200-9800ft) depth along a strike length of at least 14km (8.6mi) along the west side of the valley (from the DVPF to Dixie Comstock Mine. Their analysis generated a steady state numerical model with upflow along a permeable range-bounding fault that dips 65°. The temperature and heat loss are dependent on the permeability of the basement. For lower permeabilities the modeling shows little convective heat transfer while high permeabilities imply that the system cools to a low regional temperature over time. The range of basement permeability considered is  $10^{-15} \text{ m}^2$  to  $10^{-16} \text{ m}^2$ . It is noted that the model uses a single 65° dipping range-bounding fault to characterize the permeable upflow zone, while evidence presented in [Section 2.2.2](#) show the structural setting is more complicated. For the purposes and scale of the model, this discrepancy should not greatly affect the modeling results.

### *Temperature Modeling Conclusions*

- Temperatures in B&R geothermal systems are time dependent;
- Temperature is not a function of the fault permeability or fault depth as the modeling showed that a fault about 2km (6560ft) deeper than the standard model has similar behavior/temperature;
- Regional permeability deeper than 6km (3.7mi) was not required to generate the observed temperature distribution in the geothermal reservoir;
- A high temperature reservoir within an extensional geothermal system (>280°C [536°F]) is a function of oscillating high/low fault permeability maintained by seismicity along the range-bounding fault;
- Application of the model results to Dixie Valley indicate that the age of present thermal flow is within the range of 50,000 to 500,000 years. This indicates that the geothermal

system is younger than the Dixie Valley fault zone (implied periodicity) and this finding is also supported by spring deposit age-dates (see [section 5.2.1](#)); and

- Temperatures are high enough for sustained geothermal development ( $>150^{\circ}\text{C}$  [ $302^{\circ}\text{F}$ ]) as long as the permeability channels remain open and the fault conducting the geothermal fluids doesn't seal.

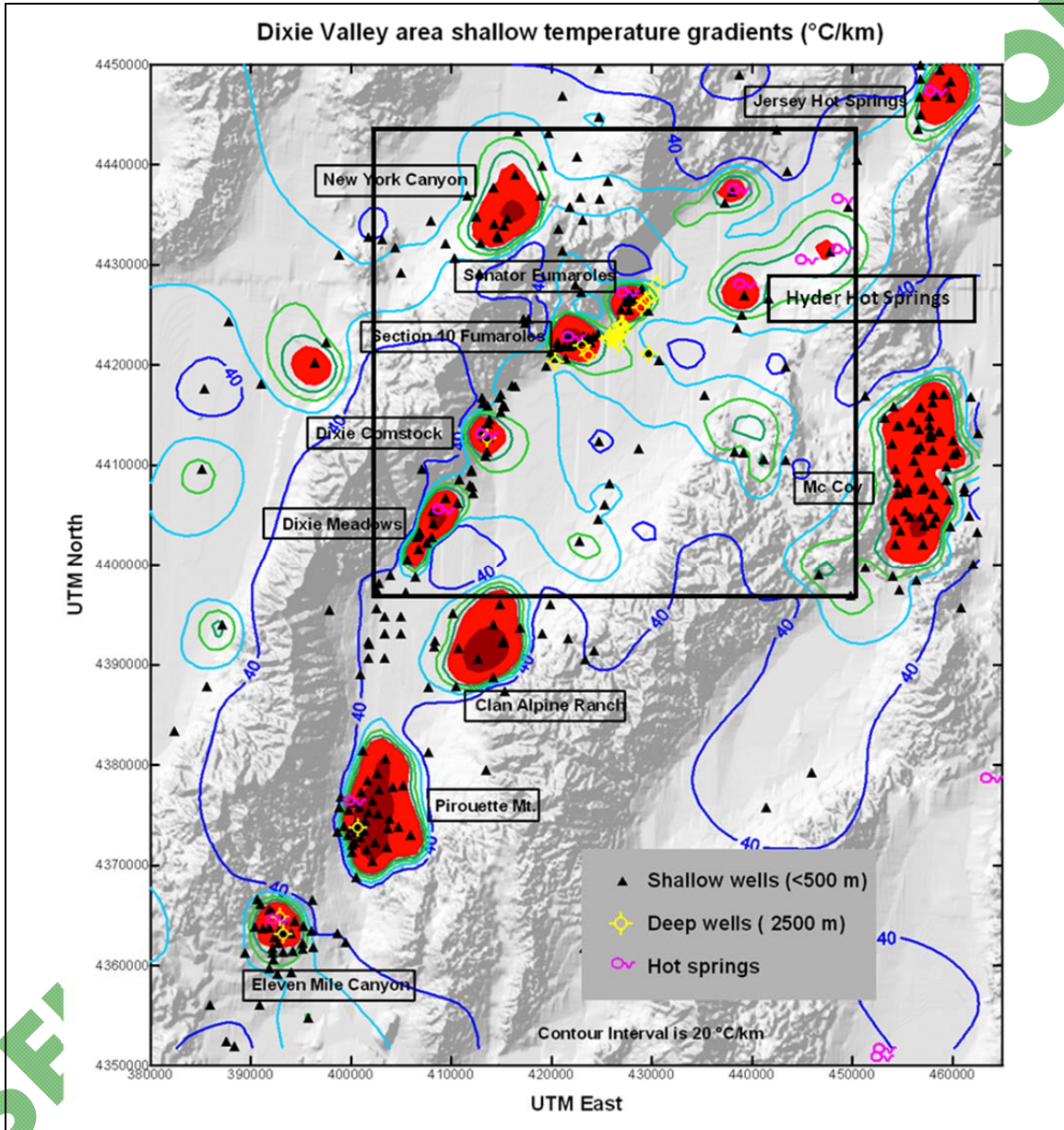


**Figure 30.** Thermal gradient and well locations in the Dixie Valley area. Contour intervals are ( $20^{\circ}\text{C}/\text{km}$  [ $1.5^{\circ}\text{F}/100\text{ft}$ ]). From ( $120\text{--}250^{\circ}\text{C}/\text{km}$  [ $8.75\text{--}18.5^{\circ}\text{F}/100\text{ft}$ ]) the contours are a red fill and from ( $500^{\circ}\text{C}/\text{km}$  [ $37^{\circ}\text{F}/100\text{ft}$ ]) the contours are a dark red fill. Contours in the ranges are diagrammatic due to the lack of data. Well gradient locations are shown as black triangles for shallow wells (<500meters [ $1640\text{ft}$ ]) and as black circles for wells deeper than 500m ( $1640\text{ft}$ ). Black bounded box is the approximate boundary of the EGS Exploration Methodology Study Area. The figure and caption are after Blackwell et al. (2005).

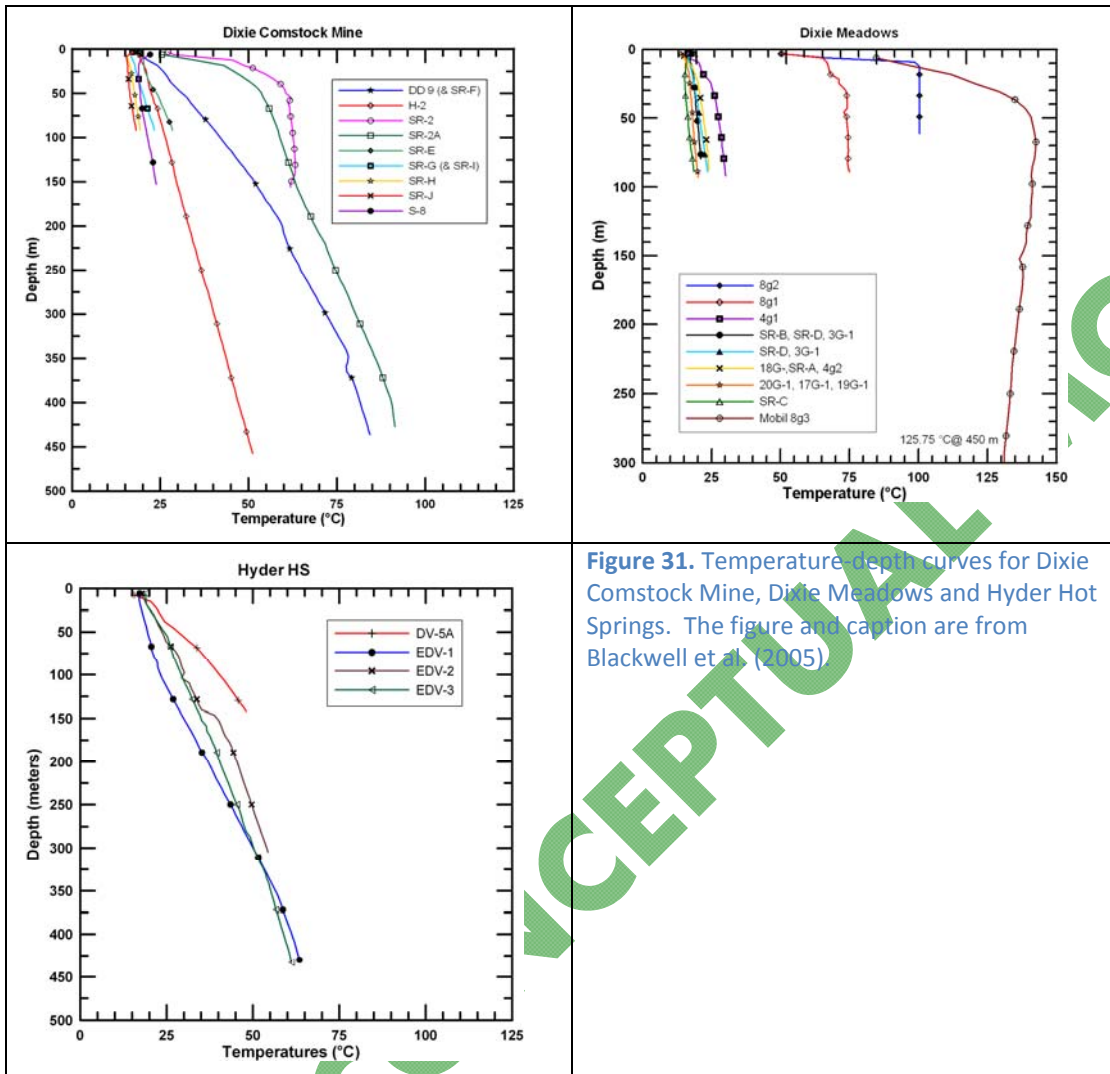


Figure 31. Temperature-depth curves for Dixie Comstock Mine, Dixie Meadows and Hyder Hot Springs. The figure and caption are from Blackwell et al. (2005).

## 4. Hydrology

### 4.1 Regional Setting

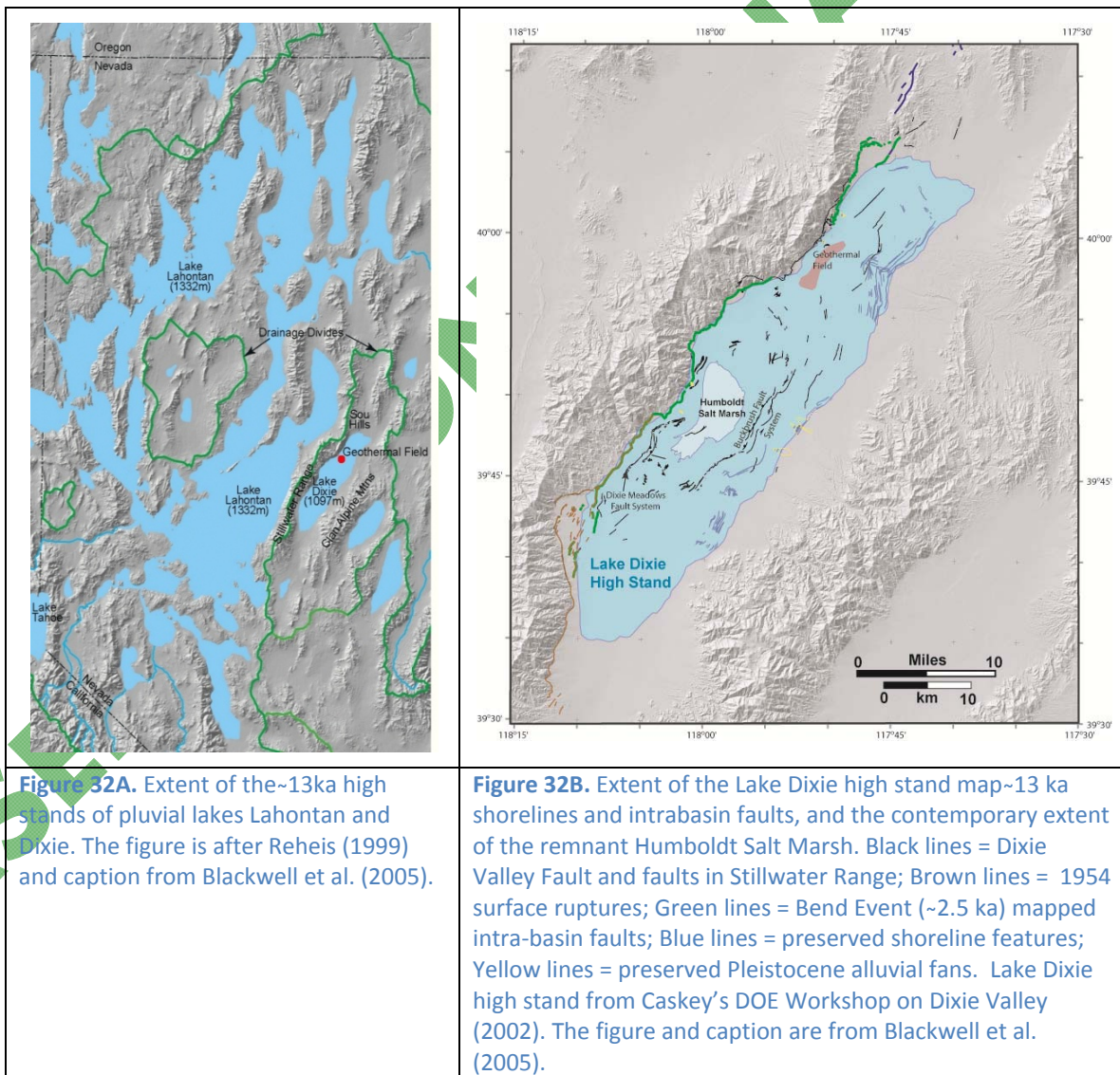
Dixie Valley is part of a larger drainage basin that includes Pleasant Valley and Jersey Valley to the north and Fairview Valley to the south, both of which flow (groundwater and surface water) into Dixie Valley. The Humboldt Salt Marsh is the lowest elevation in the basin and has no surface outlet. Evapotranspiration is the principal mechanism for shallow aquifer water and geothermal water to escape from this closed system, occurring at the Humboldt Salt Marsh and other playa settings within adjacent valleys.

During the Pleistocene, Lake Lahontan occupied the topographically enclosed valleys of the Western Great Basin including the Carson Desert and Carson Sink, immediately to the west of Dixie Valley (Figure 32A). Even during the highest stands of the lake, it was separated from the lower elevation Lake Dixie by a series of high passes. Lake Dixie was formed from local precipitation and glacial melt water and occupied the area within Dixie Valley (Figure 32B). The high stand of Lake Dixie was about 1097m (3566ft) above sea level, evident from preserved

shorelines features on alluvial fans within the basin and bedrock on the range front. It covered an area of about 715km<sup>2</sup> (276mi<sup>2</sup>) with a maximum water depth of about 70m (230ft) above the Humboldt Salt Marsh, and inundated a large portion of the length of the DVFZ. The high stand occurred at ~12-13 ka, coeval with the high stand of Lake Lahontan.

#### 4.2 Groundwater

Shallow groundwater within Dixie Valley is recharged from precipitation in the drainage basin and surrounding ranges, and from adjacent valleys that provide surface and subsurface recharge to Dixie Valley. Groundwater is stored in both unconfined and confined (artesian) aquifers within the basin-fill sediments. Artesian aquifers in the Dixie town site area and in the area east of the Humboldt Salt Marsh are described as sandy to gravelly alluvial layers between fine-grained sediments (silts, clays). They occur at depths less than 70m (230ft) and are pressurized from infiltration in and near the Clan Alpine Range. Where these artesian aquifers intersect intrabasin faults, e.g., just east of the Humboldt Salt Marsh along the Buckbrush fault system, freshwater springs occur (Figure 33).



Another significant influence affecting groundwater in Dixie Valley is the outflow of geothermal fluids from the DVFZ into the basin-fill sediments. Salient features of the groundwater setting in Dixie Valley are:

- Depth to water table ranges from the surface at the Humboldt Salt March to over 60m (197ft) in the southern valley;
- Contemporary precipitation is not sufficient for recharging valley aquifers and deeper geothermal systems;
- Recharge of shallow aquifers due to (1) precipitation on the mountains surrounding the basin, and (2) outflow of geothermal fluids from fault zones into basin-fill sediments;
- Considerable input of deep geothermal waters into the shallow aquifers (Nimz et al., 1999; Bruton et al., 2002); and
- Isotopic and geochemical data (Janik et al., 2002) suggest that a 10 to 25% addition of deep geothermal waters to the shallow aquifer waters is necessary to explain their isotopic and chemical composition.

#### 4.2.1 Buckbrush Fault System

Intrabasin springs occur along the Buckbrush fault system near the Humboldt Salt Marsh and along a northerly trend between the north end of the fault system and the southern part of the producing geothermal field ([Figure 33](#)). All the springs tap gravelly artesian layers containing shallow groundwater that are described in well logs within the area. Springs along the fault system are active presently while springs along the northern trend just to the north are considered recently active, but not active presently. It is suggested that the 1954 earthquake could have opened channels along the Buckbrush system and closed those just south of the geothermal system. Several of these shallow wells (TGHs) near the fault have warm water, as geochemical and isotopic data show that the artesian water in these wells and springs represents a mixture of cold meteoric water and warm water from geothermal activity derived from the Buckbrush fault zone.

#### 4.3 Geothermal Waters

The geothermal system is derived from recharge water that entered the fault zones and permeable sediments on the margins of the valley floor during the last glacial cycle. This requires long-term (thousands of years), and continuous flow-through of these deep seated waters. The majority of this flow enters the basin-fill sediments, with a small amount actually escaping to the surface in a few, scattered hot springs and fumaroles.

Geothermal gradients measured in wells throughout the valley define several places along the Dixie Valley fault where geothermal waters discharge into valley-fill sediments and flow basinward in the shallow subsurface. Outflow zones include Sou (Seven Devils) Hot Springs/Hyder Hot Springs in the northern valley, Senator Fumaroles (DVPF), Section 10 Fumaroles (DVPP), and Dixie Hot Springs (southern end of Humboldt Salt Marsh) which are shown in [Figure 33](#). The location of these hot springs are controlled by the range bounding fault within the DVFZ and lie within the areas of high geothermal gradients within Dixie Valley ([Figure 33](#)). Additionally a local thermal gradient high east of Dixie Meadows referred to as the Clan Alpine Ranch anomaly ([Figure 30](#)) could also be considered an outflow zone of geothermal fluids derived from a dilatational zone occurring at a fault termination of a significant range-bounding fault on the eastern edge of Dixie Valley. This occurs within the southernmost boundary of the Project Area. Salient highlights of the origin of geothermal waters are:

- Isolated from present day meteoric recharge;
- Vertical local recharge from Lake Dixie with model dependent isotopic ages indicating waters are 12-20 ka;
- Recharged during the Pleistocene as the oldest recharge waters measured are ~14,000 years old based on model dependent  $^{14}\text{C}$  ages; and
- Exact age of the system cannot be accurately assessed because the reservoir has been contaminated during nearly 20 years of production, steam separation and injection.

#### 4.4 Hydrogeochemistry

The waters within the Dixie Valley basin compositionally overlap the waters from the Stillwater Range and the Clan Alpine/Augusta Ranges to the east. Stillwater Range derived waters typically have higher Mg and Cl, and lower Ca than waters from the Clan Alpine/Augusta Range most likely reflecting lithologic differences in the ranges. The overlap is expected as the valley sediments are derived of bedrock detritus from both of the surrounding ranges. Additionally the basin waters tend to have higher Na and K, which is typical of waters with the input of geothermal fluids, which indicate a third distinct source in their history.

While the sources for the Dixie Valley basin waters are largely constrained, the stable isotope geochemistry of the Dixie Valley related waters can be used to determine the possible recharge areas for the geothermal reservoir and associated hot spring systems. A plot of  $\delta\text{D}$  vs.  $\delta^{18}\text{O}$  (Figure 34) of waters from the Stillwater Range, Clan Alpine Range, Dixie Valley Basin, and the production zone is used to determine spatial isotope distributions and relations among geographic areas (elevation). Waters from the pre-production reservoir do not isotopically resemble the waters from the surrounding ranges indicating that the ranges are not recharge sources for the reservoir. Additionally these cold waters from the ranges are isotopically enriched relative to cold waters in Dixie Valley basin which is unexpected as waters of high elevations usually show depleted isotopic compositions compared to those of lower elevation. According to Blackwell et al., (2005) and observations from Goff, Janik and others (1998; 2002), a reasonable explanation for this anomaly is that the basin waters are older and recharged when isotopic compositions of meteoric recharge were more depleted (Pleistocene recharge). Instead fluids from geothermal reservoir have similar  $\delta\text{D}$  values to Dixie Valley basin but are enriched in  $\delta^{18}\text{O}$  by about 2.5 ‰, consistent with significant water-rock isotopic exchange. The authors imply that Dixie Valley was recharged at elevations higher than samples collected in the ranges or originated from an earlier time when precipitation was isotopically different.

## 5. Geochemistry

### 5.1 Introduction

Numerous geochemical studies have been undergone in Dixie Valley, with a more recent and comprehensive report compiled (Goff et al., 2002) that includes an extensive geochemical database based on samples collected and analyzed from 1996-1999. This report can be found as Appendix 7. General characteristics as summarized in Blackwell et al. (2005) can be found in Appendix 8 with the salient aspects described below. The geochemical studies conclude that groundwater samples from Dixie Valley are derived from either (1) younger meteoric waters from the surrounding ranges, (2) High Temperature Geothermal Fluids (HTGF) characteristic of the Dixie Valley producing reservoir, or (3) more commonly a mixture of the two.

The preliminary analysis of the geochemical data has further identified at least three primary fluid types within Dixie Valley that are geochemically distinct from the HTGF encountered in the geothermal wells. The distribution of these primary fluid types with respect to the regional Dixie Valley setting is shown in [Figure 35A](#). The fluid types are characterized as (1) High Cl-low HCO<sub>3</sub>,

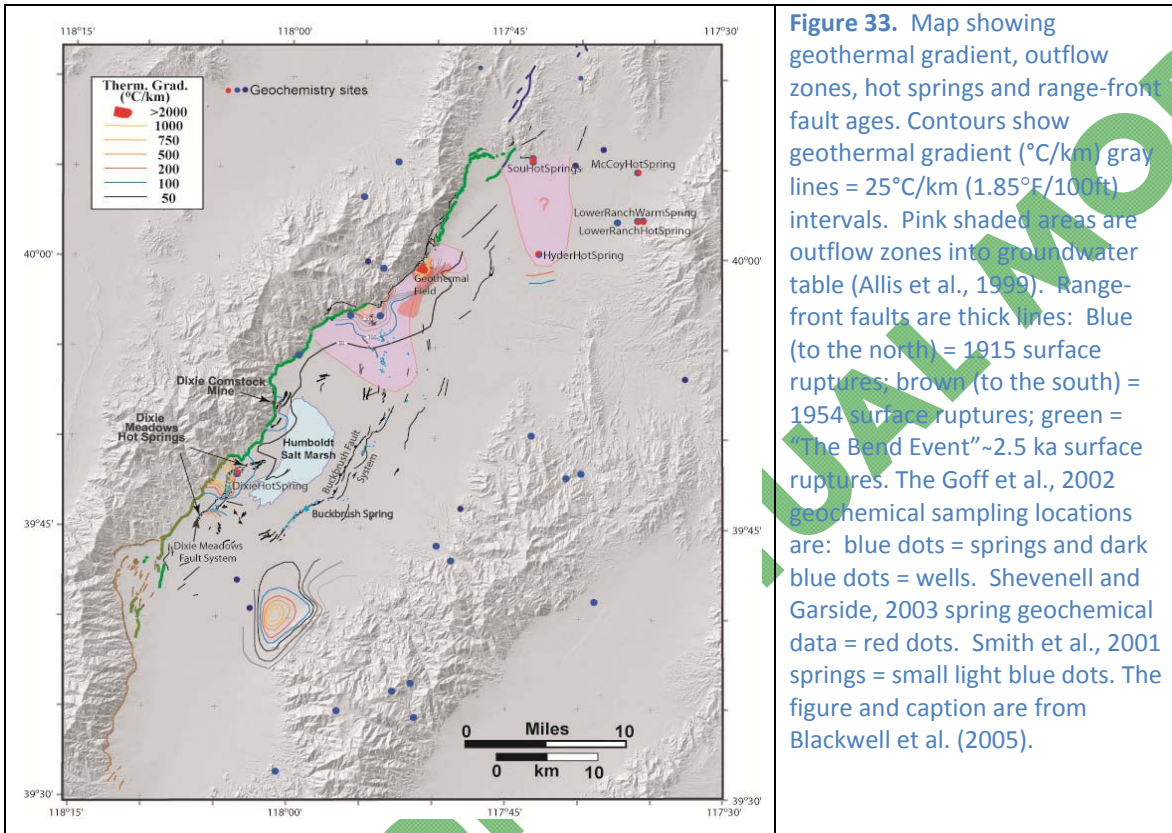


**Figure 33.** Map showing geothermal gradient, outflow zones, hot springs and range-front fault ages. Contours show geothermal gradient (°C/km) gray lines = 25°C/km (1.85°F/100ft) intervals. Pink shaded areas are outflow zones into groundwater table (Allis et al., 1999). Range-front faults are thick lines: Blue (to the north) = 1915 surface ruptures; brown (to the south) = 1954 surface ruptures; green = "The Bend Event" ~2.5 ka surface ruptures. The Goff et al., 2002 geochemical sampling locations are: blue dots = springs and dark blue dots = wells. Shevenell and Garside, 2003 spring geochemical data = red dots. Smith et al., 2001 springs = small light blue dots. The figure and caption are from Blackwell et al. (2005).

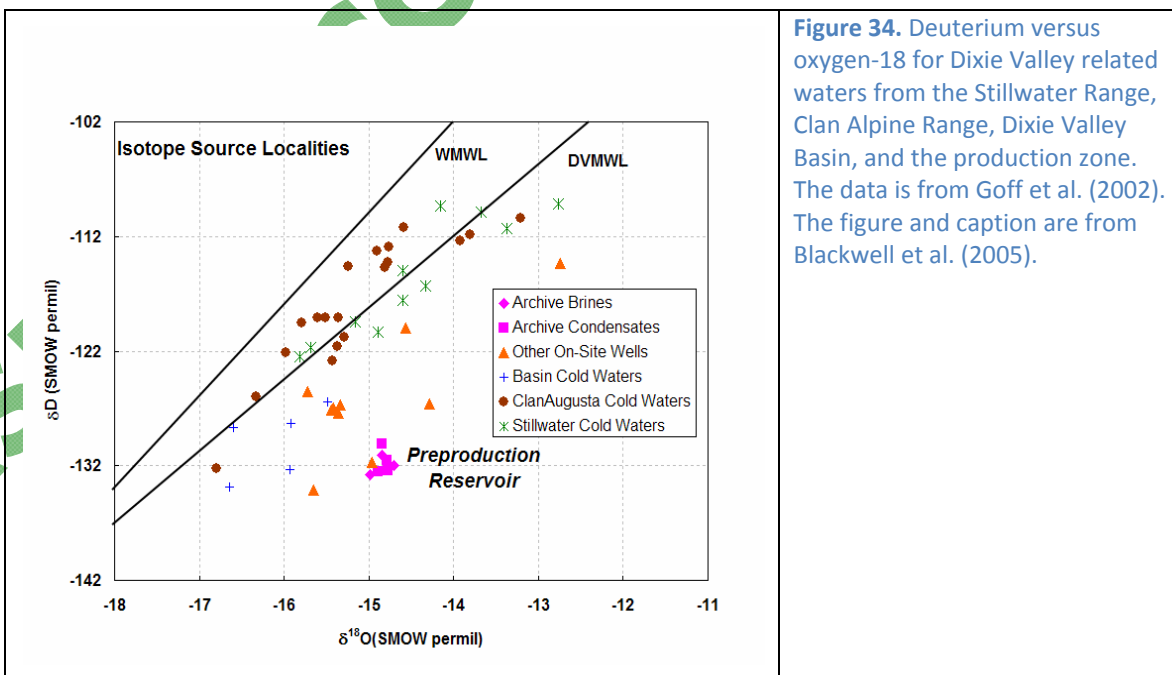


**Figure 34.** Deuterium versus oxygen-18 for Dixie Valley related waters from the Stillwater Range, Clan Alpine Range, Dixie Valley Basin, and the production zone. The data is from Goff et al. (2002). The figure and caption are from Blackwell et al. (2005).

(2) Low Cl-high  $\text{HCO}_3$ , and (3) Low Cl-low  $\text{HCO}_3$ . A further evaluation indicates significant fluid mixing and the presence of a fourth very dilute fluid component (B.M. Kennedy, pers. comm., 2010), [Figure 35B](#). This component is classified as geochemically un-evolved near surface ground water. The evidence of mixing may explain inconsistencies in calculated chemical geothermometer temperatures, help deconvolve the impact of mixing, and enable more accurate calculations of water-rock equilibration temperatures.

Geochemical features of HTGF and mixed fluids are listed below:

#### **Characteristics of High Temperature Geothermal Fluids (HTGF)**

- reservoir pH between 6-9;
- Na-K-Cl waters;
- relatively high  $\text{SiO}_2$ , As, B, Br, and Li;
- dissolved  $\text{CO}_2$  is another major component;
- relatively low concentrations of divalent cations (Ca, Mg, and Sr); and
- very low concentrations of trivalent cations (Al and Fe).

#### **Characteristics of Mixed Fluids**

- relatively high concentrations of  $\text{SiO}_2$ , Cl, Na, K;
- relatively high concentrations of four key trace elements, As, B, Br, and Li; and
- retains constant ratios such as B/Cl and Li/Cl.

### ***5.2 Springs, fumaroles and shallow wells***

Most of the thermal/mineral springs in the Dixie Valley region ([Figure 35A](#)) do not possess the high-temperature geochemical signatures described above and indicative of the geothermal reservoir. This implies that these waters either haven't equilibrated at high temperatures or are of mixed fluid composition consisting of high temperature fluids and cooler groundwaters. While mixed fluid generally retain constant ratios of conservative components (B/Cl and Li/Cl), the shallow well and spring waters display different ratios among themselves and when compared to the DVPF production fluids. Additionally shallow well and spring waters have very low arsenic to chloride ratios further suggesting that they are not related to production fluids. The lack of trends between the different fluids implies that each of somewhat isolated geothermal systems has a different geochemical history. Thus, each thermal system is geochemically unique and has evolved along a distinctive path that is influenced by the sources of water, interactions with local wall rocks, and relationship to crustal heat sources.

The As/Cl relationships of pre-production fluids (referred to as archive brines), production brines, thermal/mineral springs and thermal/mineral wells are shown in [Figure 36](#). While the pre-production and production fluids define a similar trend, the thermal/mineral well and spring waters of the Dixie Valley region define no such trend. These waters do not lie on the mixing trend of the production fluids and also do not lie on a similar trend among themselves. This further indicates that all fluids originated from separate geothermal cells and that the geothermal fluids from springs and shallow wells are not part of the same system as the current electrical generation producing system at the DVPF.

### 5.2.1 Hot Springs and Fumaroles

Hot springs and fumaroles are located along the DVFZ and associated intrabasin faults where geothermal fluids rise along permeable segments of the fault and either discharge into the basin-fill sediments or more uncommonly at the surface. The following is an overview of the major hot springs and fumaroles within and around the Project Area (for locations see [Figure 33](#)). Provided below is a summary of the characteristics of the various hot springs in Dixie Valley.

#### *Dixie Meadows*

- max T=84°C (183°F)
- Group of at least 20 springs and seeps near the southern half of Humboldt Salt Marsh;
- Emerges from a hydrothermal plume rising along the DVFZ (range front or buried piedmont fault);
- Total discharge of as much as 200 liters/min (52gpm); and
- Relatively high silica and chloride.

#### *Hyder HS*

- T= 77°C (171°F) and 40 l/min (11gpm);
- Located near the middle of Dixie Valley about 4km (2.5mi) east of the DVPF;
- Two or more seeps and springs discharge from a soft travertine deposit (hill);
- Controlled by the intersection of buried faults or possibly explained by an accommodation zone between two adverse structures (Drakos et al. 2011);
- Mixed fluids including a parent fluid similar to the 62-21 well waters, but mixed with shallow aquifer water; and
- Spring system lies at the northernmost end of a positive aeromagnetic anomaly associated with a buried basement block of the Jurassic mafic complex.

#### *Jersey HS*

- T= 59°C (138°F) and 200 l/min (53gpm); and
- Issues from a modified pool with no obvious structural control except a localized step-over.

#### *Lower Ranch HS*

- max T = 41°C (106°F);
- Five HS and seeps from a major faulted travertine deposit in eastern Dixie Valley; and
- Water does not resemble Dixie production fluids.

#### *Section 10 (unnamed) fumaroles*

- max T = 98°C (208°F);
- NW of DVPP lease, no associated hot springs, steam vents only;
- Fumarole activity occurs directly along the range-front fault within a localized alteration zone;
- Also referred to as the Frying Pan fumaroles (Al Waibel, pers. comm., 2011);
- Sinter deposits with intergrown travertine, sulfur and other sublimates; and
- Fossil hot springs related to previous seismic activity on the DVFZ.

### Senator fumaroles

- max T = 98°C (208°F);
- Only surface thermal manifestation of the subsurface, high temperature thermal anomaly;
- Present fumarole activity occurs on the northeast edge of an altered "mound" structure around 500m (1640ft) valleyward from the main range-front contact;
- No fossil hot springs or sinter deposits, forms a cluster of springs extending 600m (1970ft) along the DVFZ;
- The increased activity observed at the present time is mostly production related and due to draw-down of the geothermal reservoir (B.M. Kennedy, pers. comm., 2011); and
- Rocks within the main fumarole cluster are highly fractured and faulted Jurassic quartzite (Boyer Ranch) and overlying alluvial fan deposits.

The Dixie Valley region contains many hot spring deposits and alteration zones related to present and past hydrothermal activity and some of these deposits have been age-dated ([Table 2](#)).

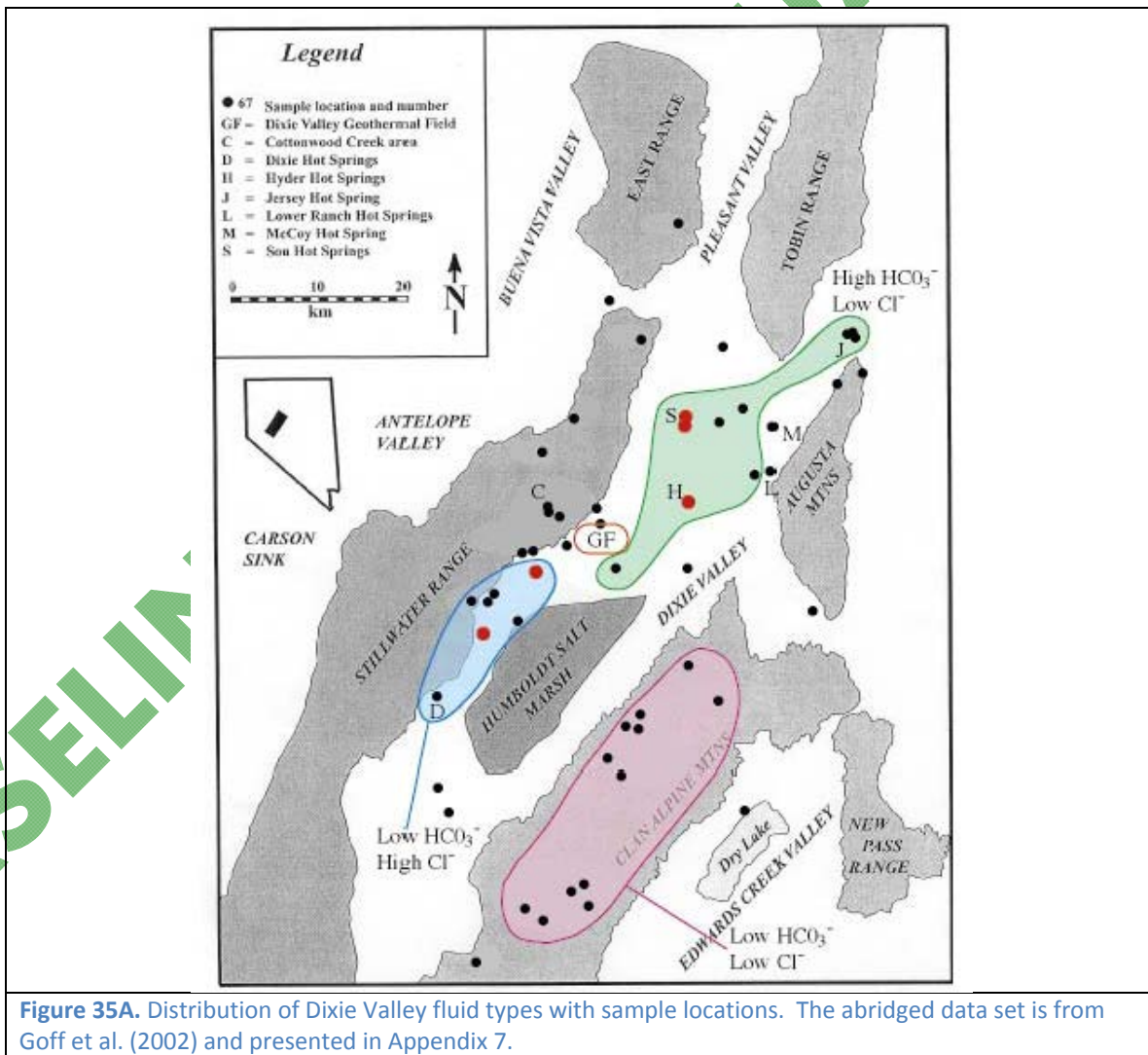
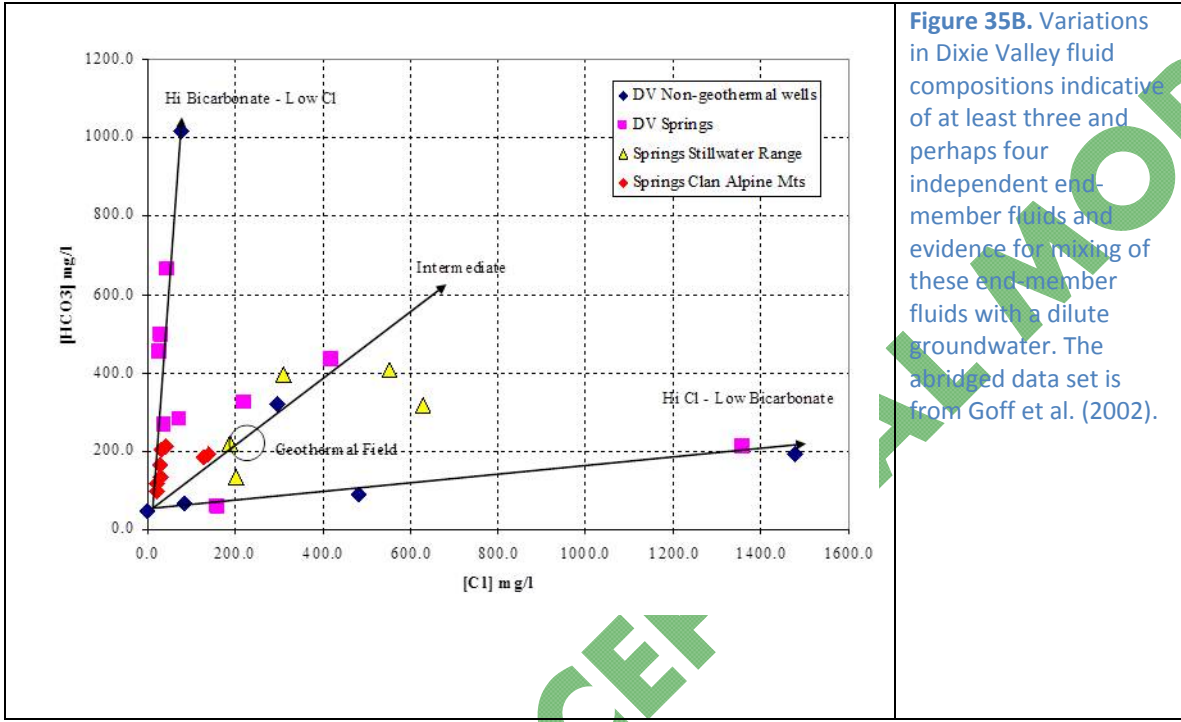


Figure 35A. Distribution of Dixie Valley fluid types with sample locations. The abridged data set is from Goff et al. (2002) and presented in Appendix 7.

### 5.3 Deep Wells

The following section details the salient elements of wells containing thermal waters but no associated near-surface thermal features .



**Figure 35B.** Variations in Dixie Valley fluid compositions indicative of at least three and perhaps four independent end-member fluids and evidence for mixing of these end-member fluids with a dilute groundwater. The abridged data set is from Goff et al. (2002).

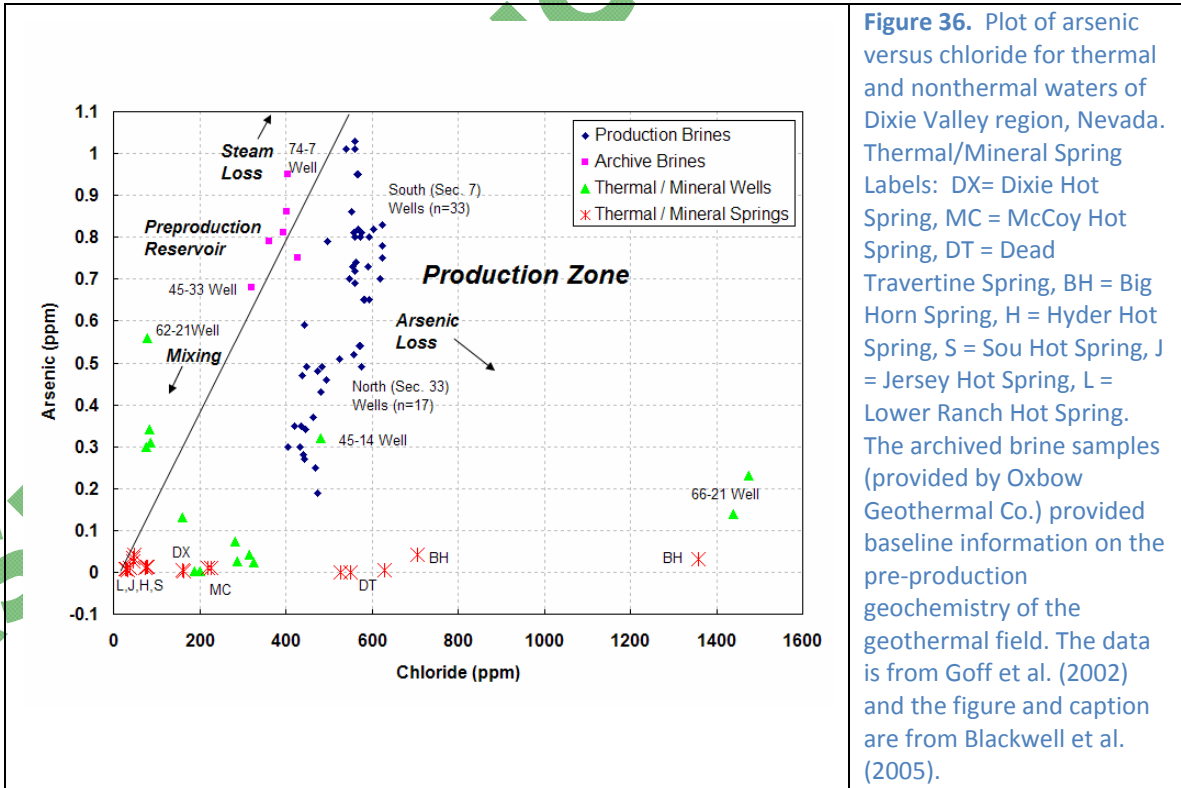


**Figure 36.** Plot of arsenic versus chloride for thermal and nonthermal waters of Dixie Valley region, Nevada. Thermal/Mineral Spring Labels: DX= Dixie Hot Spring, MC = McCoy Hot Spring, DT = Dead Travertine Spring, BH = Big Horn Spring, H = Hyder Hot Spring, S = Sou Hot Spring, J = Jersey Hot Spring, L = Lower Ranch Hot Spring. The archived brine samples (provided by Oxbow Geothermal Co.) provided baseline information on the pre-production geochemistry of the geothermal field. The data is from Goff et al. (2002) and the figure and caption are from Blackwell et al. (2005).

### 5.3.1 Bolivan Artesian Well

This well is located well within the Stillwater Range at an elevation of around 1500m (4900 ft) within Cottonwood Canyon just upstream of an abandoned mining community (location shown on [Figure 17a](#)). It was originally drilled as a thermal gradient hole within highly altered Jurassic gabbro and limestone and is indicative of a localized geothermal anomaly in this area of the Stillwater Range (S. Johnson to D. Blackwell, pers. comm., 1997). The flow and geochemical characteristics of this well has been reported by Goff et al. 2002 as:

- Artesian well (40 l/min [11gpm] of 29°C [84°F] water);
- No free gas observed discharging from the well water; and
- Low Si, As, B, Br, Li; but 290ppm Cl indicating the waters don't resemble DVPF fluids.

Currently, a small amount of fluid (1-2 l/min, 0.3-0.5 gpm) has been observed discharging from a near surface pipe (T. Cladouhos, pers. comm., 2010).

### 5.3.2 Dixie Federal Well 45-14

This well is located about 1km (3200ft) SE of the abandoned Dixie Comstock gold mine and is about 12km (7.4mi) SW of the DVPF (see [Figure 40a](#)). The well was drilled in 1979 within a fault block bounded by a north-trending segment of the range-front fault and the surface expression of the main piedmont fault within the DVFZ. Temperature surveys show a maximum temperature of 196°C (385°F) at a total depth of 2750m (9022ft). Chemical characteristics of the produced fluid are:

- High concentrations of SiO<sub>2</sub>, As, B, Br, and Li;
- Low concentrations of Ca and Mg with a Cl content of 481ppm;
- Most similar in general composition to deep reservoir waters (Figure 26);
- Chloride variation plots indicate the fluid is not derived from the 245°C (473°F) reservoir;
- Very weak (8-15 l/min, 2-4 gpm) artesian flow (Dick Benoit of Magma Power Company to Joe Iovenitti of AltaRock, pers. comm., 2011); and
- Fluid entries at 1940m (6365ft) and 2510m (8235ft); rate of flow= 1.1 l/s or 14 gpm (Williams and Sass, 1997).

### 5.3.3 Dixie Comstock Mine

- The mine is located within the DVFZ, adjacent to a north-trending segment, just west of 45-14 (see [Figure 40a](#));
- Typical stockwork epithermal ore deposit with "hot" rock faces reported in mine; and
- Possibly related to present hydrothermal activity in Dixie Valley.

### 5.3.4 Dixie Federal Well 66-21

The well is located in the valley just south of DVPP; and only 2km (6560ft) SW of the section 10 fumaroles (see [Figure 40a](#)). The well was also drilled in 1979 with a maximum recorded temperature of 215°C (419°F) at 2740m (8990ft).

- Weak artesian flow (Dick Benoit of Magma Power Company to Joe Iovenitti of AltaRock, pers. comm., 2011);
- Relatively moderate to high contents of (SiO<sub>2</sub>, As, B, Br, and Li);
- Not part of the producing reservoir but has the general characteristics of HTGF;

- The Cl-concentration is 3x (1460ppm) that in the DVPF and represents the most saline groundwater in DV; and
- Water entry near the bottom has equilibrated at about 210°C (410°F).

**Table 2.** Summary of Ages of Dixie Valley Spring Deposits (from Blackwell et al., 2005).

Site	Type	Material	Method	Date (ka)	Reference
Dead Travertine	Vein	Calcite	U/Th Disequilibrium	182 ± 4	Goff et al. (2002)
	Vein	Calcite	Protactinium-231	161 ± 15	Goff et al. (2002)
	Travertine	Calcite	U/Th Isochron	100 ± 5	Dixon et al. (2003)
Lower Ranch	Travertine + Sinter	Quartz	U/Th Disequilibrium	54 ± 4	Goff et al. (2002)
	Travertine + Sinter	Quartz	Protactinium-231	39 ± 2	Goff et al. (2002)
The Mirrors	Fault Gouge	Quartz	U/Th Disequilibrium	287 ± 16?	Unpublished, from Lutz et al.
Dixie Comstock Mine	Sinter Clast	Pollen/Organics	<sup>14</sup> C AMS	10.72 ± 0.07	Lutz et al. (2003)
Section 11 Altered Zone Terrace	"Zebra" Travertine	Unknown	<sup>14</sup> C AMS	5.04 ± 0.06	Lutz et al. (2003)
	Black Travertine	Calcite	U/Th Isochron	3.75 ± 0.33	Dixon et al. (2003)
Section 10 Sinters	Four Sinter Layers	Quartz, Opal, Calcite	U/Th Isochron	4.1 ± 0.1	Dixon et al. (2003)
Section 11 Sinter	Sinter	Organics	<sup>14</sup> C AMS	2.18 ± 0.06	Lutz et al. (2003)
Section 15 Sinters	Sinter	Organics	<sup>14</sup> C AMS	2.47 ± 0.05	Lutz et al. (2003)
	Sinter	Organics	<sup>14</sup> C AMS	2.52 ± 0.05	Lutz et al. (2003)
	Sinter	Quartz, Opal, Calcite	U/Th Isochron	3.6 ± 0.1	Dixon et al. (2003)

### 5.3.5 Dixie Federal Well 62-21

This well occurs near the middle of DV about ~10km (6mi) east of 66-21 and ~4km (2.5mi) SE of DVPF. It is the deepest well drilled in DV at 3810m (12,500ft) and has a recorded maximum BHT of 184° (363°F). The intention was to target a major west-dipping intrabasin fault, that appeared to connect to Hyder HS (D. Blackwell, pers. comm., 2012).

- Contains moderate amounts of SiO<sub>2</sub>, Br, and Li, and high amounts of As and B;
- Low concentrations of Ca and Mg with a Cl content of only 80 ppm;
- Fluid entry occurs at 2900m (9500ft) at the contact of gabbro and underlying Triassic slate;
- Open head: flows 140 l/min (37gpm) of water at about 76°C (169°F);
- Waters don't resemble Dixie production fluids (low Cl);
- Chemically and isotopically similar to Hyder HS; and

- Characteristics of moderate temperature geothermal fluids.

#### 5.4 Geothermal and Production Fluids

The DVPF production fluids show all the same characteristics as HTGF and are assumed to derive from deep circulation along the DVFZ. The pre-production fluids define a trend of similar As/Cl ratios, indicating that all the production fluids are interrelated (Figure 36). Within this figure, increased As and Cl would indicate steam loss (without loss of arsenic), while a decrease indicates mixing of reservoir fluids with more dilute groundwaters.

The cation and anion chemistry within the geothermal system indicates that a major NE-SW trend is apparent with an increase in Cl concentration and decrease in downhole flowing enthalpy of the pre-production fluids. This trend takes place in the DVPF and extends from section 33 (northwestern most producers, lowest Cl and highest enthalpy) to section 7 (central producers) to section 18 (southeastern most injectors, highest Cl and lowest enthalpy). Figure 40a shows the location of these sections representing the main production and injection zones within the producing field. The trend, when coupled with Na and K contents of the pre-production fluids, implies the presence of at least three fluids with distinctly different thermal and chemical histories. Non-condensable gas data also support the mixing of multiple fluids.

#### 5.5 Helium Isotopic Data

The helium ( $^3\text{He}/^4\text{He}$ ) isotope ratio provides very strong evidence for the presence of mantle derived fluids in geothermal systems, and therefore may be an indication of a potential heat source and the potential role mantle melting plays in the formation of a crustal geothermal system. Helium associated with crustal fluids with no mantle influence is characterized by low  $^3\text{He}/^4\text{He}$  ratio (~0.02 Ra where Ra is the  $^3\text{He}/^4\text{He}$  ratio in air). Helium associated with mantle fluids is enriched in  $^3\text{He}$ , e.g., mid-ocean ridge basalts, and have  $^3\text{He}/^4\text{He}$  ratios of ~8-9 Ra. Extensional geothermal systems in the B&R that have moderately elevated  $^3\text{He}/^4\text{He}$  ratios ( $\leq 0.8$  Ra), with no known mid to upper crustal magmatic activity, indicate a mantle component and suggest the occurrence of deep permeable pathways that cut through the upper and lower crust delivering mantle helium to the crustal hydrologic system. Helium sample sites in the B&R (Figure 37), show that Dixie Valley has moderately elevated helium ratios when compared to the surrounding B&R, and is described as a low level "He spike" not related to current magmatism (Kennedy and van Soest, 2007). It has been mentioned by Kennedy and others that the long history of seismicity along the DVFZ has possibly prevented the fault from permanently sealing, and thus keeping the pathways open.

The helium associated with fluids from the productive geothermal reservoir has an isotopic composition of 0.70 - 0.76 Ra and represents the highest ratios measured in the valley. The helium component in the Dixie Valley geothermal field fluids indicates that ~7.5% of the total helium in the system is derived from the mantle. Since there is no recent volcanics or other potential sources, the mantle derived helium is assumed to originate from upflow along the DVFZ. The helium composition from springs and wells that are not in direction communication with the fault zone are a mixture of this deep fluid with younger less helium enriched groundwater. The exception to this simple mixing trend are the fumarole sites (Senator and section 10) and Dixie Meadow HS which are not affected by shallow ground water and are directly connected to the deep geothermal system (Figure 37).

Spring geochemistry coupled with the local geology also indicates that the helium signature is not related to magmatic activity, and reflects localized zones characterized by deep permeable

pathways and high vertical fluid flow rates. Kennedy and van Soest (2006) suggest two mechanisms for the modest enrichment of mantle Helium in the geothermal system (1) fluid circulation through an aged and non-active magma chamber (perhaps the source chamber for local Miocene basalts; and (2) fluid transport along the range-front fault from deep mantle sources. The data supports the latter mechanism and concludes that the most viable source for the  $^3\text{He}$  is fluid transport up through faults, that are in direct communication with the mantle.

Fluids from springs, wells and fumaroles throughout Dixie Valley including from the DVPF were analyzed for noble gas abundances and isotopic compositions (Kennedy et al., 1996; 2002; 2005) and shown in Figure 38. The highest helium ratios occurred in the DVPF and at the Dixie Meadows, Section 10 fumaroles, and in a fluid sampled from 36-14. The noble gas data provides support for (1) fluid mixing; (2) gas loss related to boiling and phase separation; and (3) provides evidence that all of the springs, fumaroles, and non-geothermal wells sampled for noble gas analyses contain a noble gas component that is indistinguishable from the noble gases in the production fluids from the DVGS (Figure 38).

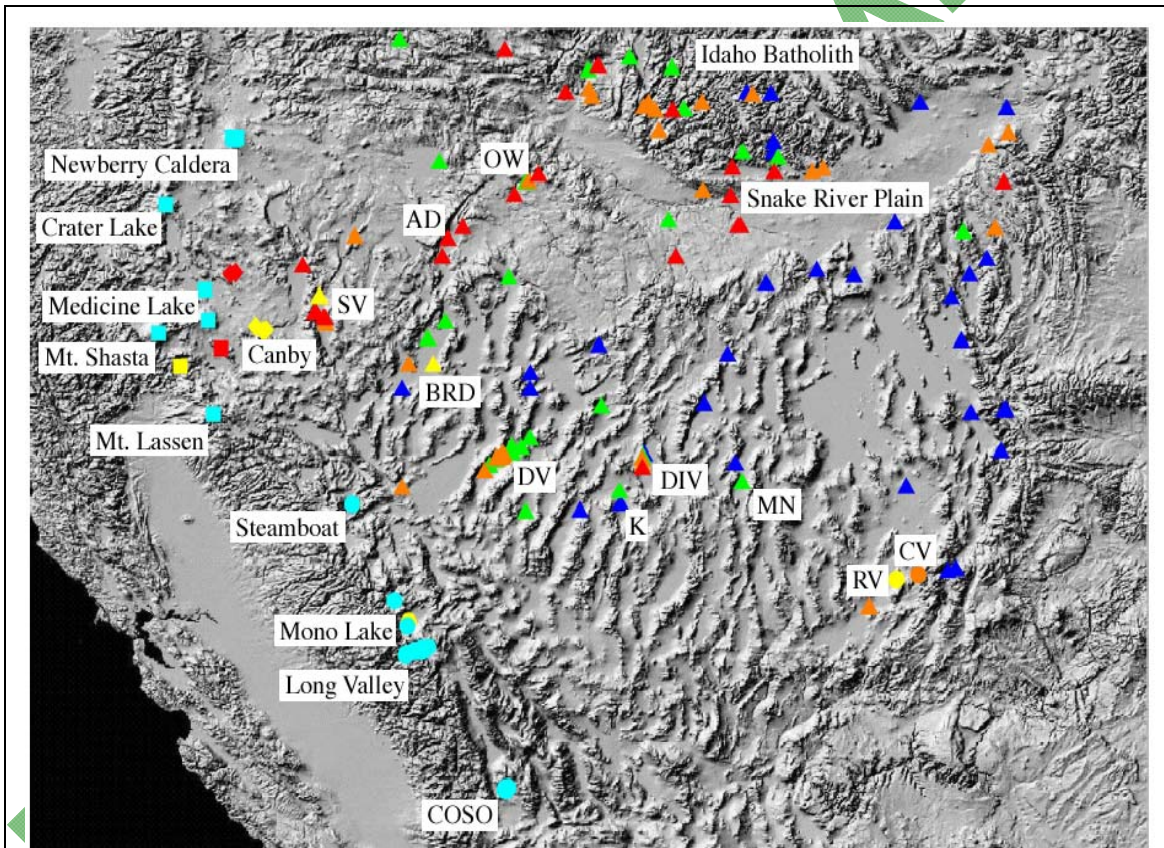
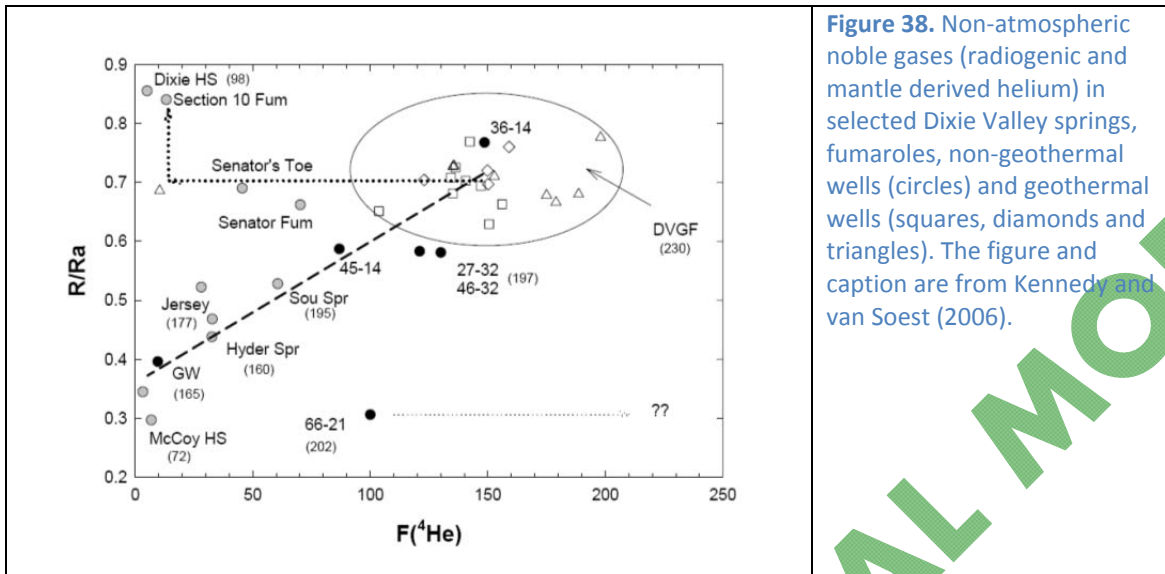


Figure 37. Shaded relief sample location map of the B&R and surrounding areas. The different symbols give an indication of the heat source: circle and squares, magmatic; triangles, extensional; and diamonds, not sure. The magnitude of the  $^3\text{He}/^4\text{He}$  ratio at each locality is coded by color as follows: blue  $\leq 0.3 \text{ Ra}$ ;  $0.3 \text{ Ra} >$  green  $\leq 0.6 \text{ Ra}$ ;  $0.6 \text{ Ra} >$  orange  $\leq 1.0 \text{ Ra}$ ;  $1.0 \text{ Ra} >$  red  $\leq 2.0 \text{ Ra}$ ;  $2.0 >$  yellow  $\leq 3.0 \text{ Ra}$ ; cyan  $> 3.0 \text{ Ra}$ . Certain features are labeled: SV: Surprise Valley; BRD: Black Rock Desert; AD: Alvord Desert; DV: Dixie Valley; OW: Owyhee River Canyon; DIV: Diamond Valley; K: Klobe hot spring: so far the lowest observed  $^3\text{He}/^4\text{He}$  ratio in the B&R at 0.014 Ra; MN: Monte Neva hot spring; RV: Roosevelt hot spring and geothermal energy plant; CF: Cove Fort geothermal energy plant. The figure and caption after Kennedy and van Soest. (2007).



**Figure 38.** Non-atmospheric noble gases (radiogenic and mantle derived helium) in selected Dixie Valley springs, fumaroles, non-geothermal wells (circles) and geothermal wells (squares, diamonds and triangles). The figure and caption are from Kennedy and van Soest (2006).

### 5.6 Fluid-inclusion Gas Chemistry

Lutz et al. (2002) analyzed the composition of fluid-inclusion gases from (1) hydrothermally altered samples from outcrops along the eastern Stillwater Range, and (2) scale and vein samples from geothermal wells. The following section summarizes the work performed.

The purpose of the study was to establish the chemistry of the fluids trapped during alteration and mineral deposition and use such relationships to evaluate the origins of the inclusion fluids. The analysis indicated that fluids of different origins were involved in the formation of alteration minerals during the evolution of the Dixie Valley geothermal system, with a mixing between shallow meteoric, evolved meteoric (crustal), and magmatic end members. Geothermal vein samples from the wells are interpreted as mixtures of shallow meteoric and evolved meteoric (crustal) fluids. Fluid-inclusion gases from epidote-bearing fault gouge appear to have a strong crustal signature (low  $\text{CO}_2/\text{CH}_4$  ratios), while hematite-bearing vein assemblages are purely meteoric in origin. Analyses with high  $\text{N}_2/\text{Ar}$  ratios indicate a magmatic origin for some fluid inclusion gases which agrees with the slight mantle-derived helium signature. There is also a small magmatic component to the gases in quartz-calcite veins from production wells, which was unexpected as the geothermal system was thought to be related to deep-circulation non-magmatic processes. The source of this magmatic component is unclear as no shallow magmatic bodies exist in the vicinity of Dixie Valley. The magmatic gases could originate from:

- An isolated, aged magma chamber supplying magmatic gases from U and Th decay (Kennedy et al., 1996);
- Miocene basalt which could be the source of the magmatic gas in the geothermal veins (Lutz et al., 2002); and/or
- Directly from the mantle through a deep-seated range front fault (Blackwell et al., 2005; Kennedy et al., 2005).

### 5.7 Injection Studies

The geothermal field's main production and injection zones are overviewed in [Section 6.2](#). Geothermal Reservoir and shown previously in [Figure 17A](#) and as well as [Figure 40A](#). Presented

here is a discussion of the geochemistry injection investigations as summarized from Blackwell et al. 2005.

Since the onset of production in mid-1988, ~300 x 10<sup>9</sup> kg (6.6 x 10<sup>11</sup> lbs) of flashed brine, condensed steam, and shallow groundwater has been injected into the Dixie Valley reservoir. The fluids were injected into three general zones (1) the shallow range-front fault near section 5 (depths near 1800m [5900ft]); (2) the piedmont fault in section 18 (depths of 2700 to 3000m [8860-9840ft]); and (3) the Miocene basalt aquifer overlying the southern part of reservoir in section 18 (2170 to 2230m [7120-7320ft]). The brine is distinguished from the production fluid as it is enriched in Cl, <sup>18</sup>O and D, and depleted in non-condensable gases. Chloride trends and tracer testing show a high degree of connectivity between the injection and production wells. This assumes there is only one indigenous geothermal fluid entering the reservoir or individual wells within the DVPF.

### 5.7.1 Tracer Test - Reservoir Connectivity

Tracer testing performed within the geothermal system revealed a high degree of reservoir connectivity between all the injection wells (section 18 and 5) and the section 7 production wells (Rose et al. 2002). For the location on injection and production zones, see Section 5, [Figure 17a](#) and [40A](#). In previous studies including Rose et al. 2002, no tracers from section 5 or 18 injectors has ever been observed in the northern-most section 33 production wells. While section 32 injector wells show a degree of connectivity with the northern wells within section 33, a major flow barrier was thought to exist between the Section 5 wells and southern wells within section 33 ([Figure 39](#)). However findings from Lutz et al. (2003) and an analysis by Reed (2007) show that all of the section 33 wells (27-33, 28-33, 37-33) and the section 7 producers received the tracer from injection well 25-5 and thus there is no barrier to fluid flow in the geothermal reservoir. According to this more recent study, augmentation fluid injection may have re-established fluid pathways and reversed indications of the proposed barrier described above.

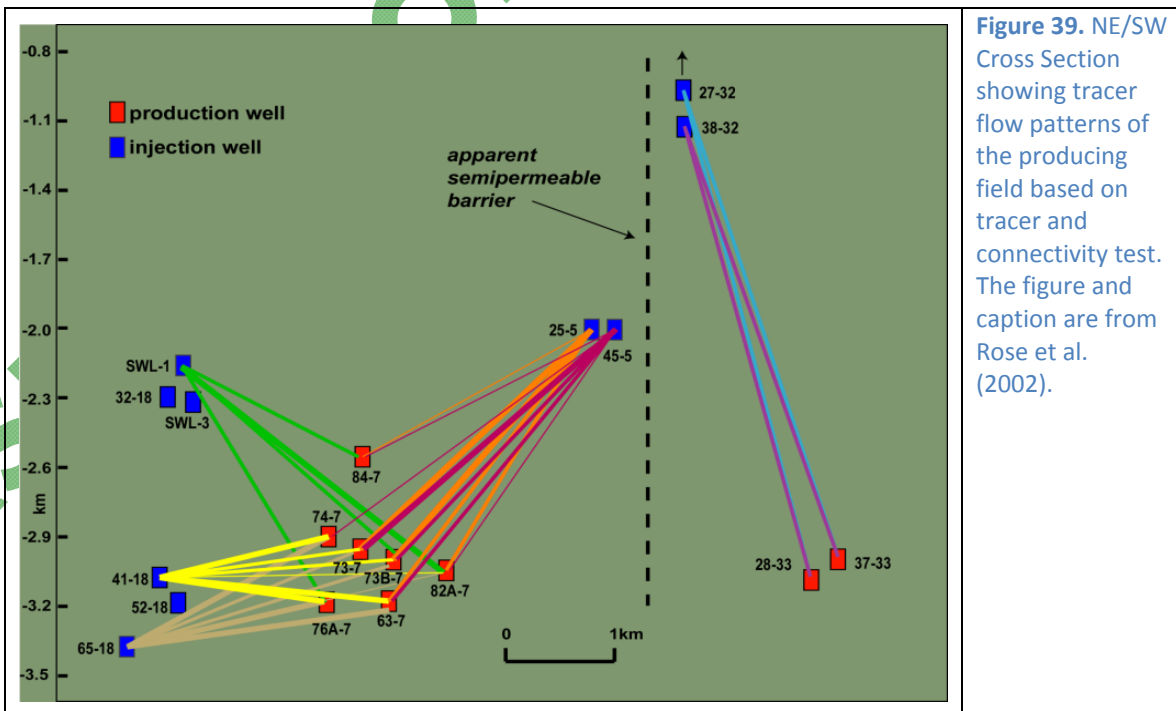


**Figure 39.** NE/SW Cross Section showing tracer flow patterns of the producing field based on tracer and connectivity test. The figure and caption are from Rose et al. (2002).

## 6. Dixie Valley Geothermal Wellfield

This section represents the available wellfield assessment acquired from the public literature, Blackwell et al. 2005, and selected proprietary data provided by Terra-Gen Corporation.

The DVGW encompasses the area (1) in and around the producing and injecting portions of the geothermal field, and (2) dry and sub-commercial wells to the northeast and southwest of the producing area, and lies primarily within the DVFZ (Figure 40a). The producing portion of the wellfield (DVPF, Figure 1) also lies adjacent to the Stillwater Seismic Gap (see Section 2.2.2). The DVGW for the purposes of this report incorporates all the geothermal wells<sup>1</sup> drilled in the Project Area and extends from 45-14 to the southwest, to 76-28 to the northwest, and to 62-21 to the east in central Dixie Valley (Figure 40A). The wellfield is bounded by the range-front fault to the west, as no geothermal wells have been drilled within the Stillwater Range. The DVGW contains the highest measured geothermal gradients (see Figure 33), surface expressions of hydrothermal circulation including Senator and section 10 Fumaroles, and numerous intrabasinal faults. As reported by Blackwell et al. (2005) the producing area lies at a complex structural intersection of intra-range normal faulting, the main range-bounding fault and two piedmont faults, a Landsat lineament, an InSAR lineament (Foxall and Vasco, 2003), and the gravity gradient maxima along the western margin of the basin (Figure 40B).

### 6.1 Structure

The structural model for the DVGW proposed by Okaya and Thompson (1985) and Benoit (1999) (discussed in Section 2.2.2) was a single range-bounding fault dipping at ~54° toward the basin. This model was based on the assumption that the faults encountered in the producing wells could be projected to the topographic break between the valley and range. A variety of geophysical data has been collected (Blackwell et al., 2005) supporting an alternative hypothesis that the contact between the range and valley blocks occurs along 2 or more, steeply dipping faults – rather than a single moderately dipping fault. This evidence includes reprocessed seismic lines (Figure 17a and 18), aeromagnetic and gravity data (Figure 12), geologic mapping, well data including temperature profiles (see Section 6.3), and interpretations from MT profiles (Figure 16A-16C). The baseline conceptual model assumes a steeply dipping multi-fault model along the entire length of the DVFZ through the study area as is required by the geologic, drilling, and geophysical evidence available (see Section 7.2 for a detailed discussion). Salient structural setting features within the producing field are that:

- Fractures feeding the geothermal system are steep (70° to 90°) within the upper 3.5km (11,200ft) of the crust;
- The DVFZ is complex and distributed laterally over several kilometers extending from within the range to deep in the basin fill;
- The source of heat is the flow of fluids within dilated zones along two steeply dipping faults, specifically the range-front fault and a major sub-parallel piedmont fault segment. For example 36-14, a sub-commercial well, records the highest temperature (~285°C [545°F]) and is inclined almost directly beneath the exposed range-front fault and encountered fractures with limited production in the last 30m (100ft) of the

---

<sup>1</sup> TGHs are not considered in this report.

deviated wellbore. The majority of producing wells penetrate the steeply dipping, hydrothermal-bearing piedmont fault structure;

- The dip separation between the basement rocks exposed in the range and the basement below the valley is distributed between at least two faults: the range-front fault and the piedmont fault. The range-front fault creates the surface topographic break; a major piedmont fault takes up much of the displacement between the range and valley bottom; and
- Antithetic faults form mini-grabens on the hanging wall block of the major faults and are important features of the geothermal reservoir.

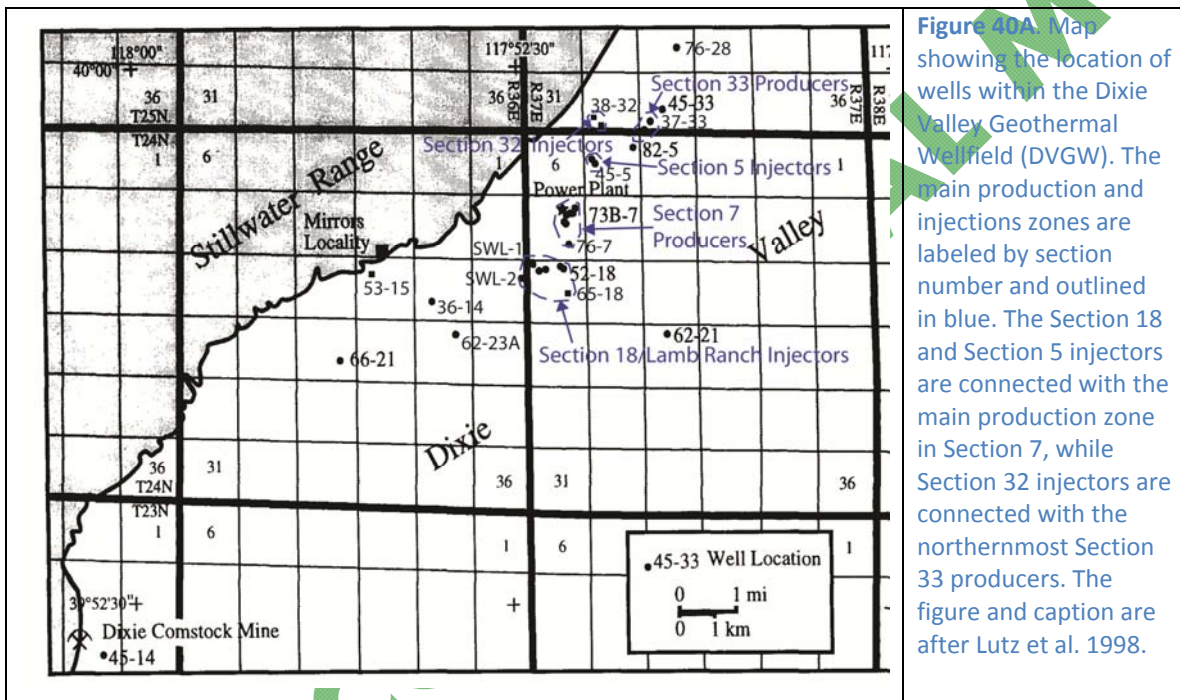
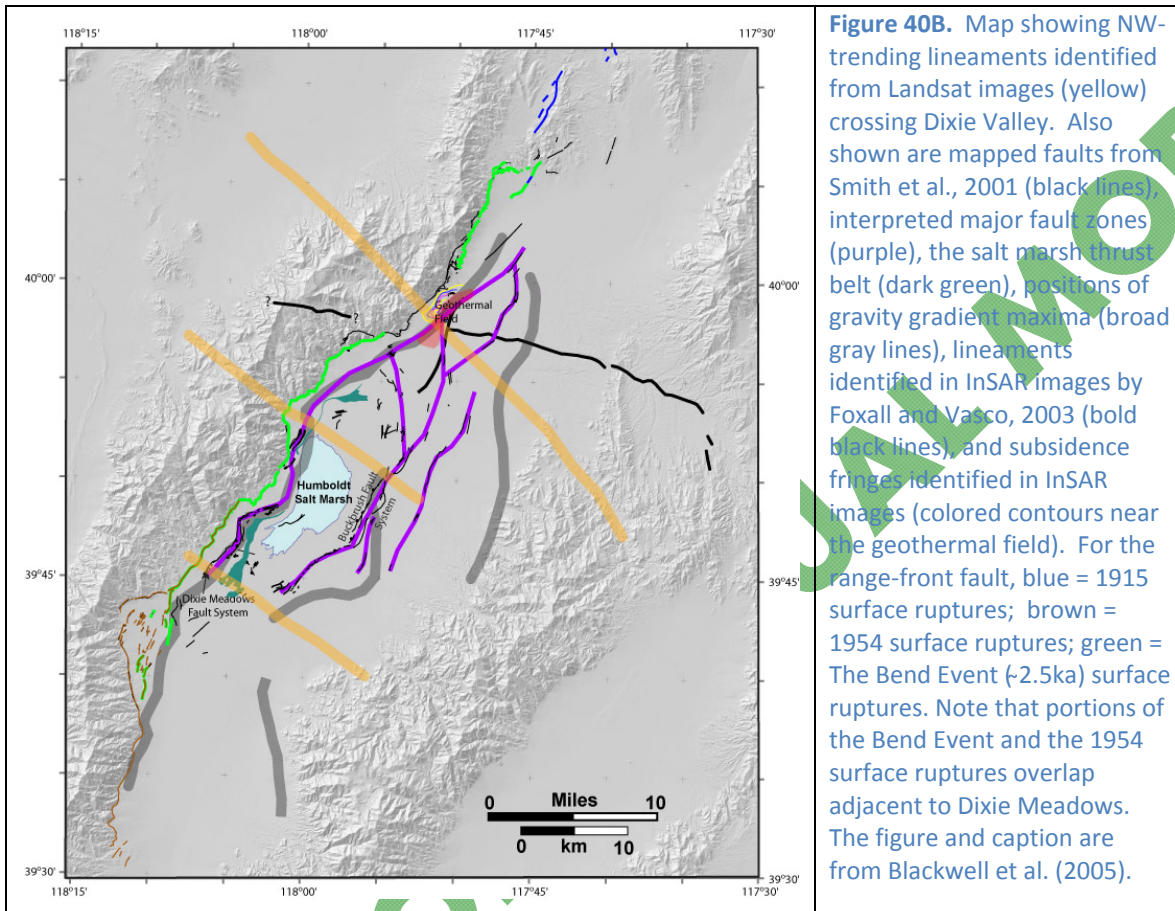


Figure 40A. Map showing the location of wells within the Dixie Valley Geothermal Wellfield (DVGW). The main production and injections zones are labeled by section number and outlined in blue. The Section 18 and Section 5 injectors are connected with the main production zone in Section 7, while Section 32 injectors are connected with the northernmost Section 33 producers. The figure and caption are after Lutz et al. 1998.

### 6.1.1 Stress Analysis

Borehole imaging and hydraulic fracturing experiments have been carried out in a number of Dixie Valley wells including 45-14 and 66-21 to the south, and production wells 37-33, 62-21, 73B-7 and 74-7 in the DVGW (Barton et al., 1997; 1998, and Hickman et al., 1997; 1998). Based on (compressional) breakouts and tensile fractures in the boreholes, the orientation of the least horizontal principal stress in the productive wells was determined to be  $135^{\circ} \pm 8^{\circ}$  (NW-SE). The dip of the permeable fractures in the productive wells is about  $60^{\circ}$  to the SE, thus the authors further conclude that the producing wells intersect fractures that are optimally oriented for normal slip in the current stress field, and that shear slip maintains the permeability along primary and secondary fault planes. Sub-commercial to dry (nonproducing) wells such as that south of the DVPF have permeable fractures of more varied orientations. Well bore breakouts in wells 45-14 and 66-21 (Hickman et al., 1998) indicate greater horizontal maximum stress values in the vicinity of those wells than for either of the producing wells studied or well 62-21. They suggest that the higher ratio of maximum horizontal stress to vertical stress decreases the shear stress which drives fault slip, and thus even optimally oriented fractures are not critically stressed for frictional failure. In general, the zone of permeability in the subsurface is not limited to a single fault plane, rather, the geothermal system produces from primary and secondary

features in intermittent areas along the DVFZ which appear to be dilatational due to the local relationship between the main fault and the stress field (see [Section 7.3](#)).



**Figure 40B.** Map showing NW-trending lineaments identified from Landsat images (yellow) crossing Dixie Valley. Also shown are mapped faults from Smith et al., 2001 (black lines), interpreted major fault zones (purple), the salt marsh thrust belt (dark green), positions of gravity gradient maxima (broad gray lines), lineaments identified in InSAR images by Foxall and Vasco, 2003 (bold black lines), and subsidence fringes identified in InSAR images (colored contours near the geothermal field). For the range-front fault, blue = 1915 surface ruptures; brown = 1954 surface ruptures; green = The Bend Event (~2.5ka) surface ruptures. Note that portions of the Bend Event and the 1954 surface ruptures overlap adjacent to Dixie Meadows. The figure and caption are from Blackwell et al. (2005).

This section summarizes studies that used the borehole televiewer (BHTV) to determine stress and permeability within the reservoir (Hickman et al., 1998; 2000). BHTV images analysis in well 82-5 focused on the fault zone at a depth of ~2071-2724m (6800-8940ft) to determine the nature, distribution and hydraulic properties of fractures within the DVGW and their relation to the local stress field. The orientation and magnitude of the horizontal minimum stress ( $S_{hmin}$ ) is important for determining if fractures are optimally oriented and critically stressed in the current stress field. This is calculated using (1) tensile cracks forming perpendicular to the azimuth of  $S_{hmin}$ , (2) borehole breakouts (compressive rock failures) which form parallel to  $S_{hmin}$ , and (3) hydraulic fractures which will propagate in a plane perpendicular to the maximum principle stress (parallel to the strike of the fault zone). A necessary condition for high reservoir permeability is that the DVFZ be critically stressed for frictional (shear) failure in the current stress field. Tensional stresses along optimally oriented fractures result in shear slip along the fractures planes that force open the fractures due to irregular grooves and asperities along the slip surfaces. This develops permeability within the fault zone, which is maintained as tectonic forces re-stress the fractures to critical levels that results in another slip event (extensional failure) along the fracture planes. This intermittent seismicity is responsible for preventing the open fractures from becoming sealed by geothermal fluids over time.

Wells used in these studies are summarized below and reported to encounter the Stillwater Fault Zone (SFZ) at depths of 2 to 3km (6600-9800ft). The term SFZ is synonymous in this context with the DVFZ and more specifically refers to the both the range-front and piedmont fault portion of the DVFZ within its northernmost segment adjacent to the Stillwater Seismic Gap. Wells 73B-7, 82A-7, 74-7, 82-5 and 37-33 penetrate the piedmont fault, the highly permeable (producing) segment of the DVFZ, which is referred to as the SFZ within the Hickman et al.'s studies. Wells 66-21, 82-5 and 45-14 failed to encounter enough permeability within the adjacent fault/fracture zones.

**Well 82-5 (dry well)**

Well 82-5, located near the Section 5 injectors ([Figure 40a](#) and [41](#)), and only 600m (2000ft) southwest of the most permeable production wells within the DVGW has been reported to pass through the main range front fault at 2833m (9300ft). According to the baseline conceptual model, (see [Section 7](#)) this well actually penetrates the steeply dipping piedmont fault. For reference purposes herein, where the SFZ is mentioned relative to this well, it refers to the piedmont fault segment of the DVFZ. Despite the favorable location, the well encountered low permeability in the fault zone and was dry. The authors here suggest that this well was deviated within a compressional zone where a N-S trending structure with a suggested right lateral component intersects the NE-trending piedmont fault (see [Figure 14](#) and [Section 7.2](#)). The adjacent permeable section 33 producers lie within the corresponding dilated quadrant at this structural intersection. The following points detail the stress conditions based on the aforementioned fracture analysis (Hickman et al., (2000).

- Sealed fractures starting at ~2740m (8990ft) were encountered within the fault zone;
- $S_{hmin}$  (observed just above the SFZ, i.e., the main piedmont fault within the DVFZ) :
  - Above 2660m (8730ft):  $N23^{\circ}E \pm 12^{\circ}$  (parallel to the strike of the SFZ);
  - Below 2660m (8730ft):  $S66^{\circ}E \pm 13^{\circ}$  (perpendicular to the strike of the SFZ);
- A nearly  $90^{\circ}$  rotation in the azimuth of the least horizontal principle stress ( $S_{hmin}$ ) at ~2.7km (8800ft) depth is hypothesized to have been the results of a moderate-sized earthquake on a fault subparallel to the SFZ;
- Stress direction below ~2.7 km in 82-5, a dry well, agrees with stress directions observed in 73B-7 and 74-7 (producing wells), and 25-5 (injection well);
- Based on the orientation of  $S_{hmin}$  measured from borehole breakouts, the natural fractures within 50m (164ft) of the SFZ, are optimally oriented for normal slip; and
- Low productivity within this optimally oriented fracture zone is due to localized increases in the magnitude of  $S_{hmin}$  (reduction in shear stress) related to lithology with the presence of weak talc ( $\mu < 0.25$ ) within the main shear zone of the SFZ. This reduces the differential stress in the adjacent country rock and shields potential permeable fractures from high tectonic shear stresses.

The following wells were discussed in the Hickman et al. (1998, 2000), see [Figure 41](#). Where only the calculated horizontal minimum stress is mentioned no other data was available. Note that if the horizontal minimum stress is perpendicular to the DVFZ and parallel to the ESE extensional axis, then the fractures are optimally oriented for normal faulting. Whether they are opened is a function of local lithology, stress magnitudes, alteration mineralogy and the degree of sealing.

**Well 66-21:  $S_{hmin} = N20^{\circ}W \pm 20^{\circ}$  (dry well)**

- Orientation of ( $S_{hmin}$ ) is optimal for normal faulting on the piedmont fault segment of the DVFZ ; and

- Magnitude of  $S_{hmin}$  is too high to result in incipient frictional failure.

**Well 45-14:**  $S_{hmin} = N41^\circ W \pm 12^\circ$  (dry well)

- Magnitude of  $S_{hmin}$  is low enough for frictional failure (on optimal orientations);
- Fractures are not optimally oriented for normal faulting; and
- The range front fault segment of the DVFZ is locally rotated  $\sim 40^\circ$  from the optimal orientation for failure.

**Well 73B-7:**  $S_{hmin} = N57^\circ W \pm 10^\circ$  (Production well)

**Well 25-5:**  $S_{hmin} = S64^\circ E \pm 14^\circ$  (Injection well)

**Well 74-7:**  $S_{hmin} = S55^\circ E \pm 15^\circ$  (Production well)

- Humboldt igneous group contains all the producing fractures; and
- The Stillwater Fault, i.e. range-front fault segment of the DVFZ, at this location reportedly dips  $S45^\circ E$  at  $\sim 53^\circ$ , which is the optimal orientation for normal faulting in current stress field. This shallow dip likely assumes that the Stillwater Fault (range-front fault) projects to the vicinity of section 7 producers, where actually the section 7 wells lies along a more steeply dipping piedmont fault.

## 6.2 Geothermal Reservoir

The basic setting of the producing geothermal reservoir lies within an open fracture network developed where crystalline portions of the Jurassic igneous complex within the hanging wall of the DVFZ are juxtaposed against Cretaceous granodiorite in the footwall (Lutz et al., 1997), as seen in the lithology logs of the Section 7 production wells (Appendix 9). Lutz et al. (1997) reports that production originates from two high temperature subhorizontal aquifers, mostly the Jurassic igneous rocks/quartzite at around 2500-3000m (8200-9800ft), and also from the Miocene basalt at around 2000-2500m (6600-8200ft). The authors of this report believe that the current geothermal production is originating from the piedmont fault segment of the DVFZ. Brittle rocks including the Jurassic diorites and gabbros (lower section of the Humboldt igneous complex) and the Boyer Ranch quartzite (within the narrow zone of faulting) are the best reservoir rocks in the producing field due to their fractured nature and high permeability. Productive zones within some wells (e.g. 76A-7 and 38-32) may lie within a re-activated thrust (ex. Boyer thrust) tectonically bounding the Jurassic igneous complex from the underlying Triassic marine sediments. It has been mentioned that a piedmont fault representing a major strand of the DVFZ is the major producing structure in the geothermal system. Thus, it is thought that the geothermal reservoir lies within the fault zone, intersecting structures and associated faults and fractures in the hanging wall block of this piedmont fault. The bounding conditions for the reservoir as defined by Lutz et al. (1997) are outlined below:

- **North:** leading edge of the Fencemaker allochthon that carries the Jurassic igneous complex;
- **South:** White Rock Canyon (Figure 1) that separates NNW-oriented fault segments from NE orientations;
- **East-West:** restricted to the narrow band of fracturing within the DVFZ;
- **Upper:** lithologic contact between Jurassic igneous rocks and younger sedimentary rocks; and

- **Lower:** Mesozoic (Boyer or Fencemaker) thrust at the base of the Jurassic section.

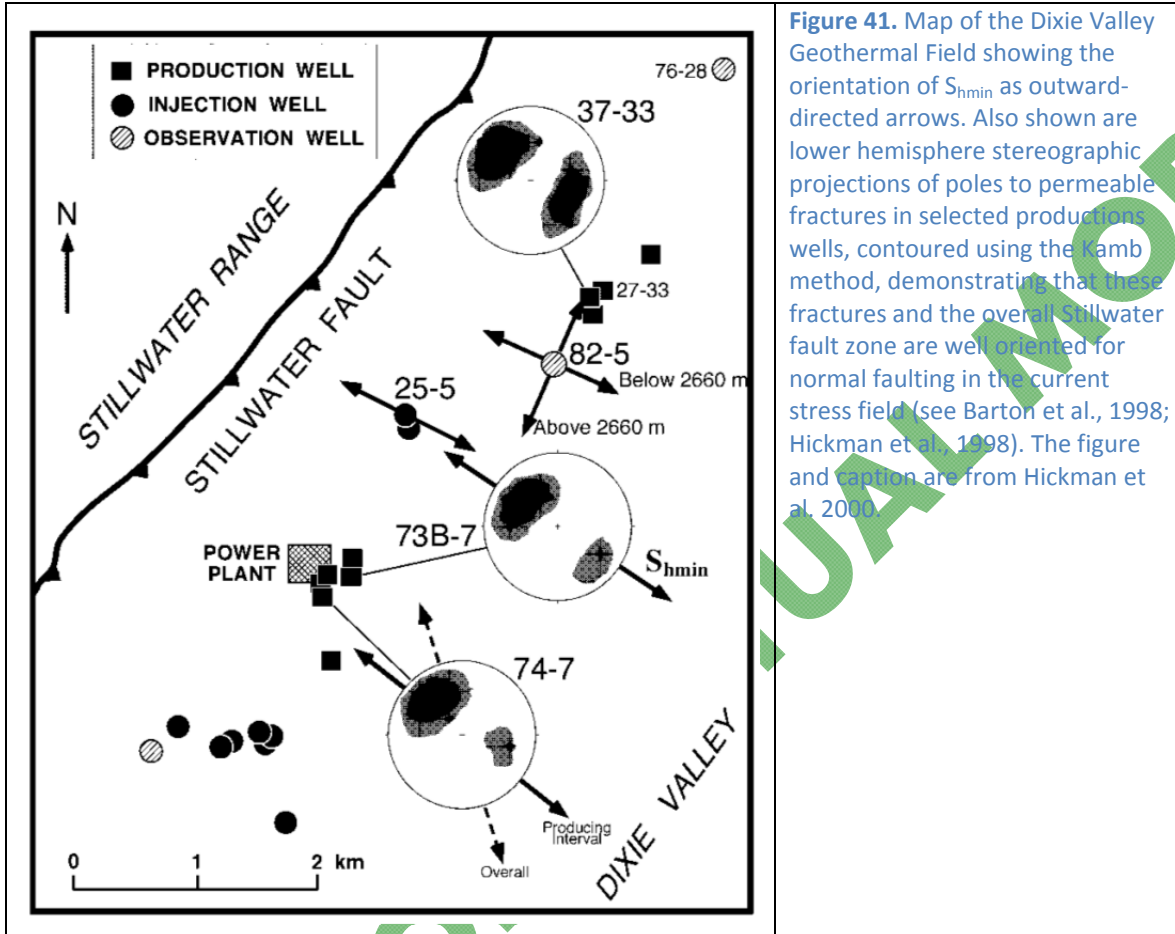


**Figure 41.** Map of the Dixie Valley Geothermal Field showing the orientation of  $S_{hmin}$  as outward-directed arrows. Also shown are lower hemisphere stereographic projections of poles to permeable fractures in selected production wells, contoured using the Kamb method, demonstrating that these fractures and the overall Stillwater fault zone are well oriented for normal faulting in the current stress field (see Barton et al., 1998; Hickman et al., 1998). The figure and caption are from Hickman et al. 2000.

The Project Area lithology data per well is presented in Appendix 10. The temperature data for the DVGW is presented in Appendix 11. The wells in the producing field are shown in [Figure 42](#) and a summary discussion of these wells by Reed (2007) is presented below.

- Wells SWL-1, SWL-3, and 52-18 inject fluid into a sub-horizontal, lower temperature 220°C (428°F) aquifer in Miocene basalts east of the range-front fault along the piedmont structure at depths between 2192m and 2248m (7200ft and 7373ft).
- Wells 25-5 and 45-5 inject fluid into shallow, lower temperature 205°C (401°F) zones associated with the Miocene basalt and/or Jurassic volcanics within the DVFZ (piedmont segment) at depths between 1776 and 1876m (3860 and 6155ft) according to Benoit (1992). It is reported in the 45-5 well log (Appendix 9), that a mylonitized fault zone, assumed to be the piedmont fault segment of the DVFZ was encountered at a depth 1814-1881m (5951-6171ft).
- More recent wells 27-32 and 38-32 have only been used for injection of cold steam condensate and augmentation water into a shallow (180m [590ft] deep) fault zone which was originally an outflow plume from the reservoir.
- Section 33 wells (37-33, 28-33, 27-33) are assumed to produce from fractures in the encountered Jurassic igneous rocks and Boyer Ranch quartzites along the piedmont structure (see summarized well logs in Appendix 9).

The geothermal reservoir has been described above by Lutz et al. (1997) as occurring within specific fractured formations. Reed (2007) emphasizes the structure and relating fracturing in describing the geothermal reservoir as a set of sub-parallel fractures with narrow apertures (volumes up to  $3.5 \times 10^7 \text{ m}^3$  [ $1.2 \times 10^9 \text{ ft}^3$ ]), long mean residence times (up to 1197 days) and large surface areas (for high heat transfer) developed in the fault zone and adjacent damage zone that provide permeability. The permeable zones provide conduits for fluid rising from depth and fluid flowing from injection to production wells. Antithetic sets of fractures provide permeable pathways for fluid injected into the Tertiary basalt zones to reach the main fractures.

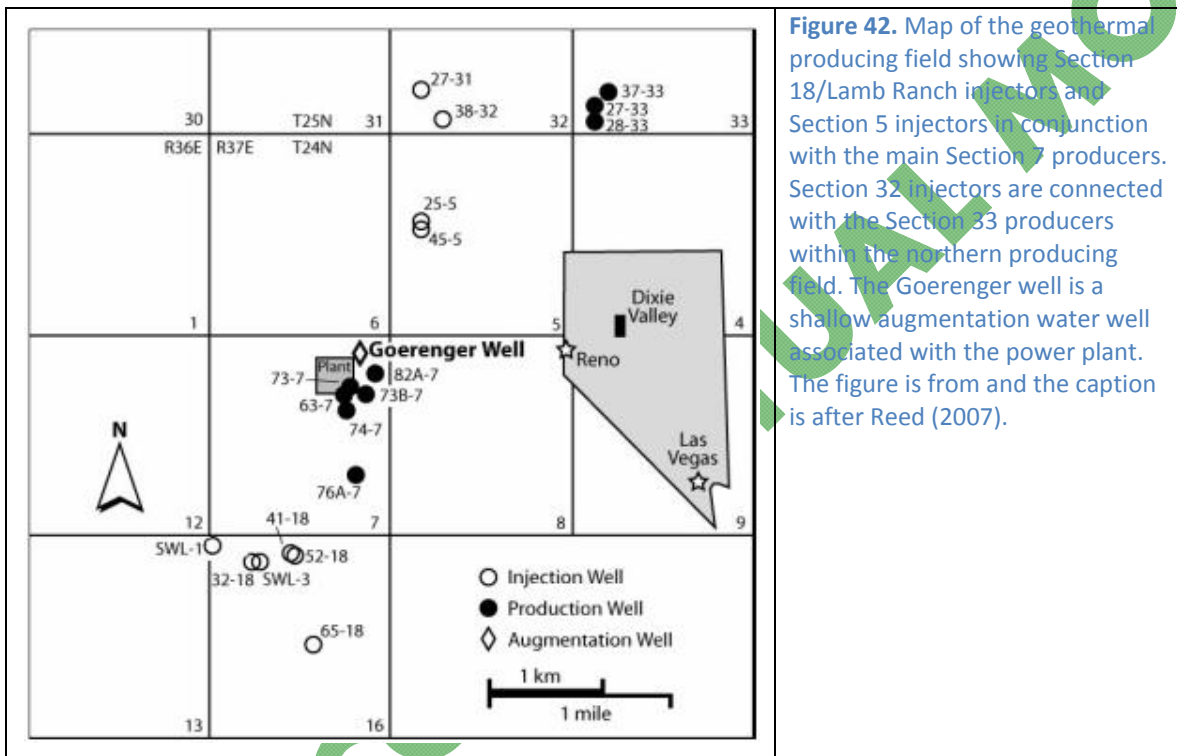


**Figure 42.** Map of the geothermal producing field showing Section 18/Lamb Ranch injectors and Section 5 injectors in conjunction with the main Section 7 producers. Section 32 injectors are connected with the Section 33 producers within the northern producing field. The Goerenger well is a shallow augmentation water well associated with the power plant. The figure is from and the caption is after Reed (2007).

### 6.3 Thermal Data

Due to the high thermal gradient, surface features including springs and fumaroles, the close proximity to the DVFZ, and high temperatures encountered at depth, the DVPP and the DVPF are the most explored and studied areas of Dixie Valley. While the setting of the subsurface within Dixie Valley is generally constrained based on geophysical work, the producing field has the most detailed subsurface information due to a number of temperature gradient holes (TGHs) and deep wells. Temperature-depth profiles for shallow wells (TGHs) within the DVPF and the DVPP are shown in Figure 43. Of the approximately 223 wells/TGHs drilled, 96 have available temperature-depth data as part of the SMU Western Geothermal Database (WGD): <http://smu.edu/geothermal>.

#### 6.3.1 Shallow thermal regime

The highest gradients in shallow TGHs occur near the exposed range front fault, with the maxima near the Senator fumaroles (DVPF) and the section 10 fumaroles (DVPP) near well 53-15 (Figure 44). The occurrence of high gradients near 36-14 and 62-A23 bulge out into the valley for several kilometers and occur near the projected location where the Buckbrush fault system merges with the DVFZ (see Figure 30). The shallow thermal contours clearly show two plumes of

thermal water leakage from the range front fault into the valley fill at depths less than around 100m (328ft), with the plumes appearing to originate at the two fumarole areas along the range/valley contact. While both the range front and piedmont fault are considered the major thermal bearing structures, the piedmont fault does not appear to contribute hot fluid to the shallow thermal regime. Its effect is likely masked by the shallow outflow of fluids from the range front fault as geothermal fluids derived from the piedmont structure are known to occur at deeper levels. The TGH temperature-depth profiles within the geothermal field around the Senator Fumaroles indicate significant lateral flow of warm water at shallow depths of around 25 and 100m (82 and 328ft) and at depths around 20 and 70m (65 and 230ft) within the DVPP (Figure 44). The southern plume coincides with a negative aeromagnetic anomaly between two positive anomalies (see Figure 10), also indicating probable leakage of geothermal water into the shallow valley fill with no surface manifestation directly associated with it.

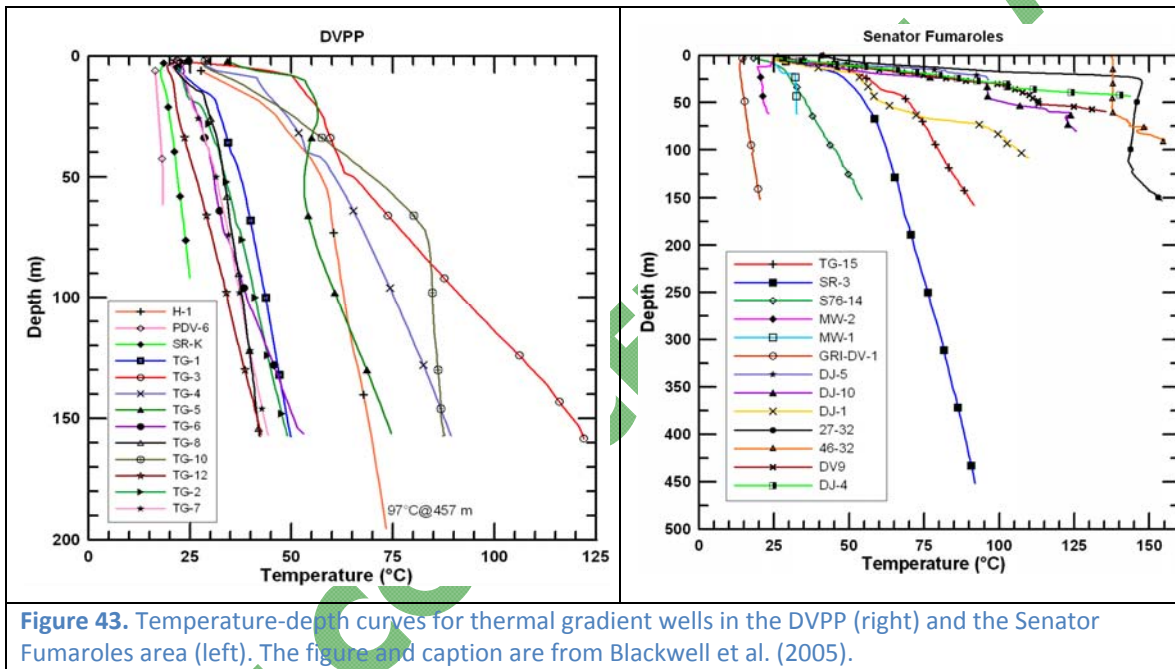


Figure 43. Temperature-depth curves for thermal gradient wells in the DVPP (right) and the Senator Fumaroles area (left). The figure and caption are from Blackwell et al. (2005).

### 6.3.2 Deep thermal regime

Data from deep wells within the DVPP show temperatures vary from 225°C to 245°C (437°F to 473°F) at depths of about 2500m (8200ft). The temperature in 36-14 (DVPP) produced from fractures near the bottom of the well and is by far the highest bottomhole temperature observed (~285°C [545°F]) in a B&R extensional geothermal system. Geologic and thermal data from wells support a steeply dipping fault zone consisting of at least two major structures as evident by the drilling of wells 62-23 (two legs) and 36-14 within the DVPP. Both legs (62-23 and 62-A23) were impermeable but the 62-A23 leg recorded a BHT of 267°C (512°F) at 3592m (11,785ft), which was hotter than the production wells in the DVPP to the north. A generalized cross-section (Figure 45A) shows that temperatures never became isothermal or decreased with depth in 62-A23, and that the piedmont fault, believed to be the main high-temperature geothermal upwelling zone was not crossed in either well 62-A23 (at depth) or 36-14, which crossed the fault at a very shallow depth. Furthermore, drilling of 36-14 unexpectedly intersected basement rocks (presumably the Jurassic mafic section) at only 1km (3300 ft) depth

with no fault encountered. The well was then deviated towards the range-front fault of the DVFZ and continued to show increasing temperatures with depth.

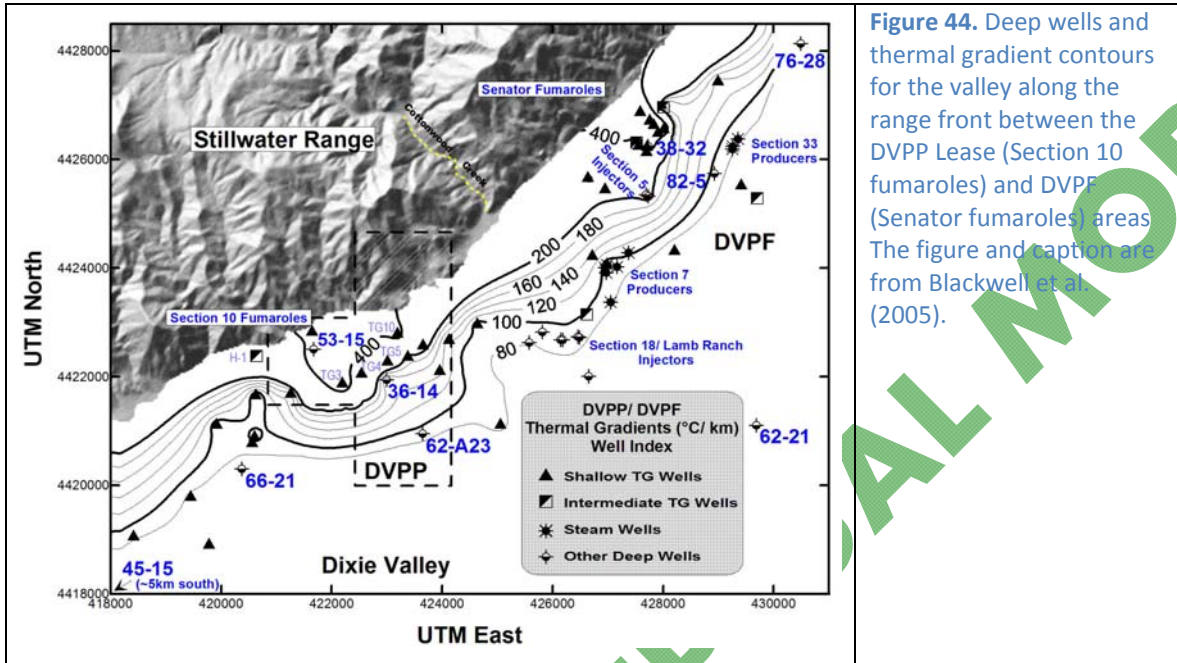


Figure 44. Deep wells and thermal gradient contours for the valley along the range front between the DVPP Lease (Section 10 fumaroles) and DVPP (Senator fumaroles) areas. The figure and caption are from Blackwell et al. (2005).

The thermal and lithologic data, in particular the data from wells 45-14 and 36-14, indicate that the range-bounding fault must have a fairly steep dip ( $>70^\circ$  E) at the north-trending segment near 45-14, and a near vertical dip along a northeast-trending segment adjacent to the DVPP, assuming the fault was not crossed within 36-14. Additionally the thermal data indicates a major geothermal fluid bearing structure (piedmont fault) is present between the wells 36-14 and 62-A23 (Figure 45A). The structure must also be steeply dipping and coincides with the inferred location of the maximum gravity gradient (see Figures 11 and 13). A cross section through the northern producing field (Figure 45B) also shows two major steeply dipping structures comprising the DVFZ based on the thermal data described above.

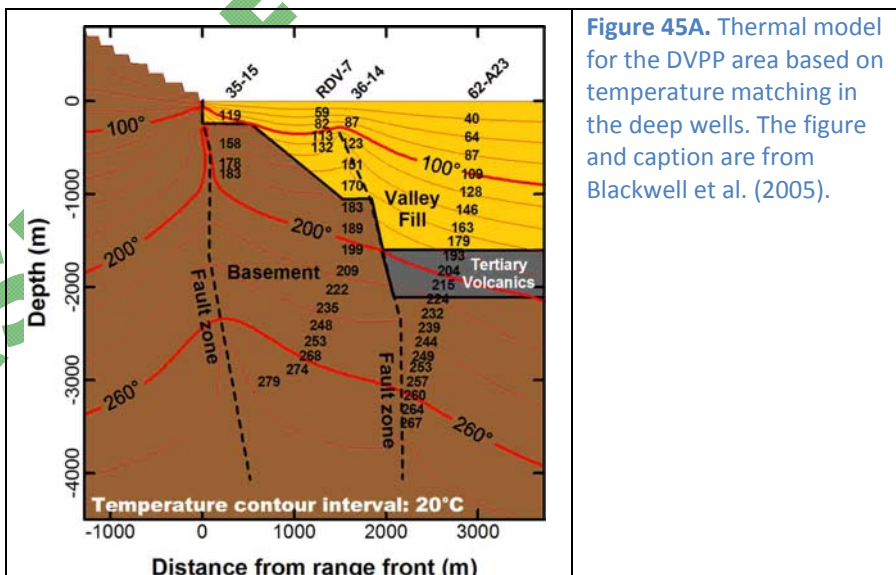


Figure 45A. Thermal model for the DVPP area based on temperature matching in the deep wells. The figure and caption are from Blackwell et al. (2005).

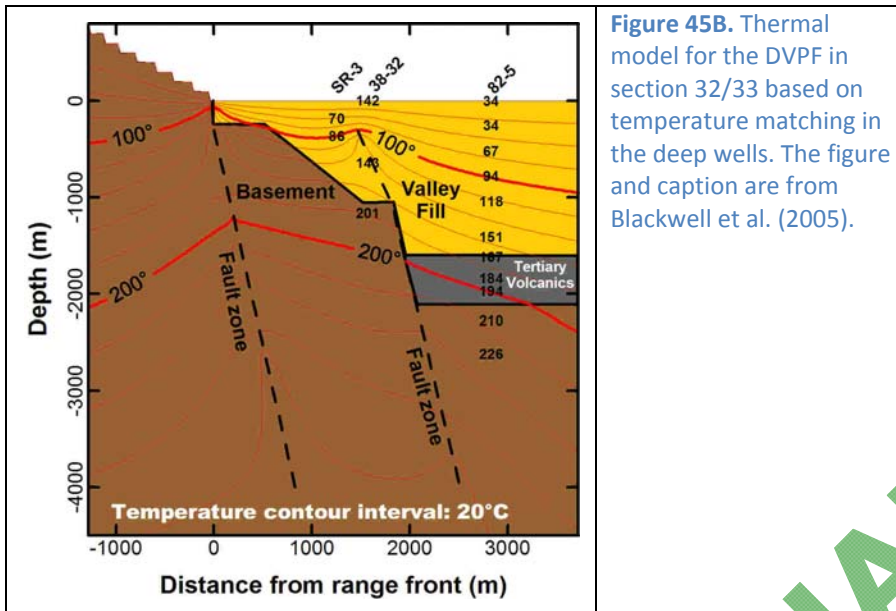


Figure 45B. Thermal model for the DVPF in section 32/33 based on temperature matching in the deep wells. The figure and caption are from Blackwell et al. (2005).

## 6.4 Summary of Geothermal Wells

Table 3 summarizes well data from Blackwell et al. (2005). This table is incomplete and doesn't have information on the entire well database for the Project Area. Additional well information from other sources including both the public domain and private sector can be found in Appendix 9. This appendix contains: (1) Sunoco well lithology summary based on Sunoco mud logs and acquired with the permission from Terra-Gen Corporation (Terra-Gen), and (2) lithology summary based on the Nevada Bureau of Mines and Geology (NBMG) online geothermal database (see below). It is important to note that some of the wells included in both sources (Sunoco and NBMG) are not consistent, and the NBMG database is considered the less accurate source. Appendix 10 presents the general lithology from the wells that divides the geology into six stratigraphic units. Appendix 11 summarizes the temperature data that has been acquired mainly from the SMU geothermal database (see below) and data provided by Terra-Gen and includes mostly BHT measurements. Additional temperature data was extracted from the temperature-depth profiles shown in Figure 46, derived from Blackwell et al. (2005). The complete temperature data for the remaining wells was not available to this investigation. Links for the geothermal databases available online are provided below.

Southern Methodist University (SMU) geothermal database: <http://smu.edu/geothermal>

Nevada Bureau of Mines and Geology (NBMG) geothermal database: <http://www.nbmge.unr.edu/geothermal/mapfiles/nvgeowel.txt>

### 6.4.1 Geothermal Wells within the DVPF

The well distribution within the DVPF can be found in Figure 42 which outlines the main production and injection zones. The production wells are clustered in two locations, section 7 in the center of the field and section 33 to the north. Injection wells include the section 18 wells and the section 5 wells between the two producing zones. Section 32 injectors in the northern producing field are in connection with the section 33 producers. Complete temperature-depth profiles for wells within and outside of the producing field are shown in Figure 46. Lithology and additional temperature data that has been acquired can be found in Appendices 9-11.

**Table 3.** Well data outside of the producing field (from Blackwell et al., 2005)

Well	Location	Depth	Temperature	Lithology	Notes
45-14	Dixie Comstock Mine Southern-most well	2750m 9022ft	196°C (385°F)	0-335m (0-1100ft): unconsolidated fill 335-792m (1100-2600ft): silicic Cz volcanics 792-2774m (2600-9100ft): Tr metasediments	Most similar in comp. to deep reservoir waters, limited flow
66-21	South of DVPP	2988m 9800ft	215°C (419°F) @2470m	0-1250m (0-4101ft): basin-fill deposits 1250-1585m (4101-5200ft): Cz volcanics 1585-2455m (5200-8054ft): granodiorite 2455-2989m (8054-9806ft): metasediment Ophiolitic bottom	Most saline groundwater in DV HTGF water entry at 1463m (4800ft) (cased) and bottom
62-21	Middle of DV East of DVPP	3810m 12,500ft	184°C (363°F) @3318m	Lithology found in Appendix 9	Fluid entry@2900m (9512ft) (contact of gabbro and underlying Tr slate)
82-5 (dry)	DVPF	~2750m 9022ft	226°C (439°F)	Lithology found in Appendix 9	Tight, does not flow Low permeability
38-32	DVPF	~1100m 3610ft	201°C (394°F)	0-150m (0-492ft): Basin-fill sediments 150-777m (492-2549ft): Boyer Ranch quartzite 777-1006m (2549-3300ft): Jz mafic igneous 1006-1113m (3300-3652ft): Brecciated FZ 1113-1168m (3652-3832ft): Tr phyllites	Intersected a stranded block between range front and piedmont fault Drilled in '00 Used as main injection well in Section 32
53-15	DVPP	1200m 3937ft	150°C (302°F)	Lithology unknown	500m (1640ft) from range-front
62-23 62-23A	DVPP DVPP	2900m 9514ft 3492m 11,457ft	250°C (482°F) 267°C (513°F)	Lithology unknown	Drilled in '92-92 Both legs tight Drilled within piedmont structure
36-14	DVPP	3050m 10,007ft	285°C (545°F)	Intersected basement at only ~1km (3280ft) Lithology unknown	Nearly vertically below topographic edge of Stillwater Range, limited flow from fractures in bottom of well

**Well 38-32**

This injection well was drilled in December 2000 between the range front and the producing wellfield (adjacent to Senator Fumaroles) and west of section 33 producers (see [Figure 42](#)). The well was thought to penetrate an extensive basin-fill section, however the well encountered a shallow zone of highly altered alluvium and intersected bedrock consisting of the Boyer Ranch quartzite at only ~400m (1312ft). The lithology of the well is included in [Table 3](#), while a general cross-section within the vicinity of the well is shown in [Figure 45B](#). Additionally a brecciated fault

zone encountered at ~1000m (3300ft) complicates the structural framework. If this fault zone connects with range-bounding fault then a shallower fault dip is required within this area. This unexpected lithology has been interpreted by Johnson and Hulen, 2002 as a stranded “gravity slide” block between the Dixie Valley range-bounding fault and a shallowly buried fault to the

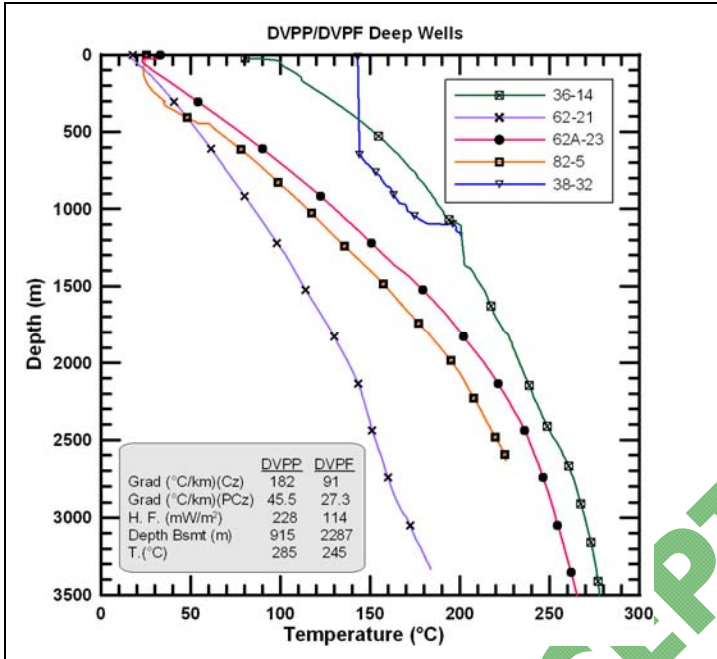
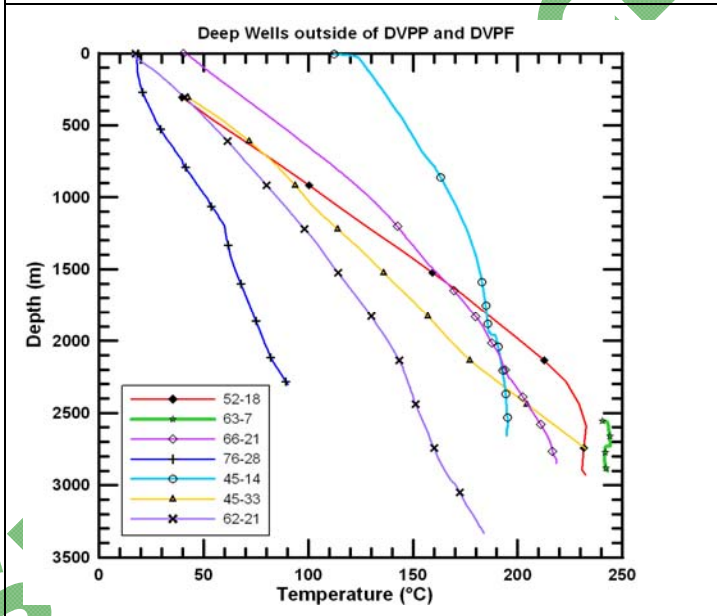


Figure 46. Temperature-depth curves for wells within the Dixie Valley Geothermal Wellfield. All profiles are equilibrium static profiles except 36-14, 66-21, and 45-14. The 36-14 profile below 2600m was derived from a Horner Plot build-up at various depths and these temperatures are considered equilibrium bottomhole temperatures. The wells 66-21 and 45-14 are weakly artesian and only the bottomhole temperature is considered static. Figure is taken from Blackwell et al. (2005). Caption derived from oral and written communication with D. Blackwell.



east, of which the majority of the structural offset between the valley and the range occur on the latter fault (Figure 47). This cross-section depicts the “stranded block” which was buried by recent alluvium relies on the assumption that Cenozoic volcanics found within the brecciated zone are not derived from the Jurassic volcanic sequences. The major displacement on the piedmont fault east of the well is explained as either a relay ramp or a major splay from a

steeply dipping master structure that curves to a more shallow dip near the surface (Johnson and Hulen, 2002).

Authors herein infer that this could also be explained by (1) a steeply dipping subsidiary structure within the DVFZ that lies between the range front and piedmont fault, or (2) a more northerly-trending cross or transfer fault that projects from the range to the vicinity of 38-32 to a change in strike along the piedmont fault (D. Blackwell, pers. comm., 2011). The wellfield is mostly distributed basinward, as this structure is not encountered by any wells other than 38-32. Additionally northeast of this area, geophysical evidence show that piedmont fault is distributed along at least three sub-parallel and merging segments, that could extend to the SW in the vicinity of Section 32. It is also noted that the Boyer Thrust is exposed a few kilometers to the west in the Stillwater Range and likely projects to the vicinity of this well, although the younger volcanics clasts within the fault zone suggest a younger structure.

#### **Well 25-5**

This is an injection well into Miocene basalt at 1820, 1850 and 1870m (5970, 6070, 6135ft); sediment-basalt contact is at 1580m (5185ft) (Mallan and Wilt 2000).

#### **Well 37-33**

According to Hulen et al., (1999), this well:

- Yielded a small quantity of oil at the wellhead 170°C (338°F);
- Has the source of oil inferred to originate from the Oligocene-Miocene lacustrine sediments (Tma), which occur depositinally below the Miocene basalts;
- Is cased to a depth of 2604m (8543ft) with open hole section to a depth of 2816m (9240ft);
- Has thermal-fluid production from the piedmont fault within the DVFZ in the open hole section;
- Encountered the following lithology at the depths indicated: Tmb (1759-2158m[ft]); Tma (2158-2524m[ft]); Jhg (2524-2646m[ft]); Jbr (2646-2718m[ft]); Kgr (2718-2758m[ft]);
- Encountered the piedmont fault at 2718m (8917ft) between quartzite in the hanging wall and Cretaceous granodiorite in the footwall block.

#### **Well 45-33**

According to Lutz et al. (1998), this well has the following lithology at the depths indicated:

- Lithology(m): Ts (0-2737m[0-8980ft]); Jhg (2737-2926m[8989-9600ft]); Jbr (2926-3124m[9600-10,250ft]); and
- The abbreviated lithology notations correspond to the following stratigraphic units: Ts: Tertiary basin-filling sediments; Tmb: Miocene basalts; Tma: Miocene lacustrine sediments; Tv: Oligocene silicic volcanics; Jhg: Jurassic Humboldt igneous group; Jbr: Jurassic Boyer Ranch quartzite; Kgr: Cretaceous granodiorite. The stratigraphic units are discussed in the next section in the Baseline Conceptual Model.

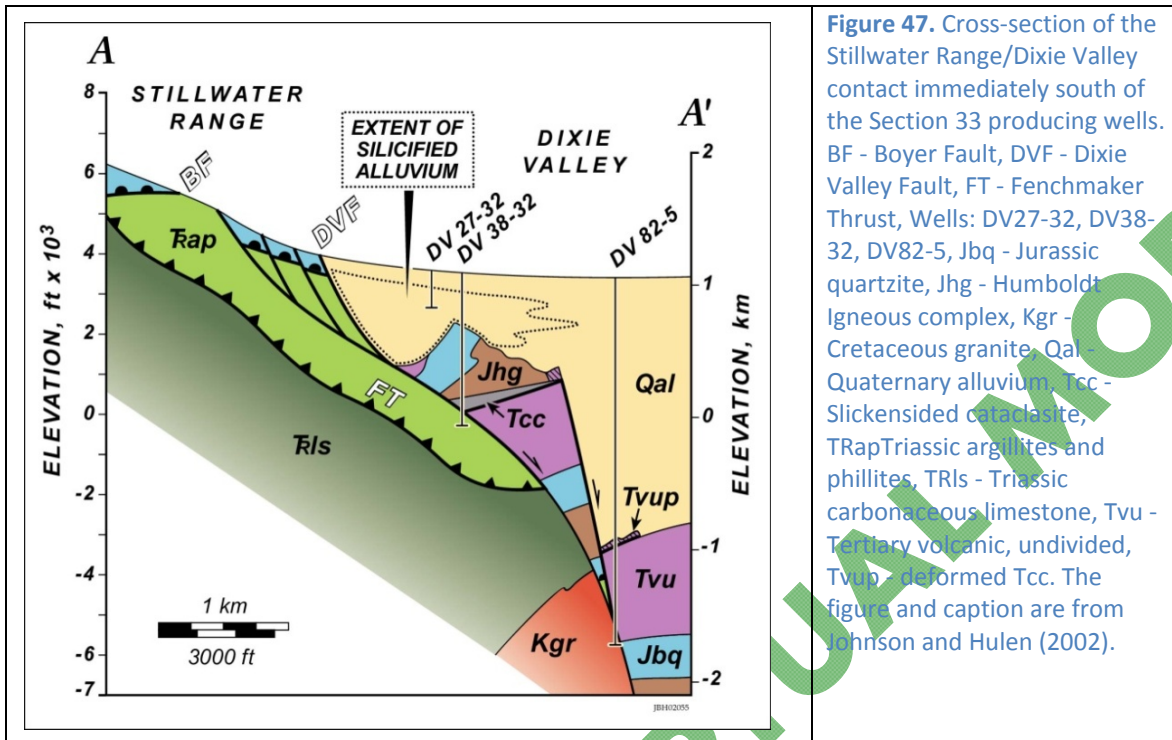


**Figure 47.** Cross-section of the Stillwater Range/Dixie Valley contact immediately south of the Section 33 producing wells. BF - Boyer Fault, DVF - Dixie Valley Fault, FT - Fenchmaker Thrust, Wells: DV27-32, DV38-32, DV82-5, Jbq - Jurassic quartzite, Jhg - Humboldt Igneous complex, Kgr - Cretaceous granite, Qal - Quaternary alluvium, Tcc - Slickensided cataclasite, TRap - Triassic argillites and phillites, TRls - Triassic carbonaceous limestone, Tvu - Tertiary volcanic, undivided, Tvup - deformed Tcc. The figure and caption are from Johnson and Hulen (2002).

## 7. Baseline Conceptual Geothermal Model

### 7.1 Introduction and Background

#### 7.1.1 Public Domain Highlights

The following Section 7.1.1 overviews important observations from the Baseline Model and reflects the salient highlights reported by Blackwell et al. (2005) with some additional commentary by the authors of this report.

The DVFZ has been determined to be a complex zone of faults (1-2km [3300-6600ft]wide), with multiple strands showing steep dips (75-85° or greater to a depth of at least 3km [1.9mi]) in the range and valley, in addition to the main range-bounding fault. A steeply dipping system of multiple fault strands is required by the gravity, temperature, drilling, surface mapping, and aeromagnetic survey results. Thus the structural offset is distributed across multiple zones rather than a single range-front fault plane as the extensional strain in Dixie Valley is not only accommodated by the range-front fault, but also by a multitude of other range and valley structures. The production wells within the DVFP and DVPP areas are located 2-3km (1.2 -1.9mi) into the valley and produce from blind valley (piedmont) segments of the piedmont fault segment of the DVFZ. The section 7 producers and section 18 injectors (Figure 40A) lie along the piedmont structure, which accommodates the majority of vertical displacement along the fault zone. As identified in this investigation, the producing geothermal system lies within intermittent dilatational zones along the DVFZ where fractures are optimally oriented and critically stressed for normal faulting and are open. Other important observations of the structural setting are listed below.

- The Dixie Valley setting shows the importance of buried relay ramps that lie basinward of exposed range-faults for future exploration.

- The “Stillwater Gap” could likely experience low level movement “creep” that maintains the fracture permeability along the fault.

Main points from the hydrology and geochemistry assessment are:

- Fluid loss in the geothermal system is due to leakage from the range front fault, piedmont faults, and interconnected intrabasin faults that all outflow directly into the valley-fill within several gravely interbedded artesian layers.
- Spring chemistry indicates a mixture of cold meteoric water derived from precipitation in the basin and surrounding ranges and deeply circulating geothermal water derived from the DVFZ.
- Shallow groundwater is derived from regional recharge from precipitation with 15-25% input of geothermal brines from depth.
- Geochemistry and isotope analysis show that the geothermal fluids are Pleistocene in age that have remained isolated from meteoric recharge. The isotopic ages for Dixie Valley geothermal waters are 12-20ka.
- The geothermal system has been intermittently to continuously active for approximately 100,000 years.
- Helium isotope data indicate small amounts of mantle derived fluid that infer a through-going fracture network that provides fast pathways from upper mantle to lower crust and agrees with a deep-seated range-front fault model and deep meteoric water circulation interacting with the mantle-lower crust derived fluids.
- The helium data also suggest that the entire DVFZ extending south of the EGS study area may be a geothermal target.

Highlights from the thermal regime are:

- A 20+km strike length of the fault zone is presently the locus for fluid(s) circulating at temperatures over 200°C (up to 285°C) at 2 - 3km depth.
- Two distinct thermal fluid bearing structures (faults) include the exposed range front fault at shallow levels and a buried piedmont fault at deeper levels which is connected to the producing geothermal reservoir. However, the very high measured temperature in 36-14 which is in close proximity to the range-front fault indicates that hotter geothermal fluid is upwelling from depth along that structure.
- The explored known portion of the existing geothermal resource system (see definition in [Section 7.2.1](#)) can be defined as consisting of at least three separate geothermal cells/systems. The two main areas (5km [3.1mi] apart and 2km [1.2mi] wide) are showing temperatures (225 to 245°C [437 to 473°F) at depths of 2500m (8200ft) and over 265°C (509°F) below 3000m (9800ft). These areas lie adjacent to Senator and section 10 fumaroles, respectively. A third geothermal cell is evident to the south within the DVPP area.
- The geothermal cell/system thermal regime is locally in equilibrium in the 1-3km (3300-9800ft) depth range.

### 7.1.2 Introduction

The Baseline Conceptual Geothermal Model is based on work (1) presented in the previous compendium of baseline (i.e., existing) data, Sections 1-6, that represents primarily the literature assessment (by the current authors) of the DVGS, (2) limited private sector data, and (3) interpretations by this current project team. Complete cross-sections (sections) through the

DVGW (see [Section 7.3](#)) can be found in Plates 1 & 2 with noted major assumptions within the sections found in Appendix 12. For locations of cross-section lines see [Figure 48B](#).

At the conclusion of this discussion, we present a summary description of the assessment in terms of the hydrothermal geothermal system and the EGS. Both are presented because they are two aspects of a single geothermal process. Hydrothermal cells in the B&R convectively transport heat from deeper within the crust to the surface. The thermal energy, carried by the upwelling geothermal fluid, conductively heats the host rock in the vicinity of the fracture and fault hosted geothermal cell. Over time this thermal conductive process has the potential of heating a substantial body of rock, expanding progressively outward and away from the convective geothermal cell with time and flow rate. The thermal energy contained within this conductively heated rock is the EGS portion of the geothermal system of interest here.

### 7.1.3 Calibration of EGS Methodology

The DVGS was chosen for the development of a calibrated EGS exploration methodology because it best characterized geothermal systems in the B&R with a considerable amount of geoscience data and known well results in the public domain. The calibration has been achieved by (1) qualitatively integrating geophysical, geological, and geochemical data sets; (2) cross-correlating the geoscience data with known geothermal well results; and (3) quantitatively assessing the select geoscience parameters and correlations through geostatistics. This approach was coupled with subject matter expertise (SME) throughout the process.

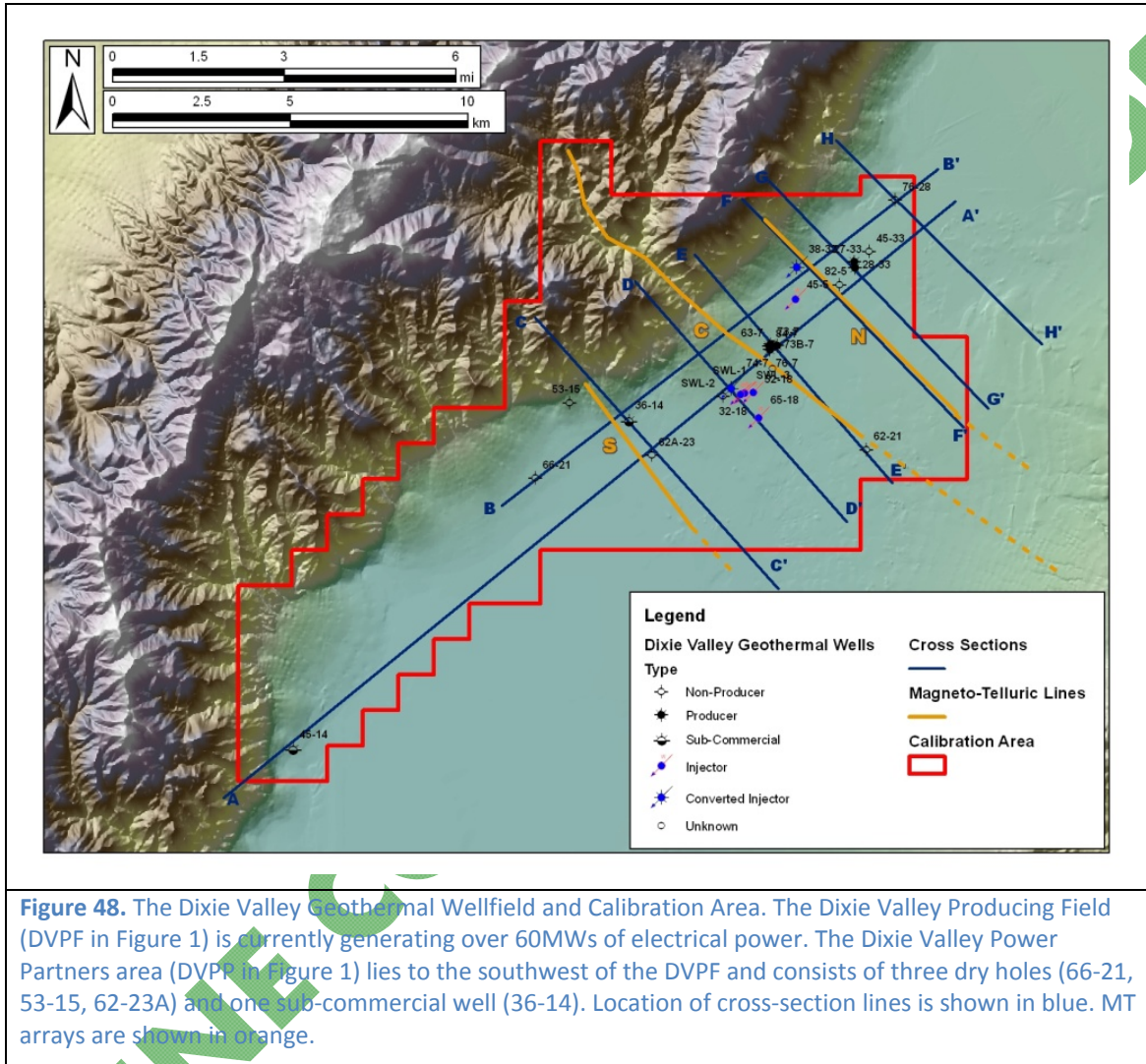
To obtain high-resolution geophysical data, we defined a Project Area that is 50km x 50km (31mi x 31mi) approximately centered on the DVGW ([Figure 48](#)). The DVGW which includes the DVPF area that is currently producing at over 60 MW of electrical generation and the DVPP area to the southwest has 30 deep wells. Well data available to this project consisted of lithology for 22 wells, thermal data consisting of BHT measurements for 26 wells, and temperature-depth profiles for 10 wells. Additionally, temperature-depth profiles were available for nine TGHs. Since the DVGW contains the wells, most of the subsurface data, and numerous geophysical surveys (see [Section 3](#)), it was designated as the Wellfield Calibration Area. This area is defined as extending from the Dixie Comstock Mine and well 45-14 at southwest end to the Section 10 and Senator fumarole areas (the DVPP and DVPF respectively), to well 76-28 to the northeast, and to well 62-21 to the southeast ([Figure 48](#)).

## 7.2 Geologic and Structural Interpretations

### 7.2.1 Re-Interpreted Structural Analysis

The distribution of geothermal cells/anomalies (see discussion below) in Dixie Valley has been reported by previous investigators to be mostly controlled by the northeast-trending structures of the DVFZ (see [Figures 30](#) and [33](#)). The significance of the inherited, older set of north-trending structures that are present bounding structural blocks within the Stillwater Range and deep fault-controlled basins in Dixie Valley has largely been ignored, with the exception of (Waibel, 1987; Smith and Blackwell, 2001; Waibel, 2011; Iovenitti et al., 2011a, 2011b). Where these two structural trends intersect within the DVFZ, the localized stress field is altered, and zones of compression and dilatation are developed. If the dominant B&R normal fault trend (NNE-trending and steeply-dipping) was sufficient alone to transmit hydrothermal fluids from depths, then geothermal systems would be potentially found along the entire strike length of these faults, while this is clearly not the case as they are mostly found along isolated structurally controlled regions. Terminology for describing geothermal for the purpose of this report are (1)

a geothermal cell is defined as a small localized conduit for geothermal fluids at a given structural setting, (2) a system is significantly larger than a geothermal cell but not sufficiently developed to be a geothermal resource, and (3) a geothermal resource represents a geothermal anomaly of sufficient size and mass that it can be produced.



Faulds et al. (2011) has described four examples of favorable structural settings for geothermal systems, specifically applicable to the B&R. These include (1) step-over or relay ramp between two overlapping normal fault segments with multiple minor faults providing hard linkage between two major faults, (2) terminations of major normal faults whereby faults break up into multiple splays or horsetail, (3) overlapping, oppositely dipping normal fault systems (accommodation zones) that generate multiple fault intersections in the subsurface, and (4) dilatational fault intersection between oblique-slip normal faults. In the case of the Dixie Valley geothermal setting, the structural mechanism appears to fall within the fourth example mentioned by Faulds involving the interaction of oblique-slip normal fault segments, and on a more broader scale, the third case. Evidence presented in this section suggests that the Dixie Valley geothermal system is strongly controlled by dilatational fault intersections.

Analysis of the overall structural setting of the Project Area reveals that the intersection of the pre-8 Ma N-trending B&R structures (Waibel, 1987) with the current NE-trending post-8 Ma B&R structures are coincident with the location of many of the shallow thermal anomalies and the current geothermal electrical production field (Figures 49A-C; Waibel, 2011; Iovenitti et al., 2011a; 2011b). In some cases, the older N-trending structures appear to offset NE-oriented structures within the DVFZ suggesting re-activation within the current stress regime. Thus, these structural intersections play an important role in the development of dilatation zones that host geothermal cells/systems/resource in the Project Area.

In the current stress regime with a least principle stress oriented NW-SE ( $S_{\text{hmin}} = N45^{\circ}W$ ) [Hickman et al., 1998; 2000], see Section 6.1.1, the N to NNE-trending steeply dipping structures would be expected to exhibit some re-activation in a dextral strike-slip sense when evaluated with respect to a strike-slip faulting regime. In theory, where the greatest principle stress is oriented  $N45^{\circ}E$ , roughly parallel to the strike of the Dixie Valley fault, a conjugate set of strike-slip faults is expected to occur at an orientation of  $30^{\circ}$  off of the greatest principle stress. Thus, when applied to Dixie Valley an inherited structure oriented approximately  $N15^{\circ}E$  would be expected to exhibit dextral (right-lateral) strike-slip motion, while a cross-structure oriented  $\sim N75^{\circ}E$  is expected to exhibit a sinistral (left-lateral) strike-slip motion. It is important to note that while Dixie Valley is located in the northern B&R province that undergoes mostly pure extension along a roughly WNW-ESE axis, it is in close proximity to the north-trending, trans-tensional structural zone known as the Walker Lane Belt. Thus, it is thought that some of the dextral shear accommodated along this trans-tensional zone is transferred into the adjacent terranes. This is reported by Caskey et al. (1996), as right-lateral offset (right-oblique slip) evident along the east-dipping Fairview fault and related ruptures, abruptly transitioned to pure normal slip along ruptures exposed to the north along the southernmost Dixie Valley Fault ruptures.

Accordingly, Smith and Blackwell (2001) have identified the continuation of two major NS-trending structures present in the Stillwater Range to extend within the basin and through the producing field (Figure 49A). They show that the axis of a syncline within the middle section of valley-fill sediments, believed to occur syn-extensional as a hanging-wall block response to normal faulting, is offset in an apparent dextral (right-lateral) motion by the N-trending structures (see Figure 14). A major assumption in this structural interpretation is that the generally N-trending faults show relatively recent strike-slip motion as they offset segments of the range-front and piedmont fault within the DVFZ. Alternatively to the slip direction inferred along the two structures, the range-front fault and piedmont fault appear to be offset in a sinistral sense along a NNW to N-trending structure in the area near 45-14, southwest of the producing field (Figure 49B). This provides additional evidence for the re-activation of these older structures, following the formation of the DVFZ, and occurring within the time frame of the current stress regime. The reason for this opposite sense of motion has not been fully investigated. Four potential reasons to account for this sinistral slip could be the (1) configuration of the fault relating to dip direction, (2) transition zone between pure normal slip on the range-front fault segment of the DVFZ and oblique-slip along Fairview Peak and other southern Dixie Valley faults, (3) a complex interaction relating to a regionally observed dextral sensed shearing of the southern portion of the Stillwater Range, and (4) some combination of the above.

Specifically in reference to the third argument, a regional dextral sensed shearing adjacent to the trend of the southern Stillwater Range has been observed in mapping relationships as

(1) northerly-trending faults appear to be offset to the NE and show a pronounced right-step within the range and (2) intervening structural blocks are tilted and rotated. This apparent NE-trending dextral shear that influences the structure in the range could explain why faults occurring on the SE edge of this structural block show sinistral offsets. A largely coherent yet slightly tilted structural block that encompasses the Table Mountain basalts exists in the central Stillwater Range bounded by major north-trending faults. This block seems to play a role in dividing the structure of the Stillwater Range and separates the apparently sheared structural block to the southwest with the highly dissected northeastern Stillwater Range block which lies north of the producing field. While this relationship has been noted as a possible explanation for the change in structure, it is outside the scope of the project and has not been investigated further.

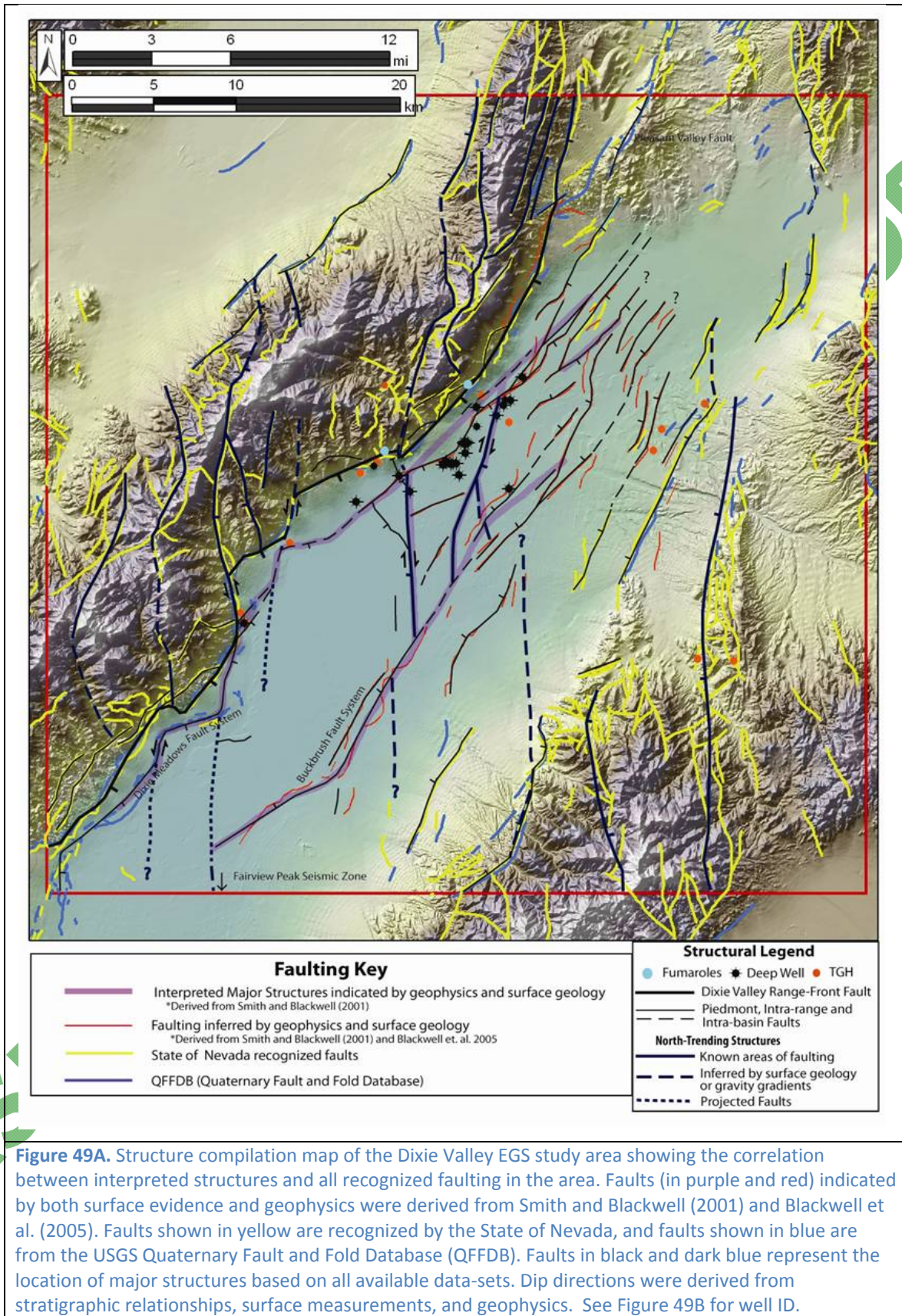
To illustrate the structural setting of the EGS Project Area, all known faults from a variety of datasets were integrated into a detailed structure map ([Figure 49A](#)). The data sets used to derive this structure map include mapping results from Page (1965) and Speed (1976), structures identified by Smith and Blackwell (2001), geophysical inferred structures including gravity/magnetic horizontal gradients (Blackwell et al., 2005), faults recognized by the state of Nevada, and from the USGS Quaternary Fault and Fold Database (QFFDB). Thus the structure map shown in [Figure 49A](#) represents the compilation and interpreted relationship of all known faults and inferred structures in the Project Area.

[Figure 49B](#) presents a detailed geologic map of the project area derived from published geologic maps including Page (1965), Speed (1976), Stewart and Carlson (1978) and other State of Nevada Geologic Maps. This map represents a more precise analysis of the occurrence of known faulting delineated from faults inferred from geophysical methods, as well as other available structural data. The map clearly shows the Stillwater Range is sub-divided into discrete structural blocks bounding by N-trending structures. The structures are all assumed to be steeply dipping with dip directions derived from stratigraphic relationships, surface measurements, and geophysics.

[Figure 49C](#) depicts the major recognized structures with respect to the wellfield and location of shallow thermal anomalies as well as the expected areas of dilatation and compression occurring at these structural intersections. Thermal anomalies occurring at these intersections include from south to north, Dixie Meadows, Dixie Comstock Mine, unnamed, Section 10 Fumaroles within the DVPP, Senator Fumaroles within the DVPF, and New York Canyon on the western edge of the Stillwater Range. Other shallow anomalies within northern Dixie Valley including Hyder and Sou HS seem to be influenced by some other structural control not directly associated with the DVFZ. Drakos et al. (2011) attribute the occurrence of these hot springs to a structural accommodation zone between Pleasant Valley and Dixie Valley faults (Faulds et al., (2011) third example, see above).

#### ***Zones of Compression and Dilatation***

The structural zones at the major fault intersections are divided into compressional and dilatational based on the expected movement within discrete structural blocks in their respective quadrants ([Figure 49C](#)). The model assumes the NE-trending normal faults exhibit pure normal slip, with slip vectors perpendicular from fault strike. For the NS-trending faults, the major assumption is the faults exhibit strike-slip motion under the current stress regime. The compressional and dilatational zones generalized the expected stress conditions due to the combination of slip on a NE-trending fault and the expected strike-slip component on a NS-trending fault. Where both vectors agree (in same directions) a zone of dilatation is inferred.



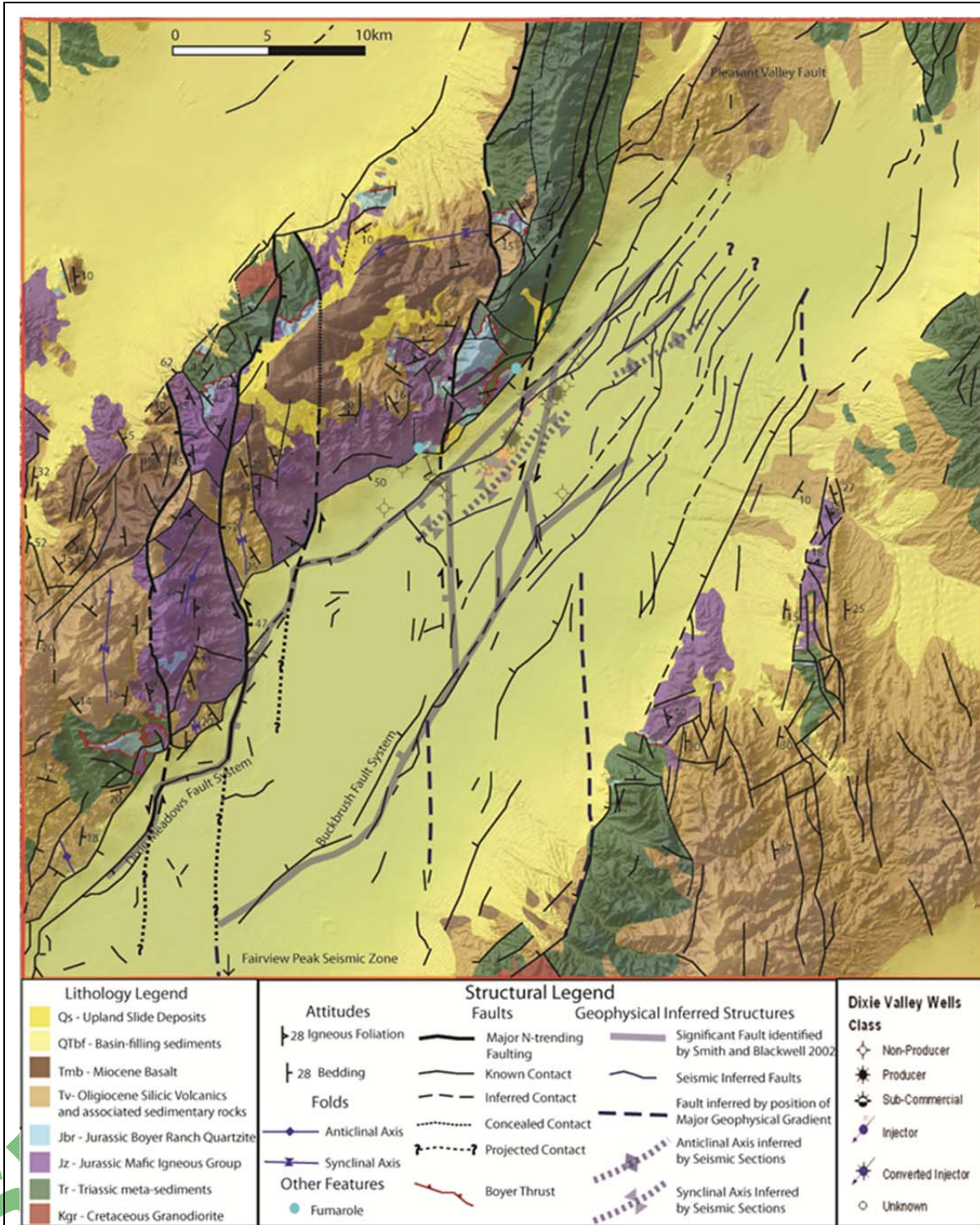
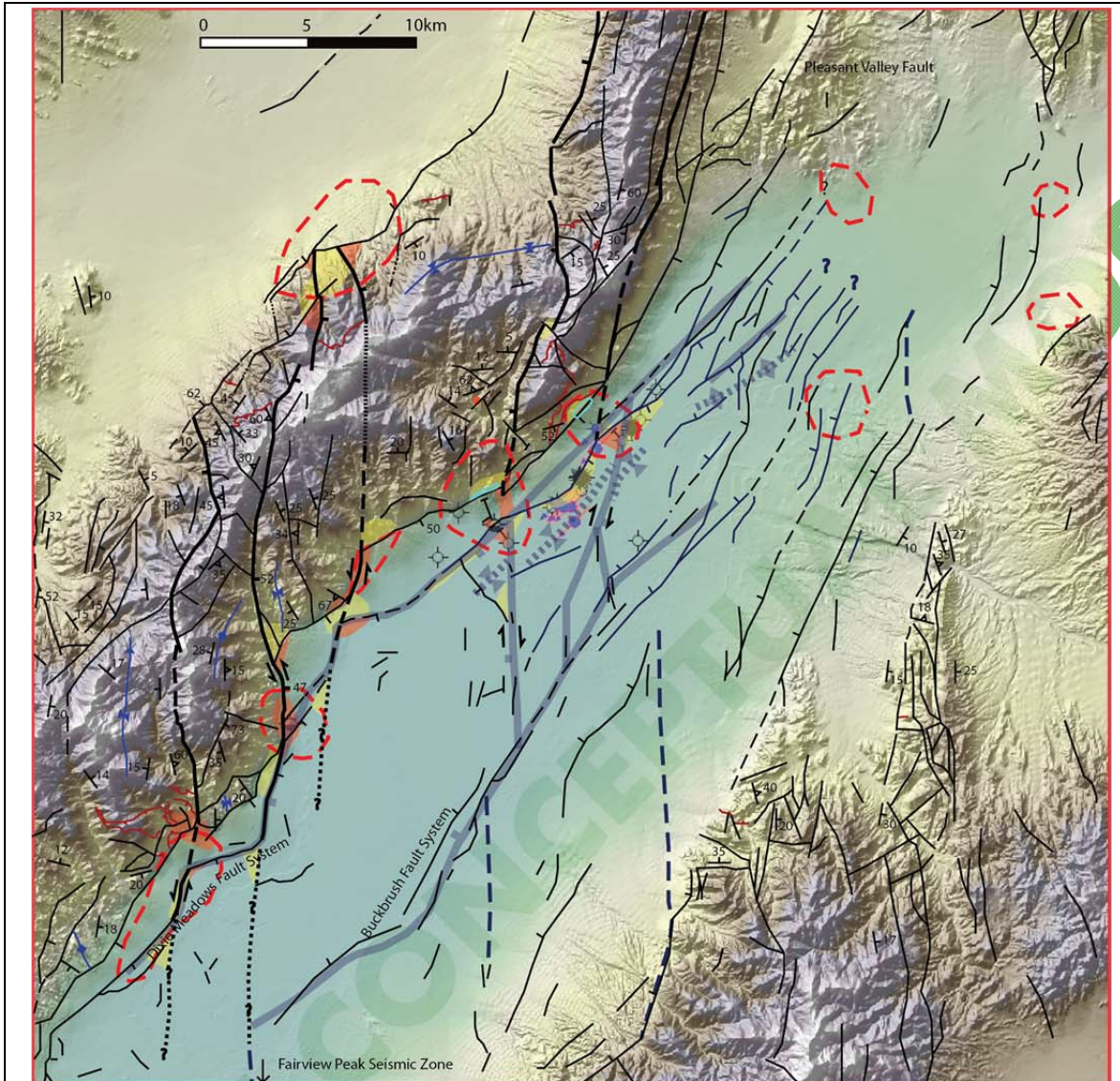


**Figure 49B.** Project Area Geologic Map showing lithology, structural data, recognized faults, and major structures recognized by geophysics. Major N-trending structures are emphasized and shown to divide the Stillwater Range into discrete structural blocks. Lithology and structural data was derived from previous published mapping results including Page (1965), Speed (1976), Stewart and Carlson (1978), and other State of Nevada Geologic Maps.



Structural Legend									
	Shallow Thermal Anomaly		Attitudes		Major N-trending Faulting		Significant Fault identified by Smith and Blackwell (2001)		Non-Producer
	Zone of Dilatation		Bedding				Known Contact		
	Zone of Compression		Folds		Inferred Contact		Fault inferred by position of Major Geophysical Gradient		Sub-Commercial
	Fumaroles		Anticlinal Axis		Concealed Contact		Anticlinal Axis inferred by Seismic Sections		Injector
			Synclinal Axis		Projected Contact		Synclinal Axis Inferred by Seismic Sections		Converted Injector
					Boyer Thrust				Unknown

**Figure 49C.** Correlation between shallow thermal anomalies (dashed red lines) and identified structural intersections of N to NE-trending faults (dark blue lines) in northern Dixie Valley, Nevada. Light blue dots indicate the Section 10 (southwest of the producing field) and Senator fumarole areas (Figure 48a). Well symbols are shown in the associated Well Class Key. Expected zones of compression (red-orange shaded areas) and dilatation (yellow shaded areas) occurring at the intersections of discrete structural blocks are inferred based on the interaction between the strike-slip and normal-slip component and other considerations. These localized structural zones were only defined where a thermal anomaly was present within the DVFZ and at New York Canyon, on the northwestern side of Table Mountain.

Where the vectors do not agree, a zone of compression is inferred, as movement on the strike-slip fault supersedes. Also a bend in a normal fault, apparent as the piedmont fault takes a significant left-step bend in the producing field, would also infer a dilated zone at the change in strike. It is noted that a convex bend relative to the hanging wall of fault would produce dilation in the hanging wall block. This structural complexity and the apparent dilated nature could likely be explained as a smaller scale but prominent NNE-oriented fault that extends from within the range, to the western side of 38-32 and appears to offset the piedmont fault as it projects directly into the major change in strike (D. Blackwell, pers. comm., 2011; see [Figures 49B and 49C](#)). This is in concert with that portion of the DVFZ being dilated.

The extent of these zones shown in [Figure 49C](#) is purely arbitrary. For the purpose of this report we choose to define these zones as extending for about 1 km away from the fault intersection. In cases where fumaroles exist at the surface, these zones of dilation are extended to include such features. One scaling problem with the model is that the identified structural zones are very small compared to the size of the surface thermal anomalies and any thermal anomaly is likely to encompass both compressional and dilatational zones. This may be attributed in part to an upflow zone creating a thermal hydrologic mound in the shallow near-surface unconsolidated sediments. The geometry of the fault intersections at depth was not considered herein as the N-trending faults are assumed to be steeply dipping and near vertical at the surface. The interpreted stress quadrants (zones of compression and dilatation) were applied to the major fault intersections that correlated with a shallow thermal anomaly within the DVFZ. One exception to this is the New York Canyon anomaly which exists on the western edge of the Stillwater Range and is not in the area defined as the DVFZ. The thermal anomalies in northeastern Dixie Valley were not included in this analysis due to a lack of subsurface data.

It is at these structural intersections and within the associated dilated zones that geothermal fluids are present. Evidence for this postulation is:

1. the major thermal anomalies associated with the DVGW, adjacent to Section 10 and Senator Fumaroles occur at these structural intersections and consist of at least three separate geothermal cells developed within the associated dilated zones (evidence developed in this investigation and in Waibel [2011]);
2. the location of the two major fumaroles occurring within expected areas of dilation;
3. the Dixie Comstock and Dixie Meadows anomalies occur at a major fault intersection coinciding with a sharp bend in the range-front;
4. the New York Canyon thermal anomaly is associated with this type of structural intersection on the northwest side of the Stillwater Range;
5. the highly permeable Section 33 producing wells lie within a dilated zone;
6. well 82-5, a hot, dry well within the producing field has its bottomhole location within an intervening zone of compression between the section 33 and section 7 production wells (also see below for an potentially alternative/complimentary explanation);
7. the very hot and low permeability wells of the DVPP, 36-14<sup>2</sup> and 62-23A respectively, lies within a compressional zone, as does 45-14; and

---

<sup>2</sup> However, 36-14 was approaching the range-front segment of the DVFZ and a dilatational zone which occurs on the Stillwater Range side of the fault.

8. well 36-14, deviated towards the Stillwater Range and the range-front fault segment of the DVFZ, encountered a fluid-bearing fracture zone within the last hundred feet of the wellbore, which correlates with the location of the range-front fault at depth and with an expected dilated zone near Section 10 (unnamed) fumaroles.

These structural intersections appear to explain the intermittent distribution of the shallow thermal anomalies that have developed within the Dixie Valley Geothermal District in the DGGW and at New York Canyon.

Additionally, the structural analysis and associated zones of compression and dilatation are also supported by the well and helium isotopic data (R/Ra), [Figure 49D](#). The majority of productive wells lie within the expected zones of dilatation, with the exception of 45-33, which is thought to be non-productive based on mechanical problems in the well. The northernmost producing wells, 27-33, 28-33, and 37-33, all lie within a dilatational zone, while an adjacent dry hole, 82-5, lies with a zone of compression separating the aforementioned wells from the main production area to the southwest. Hickman et al. (2000) also reported that 82-5 is completed in a narrowly defined shear zone with abundant talc alteration and low shear stress at the depth where the well was expected to encounter the producing fault zone.

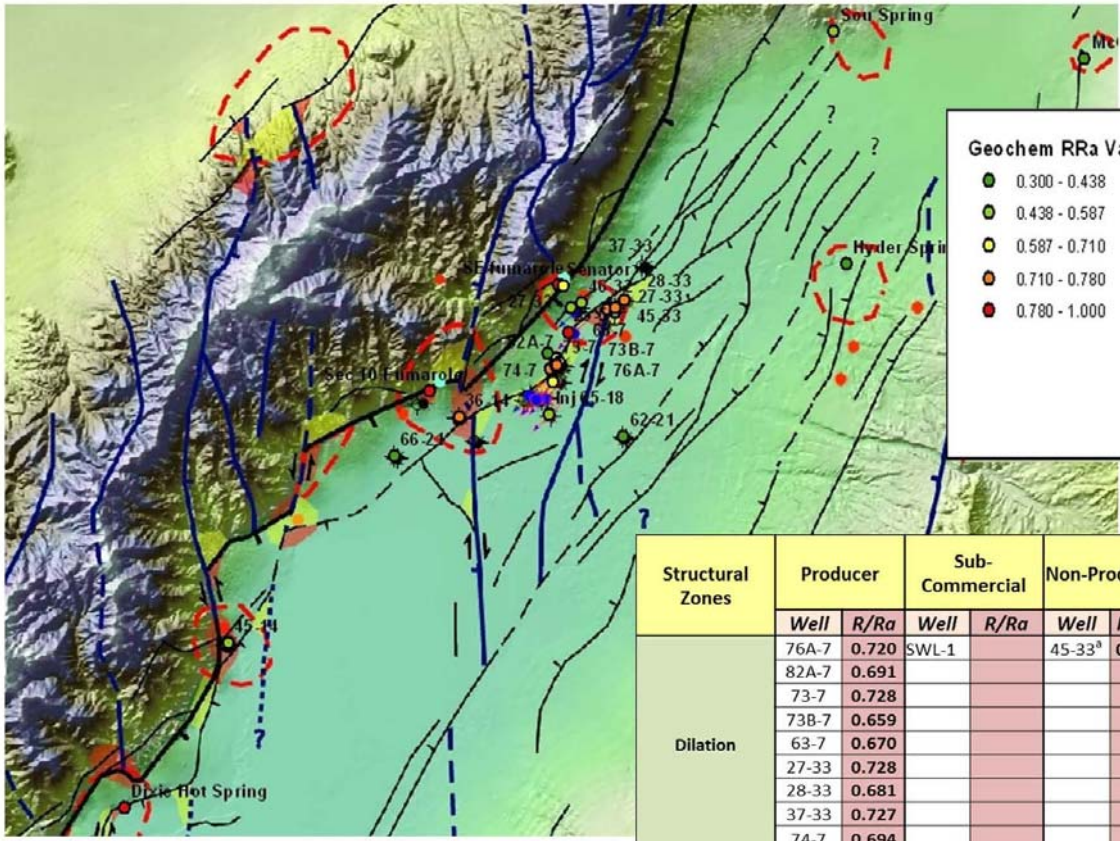
All the productive wells in the DVGW have relatively high R/Ra values indicating a magmatic gas component and deep source ([Figure 49D](#)). While 36-14 lies within a zone of compression, the high helium R/Ra value (0.77) could be explained as the well was inclined towards the range-front and is thought to nearly intersect the associated dilated zone. Fluids sampled outside of the DVFZ, e.g. 62-21, Hyder and Sou HS, have relatively lower helium R/Ra values. The two fumarole sites occurring at the range-front lie within zones of dilatation and have high reported helium R/Ra values, while it has been noted that the larger fumarole helium ratios are thought to result from air contamination (B.M. Kennedy, pers. comm., 2011).

One major factor affecting the productive nature of a well not previously discussed is the lithology overprint as some formations are not suitable to contain open fractures suitable for geothermal production. For example, non-producing wells 62-21, 62-23A and 66-21 were all completed in the Triassic shales/slates. Rock type at elevated temperature plays a significant role in whether a well is a producer or non-producer in a hydrothermal system and whether a well can host an EGS reservoir. Brittle rocks containing open-fractures are an ideal hydrothermal reservoir. When closed fractures are present in brittle rocks, the rock can be fractured through EGS. Non-brittle rocks would not be appropriate for either a hydrothermal system or EGS. Several examples of wells completed in poor reservoir rock exist within the DVGW. The non-producers 45-14 and 66-21 have bottomhole temperatures of 196°C (385°F) and 215°C (419°F), respectively, but were completed in Triassic shales/slates, not a suitable reservoir rock (D. Benoit, pers. comm., 2011) because it does not hold a fracture, in at least the areas drilled by these wells. 62-23A, had a very high reported bottom hole temperature of 279°C (534°F), but the Triassic section the well was completed in had very low permeability.

### 7.2.2 Re-Interpreted Stress Modeling

The baseline Dixie Valley stress modeling (Wesnousky et al., 2003), described in [Section 2.2.4](#), was updated using Coulomb 3.1 Stress Modeling software. The purpose was to better characterize the expected fault-induced stress and strain conditions in Dixie Valley based on the conditions required by the Baseline Conceptual Geothermal Model. The background, methodology, and results of the modeling are described in detail in Appendix 13; see also <http://earthquake.usgs.gov/research/modeling/coulomb/>.

ADEL



Geochem R/Ra Values		Dixie Valley Wells	
●	0.300 - 0.438	○	Non-Producer
●	0.438 - 0.587	●	Producer
●	0.587 - 0.710	●	Sub-Commercial
●	0.710 - 0.780	●	Injector
●	0.780 - 1.000	●	Converted Injector
		○	Unknown

**Figure 49D.** Correlation of Shallow Thermal Anomalies, expected zones of compression and dilatation at structural intersections, and well type within the Dixie Valley Geothermal Wellfield. Wells are color-coded based on their respective helium data (R/Ra). The table (bottom-right) shows the relationship between R/Ra ratios measured from wells and fumaroles and well type with respect to the well location and the occurrence of structural zones.

Structural Zones	Producer		Sub-Commercial		Non-Producer		Injectors		Fumaroles/HS	
	Well	R/Ra	Well	R/Ra	Well	R/Ra	Well	R/Ra	Name	R/Ra
Dilation	76A-7	0.720	SWL-1		45-33 <sup>a</sup>	0.725	45-5		Senator	0.662
	82A-7	0.691					41-18		SE Fum	0.855
	73-7	0.728					52-18			
	73B-7	0.659					SWL-2			
	63-7	0.670					SWL-3			
	27-33	0.728					32-18			
	28-33	0.681								
	37-33	0.727								
Compression			36-14	0.770	62-23A				Dixie	0.845
			45-14	0.587	82-5					
Other			38-32		66-21	0.306	65-18	0.560	Sou	0.528
					62-21		27-32	0.583	Hyder	0.438
					76-28				McCoy	0.345
					53-15				Jersey	0.495

<sup>a</sup>Well data available to AltaRock is limited. It is unknown why this well is a non-producer.

BASIN

Valley-bounding normal faults have produced several large earthquakes over the past ~3000 years, including the 2-2.5ka "Gap" Earthquake along the Stillwater Seismic Gap (SSG) segment of the DVFZ range-front segment, the 1915 Pleasant Valley Earthquake along the Pleasant Valley Fault (PVF), and 1954 Dixie Valley Earthquake along the southern section of the DVFZ. The updated stress model takes these three events into account while the input parameters differ from the Wesnousky et al. (2003) model in assuming that slip has occurred along SSG and that the structures are steeper dipping (70°).

The Coulomb 3.1 model can calculate the expected strain and Coulomb Stress Change (CSC) on a receiver fault (RF) due to slip constraints on a source fault (SF) to determine whether failure along the RF is promoted or inhibited (Lin and Stein, 2004; Toda et al., 2005). A positive CSC infers failure is promoted, while a negative CSC infers that failure is inhibited. The strain is divided into a positive dilatation component, inferring the fault is unclamped, while a negative compressional component infers the fault is clamped. This Coulomb model assumes a RF (with a specified strike, dip and rake) exists within each gridded cell used in this modeling (500m by 500m) and plots the CSC and strain at that location.

Several scenarios involving RFs were examined. The approach began with a "test-run" (referred to as the first scenario) that reproduced the Wesnousky et al. (2003) model results as a test to the model constraints. A second scenario assumed that slip occurs along a more complicated and multi-fault system, taking into account postulations from Blackwell et al. (2005) that the whole SSG did rupture in the "Gap" event. For Scenario 2, the range-front segment of the DVFZ (southern portion that experienced surface rupturing in 1954) is represented as 1 fault segment, the SSG as 3 segments, and unlike Scenario 1, we also include the PVF as 1 segment. These 5 segments respectively comprise the source faults and have differing orientations, slip rates and slip directions detailed in Appendix 13.

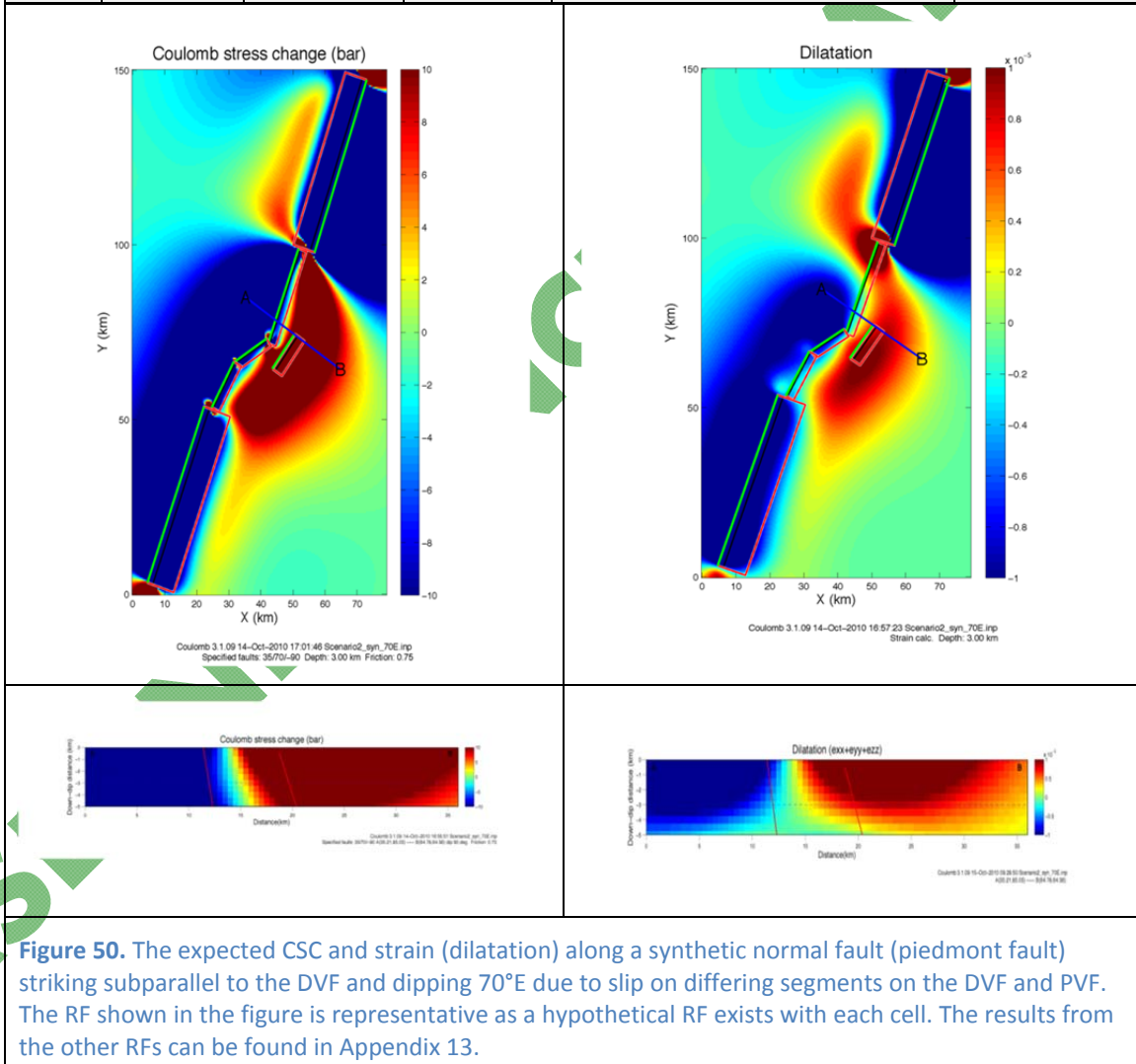
According to stress orientations and magnitudes reported by Hickman et al. (1998, 2000), the dominant population of permeable fractures within the fault zone near the DVGW is subparallel to the main fault, striking roughly NE and dipping 40-75 degrees SE, with a conjugate set striking roughly the same direction but dipping NW. Field observations suggest that roughly N-S oriented normal faults are also present (T. Cladouhos, pers. comm., 2010) and their role within the DVGW is described in [Section 7.2.1](#). To be consistent with these observations, we explore three different types of RFs:

- a. synthetic normal fault subparallel to SGS dipping 70°E shown in [Figure 50](#);
- b. antithetic normal fault subparallel to SGS dipping 70°W; and
- c. normal fault oriented roughly N-S dipping 70°W.

Assuming that the whole SGS fault segment ruptured 2-2.5 ka (in addition to the 1954 range-front fault segment of the DVFZ and 1915 PVF ruptures), the results presented in Appendix 13 show that the region near the DVGW lies within a zone of positive CSC and dilatation, suggesting that slip resulting from these Holocene ruptures promotes normal faulting on all three types of RFs. Stress data from selected wells within the DVGW supports these conclusions (see [Section 6.1.1](#) and [Table 4](#)).

**Table 4.** Information from deep wells penetrating the fault zone at 2-3km depth. Red and blue indicate critically stressed and not critically stressed well sites (Hickman et al., 1998; 2000). See text for a description of Scenario 2.

Well	Sh <sub>min</sub>	Sh <sub>min</sub> /Sv	Productive	Interpretation	Scenario 2
73B-7	N57W±10	0.45-0.62 @ 0.4-2.5 km	Y	SFZ optimally oriented and Shmin low ( <b>critically stressed</b> )	Consistent with well data
74-7	N52W	not reported	Y	SFZ optimally oriented and Shmin low ( <b>critically stressed</b> )	Consistent with well data
66-21	N20W±20	0.55-0.64 @ 1.9–2.2 km	N	SFZ optimally oriented BUT Shmin high ( <b>not critically stressed</b> )	Consistent with well data
45-14	N41W±12	0.55-0.64 @ 1.9–2.2 km	N	Shmin low BUT SFZ not optimally oriented ( <b>not critically stressed</b> )	Consistent with well data



## 7.3 Qualitative Geoscience Correlations

### 7.3.1 Summary Description of Geoscience Data Sets

The most complete 3-dimensional database for the geology, geophysics and geothermal setting of the geothermal system in Dixie Valley is located in the DVGW. It is recognized that this particular location cannot be used as a point-by-point template for geothermal cells (including the EGS target areas) throughout Dixie Valley. However it is the only area where a calibrated exploration methodology can be developed as a result of having subsurface data.

A series of cross-sections both perpendicular and parallel to the DVFZ (Plates 1 and 2) have been constructed to develop a baseline conceptual model of the geothermal system (both the hydrothermal and EGS), and provide a framework for the EGS favorability maps (see [Section 8](#)). The sections, based mostly on data from Blackwell et al. (2005), available well logs, and other public domain sources cited above, adhere to the steeply dipping multi-fault model for the DVFZ. They utilize the surface geology in the adjacent Stillwater Range, lithologic and thermal data from individual wells, and various geophysical surveys that infer the location of intra-basinal structures including gravity, magnetics, and seismic reflection profiles. The location of the eight cross-section lines (A-A' to H-H') with respect to the wellfield is shown in [Figure 48](#) and Plate 1 & 2. The sections were constructed to apply a series of 2-D sections to facilitate in the visualization of a 3-D model. The majority of the transects (C-H) were chosen perpendicular to the major structures, with the respective section locations chosen to cover the known productive (hydrothermal) and non-productive (potentially EGS) areas, all wells that had data available, and to transect major structures in the wellfield. See Appendix 12 for figures showing the various cross-sections and major assumptions used in their development.

#### Geology

The stratigraphy of the DVGS has been divided into six major and one minor stratigraphic units (Appendices 10 and 12) based on rock mechanical properties and the stratigraphic divisions used within idealized published and unpublished thermal models by Dave Blackwell (Blackwell et al. 2000; 2005). The units<sup>1</sup> include from youngest to oldest:

- Quaternary-Tertiary basin-filling sediments and lowermost tuffaceous sediments (QTbf);
- Miocene basalts (Tmb);
- Oligocene silicic volcanics including uppermost Miocene lacustrine sediments, volcaniclastics, and lowermost silicic tuffs (Tv);
- Cretaceous to late Tertiary granodiorite (Kgr);
- Jurassic mafic rocks (Jz<sup>3</sup>) known as the Humboldt igneous group or lopolith, and also interpreted as an ophiolite complex consists of an upper volcanic sequence and lower gabbro-dominated section; and
- Jurassic and Triassic meta-sediments (Tr) which also include the thrust bounded Jurassic Boyer Ranch quartzite (Jbr) which, where identified has been broken out separately because it is a favorable EGS target lithology.

The distribution of these stratigraphic units with respect to the surface geology exposed in the Stillwater, Clan Alpine, and other related ranges within the Project Area is shown in [Figure 51](#).

<sup>1</sup> Note that in this report the term stratigraphic unit, lithology and geologic formation are used interchangeably since each of the seven major formational units identified in the DVGW have specific lithologies.

<sup>3</sup> In the gravity-magnetic modeling, the Jz stratigraphic unit is referred to as Jg and Jv; see Section 3.3 and 7.3.1 for an explanation.

The geologic sections in Plates 1 and 2 are based on the following general parameters, observations, and assumptions (see Appendix 12 for a more detailed discussion):

- Steeply dipping (75-90°) faults;
- DVFZ consists of the main range-bounding and intra-range faults, a major piedmont fault recognized by geophysical data, and the associated antithetic faults and associated fracturing away from the faults;
- Thickness of the defined stratigraphic units is primarily controlled by their occurrence in available well data, conceptual sections ([Figure 31](#)), and observations made from the surface geology exposed in the Stillwater Range;
- Early B&R N-S oriented normal faults which are likely re-activated as strike-slip faults under the current stress regime have mostly unknown dip directions and are drawn vertical without any normal-sensed offset; and
- Depth of the basin-fill sediments and the configuration of the basement profile (see [Figure 18](#)) are derived from Blackwell et al. 2005 that uses seismic interpretations, geophysical inferred bounding faults, and drilling results.

### *Thermal*

The thermal sections use available well temperature data in the DVGW and thermal models through the wellfield ([Figure 31](#), [45A](#) and [45B](#)) to construct a model of the temperature distribution at depth. While we can assume that the main thermal-bearing structures are the range-front and piedmont fault within the DVFZ, the well data and geologic model demonstrate that this is the case as a direct correlation is found between elevated temperature distribution and the major faults within the DVFZ (Plates 1 and 2). The elevated temperatures associated with these faults dip relatively steeply to the east towards the center of the valley, as the only temperature constraint at depth is found in 62-21, which lies in the valley on the SE-side of the DVGW. The “fall-off” in temperature to the west, under the Stillwater Range, is conjecture due to the lack of well data in that region.

While there is no direct evidence that the range front fault is directly connected to the producing hydrothermal system, it is believed to be a conduit for geothermal fluids from depth as evidenced by the (1) reported geothermal fluids in fractures from the last 30m (100ft) of 36-14, (2) fumaroles (~98°C [208°F]) at the surface trace, (3) recent seismic activity, (4) shallow outflow of geothermal fluids into basin-fill sediments ([Figure 44](#)), (5) comparable helium R/Ra values to the known producing field (see table imbedded in [Figure 49D](#)), and (6) very high temperatures (~285°C [545°F]) encountered at total depth in 36-14 (Blackwell et al., 2005).

The superpositioning of the wellfield temperature data on the MT and geology data provide the basis for constructing a model of the geothermal resource supporting the existing power plant and inferring EGS targets. Within this segment of Dixie Valley relating to the producing zone, discrete segments of the range-bounding and piedmont faults are transmitting hydrothermal fluids to shallower depths. Current production is derived from the piedmont section of the DVFZ. The main geothermal reservoir is thought to lie within dilatational zones along the piedmont fault where Miocene basalt and other Jurassic rocks capable of maintaining open fractures are truncated against impermeable granodiorite in the footwall block.

### *Magnetotellurics*

Wannamaker et al. (2007) presented resistivity models along three MT arrays (N, C, and S) through the DVGW (see [Section 3.4](#)). The N and S arrays extend to a depth of 4km (2.5mi), while

the C array is integrated with a regional MT transect (Wannamaker et al. 2006) and extends to a depth of 10km (6mi). The Dixie Valley MT arrays resolve the structural setting and support a multi-fault and steeply dipping model for the DVFZ. The transition from low to high resistivity (~100 ohm-m) represents the basement interface within the resistivity models which is supported by drilling results, as the arrays also show a high level of correlation with geologic sections. A discussion on the significant correlations found between the various geologic and geophysical datasets is provided discussed in Section [7.3.2](#).

### *Geochemical Data*

Geochemical data within the DVGW was extracted from Goff et al. (2002) (see Appendix 7) from selected wells, TGHs, springs and fumaroles. The depth of the producing fluids sampled from the wells was estimated by our geochemistry SME, Dr. B. M. (Mack) Kennedy, Geochemistry Task Leader (see [Section 1.4](#)). The SME provided six potential geothermal indicators namely Silica (Si), Chloride (Cl), BiCarbonate, and helium F[<sup>4</sup>He] measured in ppm as well as the BiCarbonate-Cl ratio, and helium R/Ra values. There are some difficulties in using and applying the geochemical data to the qualitative analysis, as the data is limited to isolated sampling points (point data) and it is not clear how to extrapolate the data.

### *Gravity-Magnetics*

A lithology model based on the gravity and magnetics has been constructed along four sections that lie perpendicular to the DVFZ (C-F) and along the two sections lying parallel to the DVFZ (A and B), see [Section 3.3](#). The complete Bouguer anomaly (CBA) gravity data (Ponce, 1997; Blackwell, pers. comm. to B. Karlin, 2010) and the HELIMAG aeromagnetic total field anomaly data (Grauch, 2002; Blackwell, pers. comm. to B. Karlin, 2010) were jointly modeled to create a 2 ½ D geophysical model consistent with the surface geology and selected well data (62-21) to infer the depth to basement.

The model divides the subsurface into four inferred stratigraphic units based on assigned density values that directly relate to recognized geologic units including (1) Jurassic volcanics and arenite exposed at the surface (Jv, Ja), (2) basin-filling sediments (Tbf), (3) a distinct magnetized Jurassic intrusive unit (Jg) and (4) basement inferring either Triassic meta-sediments or Cretaceous granodiorite. A near-surface low density unit within the valley was required to offset modeling effects and does not correspond to a specific mentioned unit, but could likely correlate with a near-surface clay-rich/evaporite layer. A complete description of the Gravity and Magnetics Joint-Modeling can be found in [Section 3.3](#) with results shown in [Figures 15A-D](#). The gravity and magnetic inferred lithology models are generally consistent with the geologic sections and identifies the presence of multiple faults in the DVFZ, a zone of step-faulting bounding the SE edge of Dixie Valley, and the occurrence of both a magnetized Jurassic unit (Jg) and non-magnetized Jurassic unit (Jznm) as postulated through comparison of the geologic and gravity/magnetic sections. While the geologic sections show Jurassic mafic rocks (also referred to as the Humboldt Lopolith) extending below the majority of Dixie Valley within the identified thrust sheet, the magnetic signature from these rocks isn't continuous across the area. The missing Jurassic rocks in the gravity-magnetic sections are most likely demagnetized and/or altered as a result of hydrothermal fluids in the DVFZ and correlate with the identified deep low resistivity zone along the MT sections, see discussion above.

### *Seismic Data*

A variety of seismic data derived from the reflection profile data (Anonymous, 1998) and associated well data was re-analyzed at the University of Reno (UNR) by our seismic SME, Dr.

Ileana Tibuleac (see [Section 1.4](#)). The following parameters were provided that are considered potentially useful for EGS (1) P-wave velocity ( $V_p$ ); (2) S-wave velocity ( $V_s$ ); (3) density ( $\rho$ ); and (4) attenuation of the P and S-waves ( $Q_p$ ,  $Q_s$ ). Within the baseline seismic data, the resolution was greatest for the parameter  $V_p$  (~500 m) and in the vicinity of the reflection profiles. Resolution for the other parameters was too high (maximum of >10 km) to be used in the Baseline Conceptual Model.

A general qualitative correlation was found between temperature and  $V_p$  within a specified velocity range within the wellfield, although it has been noted by some team members that the correlations found could be reflecting a function of depth.  $V_p$  has been postulated to have a direct relationship to temperature (I. Tibuleac, pers. comm., 2010; Biasi et al., 1999), while the modeled velocity changes at depth is also due to other factors including heterogeneity of the rock, structures present, fracture density, fluids present, alteration, increased vertical stress due to the weight of the overlying rock, etc. A correlation between lithology and  $V_p$  was not found using the limited baseline data. These relationships are explored quantitatively through geostatistics in [Section 7.4](#).

### *Seismic Reflection Profiles*

Interpreted seismic reflection profiles extracted from Blackwell et al. (2005) were used to partially constrain the geologic sections, especially where there is a lack of well data. The profiles were mostly used to locate the depth of the basin-fill sediments but could not be used to accurately locate the major structures within the DVFZ due to the complicated structure and its steeply dipping nature. Sections A and B that extend parallel to the DVFZ utilize corresponding segments of the profiles SRC-1N and SRC-1S as well as line 101. Seismic profiles SRC-3, Line 102, Line 9 and portions of Line 104 are used for the sections perpendicular to the DVFZ, sections C-H, respectively. The seismic profiles show a very high level of correlation with the geologic sections as expected because the profiles were used to constrain the depth to basement where well data is absent. The correlation between the profiles and the other corresponding geoscience data can be found in Plates 1 and 2, respectively. The depth of the basin-fill sediments in the gravity/magnetic inferred lithology sections along section C-F also correlate well with the seismic reflection interpretations.

### *Stress Data Sets*

Stress has been proven to be a difficult parameter model and assess. A coulomb stress model described in [Section 7.2.2](#) used the available slip constraints and orientations on the major fault ruptures to model the expected stress change and strain on a given fault orientation and dip within the 500m by 500m cell resolution. The modeling procedure and results can be found within Appendix 13 and show that areas of dilation correlate with producing wells. Results from borehole stress studies agree with the Coulomb Stress model. Other stress parameters considered was the localized dilation and compression zones resulting at structural intersections and the calculated parameter vertical stress, used in the exploratory geostatistics ([see Section 7.4](#)).

### **7.3.2 Wellfield Correlation of Geoscience Data Sets**

In an attempt to correlate the various data sets in Dixie Valley, cross-sectional data occurring within the DVGW has been directly compared to modeled geophysical data in the area. The generalized geologic and associated thermal sections (see [Section 2.1.1](#) for a detailed stratigraphic discussion, [7.3.1](#) for a summary stratigraphic discussion, and Plates 1, 2 and Appendix 12 for the geologic sections) provide a basis for a correlation analysis that compare

the sections with MT 2D models and 2 ½ D gravity/magnetic models. Other datasets included in the qualitative correlation analysis are associated interpreted seismic reflection profiles, and geophysical modeling of Vp in the vicinity of the wellfield (Plates 1 and 2). This qualitative correlation analysis is complemented by a quantitative statistical analysis discussed in [Section 7.4](#).

### *Geologic Sections*

The majority of the data occurred along sections lying perpendicular to the DVFZ (striking around N45°W) in the vicinity of the wellfield. These sections (C-H), can be directly compared with four seismic reflection profiles, three MT arrays (N, C, S), and combined gravity and magnetics modeled along lines C-F that infer the expected stratigraphy and structure at depth (Plate 1). The two sections with a northeast strike lying parallel to the DVFZ, sections A and B, compare the geology and thermal sections, segments of available seismic reflection profiles, and the combined gravity/magnetic inferred stratigraphy models along the respective lines (Plate 2). A detailed discussion on the geologic and thermal sections discussed in [Section 7.3.1](#) can be found in Appendix 12, which lists the various assumptions and inferences used to construct the sections.

The geologic sections were found to correlate well with the MT profiles and the combined gravity/magnetic sections. General observations among these sections are (1) the MT profiles show a high level of correlation with the interpreted structure as shown in the geological sections, (2) a vertical-trending low resistivity zone seen in the three MT profiles within the valley most likely reflects a major alteration zone correlating with a set of north-trending structures, (3) the gravity/magnetic profiles reflect the interpreted generalized geology, and show the magnetic signature of the Jurassic mafic rocks doesn't extend through this major north-trending intra-valley structure and is locally not present within the DVFZ, (4) the areas of elevated temperature (geothermal cells/system/resource) occur at the intersection of these earlier north-trending structures and northeast trending segments of the piedmont fault ([Figure 49C](#)).

The following details the correlations found between the different geoscience data sets on a cross-sectional basis. Four sections are included in this summary (C-C', D-D', E-E' and F-F') due to their variety of geophysical data to compare with the geologic sections (Plate 1). For individual cell<sup>4</sup> references, refer to Plate 1 as a grid with 500 meter spacing was overlain on the cross-section data for gridding and reference purposes. The horizontal scale is numbered with cell 1 starting at the NW end of the sections, while the vertical scale is lettered from A-L, starting with A that represents the cell from 2.0km to 1.5km asl. A table highlighting all significant correlations between the various data-sets is included as Appendix 14.

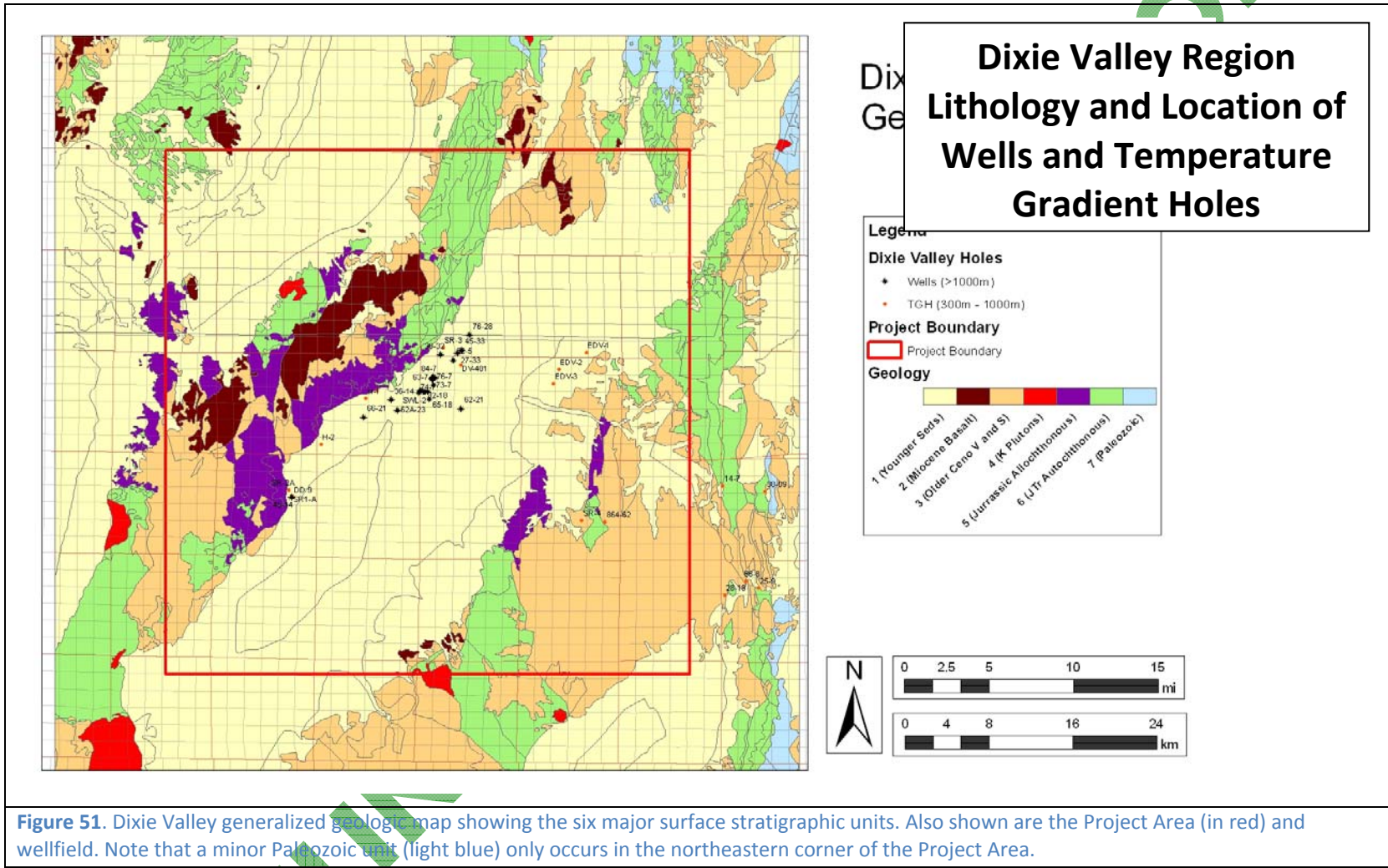
#### *Cross-Section C-C'*

Select geoscience data for section C-C' is shown in detail in [Figure 52](#). This figure exemplifies the qualitative correlation and cross-correlations found between the geology, thermal, MT, and gravity/magnetic lithologic model. The section transects through the hot, low-permeability wells within the DVPP ([Figure 48](#)), south of the producing field. Elevated temperatures are found

---

<sup>4</sup> All available geoscience data has been gridded in 500m x 500m size blocks for quantitative analysis and EGS Favorability Mapping.

ODEL



BASELINE

along both major faults within the DVFZ, expectedly due to convective fluid flow from depth. The main striking correlation is found along this section is between the geologic and resistivity model (top section in [Figure 52](#)). The resistivity distribution reflects the steeply dipping, multi-fault model for the DVFZ as the range-front and piedmont faults projected at depth tightly bound bodies of significantly higher resistivity within their respective footwall blocks. Modeled resistivity above around 500 ohm-m correlate with the interpreted location of the Cretaceous granodiorite (Kgr), a suitable rock type for EGS. A near surface zone of lower resistivity within the Stillwater Range projects where there is range-front fumarolic activity present at the surface (Section 10 fumaroles) and infers hydrothermal alteration at shallow depth. Additionally, a major NS-trending structure coincides with a vertical-trending low resistivity zone in the valley and with the termination of the magnetized Jurassic rocks (Jg). The Jg magnetic signature is also non-continuous though a portion of the DVFZ adjacent to the geophysical trace of the piedmont fault, and inferring hydrothermal alteration. The gravity- magnetic model shows multiple faults comprising the DVFZ (see cells 2-4) which is likely the case, although the structures (colored red) are placed in the model to bound discontinuous segments of the Jg unit.

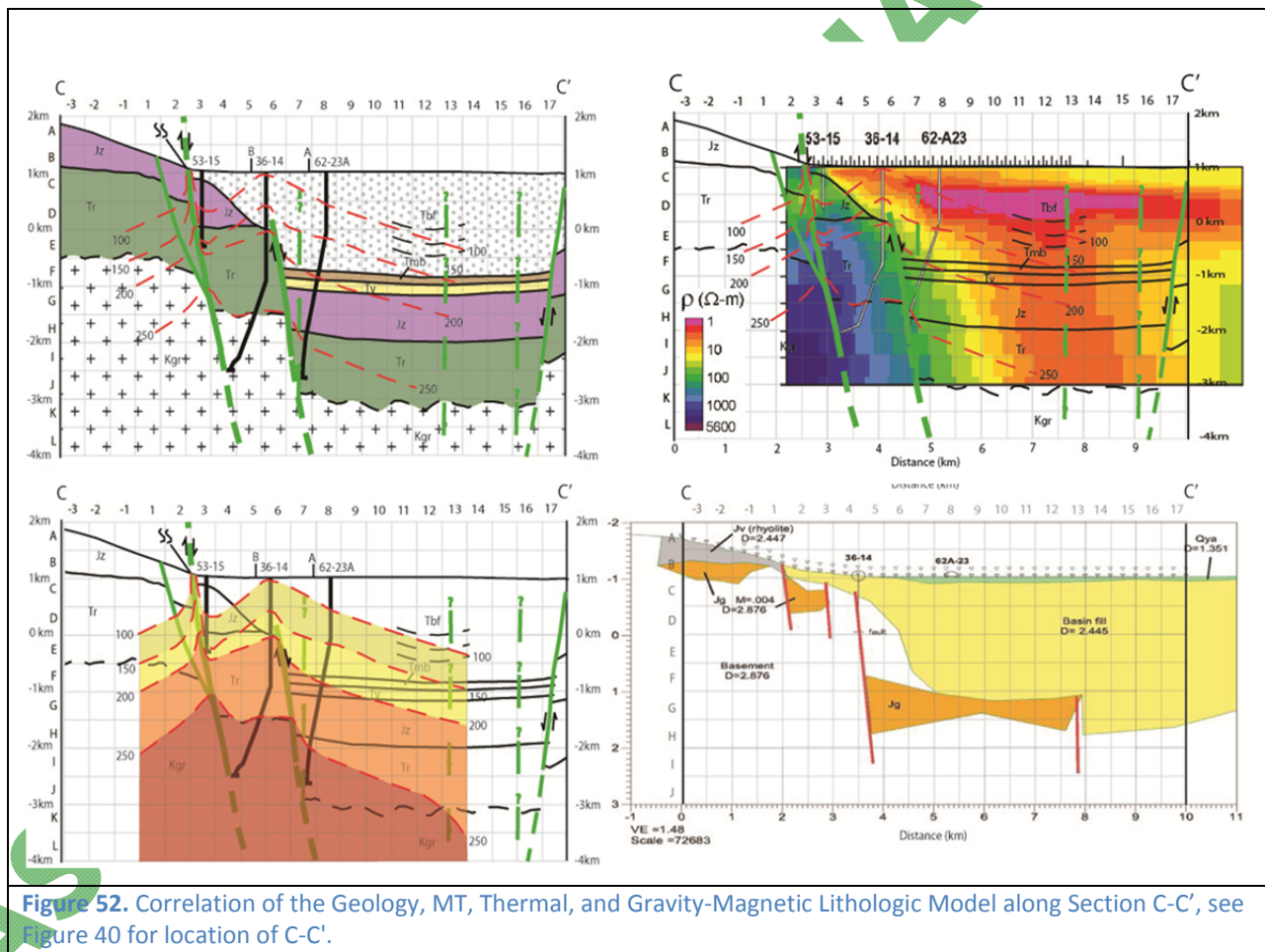


**Figure 52.** Correlation of the Geology, MT, Thermal, and Gravity-Magnetic Lithologic Model along Section C-C', see [Figure 40](#) for location of C-C'.

### Cross-Section D-D'

This section transects through the main injection zone (Lamb Ranch/Section 18, see [Section 6.2](#)) for the producing field. Significant correlations and lack thereof are listed below:

- The piedmont fault occurs in the same location in the geologic models, seismic reflection profile (Line 9/104), and within the gravity-magnetic model.
- Correlation between the volcanics (Tmb and Tv) is poor between the geologic inference and seismic reflection profile as the interpreted reflectors representing the basalt and basement horizons are thicker than the expression in the geologic sections.
- Gravity-Magnetic section intra-range structure correlates with a known surface fault in the Stillwater Range.
- Termination of Jg and bounding structure coincides with major NS-trending structure.
- Occurrence of magnetic rocks (Jg) in the vicinity of the main injection zone is much thicker than the known Jurassic rocks encountered in the wells.

### Cross-Section E-E'

This "key" section has the most variety of geoscience data and extends through the Section 7 production wells adjacent to the power plant ([Figure 53](#)). The area of very high resistivity (above 1000 ohm-m) beneath the Stillwater Range along Array C has been attributed to the presence of relatively unaltered bodies of Cretaceous granodiorite at depth. Interestingly, the body lies a few kilometers NW of the range-front fault in contrast to the relationship found in Array S and appears to be bounded by a major intra-range steeply dipping fault that coincides with a recognized surface fault. This fault is shown as a moderately dipping (~65°) lower resistivity zone (~100 ohm-m) occurring around 1-2km (3300-6600ft) range-ward of the projection of the current range-front fault and infers significant hydrothermal alteration and/or thermal fluid bearing structures along this intra-range structure. Other correlations found along Section E-E' are:

- The extended region of relatively low resistivity northwest of the range-front fault along Array C coincides with a region of extensive parallel to subparallel faulting to the range-front fault ([Figure 14](#) and [49A](#)). Fault structures (steeply dipping resistivity zones) suggested in the resistivity profile in this region appear to correlate with the area of extensive surface faulting.
- Interestingly, a relatively higher resistivity block along the range-front fault segment of the DVZ that extends into the main production zone near the Section 7 wells appears to correlate with the geothermal reservoir.
- The seismic reflection profile (Line 6) and the gravity-magnetic model infer multiple west-dipping faults bound the SE edge of Dixie Valley.
- The magnetic Jurassic rocks (Jg) occurring with the zone of step-faulting on the SE end of the section coincide with the geologic interpretation and surface mapping.
- A N-trending structure tightly bounds the higher resistivity present below the geothermal reservoir (see gridded cells G11-L11).
- The vertically-trending low resistivity zone in the valley correlates with the absence of magnetic Jurassic mafic rocks (Jg), referred to as a sub-unit Jznm (non-magnetic Jurassic rocks).

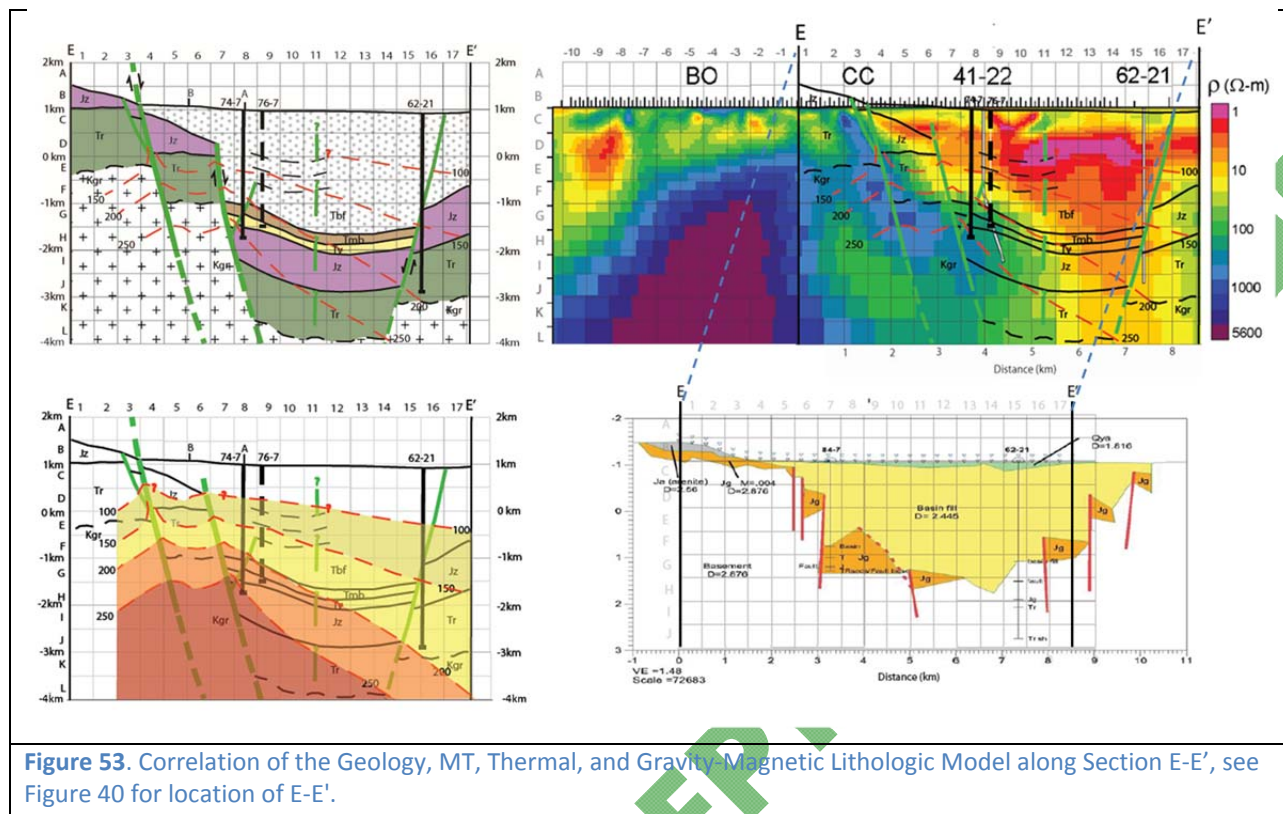


**Figure 53.** Correlation of the Geology, MT, Thermal, and Gravity-Magnetic Lithologic Model along Section E-E', see Figure 40 for location of E-E'.

### Cross-Section F-F'

The section F-F' correlates with Seismic Line 102, MT array N, injection well 38-32, and the area between production zones with the Section 7 wells to the south and the permeable Section 33 wells to the north. Some correlations found not identified in the previous sections are:

- The magnetic Jurassic rocks (Jg) are discontinuous and do not occur in the area of the low resistivity, vertically-trending MT structure and within the DVFZ. The missing Jg is referred to as Jznm, see [Section 8.6.1](#).
- Along Array N, a prominent fault occurring within the zone of step-faulting that bounds the eastern edge of Dixie Valley coincides with a sharp resistivity break.
- Range-front fumarolic activity present at the surface along Array N (Senator Fumaroles) show a correlation with a near surface zone of lower resistivity within the Stillwater Range.

### Summary of Cross-Sectional Correlations

Overall, a high-level of correlation between the various geoscience data-set is found along the four sections (C-F) perpendicular to the DVFZ and transecting through the producing field. The highest temperatures found along Section C and F coincides with the intersection of NS trending structures with the NE trending structures of the DVFZ. Major structural discontinuities within the Stillwater Range that bound segments of the magnetized Jurassic section (Jg) correlate with both an area of dense intra-range faulting and shallow lower resistivity structures shown the MT data, particularly along Array C. The distinction between magnetic and non-magnetic Jurassic rocks (Jg and Jznm) between the geologic and gravity-magnetic sections correlates with the vertically-trending low resistivity zone in the valley and the DVFZ, as non-magnetic rocks occur within the two structures. The authors herein suggest that hydrothermal alteration within the DVFZ and an intra-valley structure identified by the MT data has de-

magnetized the Jurassic mafic rocks. A summary of the correlations found with the Gravity-Magnetic and Resistivity (MT) models are found below.

#### Correlation with Gravity-Magnetic Models

The gravity/magnetic inferred geology show an excellent correlation with the geologic and MT sections constructed independently along the same section lines (Plates 1 and 2). All three data sets evidence multiple and complex faulting in the DVFZ as interpreted structures bounding the distinct magnetized Jurassic mafic rocks (Jg) are steeply dipping to near vertical. The gravity-magnetic sections (C-F) all show another small piedmont fault splay in the DVFZ between the range-front and previously mentioned piedmont fault. The occurrence of the magnetic Jurassic units (Jg) was a very sensitive parameter in the gravity/magnetic modeling and the resulting modeled sections show a good correlation with the expected Jurassic unit in the geologic sections. The discontinuous nature of these mafic rocks along the gravity/magnetic sections is attributed to demagnetization of these rocks most likely resulting from hydrothermal alteration in the area of the DVFZ and altered/conductive rock in the region of the low resistivity zone identified by Wannamaker et al. (2006; 2007) in the valley (see discussion above).

- The basement depth and occurrence of basin-fill sediments (Tbf) within the Gravity-Magnetic sections correlates with the geologic sections and the seismic profiles;
- The Gravity/Magnetic models show more structures than are shown in the geologic sections:
  - Imply the structures are steeply dipping (85-90°)
  - Show multiple piedmont faults in the DVFZ
  - Imply a zone of step-faulting bounds the southeastern edge of Dixie Valley; and
- Major intra-valley structures bounding the magnetized Jurassic rocks along the modeled sections occur in approximately the same position as the N-trending structures within Dixie Valley identified by Smith and Blackwell (2001).

#### Correlation with Magneto-Telluric (MT) Resistivity Data

Plate 1 presents the three MT profiles reported by Wannamaker et al. (2006; 2007) with the associated geologic and thermal sections (generated in this study) superimposed (see also [Section 3.4](#) and [Figures 16B-16D](#)). Arrays S and C, and their correlated geoscience cross-sections are shown in [Figures 52](#) and [53](#), respectively. A high level of correlation is found between the MT profiles and the associated geology sections and associated structure. A vertical-trending low resistivity zone extends to a depth of at least 10 km along Array C and also occurs beneath the valley along all three arrays. This feature correlates with (1) the occurrence of N-trending structures (faults) along Arrays S and C, while no such direct correlation can be found along Array N and (2) missing magnetized Jurassic rocks (Jznm) in the gravity/magnetic models (Plates 1 and 2, [Figure 15B](#) and discussion above). This low resistivity feature is not considered an active thermal feature but rather interpreted as a major ancestral alteration zone as temperatures reported from 62-21 are low with respect to the producing geothermal system (maximum of 184°C [363°F]) upwelling along the DVFZ. Other correlations found are:

- A lateral body of very low resistivity (1-5 ohm-m) occurring in the shallow subsurface at a depth of ~500m (1600ft) occurs within all three MT arrays. This may correspond to a conductive layer within the basin-fill sediments, an aquifer showing the lateral flow of geothermal fluids mixing with groundwater, or a depth to the water table. Coincidentally, a low resistivity zone of alteration extending at depth occurs below this near surface feature; and
- High resistivity below the Stillwater Range (>2000 ohm-m) may infer the presence of apparently unaltered granodioritic plutonic bodies.

Further delineation of geoscience relationships with the modeled resistivity data and expansion of these identified relationships within the DVGW is expected to be achieved after the more detailed MT survey under Task 4 is completed and interpreted. Additional questions to be addressed are (1) the potential

causes for the dramatic changes in MT resistivity at depth, and (2) the apparent correlation between dipping resistivity structures and inferred fault structures. [Table 5](#) presents the interpreted MT resistivity data relative to the geology and expressed in the sections.

**Table 5.** Correlation of the geology and MT data shown in Plate 1.

Unit	Class	Value (ohm-m)
Valley-fill sediments	Low Resistivity	<<100
Clay-rich/altered alluvium	Moderately conductive	<3-5
Basement/highly altered alluvium	Moderately High Resistivity	100
Jz and Tv sections	High Resistivity	100-500
Intrusive plutons (Kgr)	Very High Resistivity	>1000
Altered geothermal fluid zones	Low Resistivity	5-50

## 7.4 Quantitative Geoscience Correlations: Geostatistics

A variety of exploratory geostatistical techniques were applied to select geoscience parameters to (1) quantify the qualitative geoscience relationships described in [Section 7.3](#), (2) test relationships independent of the qualitative geoscience correlations, and (3) explore if statistically quantified parameters can be used in the generation of the baseline EGS Favorability Maps ([Section 8](#)). Described below is the quantitative geostatistical analysis methodology.

### 7.4.1 Database, Parameters Description, and Gridding

The following steps were taken to prepare the data for geostatistical analysis (also see [Section 8.2](#)):

1. constructing a geostatistical database to store and manage the data;
2. identifying which geoscience parameters were appropriate to perform statistical analysis including but not limited to considering the resolution of the data; and
3. gridding the data within the Calibration Area<sup>5</sup> to place it in a form that each data set could be compared.

#### Constructing the Geostatistical Database

The overall project had a number of challenges with respect to data management and manipulation. Its scope was such that a large amount of data was going to be acquired, produced, and interpreted from a number of different sources. The project required a method for storing, managing, and updating these various data sets at almost its onset. Basically, all data used for the geostatistical analysis was stored and managed using *Microsoft EXCEL*. The data was (1) transferred into the GIS database for storage, use for EGS Favorability Mapping, and determining qualitative relationships and (2) provided to the Geostatistics Task Leader who then imported the data into a statistical program (e.g., *JMP Pro* by SAS; *RStudio*) for analysis. Appendix 15-Tables 15-1 through 15-11 present the data used for the geostatistical analysis.

#### Description of Parameters

A list of all the data parameters as well as a description of all characteristics of the geoscience parameters used in the geostatistical analysis is presented in Appendix 15. A description of the various tables follows:

<sup>5</sup> The Calibration Area was chosen as the DVGW because it is the only region within the Project Area that has wells with known properties (e.g., temperature) that will allow calibration of the data generated.

- Appendix 15-Table 15-1 presents a summary description of the various data available to this investigation;
- Appendix 15-Table 15-2 presents the type of geoscience parameters considered for the geostatistical analysis including but not limited to the individual parameter resolution;
- Appendix 14-Table 15-3 describes the assumptions in the construction of the geologic and temperature sections; and
- Appendix 15-Tables 15-4, 15-5, 15-6, 15-7, 15-8, 15-9, 15-10 and 15-11 describe the lithology, well, seismic, gravity/magnetics modeling, MT parameters, temperature, Coulomb Stress Change modeling, and geochemical parameters, respectively.

Note that geochemical data was not used in the geostatistical analysis because of its limited geographic distribution and it was considered a point source nature.

Geostatistical exploratory data methods were applied to a variety of preliminary geoscience parameters (Appendix 15-Table 15-2). Task Leaders (see [Section 1.4](#)) provided potential parameters (numerical, a discrete numerical value and categorical, a descriptor for a parameter, e.g., lithology) derived from their respective field and/or models. The purpose was to create a baseline data-set that has been used to develop the Baseline Conceptual Geothermal Model and to quantify any statistical relationships between the various parameters. These quantified relationships could then potentially corroborate using the parameters to predict rock type, temperature or stress conditions, and/or provide additional sub-parameters that could be used in the generation of the EGS Favorability Maps. These sub-parameters would be used in conjunction with the major three parameters determined crucial to infer conditions suitable for EGS. The parameters are analyzed both qualitatively and quantitatively using geostatistics.

Typically geostatistical analysis is conducted on measured parameters. However, the data types available to this investigation are either measured, modeled/calculated, assigned or inferred (Appendix 15-Table 15-2) based on SME and have varying resolution. This is **not an ideal case for geostatistical analysis**. A fundamental assumption applied here is that while the exploration data set is statistically not ideal, and some parameters are more reliable than others, the data can be used to determine statistical significance. The validity of this assumption rests on the notion that whatever uncertainty exists in the different parameters can be thought of as a measurement error, and is at least from a practical standpoint, unbiased. Causal relationships for any statistical relationship identified herein have not been investigated.

The main geologic parameter is a categorical data-set, rock type. It divides the stratigraphy into seven units (Appendix 15-Table 15-1). There are four assigned parameters relative to rock type that include density, rock strength, internal friction, and EGS favorability that were inferred by the geology and stress Task Leader (Appendix 15-Table 15-4). Interestingly, these assigned numerical parameters allow lithology to be indirectly analyzed as numerical data. Other geologic parameters include vertical stress and fracture intensity, which are calculated (modeled) values. Additionally two stress-related parameters derived from a Coulomb 3.1 Stress Model are Coulomb Stress Change (CSC) and strain (Appendix 15-Table 15-10).

Parameters derived from geophysical models include a categorical data set, namely lithology inferred by the joint gravity and magnetic model (Appendix 15-Table 15-7). Temperature is considered the most important parameter for EGS and was derived from measured data in wells and temperature models along key sections indicated in Plates 1 and 2 (Appendix 15-Table 15-9). The MT parameter is modeled resistivity at depth along arrays extending through the wellfield (Appendix 15-Table 15-8). Seismic parameters from a combined UNR generated model of baseline data include P-wave velocity (Vp), S-

wave velocity ( $V_s$ ), density ( $\rho$ ), and attenuation of the P and S-waves ( $Q_p$ ,  $Q_s$ ) as indicated in Appendix -Table-15-6.  $V_p$  was considered the only seismic parameter with an adequate resolution to be used in the baseline analysis. The only other directly measured parameter, geochemistry from wells, production fluids, temperature gradient holes, fumaroles and springs, was not used in the statistical analysis due to limited data points and the data being essentially point source. These data represent the available baseline geostatistical data set.

### Gridding

The proposed plan for this project was to grid the entire EGS Project Area ( $50\text{km}^2$  [ $31\text{mi}^2$ ]). However, as the project proceeded we realized that the only area that can be calibrated was the DVGW because it was the only region where well (subsurface) data, in particular temperature, was available. As such, we focused principally on this region, referred to as both the DVGW and Calibration Area (see [Section 7.1.2](#) and [Figure 48](#)).

The Calibration Area was gridded (divided) into 500m by 500m cells to transfer the data into a consistent grid size for geostatistical analysis. A resolution of 500m (1640ft) was decided by the team to be an adequate resolution for the variety of data as a starting point. The first step was a qualitative analysis as selected cross-sectional data (lithology, temperature, MT and gravity-magnetic inferred lithology) was gridded along a pre-determined cross-section line. Section E-E' was gridded first, as a preliminary test, due to the variety of geoscience data located along the line and the proximity to the section 7 production wells. Once a qualitative correlation between the data-sets was established along section E-E', all other applicable data (e.g., seismic, MT, geochemistry, gravity and magnetics, etc.) was gridded along all six cross-section lines (A-F). The sections were divided into a 2-D grid of 500m by 500m cells from an elevation of 2km to -4km asl (6600ft to -13000ft asl). The valley floor of Dixie Valley is approximately +1km asl (3300ft), thus, a depth of -4km asl is at a depth of 5km (16,400ft). The reason the grid's upper limit is 2km instead of at 1km equal to the valley floor is to incorporate the geologic data within the Stillwater Range. For example, the upper row of gridded sections, is bounded at 2km above and 1.5km (4900ft) below, and while most of the cells occur above the surface as air, a portion of the Stillwater Range occurs above 1.5km asl elevation and thus has a corresponding value (lithology, etc.) for a respective cell. Plates 1 and 2, and Appendix 12 presents the sectional grids as shown within the digitized sections and an example of the gridding can be found in [Figure 52](#).

### 7.4.2 Exploratory Data Analysis

Only data gridded along sections C-C', D-D', E-E' and F-F' was used in the geostatistical analysis because they had the most varied and complete geoscience data and well control. Data was also gridded at 500m depth intervals with respect to wells to directly compare measured data (lithology logs, temp-depth profiles, etc.) with modeled geophysical data occurring within the intersection of the wellbore. Thus, two data sets have been used in the statistical analyses (1) **Section Data**, which includes all parameters gridded along cross-sections C-C', D-D', E-E', F-F' and the combined sections; and (2) **Well Data**, consisting of all directly measured data (temperature, lithology, faults, etc.) and all modeled data with respect to well location. These data sets can be found in the following Appendices 16a and 16b, respectively. To analyze the data, we conducted the following geostatistical analyses:

1. Correlation Analysis
  - a. global linear correlations between selected geoscience parameters along the section lines and the combined section data;
  - b. multivariate linear correlations by lithology per section and combined sections;
  - c. domain analysis by geographic/geologic sub-element along the sections (i.e., Stillwater Range, DVFZ, and valley); and

- d. Correlation Analysis using the Well data that explores the relationship between temperature and Vp (discussed below).
2. Residual and Multiple Regression analysis
3. Classification and Regression Tree (CART) analysis
  - a. Section Data; and
  - b. Well Data.

The results of the Correlation Analysis elements 1a through 1c are equivocal and are discussed in detailed in Appendix 17. This may be part due to the paucity of data available, equivocal results in the methods used, or the fact that geostatistical analysis of exploration data is inherently problematical. The “paucity of data” hypothesis will be evaluated in the assessment of the enhanced data set (see Tasks 4 and 5 description in [Section 1.1](#)). One correlation analysis that was found very interesting as well as significant to the project was the relationship between measured temperature in wells and modeled Vp data. This relationship is described and assessed below.

#### *Exploring the Temperature-Vp Relationship using well data*

One of the objectives of the proposed development of a calibrated exploration methodology has been to determine if seismic data could be used to predict rock type and/or temperature at depth. The baseline (existing data) assessment of the available seismic data with respect to Vp; Vs, S-wave velocity; rho, density of the rocks; Qp, attenuation of the P-wave; and Qs, attenuation of the S-wave, (described in [Section 3.5](#)) revealed that the baseline data resolution is not sufficient for any seismic parameter other than Vp. Presented below is an analysis of the measured temperature – modeled Vp-depth relationship. The first step was to create a correlation plot comparing measured temperature in a well versus the modeled Vp in the area around the well. Each data point represents a gridded 500m by 500m cell that contained both a temperature and Vp value and is coded by well ID and formation type in the grid to determine if the relationship was dictated by well location, lithology, or depth sampled.

1. A linear fit was applied to all data with a resulting poor r-square value ( $r^2 = 0.51$ ), see [Figure 54](#).
2. The best-fit line was determined to be skewed by shallow data (low Vp values) or values occurring at the approximate surface (1km asl [3300ft]). These values had a low resolution with respect to the baseline seismic model. Removing the surface slice Vp data found that a 2-degree fit to the remaining data had a slightly higher correlation;  $r^2 = 0.54$ , see [Figure 55](#).
3. Outlier data points corresponded to certain wells where the associated modeled Vp data had a very low confidence (trust) value (See Appendix 15, Table 15-6). Removing outlier wells (i.e., low seismic trust for Vp: 45-14, 53-15, 76-28, and 66-21) found a polynomial 2-degree fit to the data and a resulting  $r^2 = 0.73$ , see [Figure 56](#). Thus, by considering the seismic trust factor identified by Dr. Ileana Tibuleac, Project Seismic Team Leader (see [section 1.4](#)) and removing the seismic data for the surface layer, a much better correlation was detected. The regression equation that represents the relationship between temperature and Vp is shown in [Figure 56](#).
4. The data was also analyzed with respect to lithology to determine if another factor is influencing the Vp-Temperature relationship ([Figure 56](#)). Two trends can be observed from the plot relating to lithology. The data could be divided into a shallow domain within the basin-fill (QTbf) and a deep domain (depths of -1.0km asl and deeper) within the basement rocks. In general the QTbf increases in Vp with depth merging with the Vp of the basement rocks. This occurs around a Vp of 4.54 km/sec (10,200 mph).

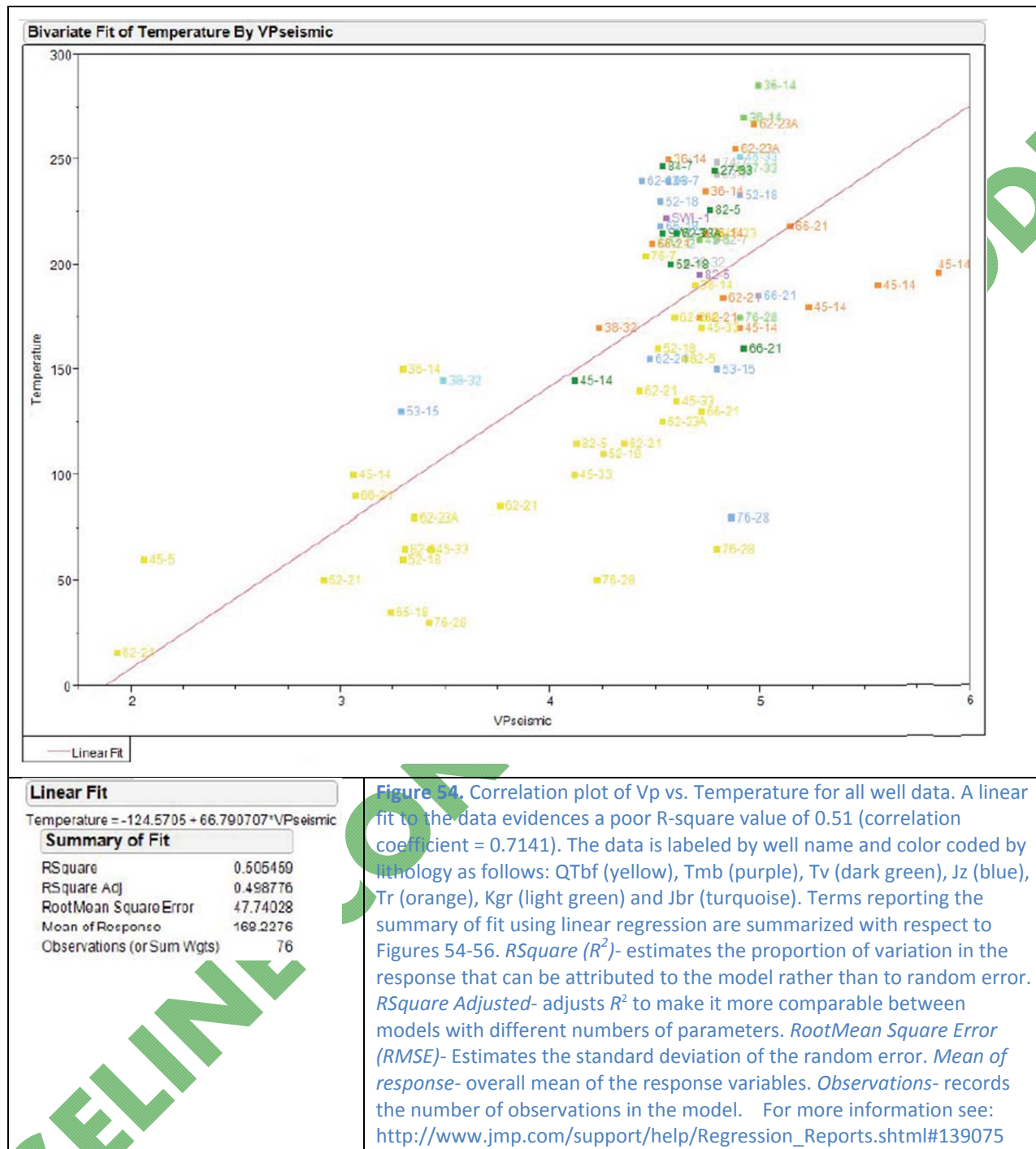
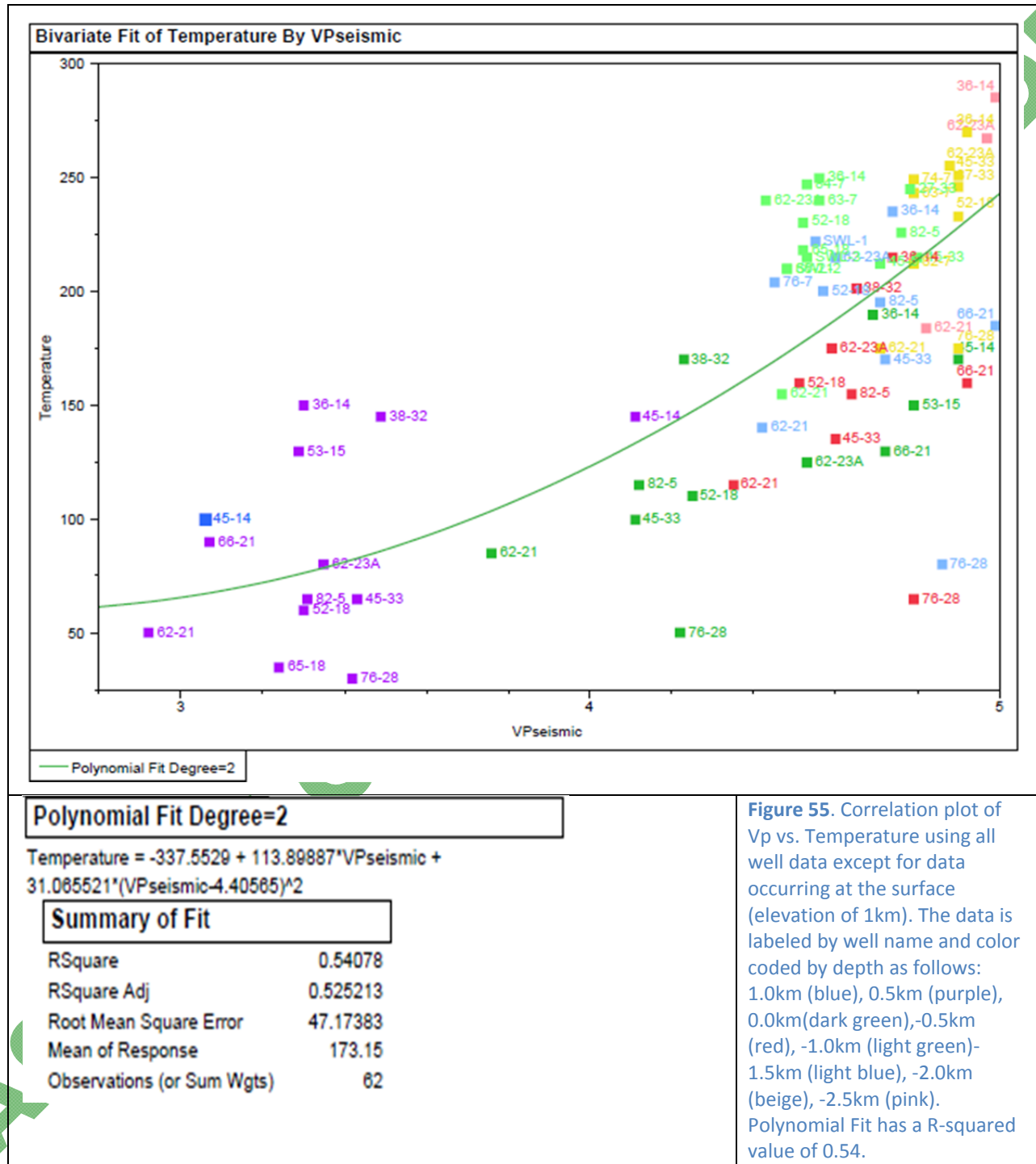


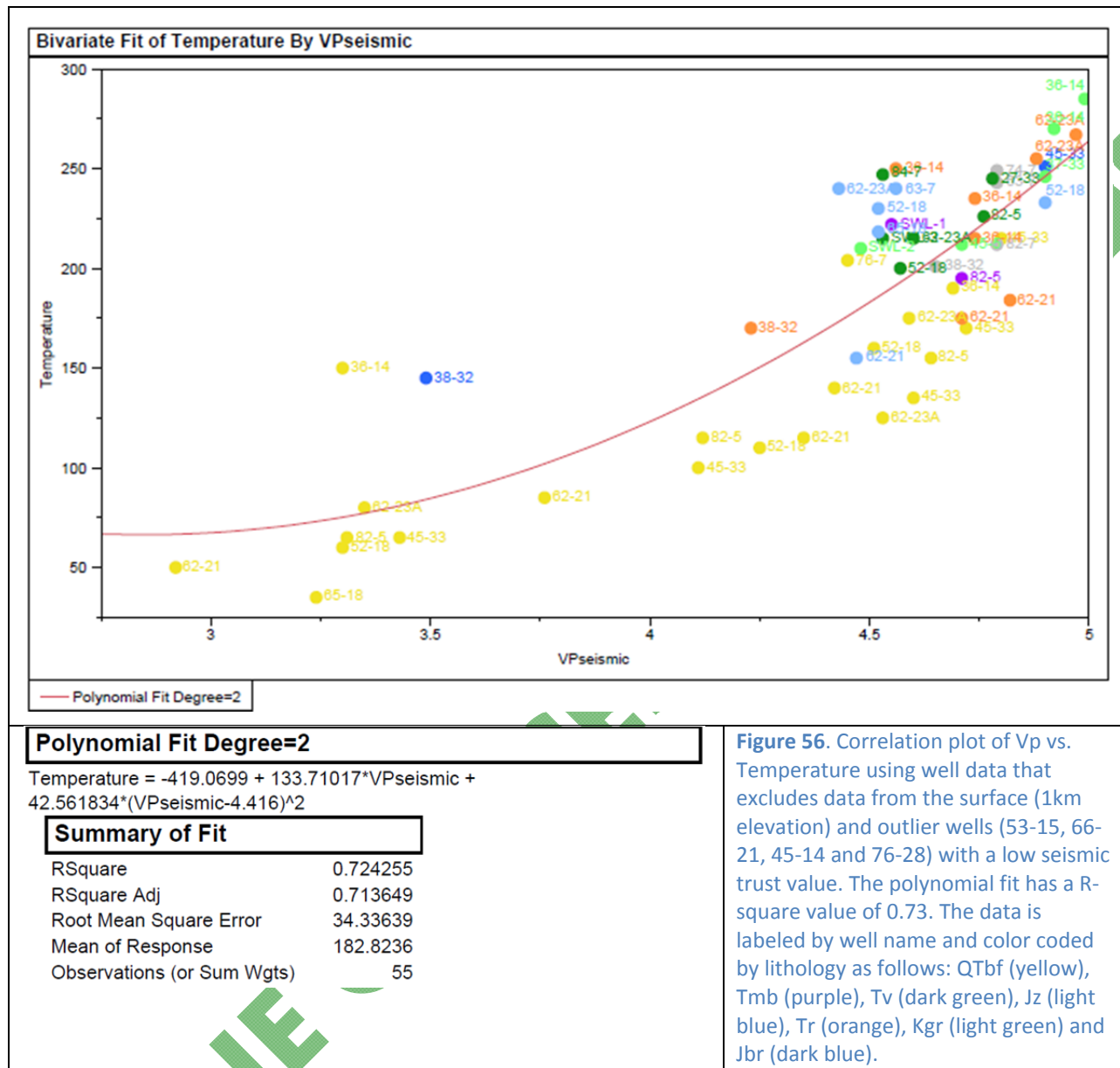
**Figure 54.** Correlation plot of Vp vs. Temperature for all well data. A linear fit to the data evidences a poor R-square value of 0.51 (correlation coefficient = 0.7141). The data is labeled by well name and color coded by lithology as follows: QTbf (yellow), Tmb (purple), Tv (dark green), Jz (blue), Tr (orange), Kgr (light green) and Jbr (turquoise). Terms reporting the summary of fit using linear regression are summarized with respect to Figures 54-56. *RSquare (R<sup>2</sup>)*- estimates the proportion of variation in the response that can be attributed to the model rather than to random error. *RSquare Adjusted*- adjusts R<sup>2</sup> to make it more comparable between models with different numbers of parameters. *RootMean Square Error (RMSE)*- Estimates the standard deviation of the random error. *Mean of response*- overall mean of the response variables. *Observations*- records the number of observations in the model. For more information see: [http://www.jmp.com/support/help/Regression\\_Reports.shtml#139075](http://www.jmp.com/support/help/Regression_Reports.shtml#139075)

### Residual and Multiple Regression Analyses

In virtually all the correlation analyses described in Appendix 17, a consistent relationship has been evidenced between vertical stress, temperature, and Vp. We recognized that all three of these parameters generally increase with depth and potentially that may be the reason for the observed strong correlation. For example, since vertical stress is a calculated value relying on depth and the density of rocks overlying a respective cell, this parameter can be viewed as strong indirect inference to depth. Thus, a correlation of increasing temperature with increasing vertical stress could likely be an insignificant correlation. To evaluate this hypothesis, a residual analysis to remove the effect of depth

was conducted and is described below. Additionally, a detailed analysis that explores the relationship between the correlated parameters, temperature and P-wave velocity, and the effect that other variables such as density, depth, etc. may have on this relationship is described in [Section 7.4.2](#).





### Sectional Data

Figure 57 presents the global linear correlations for elevation (depth) and the selected geoscience parameters (fracIntens, vertStress, CSC, dilatation, temperature, Vp, Vs, and resistivity [MT]) for the combined sections (i.e., all cross-sectional data, see discussion above). Presented in this figure are both the correlation coefficients as well as the associated scatterplot matrices. The data suggests that linear and non-linear relationships exist between elevation and vertical stress, temperature, and Vp. *Note, however, that this is a two component analysis, e.g., temperature and depth, Vp and depth, etc.* The other parameters appear to have little to no relationship with elevation.

These identified relationships were further investigated analyzing the bivariate fit of temperature, vertical stress, and Vp by elevation, Figure 58, respectively. These three relationships show  $r^2$ -values of **0.90** (correlation coefficients of 0.9487), **0.89** (0.9434), **0.89** (0.9434), indicating, as expected, a strong relationship of the selected geoscience parameters with depth (i.e., elevation). The residuals of this

bivariate fit were calculated and shown in the lower portion [Figure 58](#). Next, the linear correlation of the key variables (temperature, CSC, dilatation, and resistivity [MT]) versus the residuals of vertical stress and Vp was performed ([Figure 59A](#)). No correlation coefficient greater than 0.7400 is observed, considered the cut-off value for being statically significant (E. Issaks, pers. comm., 2011). Interestingly, the MT parameter was determined to be slightly correlated with the residuals of vertical stress. This finding is supported by a multiple regression of temperature vs. the residuals conducted to examine the relationship between temperature and temperature predicted by the residuals of vertical stress, Vp, and Vs ([Figure 59B](#)). The  $r^2$ -value for this regression analysis is **0.19** indicating that temperature cannot be predicted by the residuals. Thus, the overall two component residual analysis indicates that depth (or elevation) is the only link between (1) temperature and vertStress, and (2) temperature and Vp. However, multiple regression analyses of temperature vs. key geoscience parameters was also performed. [Figure 59C](#) shows the result of using elevation, vertical stress, dilatation, Vp, and resistivity (MT) in predicting temperature, as well as the interaction among these parameters. The  $r^2$ -value for this multi-variable system is **0.94**. The predictor profiler in this figure illustrates the complex interaction of the geoscience parameters elevation, vertical stress, dilatation, Vp, Vs, and resistivity (MT). This multi-variable analysis clearly indicates that (1) the combination of a variety of geoscience parameters (described above) can be used to predict temperature and (2) there is a complex interaction between the geoscience parameters in this prediction. In summary, the residual analysis and the multiple regression (multi-variable) analysis had contrasting results.

#### Well Data

Multiple regression analyses were also applied using the well data set to determine if depth and temperature can be predicted from the seismic data (Vp) and other geoscience parameters. The analysis indicates that depth can be predicted from a combination of Vp and MT with a  $r^2$ -value = **0.76**, see [Figure 60A](#) for all well data, and temperature can be predicted from lithology, Vp and resistivity (MT) with a  $r^2$ -value = **0.85** using all well data excluding wells which have a low Vp trust factor ([Figure 60B](#)).

#### Precision of the Multiple Regression Results

Two statistical methods were used to evaluate the precision of the multiple regression findings, bootstrap, and cross-validation.

##### *Bootstrap Method*

The bootstrap technique involves taking a sample of equal size to the original dataset, with replacement, from the actual data (i.e.<sup>6</sup> from the empirical distribution). This sampling procedure is then repeated many times (10,000 in this analysis) and for each sample the original regression analysis was done, producing a new  $r^2$  value for each sample. The empirical distribution of these 10,000  $r^2$ -values enables calculation of a bootstrap confidence interval with endpoints at the 2.5 and 97.5 percentiles. 95% of the simulated  $r^2$ -values were between these two endpoints. The  $r^2$ -value measures the proportion of the variance of the predicted variable that can be explained by variables in the model.

One way the bootstrap method was used here was to compare different weighting schemes for the regression model based on the trust values assigned to each of the values of each variable. Large trust values correspond to values believed to be more accurate, so all the schemes considered weighted the high trust values more heavily. The three weighting schemes considered were:

---

<sup>6</sup> The confidence interval gives a range that is likely to contain a value that is being estimated. Traditionally, a confidence interval is determined analytically based on the theoretical distribution of the estimator. Out of every hundred 95% confidence intervals, about 95 should contain the true value being estimated. In order to avoid distributional assumptions (usually normality), a bootstrap procedure is used since it is based just on the empirical distribution observed in the data.

1. product of trust values for all variables in model.
2. sum of trust values for all variables in model
3. discard all data which has a below median trust value for any variable.

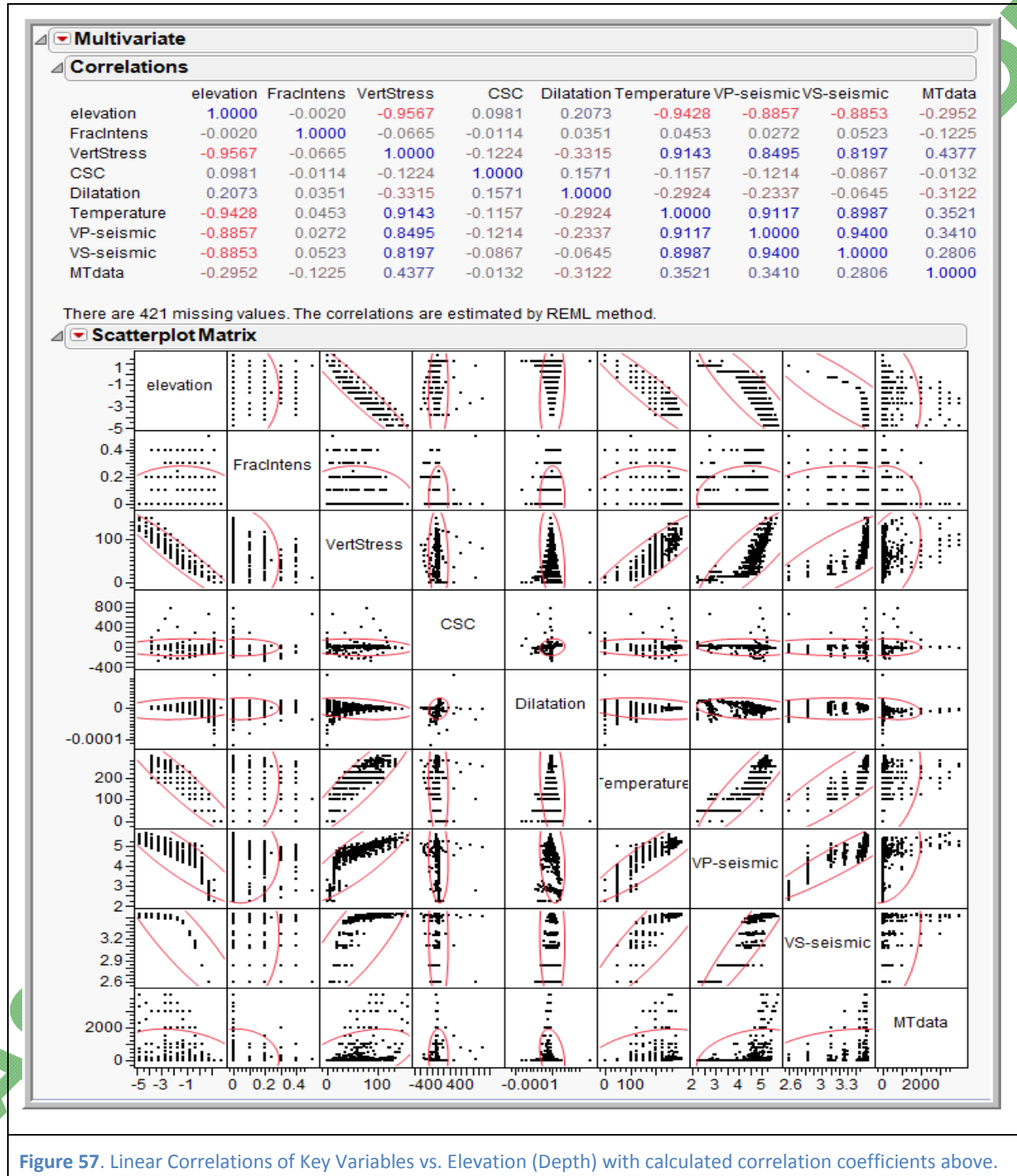


Figure 57. Linear Correlations of Key Variables vs. Elevation (Depth) with calculated correlation coefficients above.

For weighing scheme (1) and (2) above, the weighting procedure essentially treats the weights as the inverse of the variance for each observation. For example, if the trust values for temperature, dilatation, vertical stress, Vp, Vs, and MT were each 4 for a particular data point, then scheme (1) would weight this observation as  $4^6$  (or 4096) times more important than an observation with trust values of 1 for all those variables. Weighting scheme (2) would weight it  $4 \cdot 6$  (or 24) times. In weighing scheme (3), the median of each trust variable was found and any points strictly less than this value for any of the variables was simply thrown out. None of these weighting schemes performed better than regression analysis without any weights (see discussion above), and all the  $r^2$ -values were fairly close together. This is an indication that the data with lower trust values follow the same pattern as the high trust data. In addition to comparing the different weighting schemes and finding confidence intervals for the  $r^2$ -values, the values computed from the bootstrap method were used to consider whether elevation should be included in the model. Since elevation would not be relevant in eventual choice of a promising site, it is included in the model simply because it is related to temperature and thus perhaps should be controlled for. However, since vertical stress and other variables are highly correlated with elevation, inclusion of elevation is perhaps redundant. Leaving out elevation makes little difference in the  $r^2$ -value, supporting the idea that this parameter is redundant.

The 95% confidence intervals for each of these weighting schemes with and without elevation are shown in [Tables 6A](#) and [6B](#) and a summary discussion follows. The first line in each table corresponds to the model described in [Figure 59C](#). Investigations conducted are unclear why the  $r^2$ -values for this case presented in [Tables 6A](#) and [6B](#) (0.86 and 0.83, respectively) differ from that indicated in [Figure 59C](#), a  $r^2$ -value of **0.94**. Regardless, the outcome conveyed by a  $r^2$ -value of 0.94 or 0.86 is essentially the same: the model is able to explain quite a bit of the variability in temperature using these variables.

**Table 6A.** Results of the weighting analysis confidence interval determination using elevation in the parameters considered; [see text for an explanation.](#)

Weighting	Lower Bound	R squared est.	Upper Bound
None	0.84	0.86	0.88
Product of Trusts	0.83	0.86	0.88
Sum of Trusts	0.84	0.86	0.88
Discard Low Trust	0.78	0.83	0.88

**Table 6B.** Results of the weighting analysis confidence interval determination ignoring elevation in the parameters considered; [see text for an explanation.](#)

Weighting	Lower Bound	R squared est	Upper Bound
None	0.81	0.83	0.86
Product of Trusts	0.80	0.84	0.86
Sum of Trusts	0.81	0.83	0.86
Discard Low Trust	0.73	0.80	0.86

### Cross Validation

The technique of cross validation was used to assess how well the model would make predictions for data not in the model. This technique involves leaving out part of the dataset when fitting the regression model, then using the left out data to test the utility of the model in predicting temperature for data not used to fit the model. More technically, the dataset was divided into 10 parts, and the regression model was then fit 10 times, each time with one of the 10 parts left out. Then the  $r^2$ -value was computed as  $1 - (\text{variance of prediction errors}) / (\text{variance of temperature values})$ . Since every point in the data set was left out for one of these 10 regressions, each point has a prediction error and this  $r^2$ -value is actually

based on the same number of points. In general the  $r^2$ -value should be slightly smaller since the model wasn't influenced by the points for which the prediction errors were calculated. The cross validation was performed to verify that the model was successfully representing an actual relationship between the variables and not just a spurious relationship.

In addition, cross validation is useful in variable selection, particularly to avoid over-fitting, including variables which marginally increase  $r^2$ -values but whose relationship with the dependent variable does not appear to be anything more than random. The  $r^2$ -values computed based on the omitted data from the cross validation resampling were very similar to the original values, about 0.83, indicating that the model has validity in making predictions for data not used to fit the model. Furthermore, leaving out Vs and MT do not appreciably reduce the  $r^2$ -values, so those variables do not appear to add sufficient predictive ability to warrant their inclusion in the model. For the refined model based on predicting temperature using only vertical stress, dilatation, and Vp, the bootstrap 95% confidence interval for  $r^2$  is 0.81 to 0.85, with a center (actual estimated  $r^2$ ) of **0.83**. This is essentially the same model as the first line in [Table 6A](#) but with Vs and MT left out of the model.

The correlation analysis, performed by Dr. Ibsen, Project Geostatistical Task Leader (see [Section 1.4](#)), that explored the relationships between the geoscience parameters was also utilized to analyze the favorability-trust maps presented in [Section 8](#). The sensitivity of the favorability values to different weights (equal weighting compared to SME weights) was analyzed. We also considered using hierarchical modeling to assess the variability in the favorability maps in this Basien Conceptual Model. An intrinsic part of the hierarchical model is the quantification of the variability in the measurement and modeling of variables used in subsequent analysis. However, for several of the variables (e.g, MT resistivity), not much could be done that was not subjective. For other variables (e.g., gravity-magnetics), the variability could only be reasonably estimated by repeating the modeling process under different assumptions, and the modeling process itself is quite time intensive. As such, the hierarchical model was determined to be beyond the scope of the current project, especially given that the result would simply give another way to assess the variability in the favorability map without actually improving the results themselves.

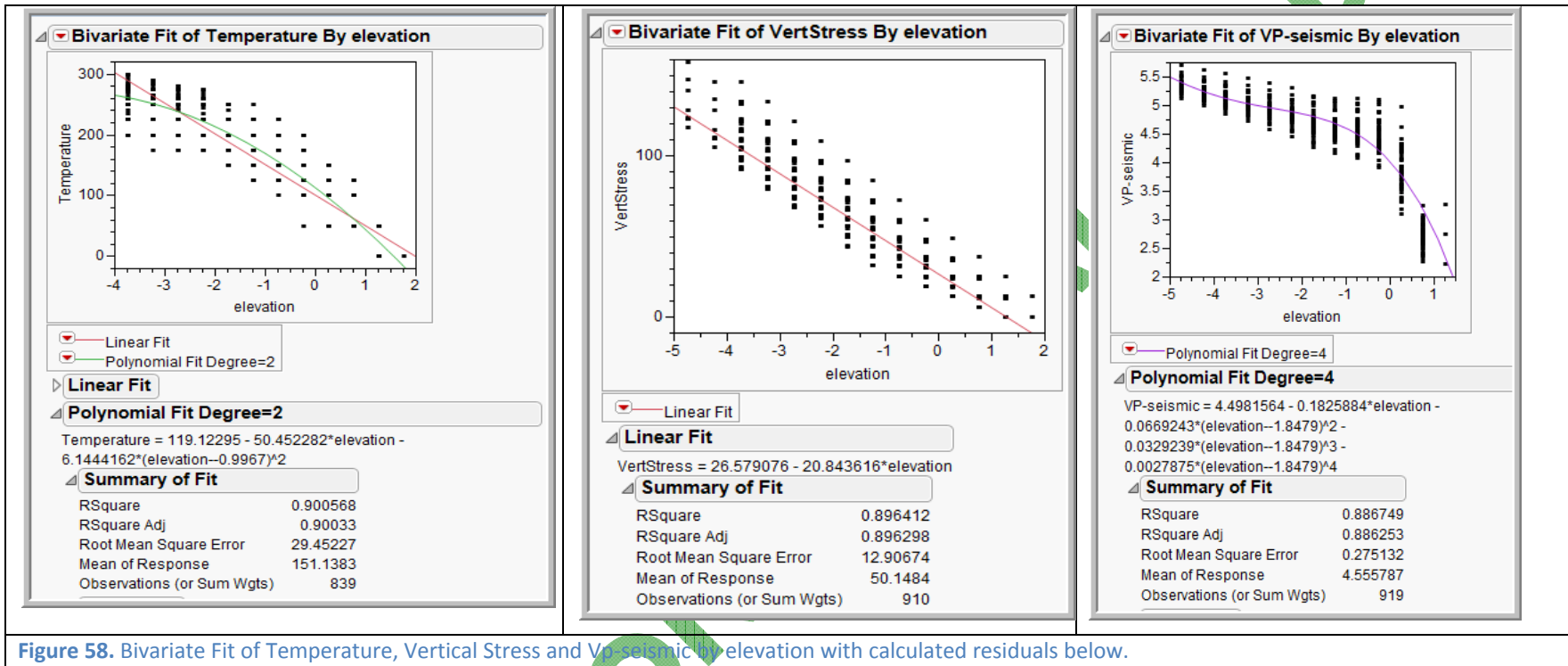
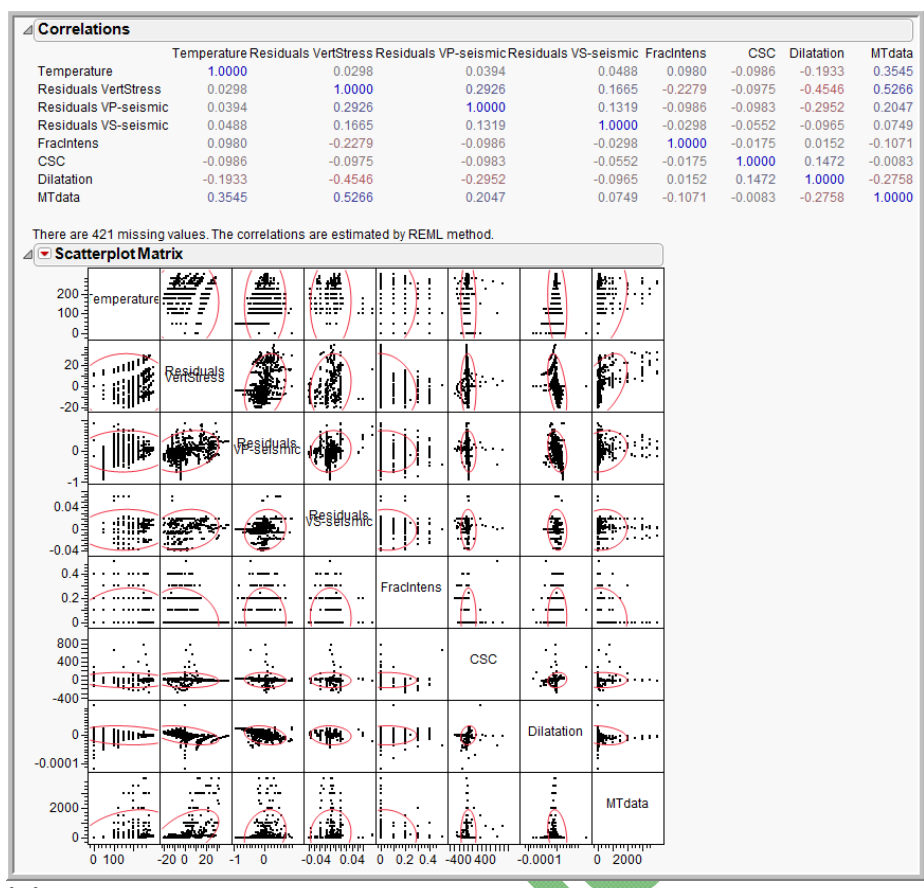


Figure 58. Bivariate Fit of Temperature, Vertical Stress and VP-seismic by elevation with calculated residuals below.

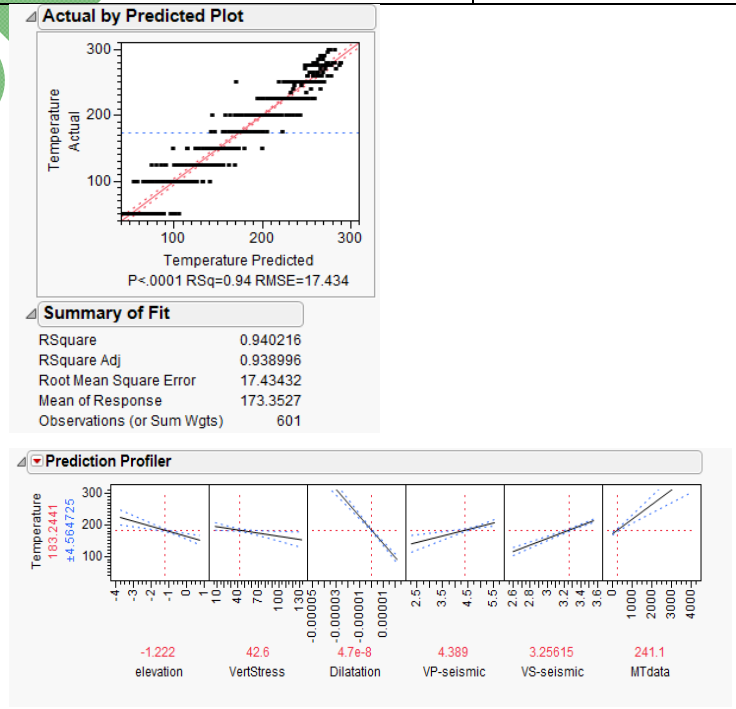
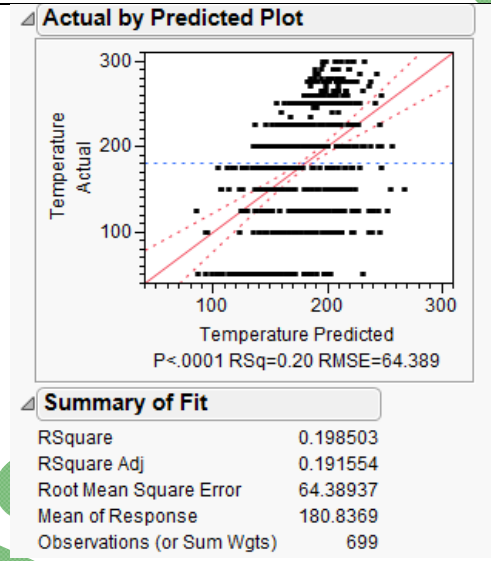


**Figure 59A.** (top) Linear Correlations of key variables vs. the residuals of Vertical Stress and Vp.

**Figure 59B.** (bottom left) Multiple Regression of Temperature vs. Residuals. A very poor relationship is found between temperature and residuals.

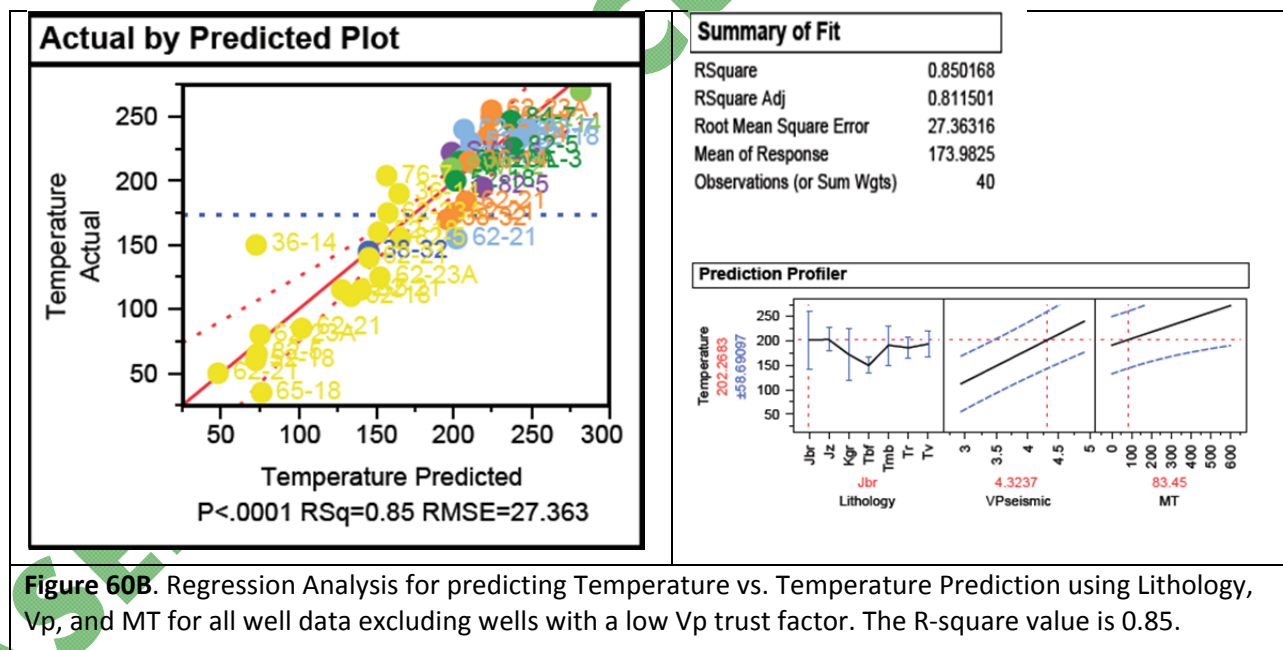
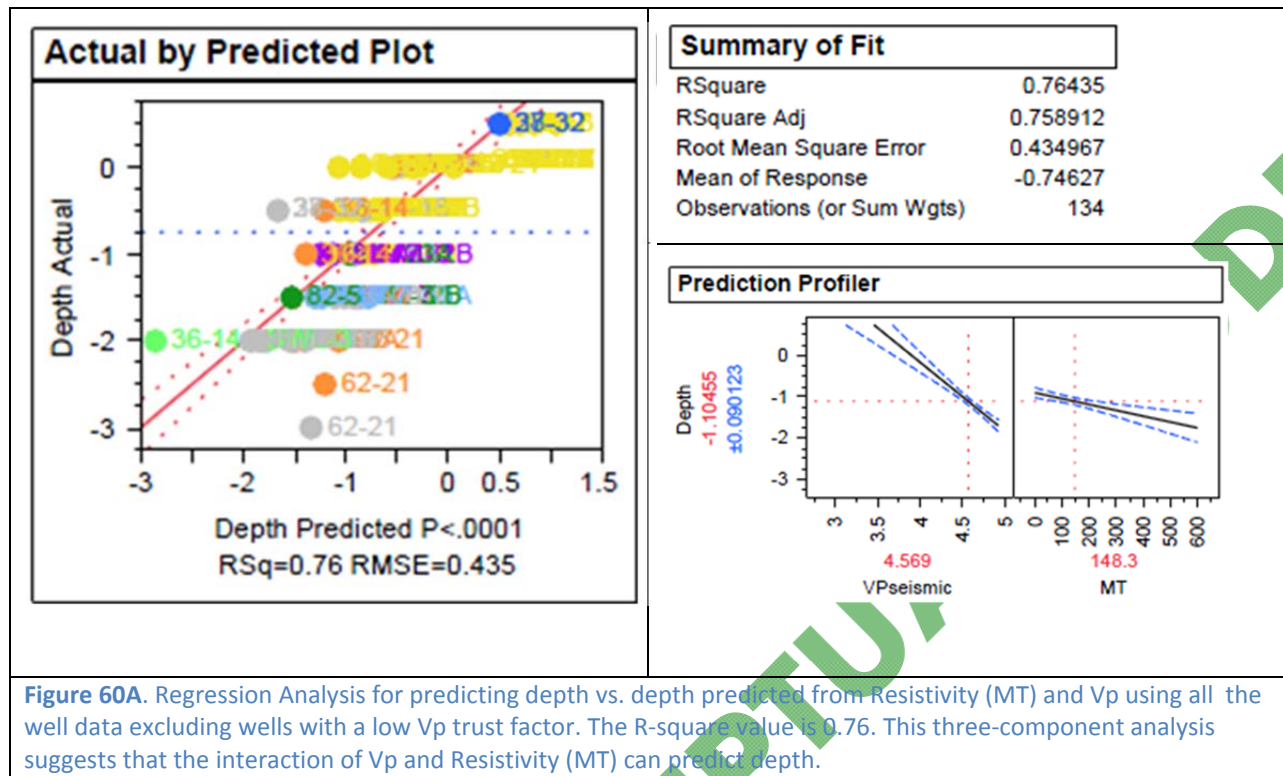
**Figure 59C.** (bottom right) Multiple Regression of Temperature vs. Key Variables.

(A)



(B)

(C)



**Vp-Temperature Relationship: Effect of Density and Depth**

The observed Vp and temperature relationship described in [Section 7.4.2](#) was found in the following analyses:

1. linear correlations along the cross-sectional data (Appendix 17);
2. multi-variate correlations with respect to lithology along the cross-sectional data (Appendix 17);

3. a direct correlation between the two variables using well data ([Figures 54-56](#));
4. multiple-regression analyses using both the cross-section and well data ([Section 7.4.2](#));
5. CART, [see Section 7.4.2](#); and
6. a geologic analysis, described herein and Appendix 18.

This relationship was explored further to determine if other factors (depth, density, etc.) were influencing or responsible for the empirically derived relationship including an analysis of the relationship with respect to depth, lithology or geologic formation, and well type. Selected results from this assessment can be found in Appendix 18.

### Geologic Analysis

The majority of the Dixie Valley wells lie within the convective heated portion on the DVFZ, while one deep well, 62-21 lies within the valley to the southeast, and is more indicative of the overall conductive regime. The previous analyses have used all the well data, indiscriminate of well location, with the exception of removing the selected wells that possessed low seismic trust values. The following analysis views the Vp data with respect to the two different domains to determine if increases in temperature and Vp with depth can be explained. By comparing Vp data within similar lithologies and at comparable depths within wells affected by the convective system to a purely conductive well, 62-21, one can analyze the Vp data independent of the influence from lithologic density or depth to determine if Vp values are different within the two domains. If Vp values are higher within the convective wells within the same lithology type at the same depth, and the temperature is significantly higher, it is inferred that the Vp values are affected by the convective geothermal system. Note that Vp should decrease with fracturing and fluid content. These factors are not considered in this analysis. The Lithology-Temperature-Vp-Depth relationship was analyzed and performed in two-parts using well data (1) per well compared to 62-21, a known conductive well, and (2) per lithologic formation. 62-21 was chosen as a "control" well as it was relatively cold compared to wells in the DVFZ, and intersected a varied group of lithologies. [Figure 61A](#) consists of a series of representative plots that show the Lithology-Temperature-Vp-Depth relationship for different wells, including the comparison to a purely conductive well, 62-21. Wells 66-21, 45-14, 53-15, and 76-28 were not included in this analysis, as these locations have low seismic trust values rendering the Vp data unreliable. The remaining wells with available data compared with 62-21 can be found in Appendix 18. The vast majority of wells show elevated temperatures and Vp values at comparable depths and lithologies when compared to 62-21 ([Figure 61A](#) and Appendix 18). The only exception is 62-23A, where at a depth of 2.5km (8200ft), Vp is slightly lower than 62-21 within the same lithology, even though the reported temperature is much higher.

Interestingly, a slight Vp decrease is found at depths of 2.5km for a number of wells ([Figure 61A](#)). This unexpected result occurred in the following wells: 36-14, 62-23A, 52-18, 65-18, SWL-1, SWL-2, and SWL-3 which consists of the DVPP area and the area of active injection within section 18. This could be a model interpolation effect, or could likely represent a decrease in Vp within the reservoir due to fluid content and/or fracturing. This also suggests that since Vp does not increase uniformly with depth, it further supports the observed empirical Vp-T relationship is not based solely on a function of depth.

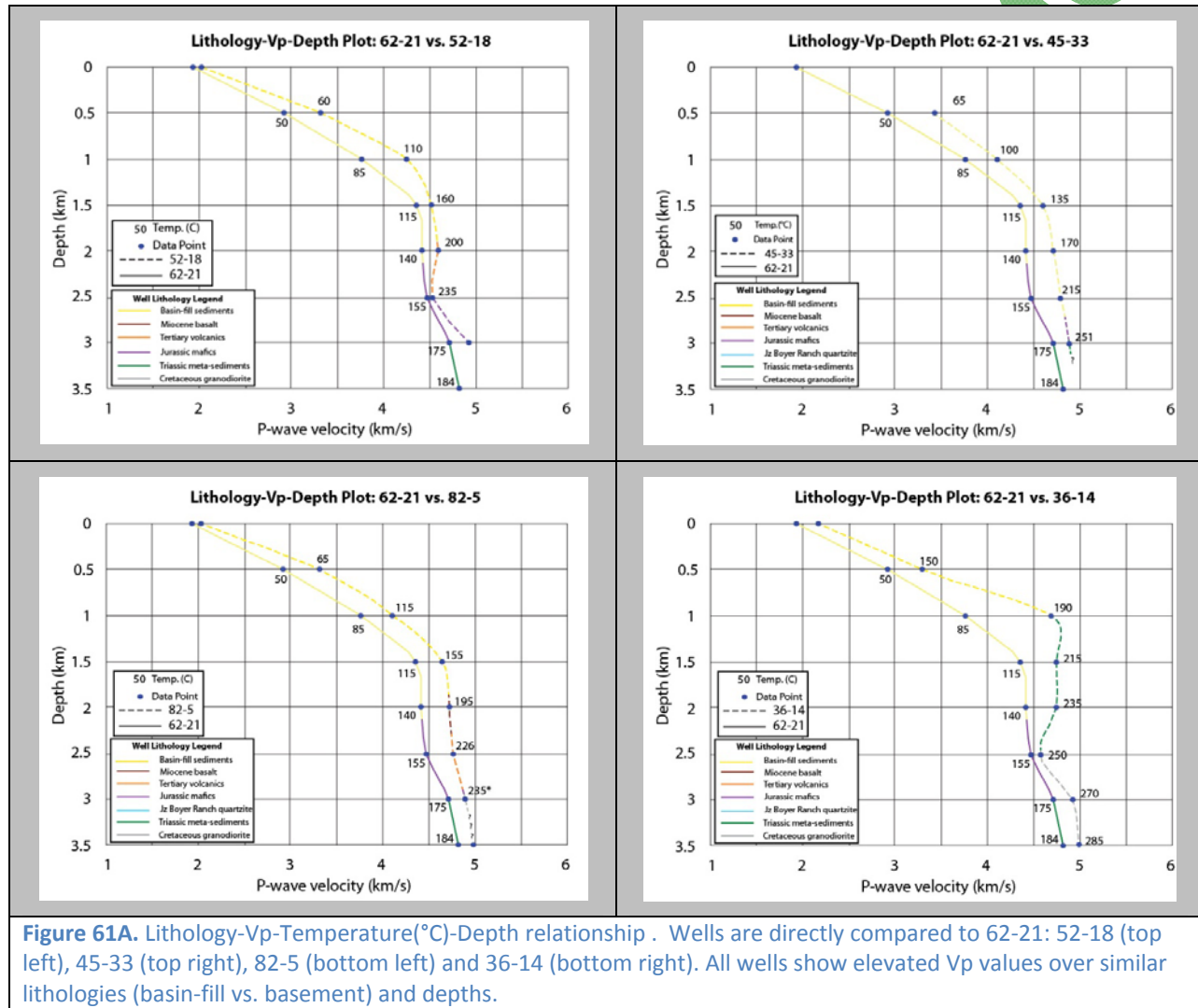
### Effect of Lithology and Depth

We recognized that both temperature and Vp are a function of depth and as such, continued evaluating this relationship both geologically and geostatistically.

The Vp data was plotted with respect to depth per the major lithologic formations identified in the geothermal wellfield and coded for temperature to determine (1) if the varied lithology, specifically the associated density (inferred by depth in this case), was a significant factor in the observed relationship,

and (2) the variation in temperature per a given depth and lithology. Data occurring at the surface and outlier wells with low seismic trust (53-15, 45-14, 66-21, and 76-28) were removed from the data set to be consistent with the previous analysis. A general relationship between Vp and temperature was observed within the basin-filling sediments (QTbf) at any given depth and over the depth range considered (Figure 61B), while the remaining formations had too few data points to produce meaningful results. For plots pertaining to all the major formations, see Appendix 18.

Within the QTbf, the effect of depth on the inferred Vp-temperature relationship was examined (Figure 62). A strong relationship was found only at a depth of 1km (0km asl), with a r<sup>2</sup>-value of 0.76. The remaining depths show no relationship, although this is based on limited data.



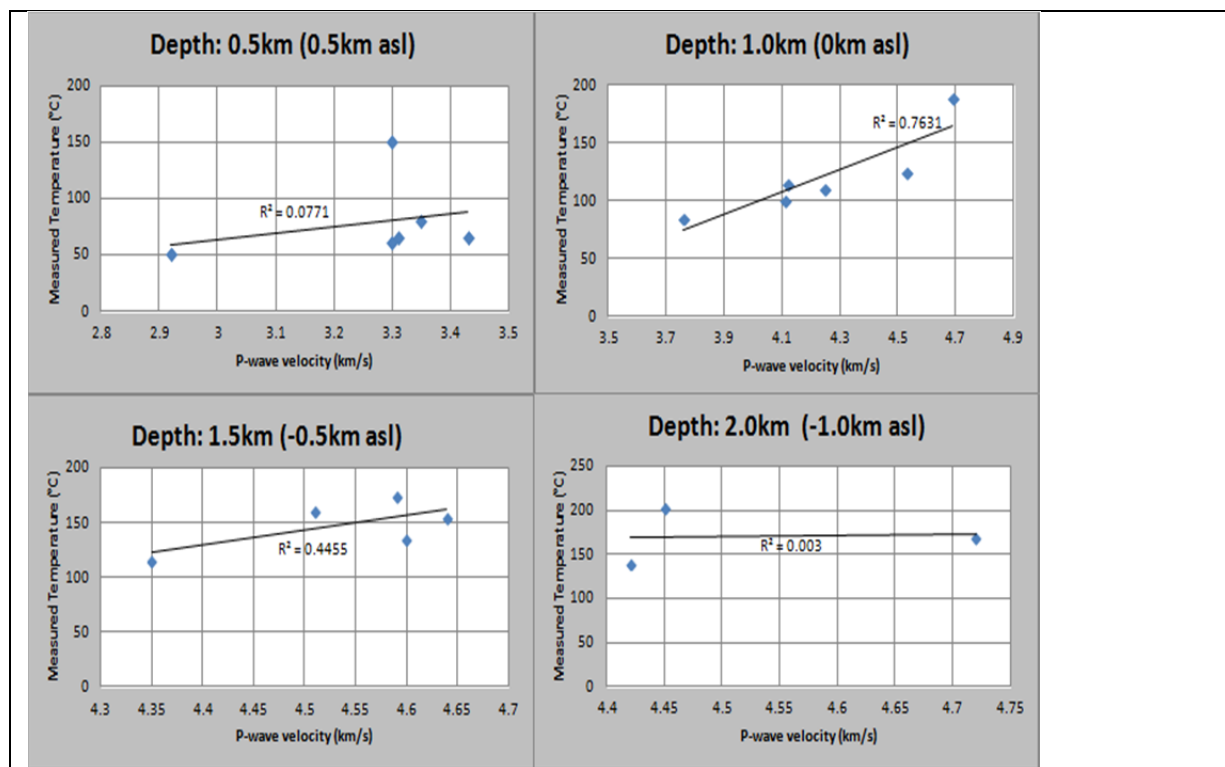
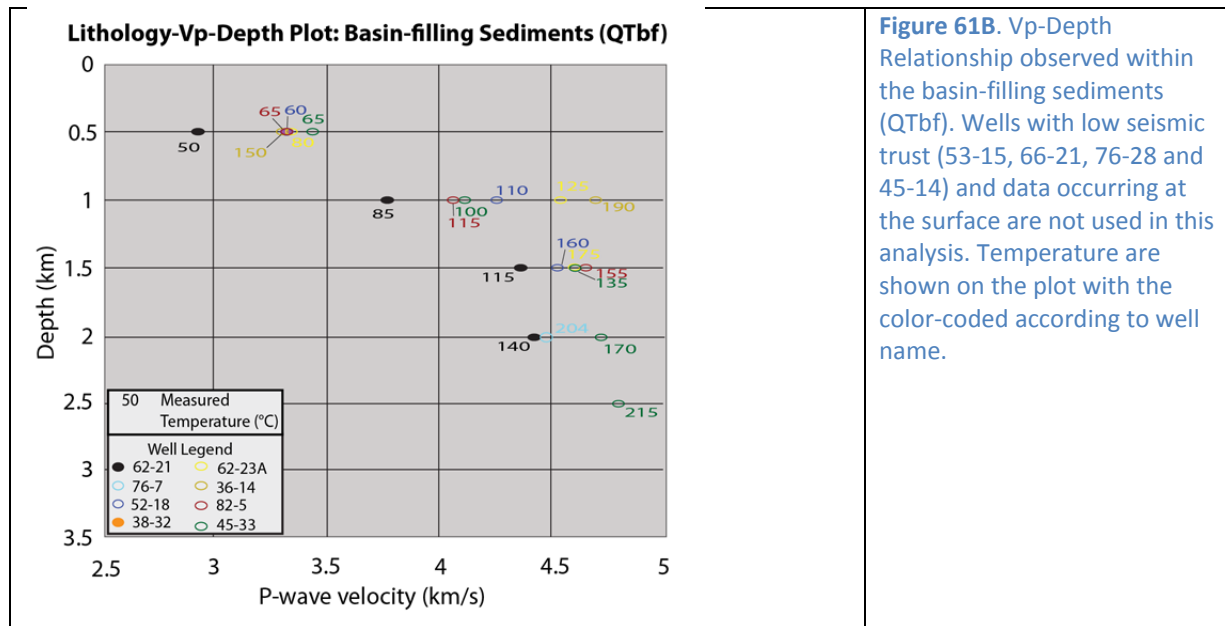
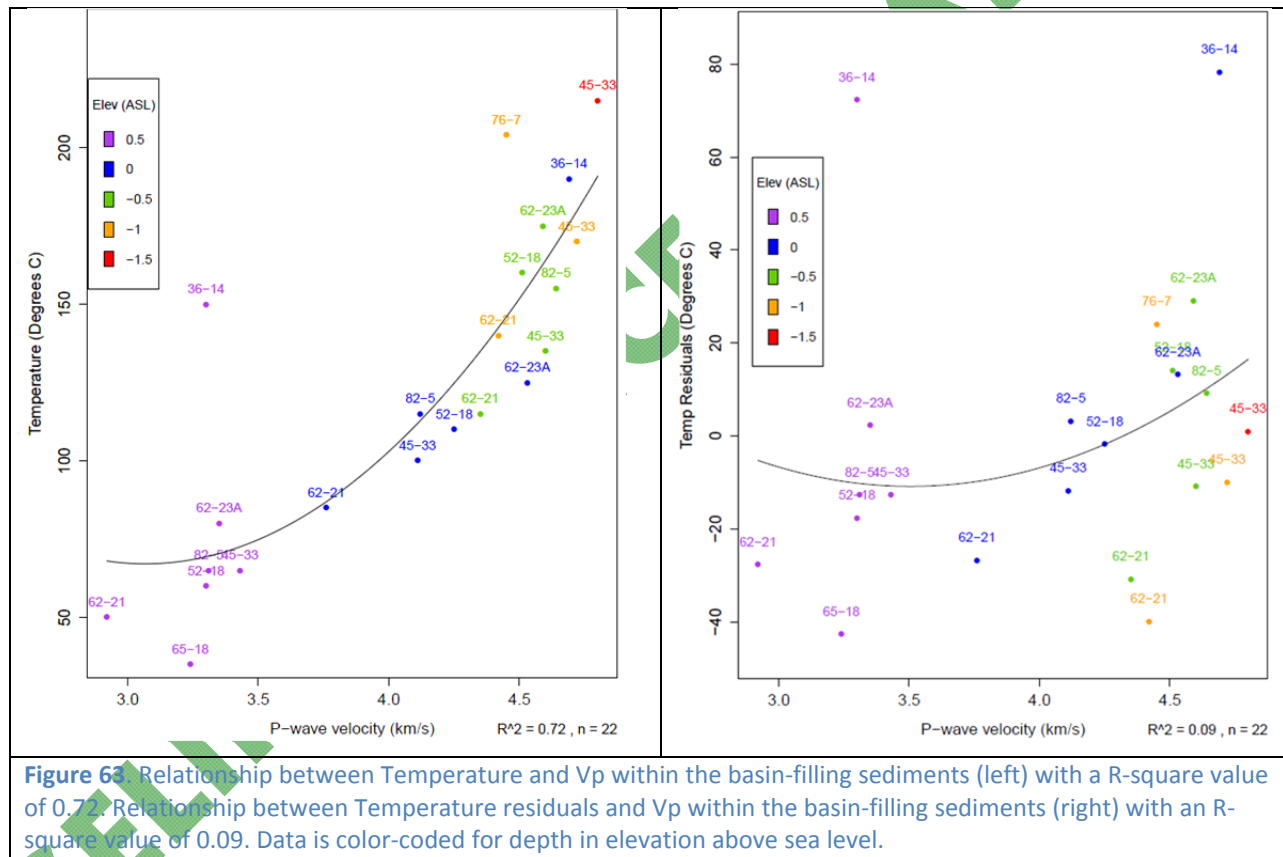


**Figure 62.** Vp-Temperature relationship observed within the basin-filling sediments (QTbf) at the respective depths.

The relationship between Vp and temperature seems to be mostly within the basin fill (QTbf) values. When those points are plotted separately, we see an  $r^2$ -value (for a quadratic fit) of **0.72** (Figure 63). The variables temperature, Vp, and depth are all strongly correlated. Since is not dependent on location, it is desirable to examine the relationship between temperature and Vp that is independent of depth. To do

this, we have taken the residuals from a linear fit of temperature on depth. These residuals are the difference between the actual temperature and the predicted temperature, so what is left gives an estimate of the amount that a cell is hot or cold compared to cells at the same depth. Any relationship that remains between these residuals and Vp is thus independent of depth.

When comparing the residuals of temperature to Vp, in place of the actual temperatures, a negligible  $r^2$ -value of 0.09 is found, and the relationship disappears (Figure 63). Thus, the effect of depth cannot be separated from the Vp and temperature parameters. These two figures exemplify the more general phenomenon that the relationship between temperature and Vp is highly confounded with depth. Attempting to establish causality is beyond the scope of this study, but a plausible story might be that high levels of vertical stress (for example, at great depth) may cause both temperature and Vp to rise. A story such as this is consistent with both plots and does not contradict lab results showing that at constant pressure, temperature and Vp tend to be negatively correlated. Further investigation of this empirical relationship is required using the enhanced data set and in other geothermal fields to determine its viability as a non-invasive tool for approximating subsurface temperature distribution.



Other analyses not included in this report that assess the Vp-Temperature relationship with respect to depth and geologic formation can be found in Appendix 18. Selected analyses and associated plots include:

1. Measured Temperature vs. Depth coded for lithology type;
2. Measured Temperature vs. Depth coded for P-wave velocity;
3. P-wave velocity vs. Depth coded for temperature;
4. P-wave velocity-Depth-Lithology plots for all wells with respect to 62-21

## 5. P-wave velocity-Depth-Lithology plots for major geologic formations.

### Summary Assessment of the Vp-Temperature Relationship

A number of potential issues, inconsistencies and discrepancies, have arisen during the assessment of this relationship. First, there is a limited amount of measured temperature data, although this database is more extensive than typical exploration data sets. The preliminary baseline Vp data is generally of poor quality and was extracted by our Seismic Task Leader, Dr. Ileana Tibuleac, from OPTIM reflection lines and associated block velocity models coupled with low resolution regional seismic models and very general crustal-scale models. The analysis of the more "raw" baseline seismic data, specifically the variance of green functions, was not available. Secondly, a number of assumptions were made including the (1) overall analysis is based on gross averages of the lithology, temperature, and Vp data for a data cell on the order of 500m by 500m, (2) relationship was established by comparing modeled data (Vp) to measured data (temperature), (3) some of the wells in Dixie Valley occur within the same cell (500m by 500m) and thus a number of temperature measurements at a given depth, all of which have the same assigned Vp value, and (4) effect of fracturing and fluid content on the Vp relationship cannot be quantified.

The issue of depth confounding in the relationship has been validated by the various residual analyses. Interestingly the multiple regression analyses inferred that using a suite of parameters including Vp could accurately predict temperature. This concept is further explored below using CART. However, it is noted that the majority of geoscience parameters have an inherent depth influence. While the discussed Vp-temperature relationship is observed using the empirical baseline data, the effect of depth cannot be removed from the parameters used to establish a unique relationship. This relationship will be further assessed using the enhanced data set (baseline + new) that utilizes, expectedly, higher quality data collected from the passive seismic survey in 2011-12 (under Task 4).

### Classification and Regression Tree Analysis (CART)

#### Introduction

One objective of the various exploratory geostatistical analyses is to define which parameters make good predictors, specifically for predicting conditions favorable for EGS. The aspects to be predicted using CART and referred to as response variables are (1) temperature; (2) lithology type using both the Section and Well Data, as well as predicting both; (3) productive hydrothermal cells; and (4) expected EGS favorable cells using the well data. Since the data is in both a numerical and categorical form, the principal geostatistical tool used in this evaluation is a CART analysis. While all potential parameters are considered as explanatory variables, a direct interest is made towards the predictive power of measurable geophysical parameters such as Vp, MT and gravity-magnetic inferred lithology (Grav\_Mag).

#### Explanation of CART

CART is a statistical technique that can be used to determine the statistical relationship between a defined predicted or response variable and multiple undefined predictor or explanatory variables. As summarized from Lawrence and Wright (2001) who describe CART as a popular form of statistical analysis that operates by recursively splitting the data until ending points, or terminal nodes, are achieved using preset criteria by analyzing all explanatory variables and determining which binary divisions of a single explanatory variable best reduces deviance in the response variable. For each portion of the data that results from this split, the process is repeated, and continues until homogeneous terminal nodes are reached in a hierarchical tree.

Decision trees used in CART are designed to predict an item's value for some variable based on other information available about the item. Classification trees predict what category an item falls into

whereas regression trees predict the numerical value of a variable. For example, if you wanted to predict gender based on weight, you could use a classification tree with a single split where people above a certain weight would be predicted to be male and people below that weight would be predicted to be female. The predictions would have some errors, and the weight to split at would be chosen to minimize the number of errors. If you also have information on height, that probably would do even better at prediction, so you might choose an initial split based on a height value, with tall people predicted to be men and short people predicted to be women. Then subsequent splits might be made based on weight so that amongst the tall people, perhaps the heavy tall people are even more likely to be male than the lighter tall people, and a similar split could be made for the short people. The split points are chosen to minimize the number of misclassifications. For more than two categories this is equivalent to choosing the split points so that a random item has the smallest possible chance of being misclassified. Thus if we have  $i$  categories, each with probability  $p_i$ , we minimize the sum of  $p_i(1-p_i)$ , summed over the  $i$  categories in each of the “leaves” at the end of the splits, or “branches.” Notice that if the categories are all perfectly classified,  $p_i$  will be 1 for exactly one value of  $i$  and then  $(1-p_i)$  will be 0 for that category.

A regression tree predicts the value of a numerical variable such as predicting height from weight. The process of splitting is done in such a way as to minimize the squared errors of the predictions when the predictions are the averages within the subgroups. So if we predict weight from height, we might first split into tall and short, and the predicted weights would be the average of the tall people and the average of the short people. Subsequent splits could be made based on weight in order to subdivide the population further into relatively homogenous groups based on weight. If the splitting is allowed to continue, the tree will grow until each person is on a leaf and the predicted weights are perfect. This splitting will have the undesirable effect of fitting noise, essentially making non-intuitive predictions. For example, if one person 66 inches tall weighs 180 pounds and someone 68 inches tall weighs 170 pounds, the full tree will predict these accurately, but that is counter to the more realistic general rule that taller people should be predicted to be heavier. Because of this pruning methods such as cross validation are used to reduce the tree in a way that presents an accurate idea of how the predictions should be done for data not including in the building of the tree. Amongst the advantages of CART are that it results in easily understandable prediction rules and it is free of underlying assumptions about the data and error structure. Drawbacks include that it is restricted by these binary splits and since the optimization is done from the top down it may not result in the globally optimal tree.

#### CART Methodology

The CART analyses described in this section were performed using the statistical program JMP Pro 9.0 by SAS which identifies CART as a partition analysis. The input data used two different data sets (1) all the combined sections (cross-sectional) data described above (Appendix 16a), and (2) the well data (see Appendix 16b). The parameters of interest are formatted in a pre-determined EXCEL sheet that lists the explanatory variable name in the column heading, while the rows correspond to specific cells or locations at specific depths that have multiple parameters. Each row must have a defined value for the various variables or the program cannot correlate other data to this value. The workbook is then transferred as a .csv file into the statistical program, where the CART analysis is conducted on the data by defining a response variable (parameter to be predicted) and one or more explanatory variables (parameters used for the prediction). The analysis then divides the explanatory variables into specific groups based on the means and standard deviation of the data. A  $r^2$ -value (from 0 to 1) is reported at each subsequent split that quantifies the accuracy of the prediction at that stage in the analysis. For selected cases, the split history and regression trees are shown in the geostatistical data figures presented in Appendix 19. The advantages of this technique are (1) the first variable that the program chooses to split on, infers that this variable is the most highly correlated to the predictor (Ed Isaaks,

pers. comm., 2011) or alternatively that this variable has a large variability and is the most efficient for the analysis to subdivide, (2) users can turn response explanatory variables on/off to determine which ones make the best predictors, (3) split history can be pruned back to stop the analysis at a suitable  $r^2$ -value, and (4) the methodology works with both numerical (continuous) and categorical variables.

**BASELINE CONCEPTUAL MODEL**

**Table 7.** Summarizes the initial CART analyses conducted on section and well data with respect to predicting temperature, lithology, and productive wells, and non-productive wells. The response variables are listed under the first column, followed by the type of data used. The eight possible explanatory variables have an X, if they were considered in the analysis, and a **bolded X** if they were used in the analysis. The  $r^2$ -value listed quantifies the analysis. Appendix 19 presents the individual CART figures for selected analyses.

Description of Analysis Conducted	Data Type	Selected Geoscience Parameters Considered (X) and Used (X) in the Data Splitting Process								$r^2$ -value	Summary
		$T^a$	Vp	Resist. (MT)	CSC	Dilatation	Fault Presence	Vert Stress <sup>f</sup>	Lithology <sup>bc</sup>		
<b>Predicting Temperature</b>	section	---	<b>X</b>	---	---	<b>X</b>	---	<b>X</b>	<b>X</b>	<b>0.91</b>	
		---	<b>X</b>	<b>X</b>	---	---	---	---	<b>X</b>	<b>0.8</b>	
<b>X</b>		<b>X</b>	<b>X</b>	<b>X</b>	<b>X</b>	---	<b>X</b>	---	<b>0.82</b>		
<b>X</b>		<b>X</b>	<b>X</b>	<b>X</b>	<b>X</b>	---	---	---	<b>0.54</b>	Removing VertStress dropped R <sup>2</sup> value by 34%	
<b>Predicting Lithology<sup>d</sup></b>	well	<b>X</b>	<b>X</b>	<b>X</b>	<b>X</b>	<b>X</b>	<b>X</b>	<b>X</b>	<b>X</b>	<b>0.66</b>	
		<b>X</b>	<b>X</b>	<b>X</b>	<b>X</b>	<b>X</b>	<b>X</b>	<b>X</b>	---	<b>0.52</b>	R <sup>2</sup> -value dropped 21% when Lithology was removed and Dilatation was considered
		---	<b>X</b>	<b>X</b>	---	---	<b>X</b>	---	<b>X</b>	<b>0.62</b>	Vp, MT and Lithology accounts for 94% of the 0.66 $r^2$ -value above
		<b>X</b>	<b>X</b>	<b>X</b>	---	---	<b>X</b>	---	<b>X</b>	<b>0.54</b>	
<b>Predicting Temperature</b>		---	<b>X</b>	---	---	---	---	---	---	<b>0.62</b>	
<b>Predicting Temperature<sup>e</sup></b>		---	<b>X</b>	---	---	---	---	---	---	<b>0.75</b>	R <sup>2</sup> -valued increased by ~21%
		---	<b>X</b>	<b>X</b>	---	---	---	---	<b>X</b>	<b>0.75</b>	Adding Resistivity (MT) and Lithology does not change R <sup>2</sup> -value relative to using Vp alone
		---	<b>X</b>	<b>X</b>	---	---	---	---	---	<b>0.78</b>	Highest R <sup>2</sup> value using Vp and Resistivity (MT)

<sup>a</sup>Temperature; <sup>b</sup>Lithologic Density is a parameter that is directly related to the various lithology identified in this investigation; <sup>c</sup>Gravity-magnetic data was found to be highly correlated to lithology and as such is not shown as a separate parameter; <sup>d</sup>Fracture Intensity was also considered in some of these analysis but not used; <sup>e</sup>Uses all data except wells with a low seismic trust (i.e., 66-21, 45-14, 76-28, and 53-15); <sup>f</sup>Vertical Stress

## Sectional Data

CART analyses were performed with respect to all parameters gridded from the cross-sectional data (C-C', D-D', E-E' and F-F'), which is mostly modeled data. The parameters were gridded within 500m<sup>2</sup> cells from the valley surface (+1km asl) in 500m depth intervals to depths below the production zone (-4km asl). The sectional data set can be found in Appendix 16a. The analyses use CART to predict the Temperature or Lithology using (1) all parameters (explanatory variables) and (2) selected parameters based on the r<sup>2</sup>-value.

### *Predicting Temperature*

- Temperature vs. all parameters; **r<sup>2</sup> = 0.91** shown in Appendix 19-Figure 1. The data split on the following parameters: Vp, vertical stress, and then dilatation. While a high r<sup>2</sup>-value infers that all the parameters can accurately predict temperature, it is noted that vertical stress is not a suitable parameter for predicting temperature.
- Temperature vs. Vp, lithology and MT; **r<sup>2</sup> = 0.80** shown in Appendix 19-Figure 6. This shows that temperature can just as accurately be predicted from the cross-sectional data using only the following three parameters: Vp, lithology and MT.

### *Predicting Temperature from Vp*

Using the cross-section data, temperature could be predicted from (1) Vp with a r<sup>2</sup>-value of **0.359**, (2) Vp and resistivity derived from the MT data with a r<sup>2</sup>-value of **0.775**, and (3) Vp, MT and Lithology with a r<sup>2</sup>-value of **0.800**.

### *Predicting Lithology*

- Lithology vs. all parameters; **r<sup>2</sup> = 0.82** shown in Appendix 19-Figure 3. The first two splits in the data occurred on vertical stress. Previous analyses have determined that this calculated value has a likely dependence on depth and should not be used to predict lithology (see previous [Section 7.4.2](#)).
- Lithology vs. all parameters excluding vertical stress; **r<sup>2</sup> = 0.54** shown in Appendix 19-Figure 2. Once this parameter is removed, the prediction capability drops significantly.
- Lithology vs. Vp, MT and temperature; **r<sup>2</sup> = 0.53** shown in Appendix 19-Figure 4. The small drop in the r<sup>2</sup> value infers that Vp, MT and temperature are best predictor variables for lithology, when other high predictive power parameters are not considered (vertical stress, dilatation, etc.).
- Lithology vs. Vp; **r<sup>2</sup> = 0.23**. Vp cannot be used to predict lithology. The SME has noted that a better seismic parameter for predicting lithology is rho (density). Once the new seismic data is collected under Task 4, this parameter should have high enough resolution to be used as a predictor for lithology shown in Appendix 19-Figure 5.

## Well Data

The Well Data includes all measured and reported well data (lithology, temperature, faults, geochemistry, etc.), calculated values (LithDensity, LithStrength, vertical stress, etc.), and modeled data (Vp, MT, Stress Data: CSC and dilatation, etc.) with respect to well location (Appendix 16b). For this data set, parameters were gridded within 500m<sup>2</sup> cells at 500m depth intervals from +1km asl to -3km asl. CART analyses can be used in this case to explore the predictive power of a variety of modeled parameters where the response variable (temperature or lithology type) existing as measured data is known with a great degree of certainty. This in a sense validates the correlations found using the section

data. A second advantage of using the well data, is that since not all of the wells are producing wells, a CART analysis can potentially determine what is unique about the other parameters that infers whether a corresponding cell is productive or non-productive (hot/cold and dry).

### *Predicting Temperature using Vp*

The CART predictions that determined if temperature can be predicted by Vp and other parameters using well data is summarized in [Table 8](#). The results of this analysis are tabulated below and shown in Appendix 19-Figures 7-10. Temperature could be predicted from (1) Vp with a  $r^2$ -value of **0.621**, after only three divisions of the data (see the first row in Table 8). When the wells with low seismic trust were removed from the analysis, temperature could be predicted from Vp with a increased  $r^2$ -value of **0.75** (Table 8, row 2). This is similar to the results from the correlation plot shown in [Figure 56](#), that show the strength of the relationship increases, when the low quality Vp data is removed. The CART analysis supports the observed empirical relationship between Vp and temperature and infers that the combination of the parameters Vp and MT cannot predict temperature better than Vp alone. This result is not consistent with the multiple regression analysis described above. In summary, Vp can be used to predict temperature using a subset of the well data. This relationship is explored further below.

**Table 8.** CART analyses predicting temperature using well data and P-wave velocity (Vp)

Data Used	R-square value	Appendix 19 Figure
All well data	0.62	7
Edited well data <sup>7</sup>	0.75	8
Edited well data + Resistivity (MT)	0.77	9
Edited well data, Resistivity (MT), Lithology	0.75	10

### *Predicting Productive Wells*

Cells that are considered part of the hydrothermal system were defined and analyzed versus multiple geoscience parameters to determine which variables were suitable for predicting a productive well. Cells are in reference to the pre-determined 500m<sup>2</sup> assigned spacing used for gridding purposes and dividing up the wells in the Calibration area into different depth slices. In general the hydrothermal system includes the injecting or producing portions of the wells, usually the lowermost cells. For purposes of this analysis, productive wells are referred to as hydrothermal. Selected results are presented in [Table 9](#). A complete table showing the wells used in the analysis, associated cells (depths in this case) that are considered productive, and cells that have a known lithology value is found as [Table 10](#). In addition to predicting hydrothermal cells, a subsidiary CART analysis was performed to predict EGS favorable cells. Using the well data, cells that were expected to be favorable for EGS and were not exclusively part of the hydrothermal system were identified. In some cases these two domains, hydrothermal and EGS, overlap due the 500m spacing resolution. The CART method was then used (1) to test if EGS favorable cells could be predicted, (2) compare the results to the prediction for hydrothermal cells, and (3) determine which response variable combination could predict EGS cells including combinations without the vertical stress parameter. See [Table 10](#) for identified EGS favorable cells.

Appendix 19-Figure 11 (Fig. 19-11) presents the CART analysis for the prediction of productive vs. non-productive cells using all the available well data and the following select geoscience parameters: lithology, temperature, Vp, vertical stress, resistivity (MT), CSC, dilatation, and presence of a fault. In this

<sup>7</sup> Removed wells with a low Vp trust factor

analysis, the data was split using lithology, Vp, resistivity (MT), CSC, and vertical stress, with a  $r^2$ -value of **0.66**.

A preliminary parametric sensitivity analysis was conducted to determine the effect of removing selected parameters (explanatory variables) from the analysis shown in Fig. 19-11 and [Table 9](#). Appendix 19-Figure 12 presents the CART analysis for the prediction of productive (hydrothermal) wells using the same suite of select geoscience parameters indicated in [Table 9](#) except lithology. In this case, the  $r^2$ -value decreases to **0.52** indicating that lithology is a critical parameter in differentiating productive from non-productive cells, as expected. Appendix 19-Figure 13 (Fig. 19-13) presents the same type of CART analysis but using only the selected geoscience parameters of Vp, resistivity (MT), fault presence, and lithology with a reported  $r^2$ -value of **0.62**. Appendix 19-Figure 14 provides the results of the addition of temperature to the parameters used in Fig. 19-11. Interestingly, the resulting  $r^2$ -value is **0.58**, lower than that in Fig. 19-13 but slightly higher than that in Fig. 19-11. This implies that temperature is not most critical parameter in predicting productive vs. non-productive cells, and that lithology, Vp and MT are the best combination of predictors for this case.

The analysis determined that the best explanatory variables for determining productivity are the combination of Lithology, Vp, and Resistivity (MT), with a  $r^2$  value of **0.66**. The first split of the data occurred within the Lithology parameter, as the majority of the productive cells occurred in expected lithologies (Jz, Jbr, and Tmb), while the non-productive cells occurred in lithologies not part of the geothermal reservoir (Tr, Kgr and Tbf).

**Table 9.** CART parametric sensitivity analysis on selected geoscience parameters predictive of productive hydrothermal wells from the database for both non-productive and productive wells. Figures are referenced from Appendix 19.

CART Analysis Figure	Selected Geoscience Parameters Considered (X) and Used (X) in the Splitting								$r^2$ -value
	Temp	Vp	Resistivity (MT)	CSC	Dilatation	Presence of a Fault	Vertical Stress	Lithology	
11	X	<b>X</b>	<b>X</b>	<b>X</b>	X	X	<b>X</b>	<b>X</b>	0.66
12	X	<b>X</b>	<b>X</b>	<b>X</b>	<b>X</b>	X	<b>X</b>		0.52
13	X	<b>X</b>	<b>X</b>			X		<b>X</b>	0.62
14		<b>X</b>	<b>X</b>			X		<b>X</b>	0.54

### **CART Sensitivity Analysis**

The CART analyses described above explored differing combinations of multiple explanatory variables to find the highest  $r^2$ -values in predicting one of the four key response variables: temperature, lithology type, productive hydrothermal cells, and expected EGS favorable cells. The analyses determined which parameters are the best predictors. An extensive sensitivity analysis was performed using *JMP Pro 9.0* and the publically available *RStudio* application to determine the prediction capabilities of the various geoscience parameters and the relationships and interactions between them. The analysis performs every possible parameter combination using seven key variables in a systematic format. Temperature and lithology type was predicted using both section and well data, while predicting the occurrence of productive hydrothermal and EGS favorable cells was determined using well data only. The individual CART analyses were evaluated mostly based on their associated  $r^2$ -value, but also due to the number of splits, explanatory variables used, explanatory variable first split on, shape of the  $r^2$ -curve and corresponding K-fold cross-validation curve. This analysis will determine (1) the best combination of explanatory variables to predict temperature, lithology type and productive hydrothermal/EGS favorable cells, (2) the influence of adding and removing variables, (3) the effect or removing depth (i.e. vertical stress) from the analysis and (4) relationships between key predictor variables.

**Table 10.** Identification of productive hydrothermal cells for Dixie Valley Wells and formations encountered at the selected depths indicated. Cells highlighted light orange are considered productive (zones of injection/production). Non-shaded cells are considered non-productive, while dark gray shaded cells lie below the wellbore. Lithologies that are bolded and in red represent the expected EGS Favorable cells, some of which overlap with the permeable (hydrothermal) defined cells.

Well Class	Well	Depth (km) above sea level								
		1	0.5	0	-0.5	-1	-1.5	-2	-2.5	
Injectors	65-18	Tbf	Tbf	Tbf	Tbf	Tmb	Jz			
	32-18									
	52-18					Tv	Jz	Jz		
	SWL-3					Tmb	Tv	Kgr		
	SWL-2					<b>Tmb</b>	<b>Kgr</b>			
	41-18					Tmb	Jz	Jz		
	SWL-1									
	38-32					Jbr	Tr			
	45-5					Tbf	Tbf	Tbf	Tmb	Kgr
Producers	27-33	Tbf	Tbf	Tbf	Tbf	Tmb	Tv	Jbr		
	28-33					Tv	Jbr			
	37-33					Jz	Kgr			
	76-7					Tbf	<b>Tmb</b>			
	82-7					Tmb	<b>Jz</b>	<b>Jz</b>		
	84-7					<b>Tmb</b>	<b>Tv</b>			
	73-7					Tmb				
	63-7					Tbf	Jz	Jz		
	74-7									
Sub-commercial and Dry Holes	62-21	Tbf	Tbf	Tbf	Tbf	Tbf	Jz	Tr	Tr	
	45-14		Tv	Tr	Tr	Tr	<b>Tr</b>			
	66-21		Tbf	Tbf	<b>Tv</b>	<b>Jz</b>	<b>Tr</b>	Tr	Tr	
	62-23A				Tbf	<b>Tv</b>	<b>Jz</b>	<b>Tr</b>		
	36-14				Tr	Tr	<b>Tr</b>	<b>Kgr</b>	<b>Kgr</b>	
	53-15		Jz							
	76-28		Tbf	Tbf	Tbf	Jz	Tr	<b>Kgr</b>		
	82-5					<b>Tmb</b>	<b>Tv</b>		<b>Kgr</b>	
	45-33					Tbf	Tbf	<b>Jbr</b>		

*Reported lithology at depth indicated as identified by Blackwell et. al 2005; Lutz et. al 1998, 2002; Reed et. al 2009; Hulen et. al 1999; Plank (1999) and proprietary data provided by Terra-Gen Power.*

**Lithology Explanation**

- Tbf:** basin-filling sediments
- Tmb:** Miocene basalt
- Tv:** Oligocene silicic volcanics
- Jz:** Jurassic mafic rocks
- Jbr:** Boyer Ranch quartzite
- Tr:** Triassic meta-sediments
- Kgr:** Cretaceous granodiorite

	Non-Productive
	Productive
	Cell lies below well

BASELINE

## Parameter Overview

Within the preceding geostatistical analyses, the various geoscience parameters have been analyzed and eight key variables that show correlations have been recognized (see [Section 7.4.1](#) and Appendix 15). These variables were chosen as the explanatory variables in the CART Sensitivity Analysis and are as follows: (1) **P-wave velocity** ( $V_p$ ), (2) **Resistivity** derived from Magnetotellurics (MT), (3) **Coulomb Stress Change** (CSC), (4) **Dilatation**, (5) **Vertical Stress** (VertStress), (6) **Gravity-Magnetic inferred Lithology** (Grav\_Mag), (7) **Lithology** derived from the geologic assessment and (8) **Temperature**.

## Methodology

JMP Pro 9.0 is a user friendly statistical program that allows the user to upload excel files containing the various data with respect to cell location, and then run a *partition analysis* using the data. The user chooses his *Input Variable* (Predictor or response variable), and then chooses the *Explanatory Variable/s* from 1-7 variables. The approach shows the effect of systematically removing one variable at a time starting with considering all variables (7) and finishing with only one variable considered. Prior to starting the analysis the user should check the tabs labeled *Split History*, *K-fold validation* and *Column Contributors*. Split History shows how the  $r^2$ -values changes vs. the number of splits. The k-fold validation option checks the validity of the  $r^2$ -value by performing the same splits subsequently on a smaller subset of the data. If the two lines are intersecting or similar then the  $r^2$ -value has a higher level of confidence. The column contributor's option allows the user to see which parameters were used in the analysis. Once analysis is set-up, the analysis begins by repeatedly *splitting* the data (manually) until the  $r^2$ -value has reached a plateau and does no longer increase with each subsequent split. The  $r^2$ -value reported by the CART analysis must also match or be close to the k-fold validation curve. The user has the option of *pruning* back the tree to terminate the analysis at the desired node. Generally the less splits of the data, the more reliable the corresponding  $r^2$ -value.

The analyses were organized into a series of tables for each unique prediction that shows the effect of removing one variable all the way to removing six out of seven possible variables. Each table shows the variables used, variables considered, variable used for the first split, corresponding  $r^2$ -value, and number of splits for each possibility. The following lists the appendices that detail the three CART Sensitivity Analyses:

- Appendix 20a. Predicting Temperature using Section and Well Data;
- Appendix 20b. Predicting Lithology Type using Section and Well Data;
- Appendix 20c. Predicting Productive (hydrothermal) vs. Non-Productive Cells using Well Data; and
- Appendix 20d. Predicting expected EGS favorable cells using well data.

In the case of predicting EGS Favorable cells, the analysis was performed using *RStudio* a publically available user interface for performing various statistics ([www.rstudio.com](http://www.rstudio.com)). Using the well data set, cells (depth intervals with respect to wells) considered favorable for EGS were designated as the response variable, while eight explanatory variables were chosen. The explanatory variables used were the same as for the previous three analyses, with the exception that the Gravity-Magnetic inferred Lithology parameter was replaced with whether a faults was present or absent. The analysis explored every combination from eight variables considered to only one considered, with the results organized by the number of variables used, and reported from highest to lowest with respect to  $r^2$ -value . Results are summarized in Appendix 20d, while selected results are highlighted in [Table 11](#).

## Results

The first variable that the analysis determined to split on was almost exclusively vertical stress, which has a strong dependence to depth. When this variable was removed, the analyses tended to choose  $V_p$

as the first split or next best choice, and the  $r^2$ -values dropped significantly. While vertical stress was considered a significant predictive parameter using CART and other geostatistical methods, a review of the results show that when vertical stress is removed from the CART analysis, similar  $r^2$ -values can be replicated with a different set of parameters ([Table 11](#)). For example, when predicting temperature using section data, a  $r^2$ -value of **0.871** is calculated using all available parameters including vertical stress, while a  $r^2$ -value of **0.885** can be achieved using only Vp, Lithology and Dilatation. This case is true for all five predictions, with the exception of the predicting Lithology using Section Data which yields a  $r^2$ -value of **0.631** using all parameters, and only a **0.453** using Vp, MT, CSC, dilatation and lithology. While this implies that the combination of other parameters can replicate the predictive power of vertical stress, it is important to note that the low value in the range of  $r^2$ -values reported in [Table 11](#), occurs when vertical stress is removed from the analysis. The results are summarized below.

#### *Predicting Lithology using Section Data*

- Highest  $r^2$ -values are in the 0.60 to 0.66 range.
- Temperature and CSC are the least used variables.
- Vertical stress was chosen as the first split the majority of the cases. The only other variables used as the first split was Vp, dilatation, and Grav\_Mag, and in that order of occurrence. The majority of the cases these secondary variables were used as the first split when vertical stress was removed from the analysis.
- The analysis tended to follow a pattern of using only the variables vertical stress and dilatation together for a  $r^2$ -value of 0.653 after 7 splits, when the variable Vp and Grav\_Mag were removed.
- Using Vp, Resistivity and Grav\_Mag yielded an  $r^2$ -value of 0.406 after 5 splits.

#### *Predicting Temperature using Section Data*

- Highest  $r^2$ -values are in the 0.85 to 0.90 range.
- Vertical stress was the dominant first split, followed by Vp, then resistivity (MT), and lastly Grav\_Mag. When none of these variables were considered, dilatation was used as the first split.
- Vertical stress and MT yielded a  $r^2$ -value of 0.876 after 4 splits, while vertical stress and dilatation yielded a  $r^2$ -value of 0.892 after 4 splits.
- Vp and MT alone can predict temperature with a  $r^2$ -value of 0.775 after 6 splits.
- CSC was rarely used in the analysis, and only when the variable dilatation was removed.
- The fact that vertical stress, when it is the only variable considered, can predict temperature with an  $r^2$ -value of 0.874 after 3 splits, suggests that depth is the controlling factor. Vp alone had a  $r^2$ -value of 0.359 after 5 splits, while resistivity alone had a  $r^2$ -value of 0.502 after 4 splits.
- Vertical stress, Grav\_Mag, and lithology show a complex interaction between the variables and tend to group together.

#### *Predicting Lithology using Well Data*

- Highest  $r^2$ -values are in the 0.60 to 0.62 range.
- When vertical stress was considered, it was used as the first split 100% of the time. The variable used as the first split when vertical stress was removed was Vp, then Grav\_Mag. If all three of these variables were removed, the analysis first split on dilatation.

- The three most commonly used variable were vertical stress, dilatation and Vp. The most common result was the analysis using these three variable regardless of the variable considered, with a  $r^2$ -value of 0.611 after 6 splits.
- Using vertical stress, Grav\_Mag and Vp resulted in highest  $r^2$ -value of 0.621 after 7 splits.

**Table 11.** Classification and Regression Tree (CART) Sensitivity Analysis results using cross-section and well data. The first row for each response variable corresponds to  $r^2$ -value ranges with vertical stress considered, while the following rows, highlighted in green, show the  $r^2$ -values when vertical stress is removed from the analysis. In most cases with the exception of predicting Lithology using Section Data, a similar  $r^2$  result can be achieved when vertical stress is removed from analysis. The explanatory variables used in the analyses include (1) temperature, (2) p-wave velocity (Vp), (3) resistivity from MT, (4) coulomb stress change (CSC) and (5) dilatational strain (dilatation) both from Coulomb Stress modeling, (6) vertical stress, (7) lithologic formations derived from the geologic assessment and (8) separately from the gravity-magnetic modeling.

Predicted Response Variable	Data Type	R <sup>2</sup> -values when Explanatory Variables are Removed from Analysis						Geoscience Parameters used when Vertical Stress is Removed			
		0	1	2	3	4	5		6		
Temperature	Section		.729 - .918	.727 - .918	.847 - .907	.735 - .898	.310 - .901	0.874			
Temperature <sup>1</sup>		0.871	0.677	0.806					Vp, Resistivity (MT), and Gravity-Magnetic (G-M) Lithology		
					0.792					Vp, Resistivity (MT), and G-M Lithology	
						0.885				Vp, Resistivity (MT), and Dilatation	
							0.775			Vp, Dilatation, and Lithology	
								0.684		Vp, and Resistivity (MT)	
						0.359		Dilatation			
Lithology	Section		.627 - .655	.541 - .653	.523 - .665	.484 - .660	.505 - .656	0.507			
Lithology <sup>1</sup>		0.631	0.438	0.453					Vp, Resistivity (MT), Dilatation, and G-M Lithology		
					0.433					Vp, Resistivity (MT), Dilatation, and G-M Lithology	
						0.421				Vp, Dilatation, and G-M Lithology	
							0.406			Vp, and Dilatation	
								0.277		Dilatation	
Temperature	Well		.769 - .841	.749 - .841	.749 - .822	.749 - .805	.749 - .803	0.749			
Temperature <sup>1</sup>		0.822	0.750	0.767					Vp, Resistivity (MT), CSC, Dilatation, and Lithology		
					0.775					Vp, Resistivity (MT), CSC, Dilatation, and G-M Lithology	
						0.730				Vp, CSC, Dilatation, and G-M Lithology	
							0.680			Vp, Dilatation, and Lithology	
								0.621		Vp and Lithology	
Lithology		0.611		.577 - .611	.562 - .611	.562 - .644	.562 - .620	.552 - .615	0.552		
Lithology <sup>1</sup>			0.611	0.521	0.529					Vp, Resistivity (MT), CSC, and G-M Lithology	
						0.600					Vp, Resistivity (MT), CSC, and G-M Lithology
							0.549				Vp, CSC, and G-M Lithology
								0.550			Vp, Dilatation, and Temperature
									0.408		Vp and Dilatation
									0.408	Vp	
Productive Hydrothermal cells	0.625		.447 - .617	.431 - .647	.523 - .665	.361 - .648	.315 - .587	0.389			
Productive Hydrothermal cells <sup>1</sup>		0.625	0.528	0.615					Vp, Resistivity (MT), and Lithology		
					0.433					Vp, Resistivity (MT), Lithology, and Dilatation	
						0.598				Vp, Resistivity (MT), Dilatation, and G-M Lithology	
							0.550			Vp, Lithology, and Dilatation	
Expected EGS favorable cells	0.727		.523 - .727	.383 - .727	.409 - .708	.369 - .661	.349 - .637	0.398			
Expected EGS favorable cells <sup>1</sup>		0.727	0.769	0.769					Vp and Dilatation		
					0.769					Lithology	
						0.708				Temperature, Vp, CSC and Dilatation	
					0.708			Temperature, Dilatation, and Lithology			
						0.398		Dilatation and Lithology			

<sup>1</sup>Vertical Stress is removed from consideration

### Predicting Temperature using Well Data

- Highest  $r^2$ -values are in the 0.80 to 0.83 range.

- Using vertical stress only yielded a  $r^2$ -value of 0.749 after only 3 splits. This was one of the most common results, even when other variables were considered.
- Vertical stress is the most common first split. When removed the data splits on Vp, then lithology, then Grav\_Mag when the subsequent variables are removed. When all of these are removed the analysis is forced to split on MT.
- Vp and MT alone can predict temperature with an  $r^2$ -value of 0.625 after only 3 splits.
- Vertical Stress, dilatation, and MT alone can predict temperature with an  $r^2$ -value of 0.83 after 6 splits.

#### *Predicting Productive vs. Non-Productive Cells using Well Data*

- The first split is lithology 100% of the time, when this variable is considered. When lithology is removed from the analysis, the first split is usually on Grav\_Mag as expected, however the choice for the second split is much more random than the previous analyses.
- Considering and using all seven variables, the analysis first split on lithology with an  $r^2$ -value of 0.625 after 6 splits.
- Highest  $r^2$ -value are in the 0.63 to 0.67 range.
- Vertical stress and dilatation used alone have a  $r^2$ -value of 0.513 after 6 splits.
- Temperature was only used as a secondary variable, and CSC and temperature were the least common variables used.

#### *Predicting EGS Favorable Cells using Well Data*

- Cells determined to possess characteristic favorable for EGS were assigned separately from cells identified as productive (hydrothermal).
- Dilatation was the most considered a significant parameter and was used in the CART data divisions for analyses which produced the highest  $r^2$ -values. Temperature and lithology type were considered important secondary parameters.
- The parameters temperature, Vp, CSC, MT (resistivity), and dilatation; temperature, Vp, CSC, dilatation and the presence of a fault could predict EGS favorable cells with an  $r^2$ -value of 0.769, while dilatation and lithology used alone yielded a 0.708  $r^2$ -value.
- Vertical Stress was not a critical parameter and the majority of the analyses yielded higher  $r^2$ -values when the parameter was not used in the analysis.

#### *Implications*

Using the data gridded along the wellfield cross-sections (Section Data) yielded slightly higher  $r^2$ -values than using the data gridded in respect to well location (Well Data). This is interesting as it suggests that more accurate predictions can be made with a larger quantity of modeled data, rather than a smaller set of data containing relatively more hard data. Modeled values such as vertical stress and dilatation seemed to make the best predictors and have a unique relationship between them. While vertical stress was used as the first split for most of the predictions, similar predictions quantified by high  $r^2$ -values could be made without this parameter. Lithology was the first split used for determining whether a cell was productive or non-productive, while temperature was the first split for predicting favorable EGS cells. This implies that the rock type is the most important factor in determining whether a cell is productive or non-productive, not temperature and adversely temperature is the most important factor for predicting favorable EGS cells. Resistivity (MT) was used almost exclusively as a secondary parameter

and when combined with Vp could predict temperature with high  $r^2$ -values. The significance or lack-of thereof will be determined when similar statistical analyses are applied to the enhanced data set under Task 5 of this Project (see [Section 1.1](#)). Some important observations are (1) each analysis is unique as  $r^2$ -values for identical trials can vary by as much as 5%, (2) vertical stress seems to be a modeled parameter suitable for CART yet highly dependent on depth and is not required to consider in future analyses, and (3) CART provided a good complementary geostatistical analysis to validate findings obtained from other methods (bi-variate correlations, residuals, multiple regression, etc.).

### *Summary of Exploratory Geostatistics and Geologic Significance*

It must be noted that this analysis should be considered a preliminary view of the exploration geostatistics of a geothermal system. Further work within this system, to be conducted using the enhanced data set (baseline + new) and in other geothermal systems should be conducted to determine (1) whether the correlations (and predictions) defined herein are universal in nature, and (2) the causal relationships within any particular correlation. The following lists the salient highlights of the geostatistical analyses:

#### Correlation Analysis

- The parameters temperature and vertical stress are correlated with p-wave velocity (Vp); All other correlations found are not consistent in the analyses conducted.
- Correlations between parameters cannot be analyzed solely on the correlation coefficient -value, but must take into account the data spread and range, effect of depth with modeled parameters, and significance based on SME and geologic inference.
- Temperature can be fairly accurately predicted from Vp using the well data set, especially when considering the variability and confidence (trust factor) of the baseline data. When the poor resolution areas were removed from the data set (surface data and wells with a low seismic trust), the  $r^2$ -value for the polynomial fit that quantifies the relationship has a value of 0.73.

#### Multiple Regression and Residual Analysis

While, the overall multiple regression and two component residual analysis indicates that depth (or elevation) is the only link between (1) temperature and vertical stress, and (2) temperature and Vp, a multicomponent analysis suggests that (1) the combination of a variety of geoscience parameters (a  $r^2$ -value of 0.94 was found using elevation, vertical stress, dilatation, Vp, and resistivity (MT) to predict temperature) can be used to predict temperature and (2) there is a complex interaction between the geoscience parameters in this prediction.

#### Classification and Regression Tree Analysis

Applying CART to both the Section and Well Data, the relationships among the geoscience parameters were investigated to determine if temperature, lithology, productive hydrothermal cells and expected EGS favorable cells can be predicted using the geoscience data and in part based on a combination of parameters that also showed high correlations within the previous analyses. The multi-step analysis showed that the geoscience data could predict the identified variables, considered the significant parameters for inferring favorable EGS conditions, both with and without the vertical stress parameter ([Table 11](#)). The exception to this result was when predicting lithology type using the section data. An important observation is that temperature could be predicted using the combination of three key measurable geoscience parameters, gravity-magnetic inferred lithology (Grav-Mag), MT and Vp. For example, temperature can be predicted using the section data with an  $r^2$ -value of **0.91** using Vp, MT and lithology, while the productive nature (hydrothermal portion) of a well can be predicted with a  $r^2$ -value of **0.63** using Lithology, Vp and MT. Additionally, Vp was the critical parameter for predicting

temperature and rock type when vertical stress was not considered. It is noted that difficulties remain for assessing the reliability of the CART results, when a number of the geoscience parameters have a embedded depth influence (vertical stress, Vp, temperature, and rock type).

The CART geostatistics have validated the qualitative correlations by the following points (1) the geologic and gravity-magnetic lithology model have a high degree of correspondence; (2) the resistivity parameter (MT) is one of the sensitive secondary parameters used to predict temperature and lithology; (3) Vp, while the parameter showed no qualitative correlation with the other geoscience data sets is a very important parameter for predicting lithology, temperature (see discussion below), the productive nature of a well, and expected favorable EGS area. It is important to note the combination of parameters had much higher  $r^2$  values quantifying their prediction power than the parameters by themselves.

#### Assesment of the Vp-Temperature Relationship

While an empirical relationship is observed between measured temperature from wells and modeled P-wave velocity, depth was a confounding parameter. The relationship was assessed using both cross-sectional and well data, through (1) standard correlation analyses, (2) correlations factoring in the trust factor of the baseline seismic model, (3) multiple regression, (4) residuals to remove the effect of depth, (5) CART analyses to determine the effect of other parameters, (6) correlation with geologic formations, and (7) correlation to conductive vs. convective domains. While the relationship certainly exists throughout some analyses, others do not support the correlation. We will evaluate this confounding relationship further using the forthcoming higher resolution seismic model using the enhanced data.

### 7.5 Summary

#### 7.5.1 Hydrothermal System

The structural interface between the Stillwater Range and Dixie Valley is complex fault zone, reflecting the interaction between the current WNW-ESE extension axis of normal faulting with an earlier generation of N-trending B&R faulting. The intersection of these structures, in the current stress regime, produces zones of compression and dilatation along the fault zone. These dilatational zones are coincident with the occurrence of shallow thermal anomalies expressed along the DVFZ and at New York Canyon on the west side of the Stillwater Range. Additionally, the subsurface well data available to this project shows an excellent correlation between productive wells and the inferred dilatation zones. While, the recognized thermal anomalies expressed at the surface occur at or near the range-front fault, additional geophysical evidence (i.e., MT data) suggest that portions of the intra-range setting are also hydrothermal, or were active in the past. Unfortunately, there is no well data in the range to validate this observation.

In reference to the structural mechanism, the data presented herein suggests that while the overall Dixie Valley geothermal system does lie in a regional accommodation zone between the west-dipping Pleasant Valley and east-dipping Dixie Valley, and occurs adjacent to a seismic gap with no recent surface breaks and inferred concentrated stress, localized dilatation on high-angle faults appears to be the dominant control for the location of geothermal cells along the DVFZ. The occurrence of the geothermal cells coincide with zones of dilatation along the fault zone and seem to be controlled by the intersection of major north-trending structures with the more northeast-trending fault zone.

The only area within Dixie Valley that has been studied extensively is the DVGW with established production and injection wells supplying the power plant now owned and operated by Terra-Gen and several dry to sub-commercial wells. Within this small segment of Dixie Valley, we observe the DVFZ comprised of the range-bounding fault and the valley-bounding piedmont fault, which are considered

the major thermal fluid-bearing structures within the fault zone. These two structures are not believed to possess extensive lateral permeability along their entire length, but rather are thought to consist of intermittent zones of dilatation and compression depending on the orientation of faults and fractures with respect to the current stress regime. Fractures occurring within zones of dilatation along the DVFZ, assessed as steeply dipping fracture sets both parallel and anti-thetic to the main east-dipping NE-trending fault trend (see [Section 6.1.1](#)), are optimally oriented for extensional failure and should create a localized, naturally-occurring open network of permeability capable of geothermal fluid production.

The main production areas supplying the power plant are to the north in section 33, and to the south in sections 7 and 18 ([Figure 30](#); [Section 6](#)). While there is shallow interconnectivity between these two areas, there is no evidence of production-depth interconnectivity. The shallow interconnectivity is currently used to facilitate the injection well array in both areas. All production (Section 7 and 33) is being derived from dilated segments within the fractured hanging wall block of the piedmont fault. Well 36-14, located approximately two miles to the west of the sections 7 and 18 production area, bottomed near the range-front segment of the DVFZ, had non-commercial geothermal production with a significantly higher temperature than that of the wells supporting the power plant, with no evidence of deep connectivity to the production wells based on the limited data available to this project. It should be noted that the significant downhole permeability and downhole productivity in 36-14 was found only in the last 30m (100ft) of the well trajectory. The well data show that within a distance of 10km there are three separate geothermal cells. There is thermal evidence that the piedmont fault extends into, or plays a role in the geothermal system encountered in the DVPP area around well 62-23A (see [section 6.3.2](#)). While geophysical data extends this piedmont structure throughout the entire length of the DVGW ([Figures 13 & 14](#)), we know that there is no single normal fault template that can describe the locations of geothermal cells in Dixie Valley. Instead, the occurrence of geothermal cells is dependent on the more north-trending faulting intersecting the current northeast-trending faults, altering the localized stress conditions and creating zones of dilatation.

The thermal fluid producing components of the hydrothermal geothermal resource at Dixie Valley are dependent on the:

- fault and fracture orientation;
- irregularity of fracture surfaces that create asperities and force open the fractures following shear slip;
- degree of open fracture permeability at depth;
- magnitude of localized stresses with respect to the current stress-regime;
- lithology of rocks and sediments in and adjacent to the fault zone; and
- degree of sealing within the thermal fluid-bearing faults and fractures.

The major domains of the hydrothermal system are considered to be:

- intermittent dilatational zones along the piedmont fault including associated fractures and antithetic faults;
- fractured permeable zones within the Miocene basalt that truncates the piedmont fault within these zones of dilation;
- Limited permeability within the intervening structural block between the steeply dipping range-front and piedmont faults, extenuated by cross-faulting which connect the two structures; and
- intermittent dilatational zones along the range-front fault including associated fractures.

### 7.5.2 Engineered Geothermal System

The commercially exploitable EGS portions of Dixie Valley geothermal resources are dependent on the conductively heated rock juxtaposed to active geothermal cells/systems. Important parameters include temperature, stress-regime and the lithologic characteristics within the fault zone and surrounding rocks at depths of much less than 5km (16,400ft). Temperatures >200°C (392°F) are known to occur along a large region in and adjacent to the DVFZ at depths of ~2-3km (6560-9840ft). Coarse crystalline and metamorphic rocks such as the Cretaceous granodiorite, Boyer Ranch quartzite, and Jurassic low grade metamorphic and igneous rocks possess the favorable rock mechanical properties for EGS stimulation. Prime areas of interest include hot, brittle and relatively unfractured rock adjacent to the current production field and the hot area with limited fractures between the Dixie Comstock geothermal cell and the Hare and Mississippi Canyons geothermal cell(s)/systems(s). The potential EGS geothermal resource in Dixie Valley can be defined within the following three domains:

- the intervening structural block between the steeply dipping range-front and piedmont fault where there is low to no naturally-occurring permeability;
- zones of compression along the range-front and piedmont faults where natural induced stresses are keeping the fractures closed;
- sealed zones of dilation along the range-front and piedmont faults; and
- the footwall block of the range-front fault, and beneath, at least, the eastern portion of the Stillwater Range.

Optimal EGS targets are subsurface regions that are hot, have low permeability, are not proximal to a fault zone, and are comprised of brittle rocks that are under the correct stress conditions to produce open fractures. An example of a potentially favorable EGS target region is the DVPP area ([Figure 1](#)) where there exists very hot, non-producing wells 36-14, 62-23A, and 66-21 located a few kilometers south of the producing area. These are all low permeable wells within suitable rock types, with the exception of 62-23A which likely intersected brittle rocks (Jz), but bottomed out in the Triassic meta-sediment section, considered not capable of holding fractures. This favorable region includes the area around the Section 10 fumaroles away from the range-front fault, which is very hot at near surface conditions, and contains a substantial block of intrusive rock, part of the Jurassic igneous complex, in the subsurface. The area lying between the Dixie Comstock geothermal area and the Hare Canyon geothermal area, a zone in which well 45-14 is located, also shows a high potential for EGS development, although the non-optimal EGS rock type at depth could be an important negative factor. The high measured  $S_{hmin}$  within 45-14, could likely be overcome through EGS stimulation. Countering the poor lithology, there appears to be a large region that is EGS favorable with respect to temperature. Somewhere in the 45-14 area there must be convective fluid flow from depth indicating permeable open structures that can be accessed through EGS techniques. Additionally, the area surrounding the permeable portions of Dixie Meadows, just to the south, also shows some EGS potential.

Our knowledge of the temperature distribution is limited to deep geothermal exploration and production wells, deep and shallow temperature gradient wells, assessment of controlling structures, and leakage of geothermal fluids and related chemical reactions on the ground surface within Dixie Valley. We can expand our thermal mapping by the identified Vp-temperature relationship, inferences from MT, possible geothermometry inferences, etc. No potential EGS targets are identified under the Stillwater Range or adjacent to the intra-range faults at this time due to the lack of any EGS indicator data at depth. We speculate that the range itself holds EGS potential due to (1) the drilling of 36-14, (2) the mining exploration hole referred to as the Bolivia well that encountered warm water, (3) zones of alteration found in the intra-range faults, (4) occurrence of active fumaroles at the range-front boundary and (5) conductive modeling that show the range is an area of high heat flow.

## 8. EGS Favorability and Trust Mapping

### 8.1 Introduction

A variety of exploratory geostatistical techniques were applied to select geoscience parameters to (1) quantify the qualitative geoscience relationships described in [Section 7.3](#), (2) test relationships independent of the qualitative geoscience correlation discussed above; and (3) explore if parameters can be statistically quantified to be used in the formulation of the baseline EGS Favorability Map. The first two points are discussed in [Section 7.4](#). This section describes:

1. the GIS database created for the EGS Exploration Methodology project;
2. parameters derived from the various geoscience data-sets;
3. the method of gridding the data within the Project Area and Wellfield Calibration Area;
4. exploratory geostatistical approaches and how the statistics factor into the EGS Favorability Map;
5. the generation of the favorability and trust maps; and
6. the findings of the favorability and trust maps.

### 8.2 GIS Database

As described in [Section 7.4.1](#), the project produced a number of data management and data visualization challenges. The project required that a large amount of varied data be acquired, produced, and interpreted from a number of different sources. As such, an efficient and effective method for storing, managing, and updating these various data sets early in project development was needed.

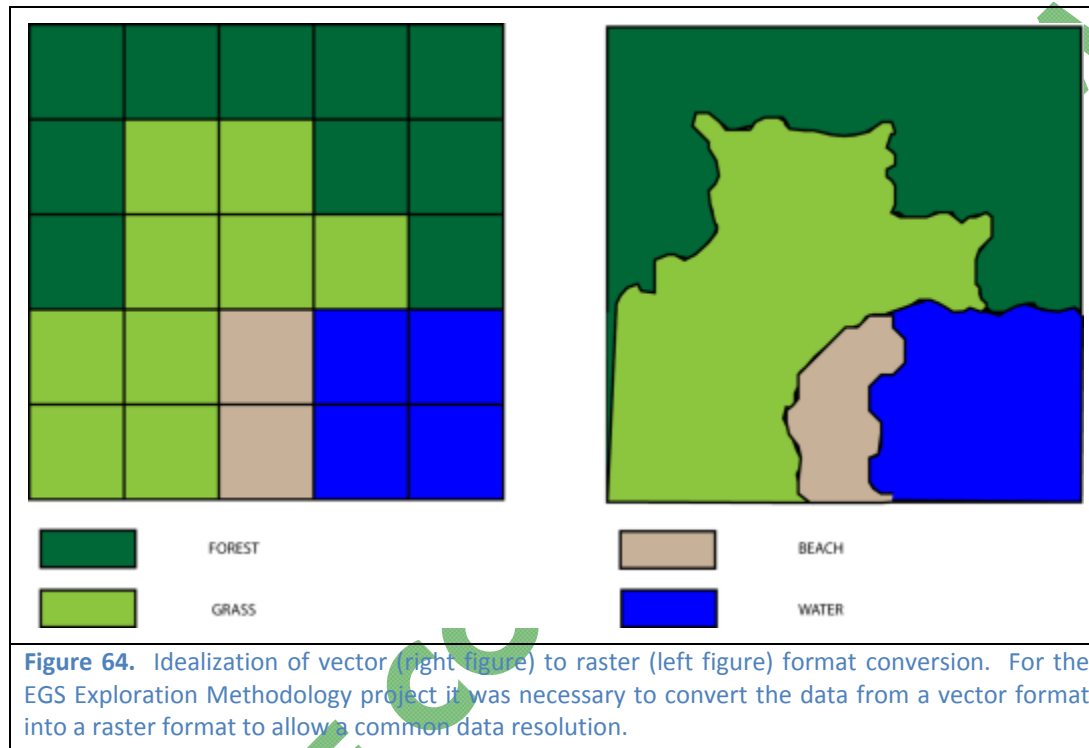
The first step in addressing these issues was polling individual task leaders ([Section 1.4](#)) for an understanding of the format and quantity of data that would be provided before deciding the optimal data container to use. This also provided an opportunity to assure that the task leaders providing the data and the initial geostatistics task leader, Dr. Edward Isaaks and later in the project, Dr. Fletcher Ibsen, were aware of each other's requirements. This process was accomplished by a series of individual telephone conference calls to the task leaders that culminated in a conference call to share the findings and initial conclusions.

We use an *ESRI ArcGIS* geodatabase (GDB) for the project. It provides a simple data container compatible for *ESRI* file types (".shp", ".lyr"), many tabular data types (".csv", ".txt"), and *Microsoft Access* data files (".mdb"). The GDB format is a relational database that combines the inheritance of object-oriented databases with the ability to assign relationships to the data, and ties tabular data, also known as attribute data, to spatial data (physical location). This allows data management in a traditional database format, while allowing for the additional functionality provided by the spatiality of the data such as interpolating data between points. *ArcGIS* is an even better fit when considering that one of the objectives of the project is to produce an EGS favorability map. For example, *ArcGIS* provides tools that greatly simplify the process of weighing the various data sets to produce favorability values. This does require, however that all data have the same resolution, a requirement that creates a significant data management hurdle that is addressed below.

To describe the complexity of the data set resolution issue, it is important to first discuss the difference between vector and raster data sets. Vector data is represented by points, lines, or polygons. It is discrete data at a discrete location. Vector data is generally used to represent things like roads, well locations, and lease ownership. Raster data is represented by pixels or grids. It is data that is generally interpolated or measured across an area. Raster data is generally used to represent things like elevation,

smooth contours, and interpolated data. Each data type has its own advantages and disadvantages (Figure 64).

Different data sets use different data types. We use gravity/magnetic data as an example to illustrate the difference between vector and raster data. Gravity/magnetic data are generally collected at discrete points where the sensor makes a measurement. The data that is collected is vector data, i.e., discrete measurements at discrete locations. This data is then often modeled across a broader area between the measurement stations. The data produced by the model is raster data, i.e., gridded or pixelated across a surface.



The “discretization” or “gridding” of the vector data and modifying existing raster data to achieve identical resolution across all the data sets was necessary before *ArcGIS* could process the models used to create a favorability map. This process required that a common raster or grid be created and that the discrete points are moved into the grids as accurately as possible. This process is either achieved by utilizing existing data models to output at the necessary resolution, or by hand, placing a grid over the vector data and assigning the values which occupy the majority of each grid block.

This method produces data at the same resolution and as such, it can be directly compared as “apples to apples.” In other words, the data values for one data set in each grid square can be compared directly to values in another data set for the same grid square. This is critical for not only creating a favorability map, but also providing a data format for performing statistical analysis. The downside of this process is a loss in data fidelity, e.g., edges that were clearly defined in the vector data set can become difficult to detect in the raster data. In generating the raster data, a data point in one grid square that does not comprise the majority of the grid is not considered in the analysis. For this reason, the original data sets in vector format are preserved.

### 8.3 Description of Parameters

Exploratory data methods (geostatistics) were applied to a variety of selected geoscience parameters. Task Leaders provided potential parameters (numerical and categorical) derived from their respective field and/or models. The purpose was to (1) create a baseline data set for the Baseline Conceptual Geothermal Model, (2) provide parameters that could be used to predict rock type, temperature, or stress conditions, and/or (3) provide additional sub-parameters that could be used in the formulation of the EGS Favorability Map. These sub-parameters would be used in conjunction with the major three parameters determined critical to determining the conditions suitable for EGS. The parameters are analyzed qualitatively and quantitatively using geostatistics. The data types are directly measured, modeled/calculated, or inferred/assigned based on SME and have varying resolution depending on the model.

A discussion of all the data parameters is given in Appendix 15 and also discussed in [Section 7.4.1](#). Data under analysis for the baseline model include lithology type and associated lithologic parameters (including density, strength, internal friction, fracture intensity), vertical stress, combined gravity-magnetic inferred lithology, temperature, resistivity derived from MT,  $V_p$  derived from the baseline seismic model, Coulomb stress change and strain from a stress model, presence of a fault, and geochemical indicators from production fluids and springs. These data represent the available baseline data set, and while they were used for exploratory statistical analyses, not all of the parameters mentioned were used in the formulation of EGS favorability maps. Other parameters not incorporated in the statistical analysis but discussed among the Project Team include but are not limited to temperature gradients, geothermometry, seismic directionality, and compression and dilated zones based on the structure analysis.

As discussed earlier, there are three parameters of interest for the purpose of producing favorability maps: temperature, lithology, and stress. A discussion amongst the team resulted in the decision to include four sub-parameters in describing stress: compression/dilation zones, fault orientation, existence of mapped faults in a cell, and *Coulomb* stress modeling data. These are the parameters of focus for the favorability mapping process, though all collected data that could be represented spatially made it through the following process into GIS software.

### 8.4 Gridding

Data for the project was gridded into  $500\text{m}^2$  or  $500\text{m}^3$  cells with respect to the following domains:

1. Along the cross-sections C-C', D-D', E-E' and F-F' for use in the statistical analysis and referred to as Section Data (Section 7.4.2)
2. With respect to wells for use in the statistical analysis and referred to as Well Data (Section 7.4.2)
3. Along the cross-sections A-A', B-B', C-C', D-D', E-E', F-F', G-G', and H-H' and applied to corresponding cells in the Calibration Area with interpolation and extrapolation techniques used on applicable data sets
4. Within the Calibration Area, consisting of  $500\text{m}^2$  cells, and used for the generation of the EGS Favorability Maps.

The cross sectional data was gridded (see [Section 7.4.1](#)) to (1) introduce the process of data gridding to the task leaders and (2) provide a initial data set in the Calibration Area that could be interpreted statistically. Since the cross sections were defined spatially, it was possible to produce data across these sections for all data sets. The process of producing these raster data sets was relatively straightforward.

To create the favorability map, the data sets were gridded in a plan view format, within pre-defined cells dividing the Calibration Area, and from the top-down along 12 horizontal slices extending from +1km asl to -4km asl (3300ft asl to -13,000ft asl). Since the grids have a finite location in space, the data in the cross sections can be directly assigned to a similar grid in a top down alignment. The data was then interpolated between cross sections and extrapolated when feasible. In situations where data accuracy or coverage was lacking, it was necessary to leave grid values empty to maintain output data integrity. At this point, the relationships between the data sets required additional definition prior to producing the EGS favorability map. This process is explained in the following sections, with a special focus on the statistical analysis.

Data gridded along the horizontal slices comprising the Calibration Area includes lithology, gravity-magnetic inferred lithology, temperature, geochemical indicators, presence of a structure, fault/fracture orientation data inferring favorable/non-favorable stress conditions, zones of compression and dilation, MT resistivity data, and Vp. This data-set will be used to formulate the Baseline EGS Favorability Map within the DVGW.

### 8.5 Data Conversion

The majority of gridding work was performed in *Microsoft Excel*. This program was used because data (1) can easily be exported to *GIS* software, (2) can be edited in a tabular format or as an overhead plan view “map”, and (3) can be automated for repetitive tasks using *Visual Basic* macros. Data was applied to *EXCEL* templates of the gridded cross-sections and plan view maps by either the Task Leader or SME, or AltaRock personnel.

The first step in the process of the data conversion was to generate a workbook with eleven worksheets, made to represent the depth slices every 0.5km from +1km asl to -4km asl. [Figure 65A](#) shows the *EXCEL* template of the Calibration Area, with each cell representing a 500m by 500m grid-block. [Figure 65B](#) presents one of the thermal worksheets as an example. The top layer was selected at 1km asl because data values existed across the majority of the Calibration Area at that elevation and approximates the surface of Dixie Valley. Data already produced and gridded for the vertical cross-sections was then transferred into these horizontal sections. This was accomplished by picking the values from the cross-section data that lined up most accurately with the cells in plan view. The process was automated by a script and repeated for all data sets. In this way, a significant amount of data was filled into the plan view format without SMEs having to produce new data sets.

The second step in the process was to add “hard” (measured) data values. The wells with existing data were located in the plan view grid and values were filled into cells at each depth where data was available ([Figure 65A](#)). This was done for every well and data set for the available hard data. Most of these values are from well logs and include temperature, lithology, and some geochemistry information.

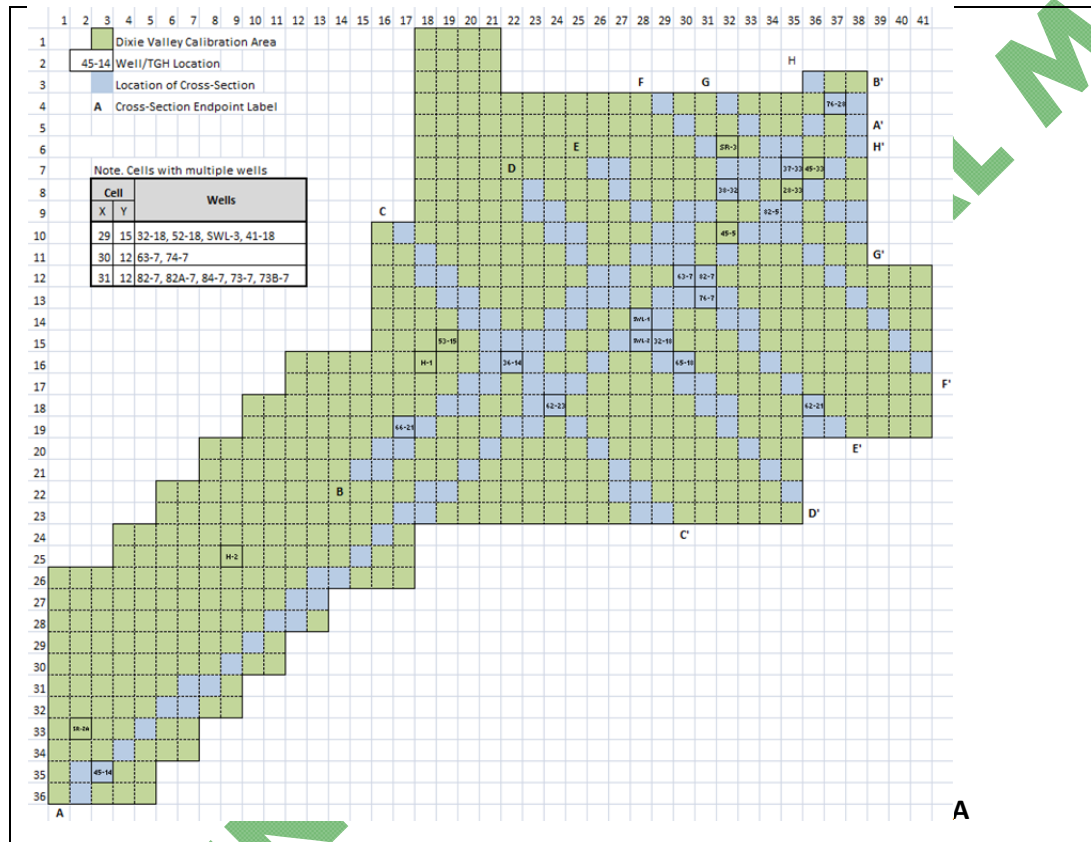
Data was then filled in between some data sets by interpolating between the existing hard and modeled data values. This was done for numerical data sets such as temperature and MT data using an automated interpolation function that was limited to a 1km (3300ft) radius around an existing data value. For categorical data sets, lithology and gravity-magnetic inferred lithology, a manual interpolation was applied between the cross-sections and hard data points (wells). The interpolation method used is described by the following equation:

$$V_t = \frac{V_1 + V_2 + V_3 + \dots + V_n}{n}$$

where  $V_t$  is the total value and  $V_n$  represents the surrounding cells (up to 8 maximum).

In most cases existing models included values to -4km asl or were extended to that depth by the SMEs. For non-numerical data sets or ranges where no data existed at depth, inferences were made. For example, temperature data was inferred to -4km asl by downward continuation of the thermal gradient measured in a well.

Once all depth slices were populated for every data set, the data was converted from plan view to x, y coordinates for export to GIS software. The UTM coordinates for the center of the cells in the Calibration Area (see Sections 7.1.3 and 7.4.1) were calculated by starting at the SW corner of the Calibration Area which coincides with the WGS 1984 UTM Zone 11 projection at 412000 Northings and 4412000 Eastings and adding 250 in each direction. From there, each cell's center can be identified by adding 500 for each cell north or east. Z values were determined from the depth slices and are relative to sea level.



BASELINE

MODEL

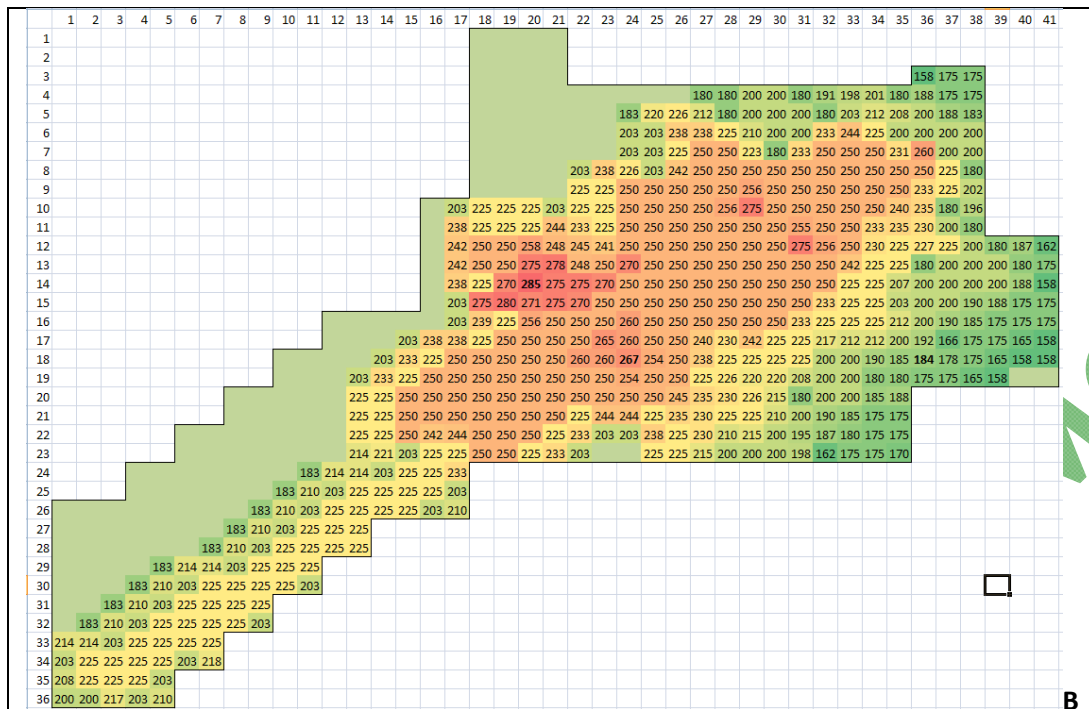


**Figure 65. A.** EXCEL template for the Calibration Area, with 500m<sup>2</sup> cells designated as either derived from a cross-section (light blue) or a well (outlined and labeled). **B.** EXCEL spreadsheet representing plan view slice of the thermal model at 2.5km below sea level. Bolder values represent measured data in wells.

The third and final step in the process was to import the point data into *ArcGIS* and convert the points to raster values. Raster values are very similar to the EXCEL plan view cells in the gridding process. Each raster cell has a location and a value. The values present in the raster cells are the same as the values in the EXCEL cells, but GIS software enables the data to be utilized in a more robust manner, such as performing spatial analyses or overlay functions. Figure 66 illustrates the process of converting from plan view, to tabular data, and then raster data in GIS.

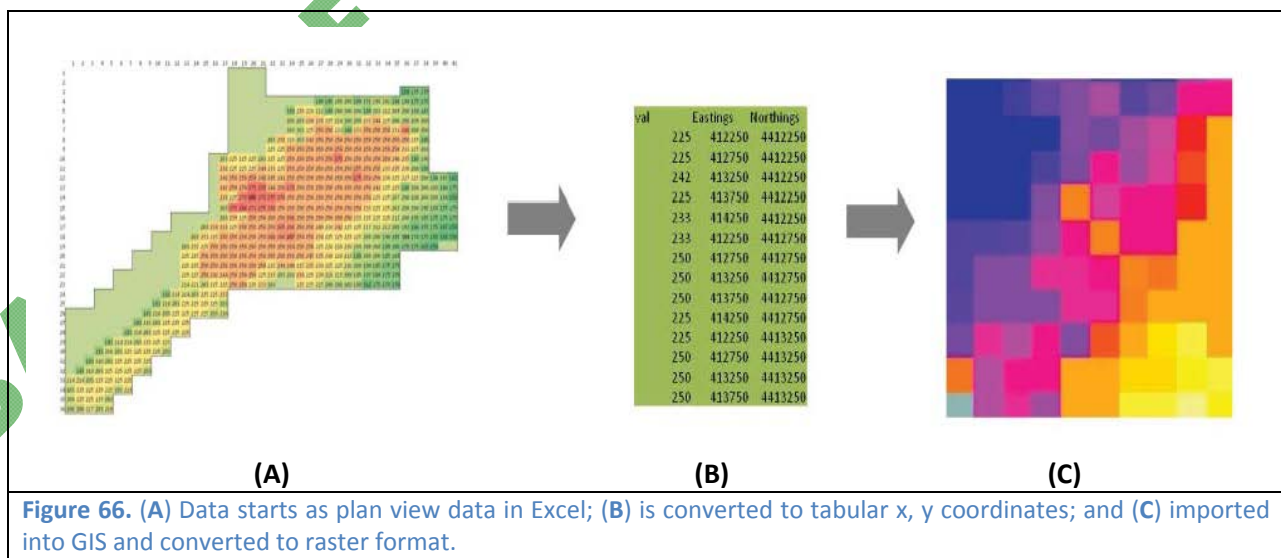


**Figure 66. (A)** Data starts as plan view data in Excel; **(B)** is converted to tabular x, y coordinates; and **(C)** imported into GIS and converted to raster format.

## 8.6 Integrated Geoscience Sections for EGS Favorability

Data generation for the three key EGS parameters of interest (lithology, temperature, and stress) is described in this section.

### 8.6.1 Lithology

The lithology<sup>8</sup> parameter incorporates the known lithologic units from the geologic sections ([Section 7.3.1](#)) with inferences from the gravity-magnetic inferred lithology ([Section 7.3.1](#)) and MT resistivity data ([Section 7.3.1](#)) to create an integrated lithology parameter. The gravity-magnetic inferred lithology sections B-B' through F-F' and MT array C were evaluated with their corresponding geology sections (see Plate 1, and Appendix 12). The gravity-magnetic inferred lithology incorporated the occurrence of a magnetized Jurassic unit (Jg) and allowed the Jurassic section (Jz) to be distinguished into magnetic and non-magnetic rocks (Jznm), see discussion in [Section 7.3.1](#), which have differing EGS implications. Where there was no well or surface data to supersede, the geologic sections were modified to (1) incorporate the presence of Jznm within the aforementioned geophysical sections, (2) alter the depth to basement and overlying low density basin-fill using the gravity-magnetic sections, (3) alter the overall thickness of the Jurassic section using the gravity-magnetic sections, and (4) incorporate the very high resistivity bodies beneath the Stillwater Range as granodiorite. A major assumption in the lithology definition is that the very high resistivity below the Stillwater Range infers the presence of dry, unfractured granodiorite at depth.

### 8.6.2 Temperature

Temperature data has been derived from thermal sections presented in Plates 1 and 2 and is based on well data, shallow temperature gradients, and the conceptual convective model for the geothermal system active in the Calibration Area (Blackwell et al., (2005).

### 8.6.3 Stress Parameter

This parameter incorporates (1) fault/fracture orientation data, (2) Coulomb Stress Change/Dilatation from stress modeling results, (3) whether a structure is present or absent, (4) interpreted stress at structural intersections, occurrence of dilated zone (DZ), zone of compression (CZ) or neither.

#### *Fault/Fracture Orientation*

The GIS database was updated with the structures identified in [Figure 49A](#). Faults with a strike of N30°E-N60°E were considered to infer favorable stress conditions as a fault oriented roughly N45°E ±15° would have a proper orientation to exhibit normal slip within the current stress regime. Another assumption was that gridded cells that have a specified fault orientation could be used to infer stress conditions in the surrounding cells or within 500 meters. All other orientations that did not fall in the N30°E-N60°E range were considered unfavorable, while gridded cells with no specified fault are considered unknown and weighted with a neutral rating. Fault dip direction was poorly constrained in areas and only considered where applicable.

#### *Coulomb Stress Modeling*

Using *Coulomb 3.1* stress modeling (see [Section 7.2.2](#) and Appendix 13), a value of the expected CSC (-10 to +10 bars) and dilatation (-1 to +1 strain) can be calculated along a particular fault/fracture plane (for example, NE strike, 65° SE dip) within each given cell based on certain model constraints such as

---

<sup>8</sup> Note that in this report the term lithology and geologic formation are used interchangeably since each of the seven major formational units identified in the DVGW have specific lithologies.

strike, dip, rake and maximum displacements along associated segments of the various range-front faults.

### ***Fault Present/Absent***

Whether a fault is present or absent in a given gridded cell within the Calibration Area has a viability inference on EGS Favorability and so has been incorporated into the integrated stress parameter. All faults gridded in the Calibration Area were derived from : State of Nevada, QFFDB, inferred structures from Blackwell and Smith (2002), inferred structures from the structure analysis in this investigation and geophysical gradients (see [Section 7.2.1](#) and [Figures 49A](#) and [49B](#)), structures inferred by gravity-magnetic modeling, and structures inferred by MT arrays. The presence of a fault within a given gridded cell is considered unfavorable for EGS due to induced seismicity concerns and potential loss of circulation zones, while the absent of a fault is considered more favorable for an EGS target. This point was a subject of debate among the team as the presence of a fault in a cell, increases the probability of that cell containing a dense fracture network, which would potentially make it more favorable for EGS when ignoring induced seismicity.

### ***Compression and Dilated Zones***

The intersections of major N-trending faults with the NE-trending structures within the DVFZ occur in several notable locations in the Calibration Area ([Figure 48C](#)). A localized stress change occurs at these intersections due to the fault orientation relative to the greatest principle stress and the apparent active strike-slip component along N-trending structures. The expected zones of compression and dilation that occur at these structural intersections show a high level of correlation with shallow thermal anomalies, well productivity, occurrence of fumaroles and geochemical data (including helium R/Ra ratios). Thus, this parameter has also been factored into the integrated stress rating. Dilated zones infer optimal stress conditions for EGS as faults/fractures are optimally oriented for normal slip in current stress regime and relatively lower  $S_{hmin}$  magnitudes exist, while zones of compression would infer slightly less favorable stress conditions, not optimally oriented and higher  $S_{hmin}$  values. One complication with incorporating this sub-parameter is a dilated zone would be expected to have geothermal fluids present at depth (hydrothermal) within open fracture networks which may not be favorable for EGS.

## ***8.7 Favorability Mapping Process***

The favorability and trust (described in [Section 8.8](#)) maps were produced using *ESRI's ArcGIS 10.0* software. *ArcGIS* software has many functions built in for analyzing data in different ways. A weighted overlay function was run on the data sets, incorporating slices of different data sets at the same depth. The use of this weighted overlay function requires the conversion of the data values to favorability values. A favorability value defines the favorability of EGS being present at a scale of one through nine. This scale was selected because it provides a neutral value (five) to describe data values which are not necessarily favorable or unfavorable and four variations of positive and negative favorability (slightly, moderately, very, and extremely).

Weights were also assigned to data sets. The reason for this is that certain data sets have a higher overall impact on favorability. For example, one can reasonably infer that temperature is a more powerful overall indicator of EGS favorability than the presence of faulting in a cell. The higher a data set's weight, the more its favorability values affect the final favorability of a cell. This allows for data sets to have a variable impact on the output, based on their importance to overall EGS favorability.

The weighted overlay function takes values from different data sets and creates a weighted average sum that is the output value for every cell. The input values of each data set must first be converted to a numerical value on a set scale. For example, favorability maps were produced by assigning favorability

values on a scale of one through nine, with higher values indicating higher favorability, for each value in each data set, multiplying those values by each data set's weight (normalized to 1), then adding the sums of the weighted values in each cell. The following equation describes this process:

$$F_v = (d_0 * w_0) + (d_1 * w_1) + (d_2 * w_2) + \dots + (d_n * w_n)$$

where  $F_v$  is the favorability value for a cell,  $d_0$  through  $d_n$  is the favorability value of a cell's geoscience parameter data, and  $w_0$  through  $w_n$  is the weight for a particular data set (Tables 12 and 13).

A preliminary set of favorability values and weights used to create the initial favorability maps is described in Table 12. These favorability values/weights and maps were created to validate the methodology and data integrity. For example, if any glaring errors or obvious gaps in data were present, the input data would need to be scrutinized. No such errors or omissions were found in the draft maps, confirming the methodology with the output in line with expectations.

Before the final favorability maps were produced, a set of favorability values and weights needed to be created. To determine these values, an inquiry was circulated to the SMEs requesting that each SME express their opinion with respect to favorability and weight values, and the final version of these values was based on an unweighted average of all SME input received (Table 13). A method to determine favorability values quantitatively was discussed among the team, but not used to avoid a number of required assumptions.

### 8.8 Trust Maps

Upon review of the output of the preliminary favorability maps, a strong trend towards increased EGS favorability at depth was apparent. While this trend is a correct interpretation of the data used as input; the determination was made that it did not reflect our complete understanding (including our known uncertainties) of the region. While it is logical that more favorable lithological, stress, and thermal conditions exist at depth, our understanding of these regions is constrained by the quality and quantity of the data available. As a result it became apparent that a second set of maps, produced in a similar fashion as the favorability maps but describing the quality of the data used for input would assist in more complete understanding and assesment of the favorability maps.

Table 12. Preliminary weights and values used to test the generation of the favorability maps (see Section 8.7).

Temperature (.50 w <sup>4</sup> )	Fav Values <sup>1</sup>	Lith- ology (.30 w)	Fav Value	Stress Sub-parameters (.20 w)							
				C/D <sup>2</sup> (.05 w)	Fav Value	Fault Orientation (.05 w)	Fav Value	Structure Present (.05 w)	Fav Value	CSC <sup>3</sup> (.05 w)	Fav Value
100	1	QTbf	1	Compression	4	30-60	6	Structure	5	< -22	1
125	2	Tmb	6	Dilation	6	Other	4	None	7	-22	2
150	3	Jz	7	Neither	5	Neither	5			-14	3
175	4	Tr	4							-6	4
200	5	Kgr	9							0	5
225	6	Tv	4							6	6
250	7	Jbr	8							14	7
275	8	Jzm	7							22	8
300	9									> 22	9
325	8										
350	7										
> 374	6										
	3										

<sup>1</sup>Favorability Value

<sup>3</sup>Coulomb Stress Change

<sup>2</sup>Compression/Dilation

<sup>4</sup>Favorability weights

Each data value was scrutinized based on the method used to produce the data. While some data sets have a significant number of hard values, others are entirely modeled. A valuation of the data based on what we've described herein as a "trust factor" was then performed. The "trust factor" reflects the reliability of the data used to determine the favorability value on a cell by cell basis. As such, each cell of each data set was assigned a trust factor, either quantitatively or qualitatively. This trust factor was based on a scale of one through five, higher values indicating higher trust in the data, and is outlined in the following table (Table 14).

Hard data (5) is data which has been directly noted (e.g., geologic formation) or measured (e.g., temperature) in the field. Strongly modeled or interpolated data (4) is data which has been modeled or interpolated from a hard data point and is within one cell (500m) of that point. Weakly modeled or interpolated data (3) is data which has been modeled or interpolated, but is >500m from a hard data point and as such, is considered to be loosely constrained. Inferred data (2) refers to data which lacks hard value constraint, but can be inferred through other methodologies, such as thermal gradients for temperature data. Areas of no data (1) occur when no hard data are present to constrain values and no appropriate methodology exists to infer values.

The process of assigning these values to the existing data sets was primarily done manually in EXCEL. Hard data points, interpolated/modeled data points, and inferred data points had already been defined in the process of creating the original data sets. Each cell was assigned a trust value based on which of these methods was responsible for the data used and distance to the nearest hard data point. Six new data sets (temperature, lithology, stress factors) were created in this effort to describe the reliability of the original data sets. In some cases a trust factor could not be assigned to the modeled data directly due to a unquantified resolution or multiple inversions used in the modeling. In these cases, a value of 2.5 was used to assign a neutral value to the data (e.g. Coulomb stress model).

**Table 13.** Final favorability and weight values using averaged values and weights based on Subject Matter Expert input.

Temp <sup>1</sup> (.51 w <sup>5</sup> )	Fav Value <sup>2</sup>	Lith-ology <sup>6</sup> (.31 w)	Fav Value	Stress Sub-parameters (.18 w)							
				C/D <sup>3</sup> (.03 w)	Fav Value	Fault Orientation (.07 w)	Fav Value	Structure Present (.05 w)	Fav Value	CSC <sup>4</sup> (.03 w)	Fav Value
< 100	1	QTbf	1	Compression	4	30-60°	7	Structure	7	< -22	2
100	1	Tmb	5	Dilation	7	Other	4	None	5	-22	3
125	2	Jz	7	Neither	5	Neither	5			-14	3
150	2	Tr	3							-6	4
175	4	Kgr	9							0	5
200	7	Tv	3							6	6
225	7	Jbr	8							14	7
250	8	Jznm	4							22	8
275	9									> 22	9
300	8										
325	7										
350	5										
> 374	3										

<sup>1</sup>Temperature in °C  
<sup>2</sup>Favorability Value  
<sup>3</sup>Zones of Compression/Dilation  
<sup>4</sup>Coulomb Stress Change  
<sup>5</sup>Favorability weights  
<sup>6</sup>Lithology formations included the QTbf (Quaternary-Tertiary basin fill), Tmb (Miocene basalt), Jz (Jurassic mafic rocks), Kgr (Cretaceous granodiorite), Tv (Tertiary silicic volcanics), Jbr (Jurassic Boyer Ranch Fm), Jznm (Jurassic non-magnetic mafic rocks)

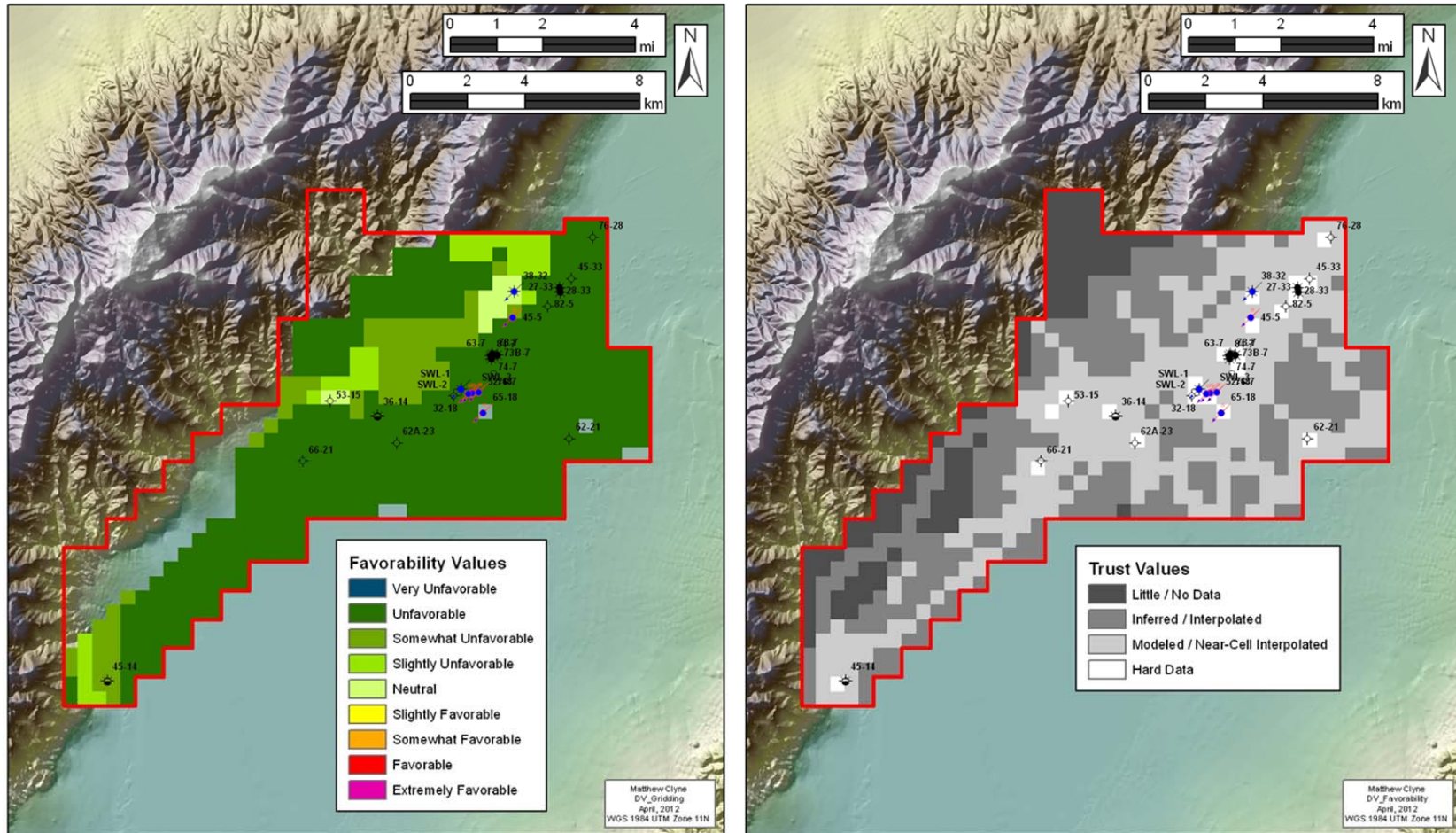
**Table 14.** Scale used to assign trust values to existing data sets

Trust Value	Description
5	Hard data (measured, e.g., well)
4	Strong interpolation / model
3	Weak interpolation / model
2	Inferred
1	No data

The same weighted overlay function to define the favorability value was then performed on the trust data sets. The scale was modified for the maps to one through five to accommodate the scale of the trust factors. The same weights were used as in the favorability maps to preserve the respective impact of the data sets. Favorability and trust map pairs from +1km asl to -4km asl in 0.5km increments are presented as [Figures 67](#) through [77](#) for average SME favorability values and weights. The favorability scale included in the figure is from 1-9 with 1 being represented by a dark blue and labeled *Very Unfavorable*, and a 9 being represented by magenta and labeled *Extremely Favorable*. The trust values scale shown is from 2-5, with 2 referring to little/no data (dark grey) and 5 referring to hard data (white).

BASELINE CONCEPTUAL MODEL

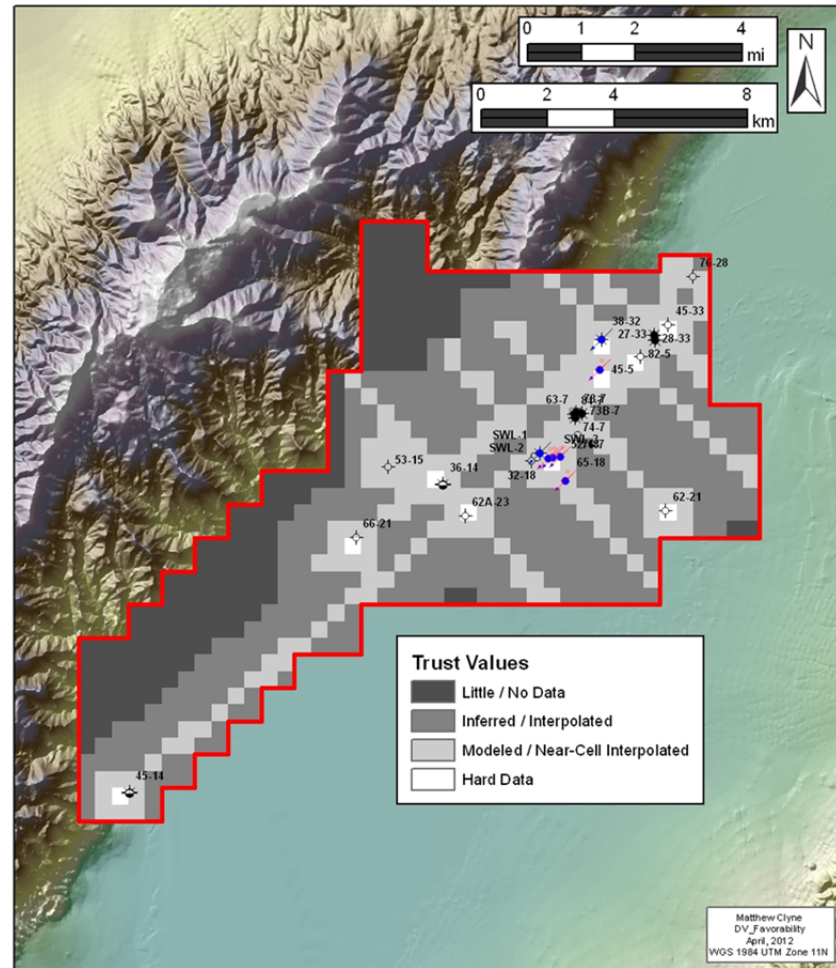
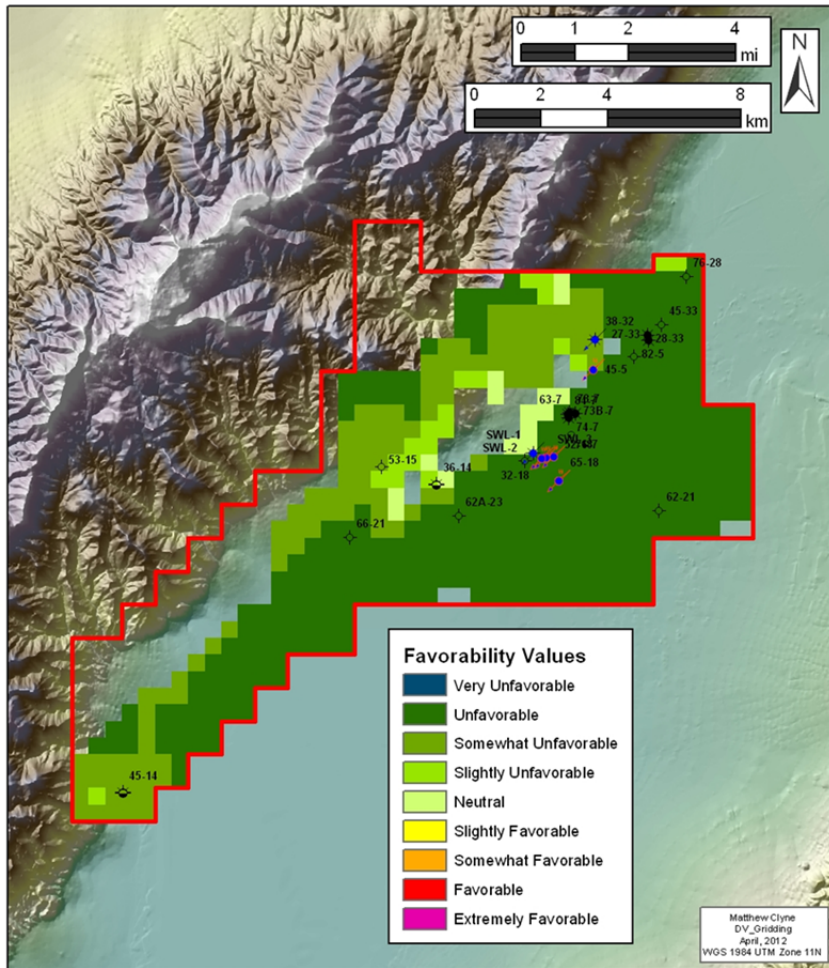




### EGS Favorability-Trust Maps: Averaged Data and Weighting Depth: 0.5km Above Sea Level

Figure 68. EGS Favorability map (left) and associated trust map (right) at 0.5km asl using average values based on Subject Matter Expertise input and weighting factors for temperature, lithology, and stress of 0.51, 0.31, and 0.18, respectively.

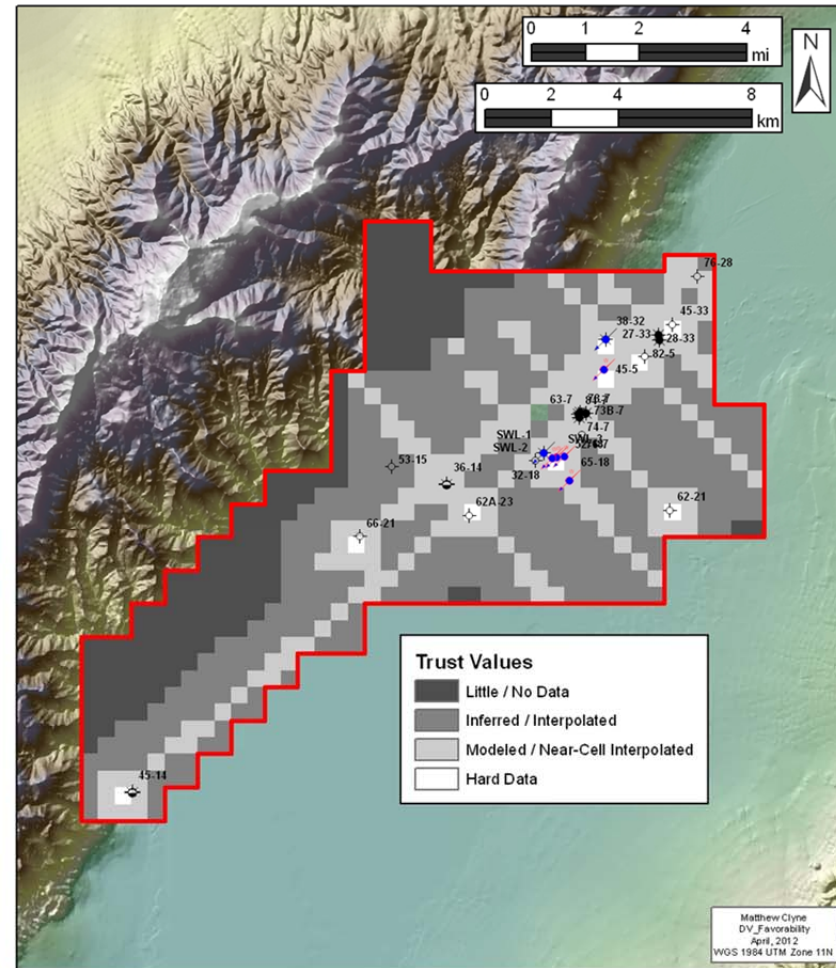
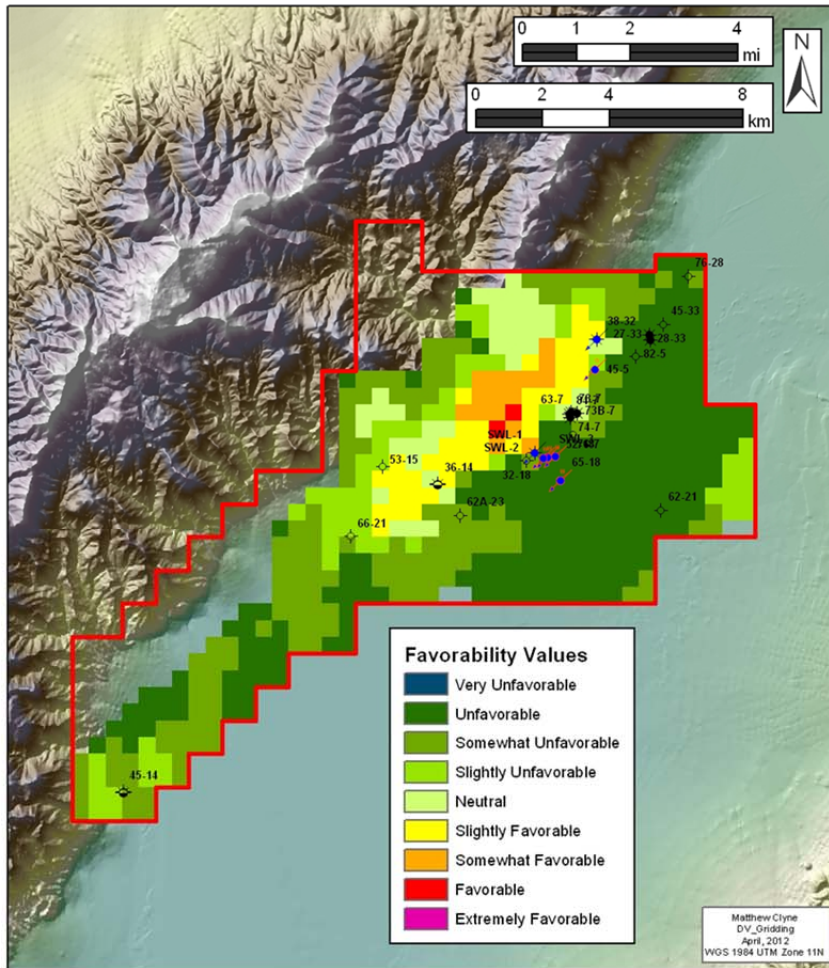
**BASELINE**



### EGS Favorability-Trust Maps: Averaged Data and Weighting Depth: 0.0km At Sea Level

Figure 69. EGS Favorability map (left) and associated trust map (right) at sea level (0km asl) using average values based on Subject Matter Expertise input and weighting factors for temperature, lithology, and stress of 0.51, 0.31, and 0.18, respectively.

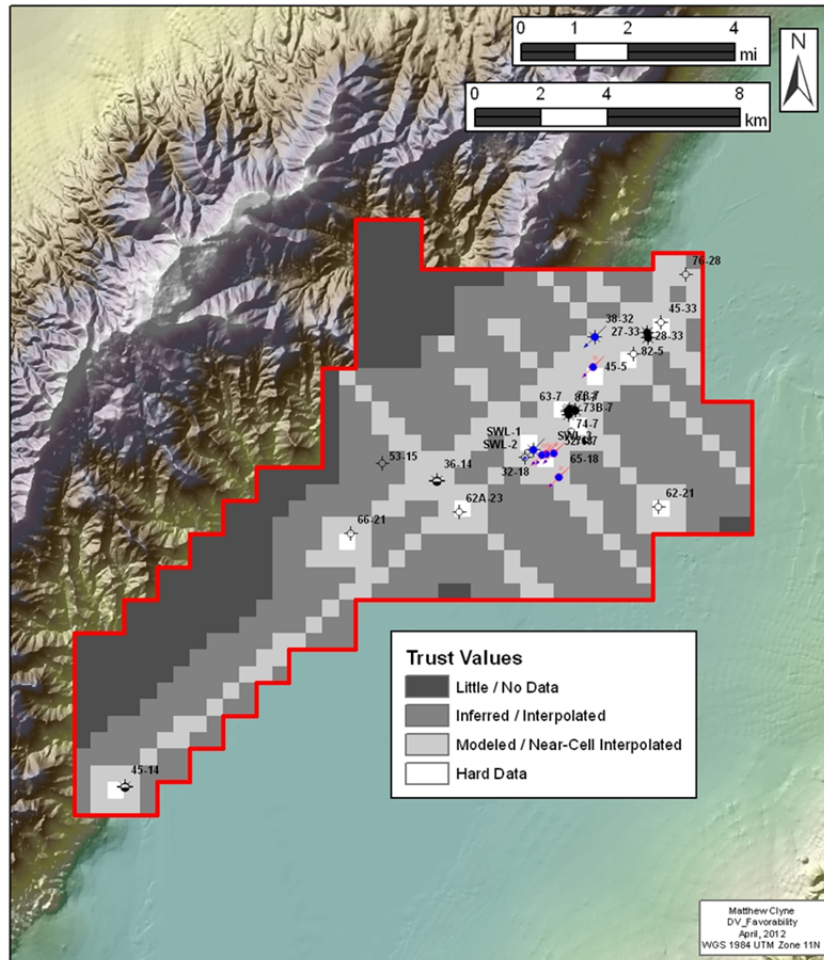
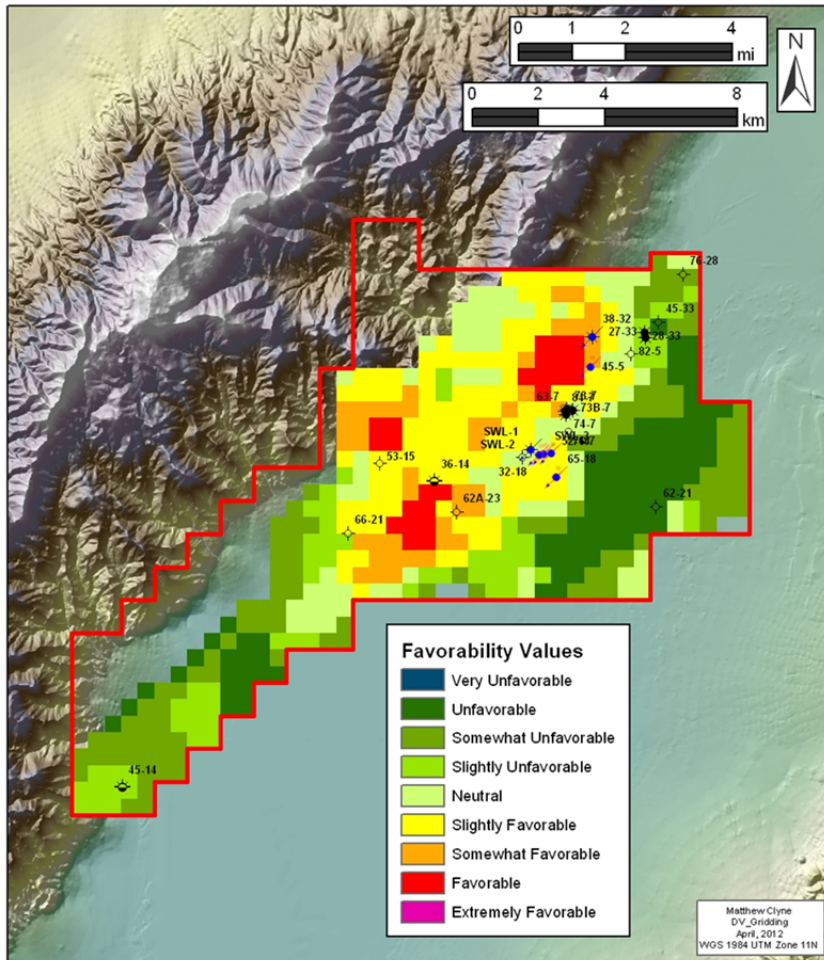
**BASELII**



### EGS Favorability-Trust Maps: Averaged Data and Weighting Depth: 0.5km Below Sea Level

Figure 70. EGS Favorability map (left) and associated trust map (right) at -0.5km asl using average values based on Subject Matter Expertise input and weighting factors for temperature, lithology, and stress of 0.51, 0.31, and 0.18, respectively.

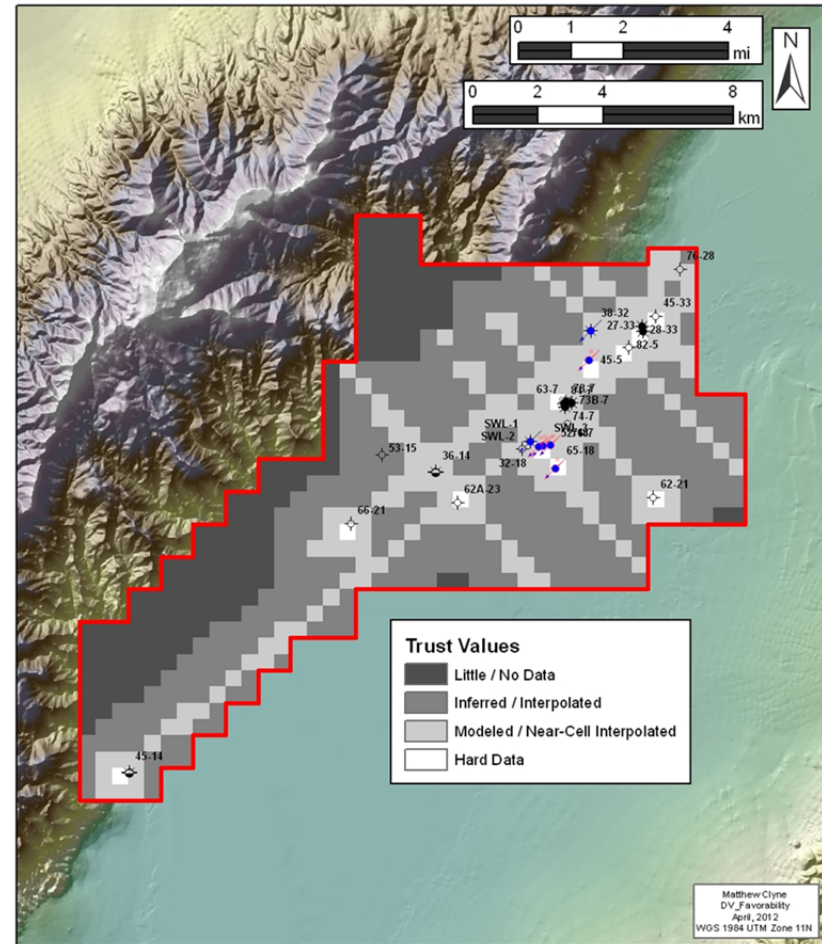
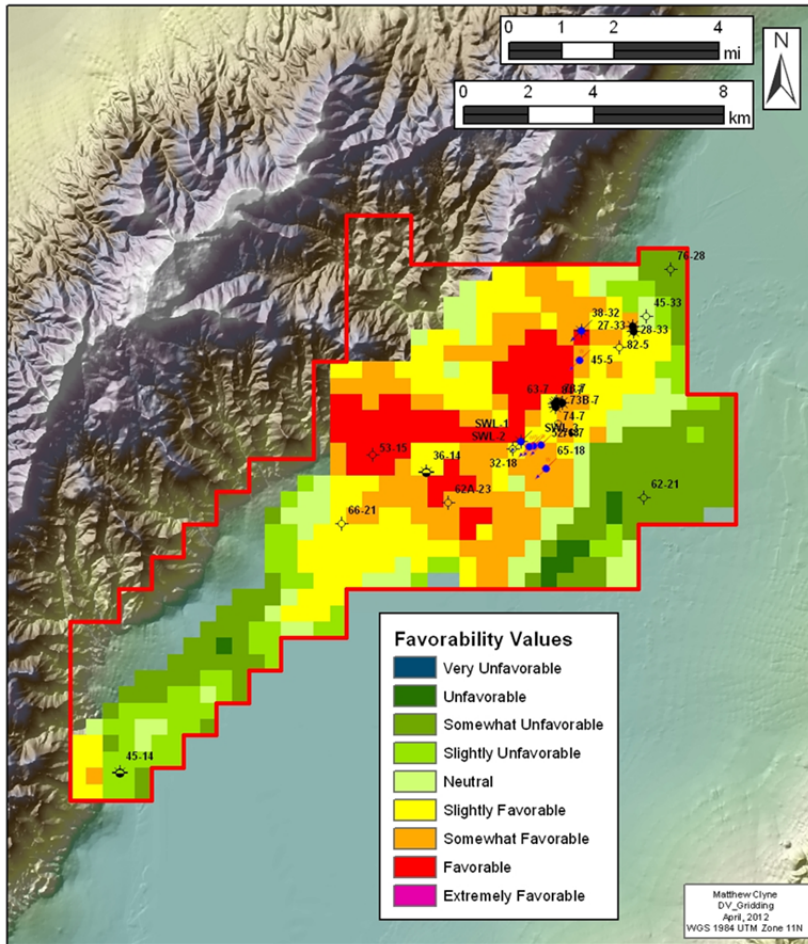
**BASEL**



**EGS Favorability-Trust Maps: Averaged Data and Weighting  
Depth: 1.0km Below Sea Level**

**Figure 71.** EGS Favorability map (left) and associated trust map (right) at -1.0km asl using average values based on Subject Matter Expertise input and weighting factors for temperature, lithology, and stress of 0.51, 0.31, and 0.18, respectively.

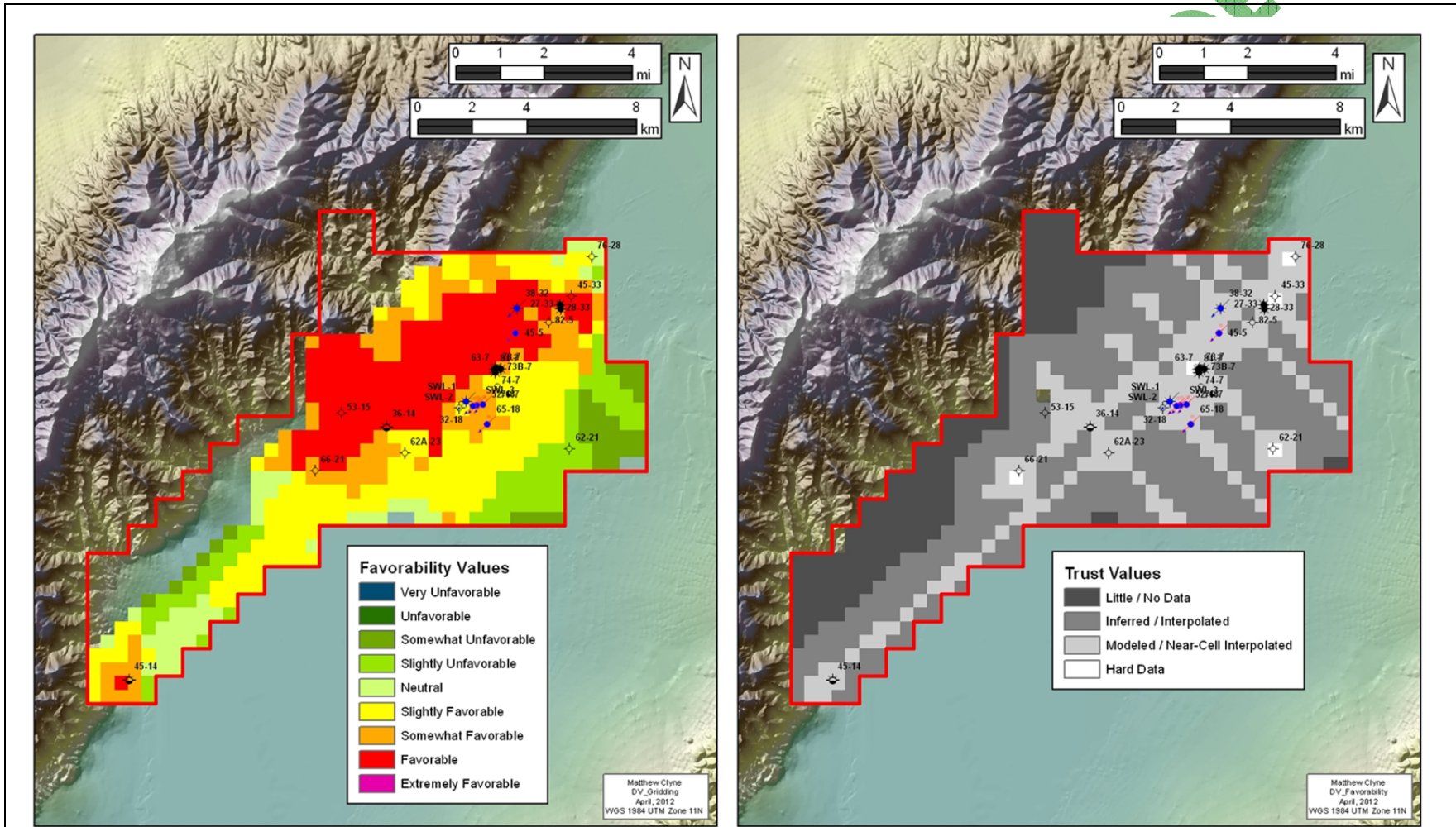
**BASSELL**



**EGS Favorability-Trust Maps: Averaged Data and Weighting  
Depth: 1.5km Below Sea Level**

**Figure 72.** EGS Favorability map (left) and associated trust map (right) at -1.5km asl using average values based on Subject Matter Expertise input and weighting factors for temperature, lithology, and stress of 0.51, 0.31, and 0.18, respectively.

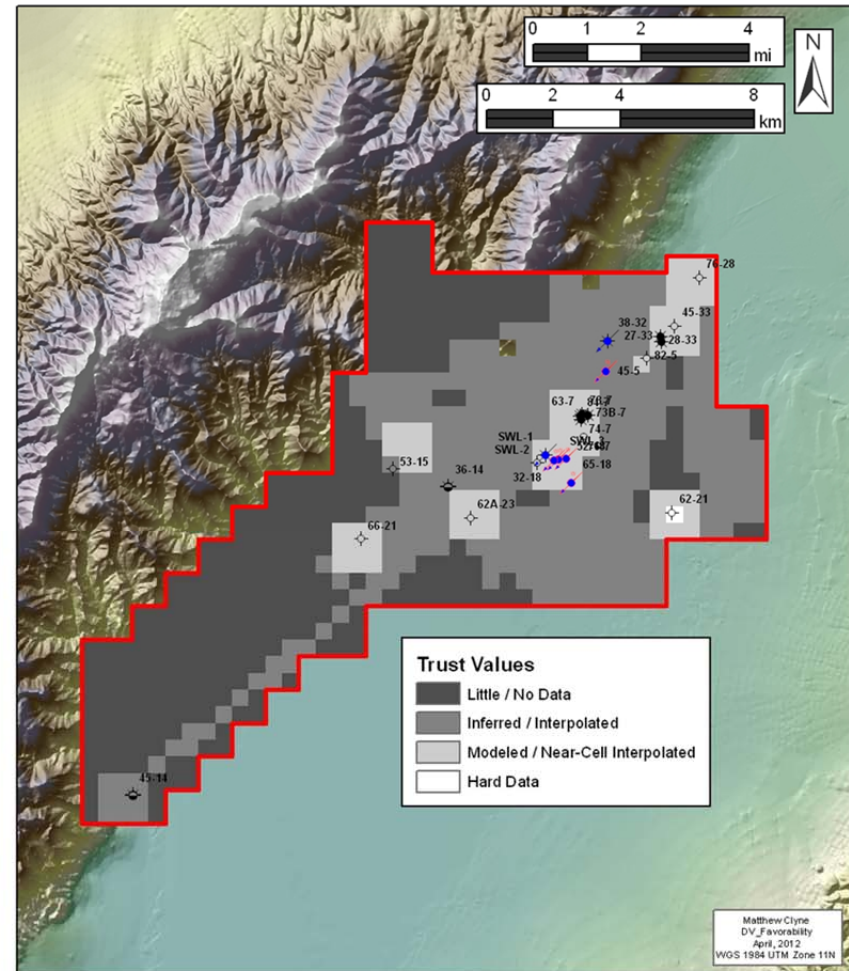
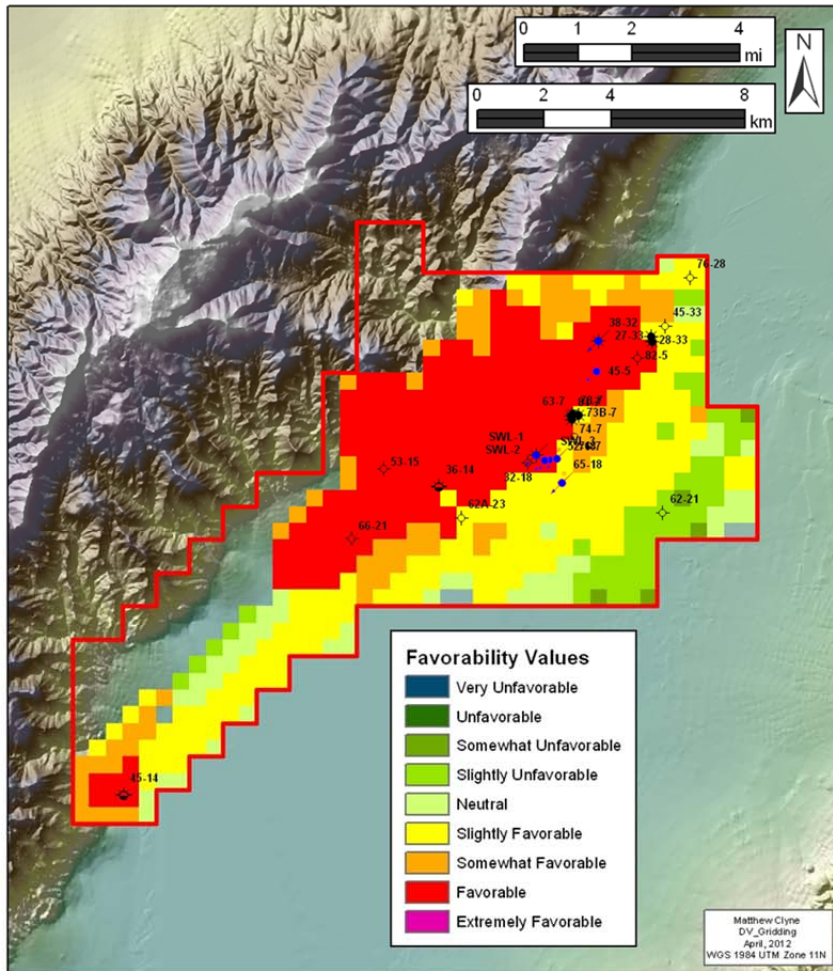
**BASIN**



**EGS Favorability-Trust Maps: Averaged Data and Weighting  
Depth: 2.0km Below Sea Level**

**Figure 73.** EGS Favorability map (left) and associated trust map (right) at -2.0km asl using average values based on Subject Matter Expertise input and weighting factors for temperature, lithology, and stress of 0.51, 0.31, and 0.18, respectively.

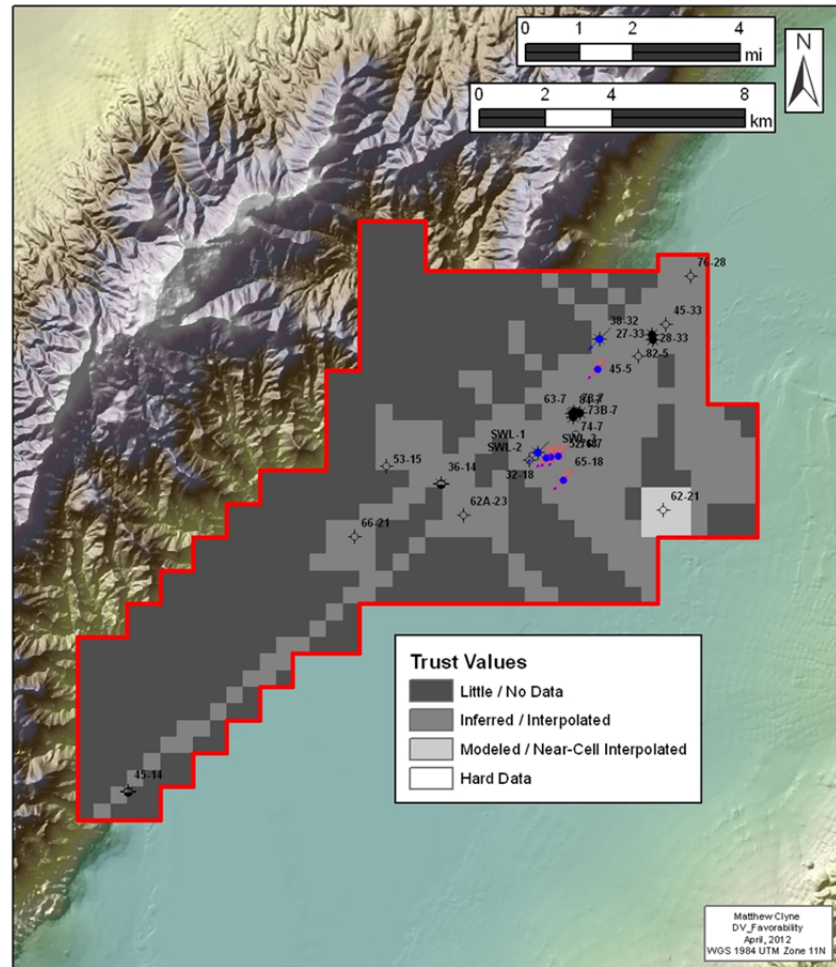
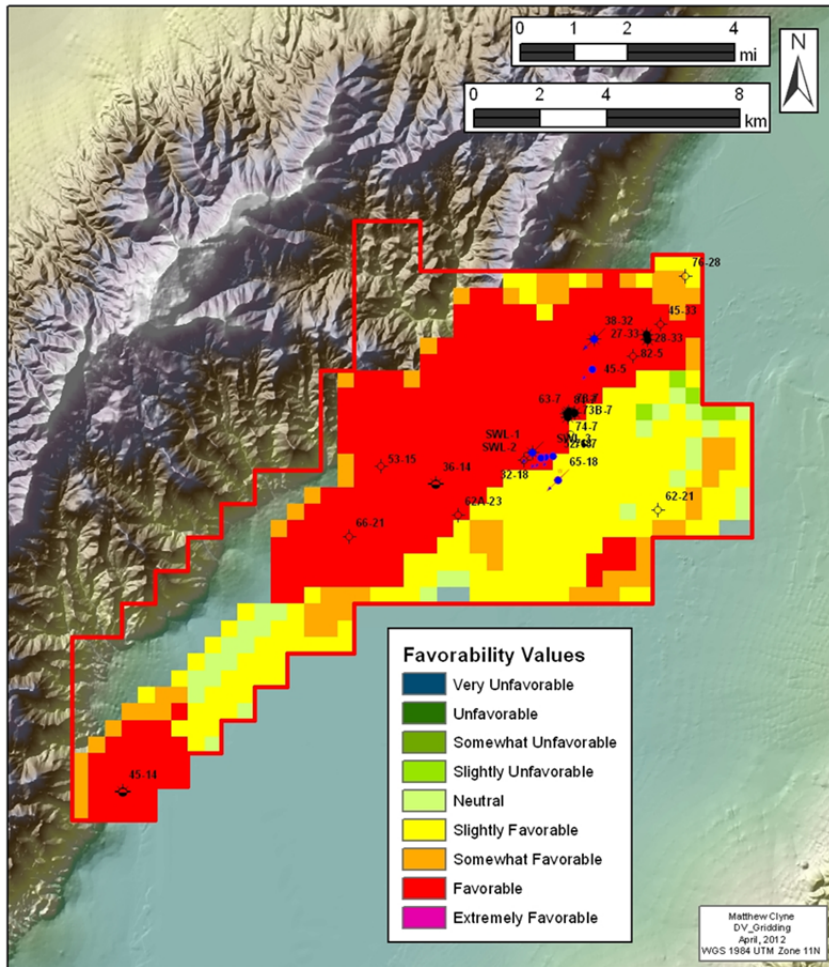
**BASEL**



### EGS Favorability-Trust Maps: Averaged Data and Weighting Depth: 2.5km Below Sea Level

Figure 74. EGS Favorability map (left) and associated trust map (right) at -2.5km asl using average values based on Subject Matter Expertise input and weighting factors for temperature, lithology, and stress of 0.51, 0.31, and 0.18, respectively.

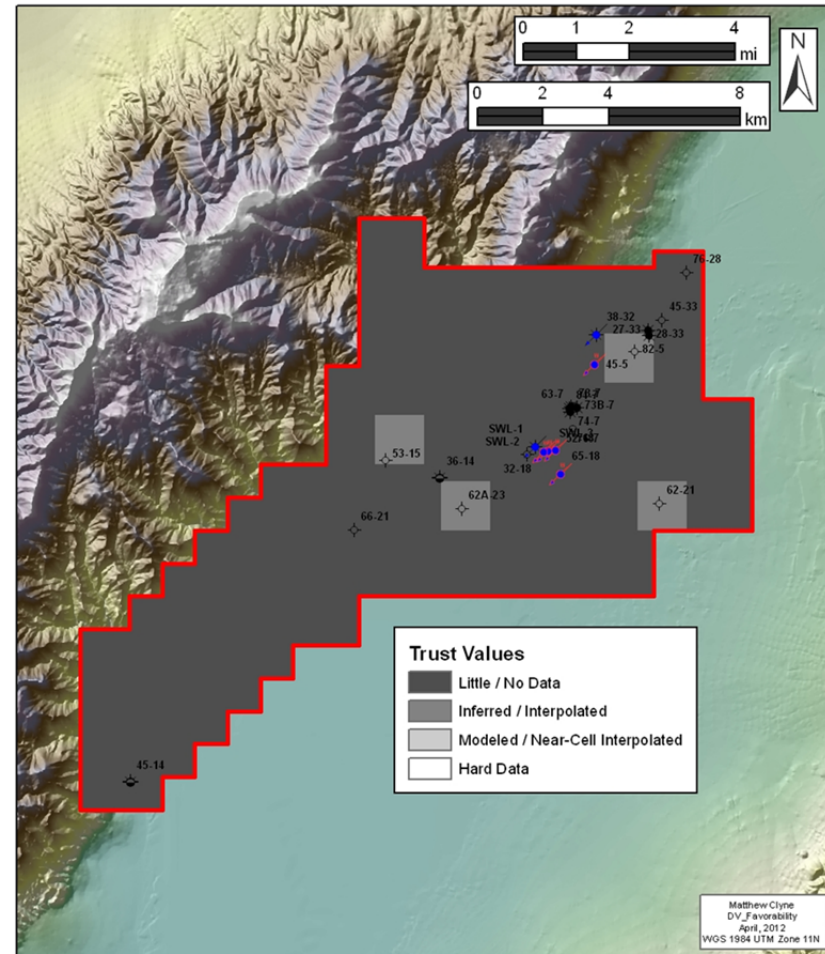
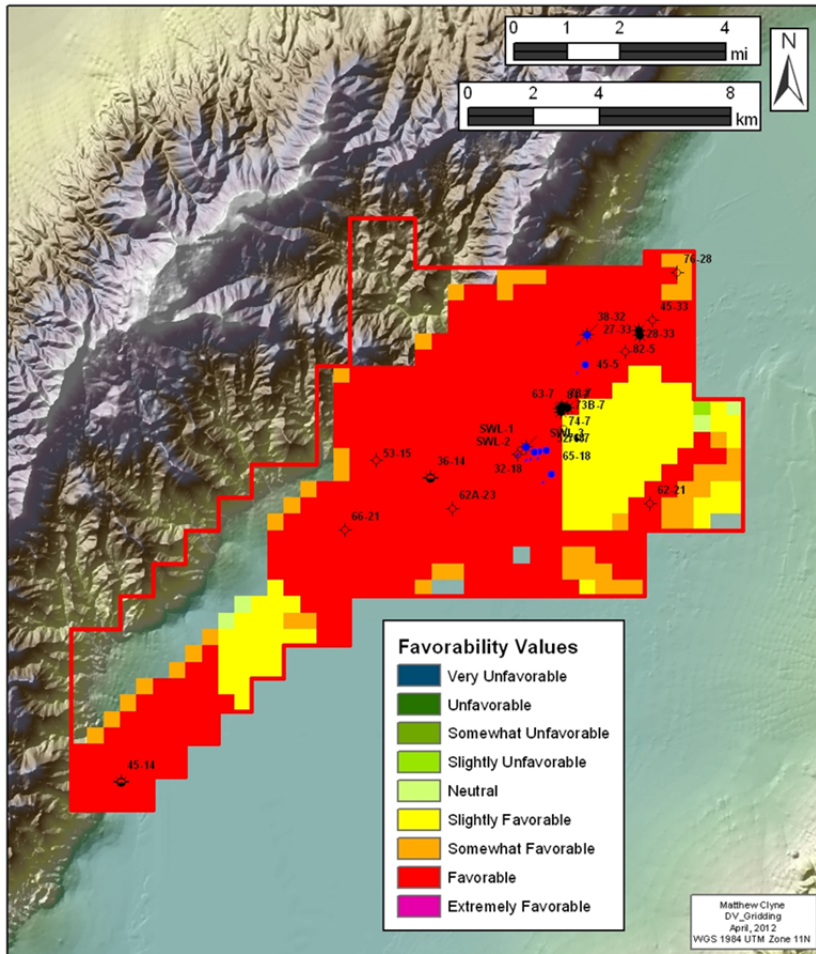
**BASEL**



### EGS Favorability-Trust Maps: Averaged Data and Weighting Depth: 3.0km Below Sea Level

Figure 75. EGS Favorability map (left) and associated trust map (right) at -3.0km asl using average values based on Subject Matter Expertise input and weighting factors for temperature, lithology, and stress of 0.51, 0.31, and 0.18, respectively.

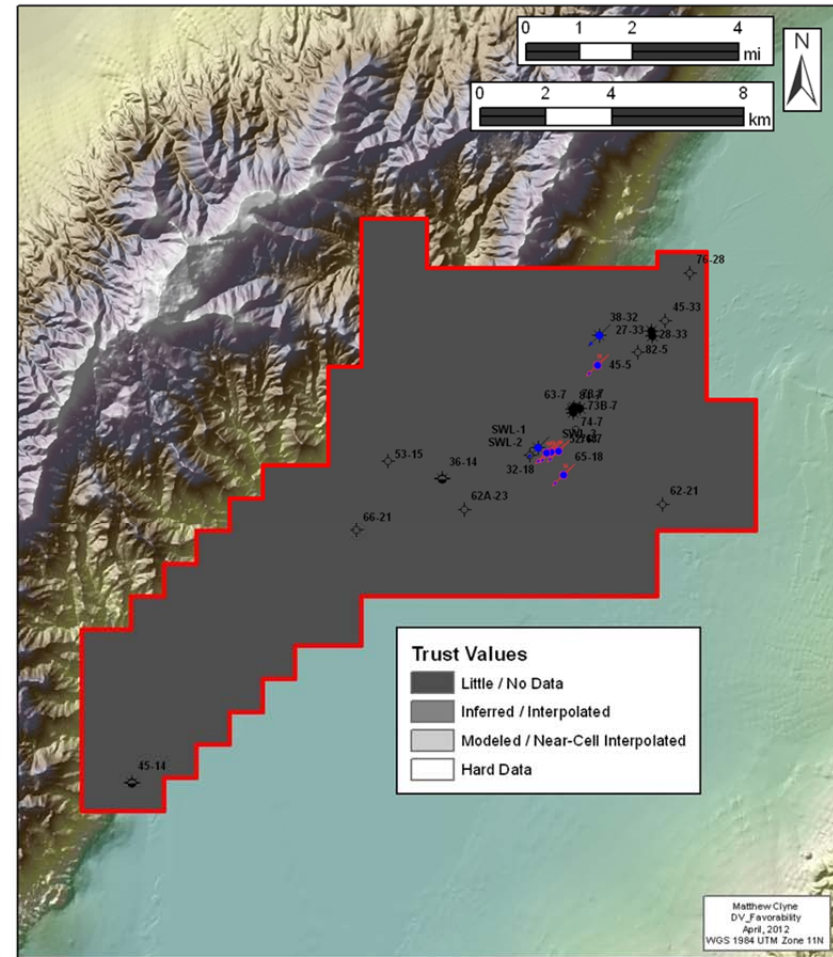
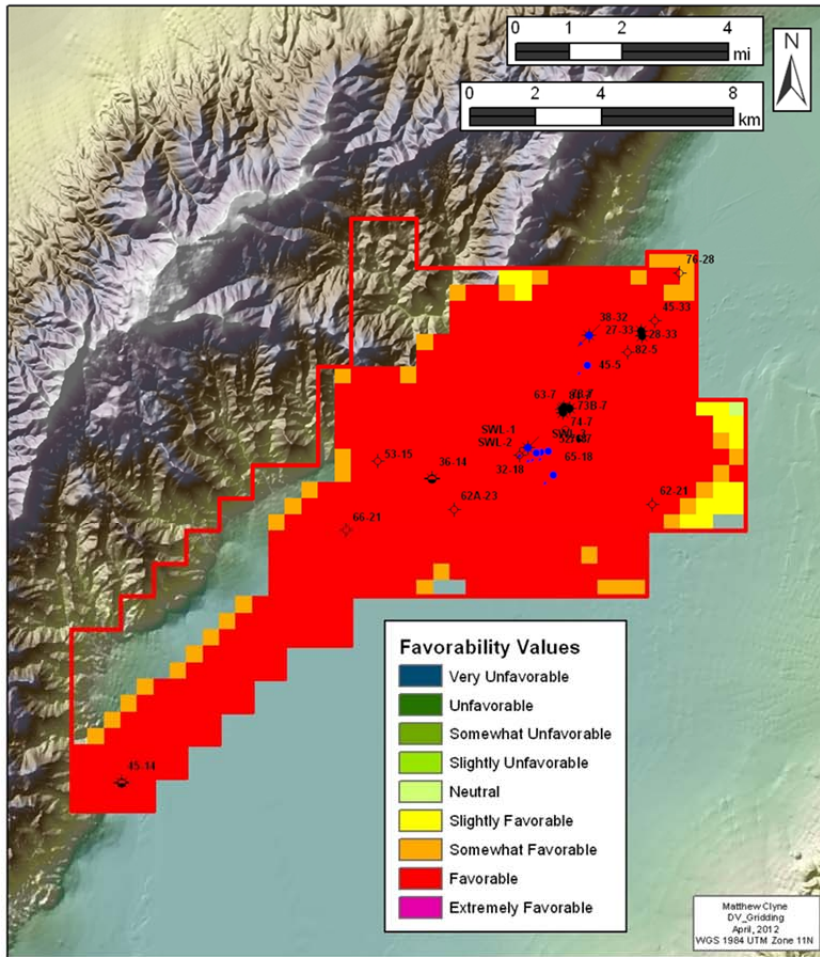
**BASELINE**



**EGS Favorability-Trust Maps: Averaged Data and Weighting  
Depth: 3.5km Below Sea Level**

**Figure 76.** EGS Favorability map (left), and associated trust map (right) at -3.5km asl using average values based on Subject Matter Expertise input and weighting factors for temperature, lithology, and stress of 0.51, 0.31, and 0.18, respectively.

**BASELINE**



**EGS Favorability-Trust Maps: Averaged Data and Weighting  
Depth: 4.0km Below Sea Level**

**Figure 77.** EGS Favorability map (left) and associated trust map (right) at -4.0km asl using average values based on Subject Matter Expertise input and weighting factors for temperature, lithology, and stress of 0.51, 0.31, and 0.18, respectively.

**BASIN**

## 8.9 Results Calibration / Verification

The weights and favorability values used to create the favorability maps represent only one set of potential values. Using the opinions of the SME to infer the range of EGS favorability for the various data sets was considered the most accurate qualitative approach. More statistical or quantitative approaches to generate a unique set of favorability maps were explored (e.g., Dempster-Scafer Theory, Weights of Evidence, Hierarchical Modeling). The fact that the specific values of the various data sets that define potential EGS systems are obscure presents a problem for validation. Still, other possible methods exist which could provide insight on how to calibrate or verify our results.

Parametric analysis was used to examine relationships between the different variables. While the significant effort made to quantify the relationships between the various datasets, described in the geostatistics section ([Section 7.4](#)), it is possible to apply a similar approach using favorability maps. By altering the favorability values and weights in an organized manner, producing a large number of different favorability realizations, and comparing the output of these models with each other, it is possible to gain a better understanding of the relationships between the data sets. This process is time intensive and a methodology for implementing such an approach was beyond the scope of this project. However, such an approach is meritorious.

For practical considerations using the baseline data, we only examined the variation on potential favorability map outcome using the following two data sets:

1. Averaged Favorability Values and Average Weights derived from the SMEs, see [Figures 67-77](#)); and
2. Averaged Favorability Values derived from the SMEs with Equal Weights, see Appendix 21.

### 8.9.1 Averaged Favorability Values and Average Weights derived from the SMEs

The set of favorability and trust map pairs based on an average favorability value and average weights derived from the SMEs are shown in [Figures 67-77](#). The favorability values for the respective data sets and the weighting of each data set were averaged from a poll of team SME. These values are given in [Table 12](#).

While the favorability values increase with depth due to the increased temperature and the presence of basement rocks (granodiorite), the paired trust maps show that the data from the lower depth intervals (-3.5 and -4.0 asl) are of very poor quality. Thus, even though the depth intervals are considered favorable, one must take into consideration the level of confidence in the data, i.e., the Trust Maps. The upper three maps ([Figure 67-69](#)) are generally unfavorable (1-5) as temperatures have not been reached levels suitable for EGS conditions. At -0.5km asl ([Figure 70](#)), a NE-trending area coincident with the DVFZ begins to show higher favorability values. This is due to elevated temperature along the fault zone due to convective processes, the presence of the Jurassic mafic rocks (a good EGS candidate rock type), and stress conditions that favor normal slip under the current stress regime (NE-aligned structures). At 1.0km and -1.5 km asl ([Figure 71](#) and [72](#)) three distinct areas are favorable including within the DVPP area, the vicinity of the bottomhole location of 36-14 at the Stillwater Range contact, and the block between the range-front fault and the piedmont fault to the northwest of the producing area. At the depth intervals -2.0km and -2.5km ([Figures 73](#) and [74](#)) the entire area DVFZ is considered favorable due to the elevated temperature and adequate stress conditions, while the lithology input is mixed.

Overall, the maps show that the area within the DVFZ is favorable for EGS, while the area within the valley in the vicinity of 62-21 is somewhat less favorable. This agrees with the large amount of evidence that supports the notion that the geothermal systems present in Dixie Valley are dependent on convective processes within the DVFZ. The area considered favorable does not extend southwest of 66-

21 ([Figure 75](#)), as there is limited data between this well and the 45-14. The gap of favorability between the DVPP and 45-14 to the SW could likely be due to a lack of data to determine favorability and decreased temperature estimates based on the limited surrounding data points. This area was a point of focus for the new data collection outlined in Task 4 of the project to enhance geophysical data resolution.

### 8.9.2 Averaged Favorability Values derived from the SMEs with Equal Weights

While the favorability values for the respective data sets did not change, an equal weighting scheme considering the three critical EGS parameters as well, i.e., temperature (0.32), lithology (0.32) and stress (0.34), was used to determine the variability between this approach and the one described above ([Appendix 21](#)). One important note is with the decrease for the temperature weighting (0.51 to 0.32) the maps are more reliant on the lithology and structure, and less so on the known elevated temperatures along the DVFZ. At the shallow depth of 1km below the valley surface ([Appendix 21-Figure 4](#)), the area west of the producers already shows *Somewhat Favorable Value* (rating of 7) relative to the previous realizations which was *Unfavorable* and described in [Section 8.9.1](#). At -1.0km asl, the three distinct favorable areas identified by the Average Weighting Realizations are less pronounced and mostly have slightly lower favorability ratings of 7 (orange).

At -2.0km asl, the favorable area (rating of 8 shown in red) is much more confined to the piedmont and more dependent on the structure than the temperature. At -2.5km and -3.0km asl, the area of high favorability occurs within the structural block between the range-front and piedmont fault. Interestingly, the NE-oriented fault that intersects 62-21 in the valley, shows a *Somewhat Favorable* rating, even though there is no elevated temperature along this structure. The lowermost depth intervals show more varied favorability than the averaged realizations ([Figures 74](#) and [75](#)), yet are still confined to known structures.

It should be noted that since the SMEs value temperature highly and temperature increases with depth everywhere, the equal weights analysis tends to score shallow areas as being more favorable and deep areas as not as favorable. Consequently, the SMEs believe the equal weight analysis presented in this subsection does not accurately assess the EGS exploration requirements.

## 9. References

- Abbott, R.E., Louie, J.N., Caskey, S.J., and Pullammanappallil, S., 2001, Geophysical confirmation of low-angle slip on the historically active Dixie Valley fault, Nevada. *Journal of Geophysical Research*, v. 106, no. B3, p. 4169-4181.
- Abers, G.A., Mutter, C.Z., and Fang, J., 1997, Shallow dips of normal faults during rapid extension: Earthquakes in the Wooklark-D'Entrecasteaux rift system, Papua New Guinea. *Journal of Geophysical Research*, v. 102, no. B7, p. 15,301-15,317.
- Anderson, D.L., 1967, A seismic equation of state. *Geophys. J. R. Astron. Soc.*, v. 13, p. 9-30.
- Anderson, E.M., 1942, *The Dynamics of Faulting*. Oliver and Boyd, White Plains, N.Y., 183 p.
- Anonymous, 1998, Report on Application of advanced seismic reflection imaging techniques to mapping permeable zones at Dixie Valley, Nevada. DOE ID 13465-TI.
- Allis, R.G., Johnson, S., Nash, G.D., and Benoit, R., 1999, A model for shallow thermal regime at Dixie Valley geothermal field. *Geothermal Resources Council (GRC) Transactions*, v. 23, p.493-498.
- Barruol, G., and Kern, H., 1996, Seismic anisotropy and shear-wave splitting in lower-crustal and upper-mantle rocks from the Ivrea Zone experimental and calculated data. *Physics of the Earth and Planetary Interiorism*, v. 95, p. 175-194.
- Barton, C.A., Hickman S., Morin, R.M., Zoback M.D., Finkbeiner T., Sass J., and Benoit D., 1997, In-situ stress and fracture permeability along the Stillwater Fault Zone, Dixie Valley, Nevada. *Proceedings, 22<sup>nd</sup> Geomechanical Wellbore Imaging: A Key to Managing the Asset Life Cycle, Proceedings, 46<sup>th</sup> Workshop on Geothermal Reservoir Engineering, SGP-TR-156, Stanford University, Stanford, California, p. 147-152.*
- Barton, C.A., Hickman S., Morin R., Zoback M.D., and Benoit, D., 1998, Reservoir-scale fracture permeability in the Dixie Valley, Nevada, Geothermal Field. *Proceedings, SPE/ISRM 47371, Eurock 98', Trondheim, Norway, July 8-10.*
- Baranov, V., 1957, A new method for interpretation of aeromagnetic maps-pseudogravity anomalies. *Geophysics*, v. 22, p. 359-383.
- Bassin, C., Laske, G., and Masters, G., 2000, The Current Limits of Resolution for Surface Wave Tomography in North America. *EOS Trans AGU*, F897, p. 81.
- Batini, F., Fiordelisi, A., Graziano, F., and Toksoz, M.N., 1995, Earthquake tomography in the Larderello geothermal area. *Transactions, World Geothermal Congress, Florence, 18-31 May*, v. 2, p. 817-820.
- Batini, F., Console, R., Luongo, G., 1985, Seismological study of Larderello — Travale geothermal area, *Geothermics*, 14, p. 255-272.
- Batzle, M.L., De-Hua, H., and Hofmann, R., 2006, Fluid mobility and frequency-dependent seismic velocity —Direct measurements. *Geophysics*, v. 71, no. 1 (January-February); p. n1-n9, 15 figs.
- Becker, D.J., and Blackwell, D.D., 1993, Gravity and hydrothermal modeling of the Roosevelt hot springs area, southwestern Utah. *Journal of Geophysical Research*, v. 98, no. 17, p. 787-97,800.
- Bell, J.W., and Katzner, T., 1990, Timing of late Quaternary faulting in the 1954 Dixie Valley earthquake area, central Nevada. *Geology*, v. 18, p. 622-25.

- Bell, J.W., and Katzner, T., 1987, Surficial geology, hydrology and late Quaternary tectonics of the IXL Canyon area, Nevada. Nevada Bureau of Mines and Geology Bulletins, v. 102, 52 p.
- Benoit, D., 1999, Conceptual models of the Dixie Valley, Nevada Geothermal Field. GRC Transactions, v. 23, p. 505-511.
- Biasi, G., Tibuleac, I., and Preston, L., 2008, Regional resource area mapping in Nevada using the USArray Seismic Network. Geothermal Energy 2008 Conference and Expo, Reno, NV, Oct 5-8.
- Birch, F., 1961, The velocity of compressional waves in rocks to 10 kilobars. Journal of Geophysical Research, v. 66, p. 2199-2224.
- Blackwell, D.D., Smith, R.P., Waibel, A.F., Richards, M.C., Stepp, P., 2009, Why Basin and Range Systems are Hard to Find II: Structural Model of the Producing Geothermal System in Dixie Valley, Nevada. GRC Transactions, v. 33, p. 441-446.
- Blackwell, D.D., Smith, R.P., and Richards, M.C., 2007, Exploration and Development at Dixie Valley, Nevada: Summary of DOE Studies. Proceedings, 32<sup>nd</sup> Workshop on Geothermal Reservoir Engineering, Stanford University, California, Jan. 22-24, 16 p.
- Blackwell, D.D., Bergman, S., Goff, F., Kennedy, B.M., McKenna, J.R., Richards, M.C., Smith, R.P., Waibel, A.F., and Wannamaker, P.E., 2005, Description, Synthesis, and Interpretation of the Thermal Regime, Geology, Geochemistry and Geophysics of the Dixie Valley, Nevada Geothermal System. in D.D. Blackwell and R.P. Smith, ed., unpublished DRAFT DOE Technical Report, 195 p.
- Blackwell, D.D., Leidig, M., Smith, R.P., Johnson, S., and Wisian, K.W., 2002, Exploration and Development Techniques for Basin and Range Geothermal Systems: Examples From Dixie Valley, Nevada. GRC Transactions, v. 26, p. 513-518.
- Blackwell, D.D., Leidig, M., and Smith, R.P., 2002, Regional Geophysics of the Dixie Valley Area: Example of a Large Basin and Range Geothermal Resource. GRC Transactions, v. 26, p. 519-522.
- Blackwell, D.D., Iglesias, E., Hunt, T., Lund, J., Tamanyu, S., and Kimbara, K., 2000, Thermal Regime in the Dixie Valley, Nevada geothermal system. Blackwell, D. D., Gollan, B., and Benoit, D., ed. Transactions, World Geothermal Congress, p. 991-996.
- Blackwell, D.D., Gollan, B., and Benoit, D., 2000, Temperatures in the Dixie Valley, Nevada geothermal system. GRC Transactions, v. 24, p. 223-228.
- Blackwell, D.D., Wisian, K.W., Benoit, D., and Gollan, B., 1999, Structure of the Dixie Valley geothermal system: A typical Basin and Range geothermal system, from thermal and gravity data. GRC Transactions, v. 23, p. 525-531.
- Blackwell, D.D., and Wisian, K., 1997, Gravity analysis of Dixie Valley, Nevada Geothermal System. unpublished report submitted to Oxbow Geothermal Corporation, Reno, Nevada.
- Blackwell, D.D., Waibel, A.W., and Kelly, S.A., 1994, Results of Dixie Valley Power Partners/Oxbow 1994 thermal gradient drilling program. unpublished report submitted to Oxbow Geothermal Corporation, Reno, Nevada.
- Blackwell, D.D., Steele, J.L. and Carter, L.S., 1991, Heat-flow patterns of the North American continent: a discussion of the Geothermal Map of North America. in Slemmons, D.B., Engdahl, E.R., Zoback, M.D., and Blackwell, D.D., ed., Neotectonics of North America. Decade Map, v. 1. Geologic Society of America Bulletin, Boulder, CO, v. 103, p. 423-436.

- Blackwell, D.D., 1983, Heat flow in the Northern Basin and Range Province. GRC Trans., Special Report No. 13, p. 81-92.
- Blakely, R.J. and Jachens, R.C., 1991, Regional study of mineral resources in Nevada: Insights from three-dimensional analysis of gravity and magnetic anomalies. GSA Bulletin, vo. 103, p. 795-803.
- Blewitt, G., Coolbaugh, M., Holt, W., Kreemer, C., Davis, J., Bennett, R., 2002, Targeting of potential geothermal resources in the Great Basin from regional relationships between geodetic strain and geological structures. GRC Transactions, v. 26, p. 523-526.
- Boitnott, G.N. and Kirkpatrick, A., 1997, Interpretation of Field Seismic Tomography at The Geysers Geothermal Field, California. Proceedings, 22<sup>nd</sup> Workshop on Geothermal Reservoir Engineering Stanford University, Stanford, California, January 27-29, SGP-TR-155.
- Brocher, T., 2008, Compressional and Shear-Wave Velocity versus Depth Relations for Common Rock Types in Northern California. Bulletin of the Seismological Society of America, v. 98, no. 2, April, p. 950–968. doi: 10.1785/0120060403
- Bruton, C.J., Nimz, G., Counce, D., Bergfeld, D., Goff, F., Johnson, S.D., and Moore, J.N., 2002, Preliminary investigation of scale formation and fluid chemistry at the Dixie Valley Geothermal field, Nevada. Presentation to Dixie Valley Geothermal Workshop, June 12-13, Reno, Nevada. <http://www.unr.edu/geothermal/oldermeetings.htm>
- Bullard, E.C., Maxwell, A.E., and Revelle, R., 1956, Heat flow through the deep sea floor; Advanced Geophysics, v. 3, p. 153-81.
- Buntebarth, G., 1982, Density and seismic velocity in relation to mineralogical constitution based on an ionic model for minerals. Earth Planet. Sci. Lett. doi:10.1016/0012-821x(82)90156.
- Burke, M.M. and Fountain, D.M., 1990, Seismic properties of rocks from an exposure of extended continental crust-new laboratory measurements from the Ivrea Zone. Tectonophysics, v. 182, p. 119-146.
- Caskey, S.J., and Wesnousky, S.G., 2000, Active Faulting and Stress Redistributions in the Dixie Valley, Beowawe, and Bradys Geothermal Fields: Implications for Geothermal Exploration in the Basin and Range. Proceedings, 25<sup>th</sup> Workshop on Geothermal Reservoir Engineering, Stanford University, California, Jan. 24-26, 16 p.
- Caskey, S.J., and Wesnousky, S.G., 1997, Static stress changes and earthquake triggering during the 1954 Fairview Peak and Dixie Valley earthquakes, Central Nevada. Bulletin of the Seismological Society of America, v. 87, p. 521-527.
- Caskey, S.J., Wesnousky, S.G., Zhang, P., and Slemmons, D.B., 1996, Surface Faulting of the 1954 Fairview Peak ( $M_s$  7.2) and Dixie Valley ( $M_s$  6.8) Earthquakes, Central Nevada. Bulletin of the Seismological Society of America, v. 86, no. 3, p. 761-787.
- Catchings, R.D., 1992, A relation among geology, tectonics and velocity structure, western to central Nevada Basin and Range. GSA Bulletin, September, v. 104; no. 9; p. 1178-1192.
- Catchings, R.D. and Mooney, W.D., 1991, Basin and Range crustal and upper mantle structure, northwest to central Nevada. Journal of Geophysical Research, v. 96 (B4), p. 6247-6267.
- Christensen, N. I., Mooney, W. D., 1995, Seismic velocity structure and composition of the continental crust: A global view, J. Geophys. Res., 100, 9761–9788.

- Christensen, N.I., 1979, Compressional wave velocities in rocks at high temperature and pressures, critical thermal gradients, and crustal low velocity zones. *Journal of Geophysical Research*, v. 84, p. 6849- 6857.
- Christensen, N. I., 1978, Ophiolites, seismic velocities and ocean crustal structure, *Tectonophysics*, 47, 131-157.
- Christensen, N.I., 1968, Compressional wave velocities in basic rocks. *Pacific Science*, V. XXII, January.
- Chung, D.J., 1977, Pn velocity and partial melting--Discussion. *Tectonophysics*, v. 42: T35-T42.
- Coolbaugh, M.F., Taranik, J.V., Raines, G.L., Shevenell, L.A., Sawatzky, D.L., Bedell, R., and Minor, T.B., 2002, A geothermal GIS for Nevada: defining regional controls and favorable exploration terrains for extensional geothermal systems. *GRC Transactions*, v. 26, p. 485-490.
- Cordell, L., and Henderson, R.G., 1968, Iterative three-dimensional solution of gravity anomaly data using a digital computer. *Geophysics*, v.33, p.596-601.
- Crafford, A.E.J., 2007, Geologic Map of Nevada: U.S. Geological Survey Data Series 249, 1 CD-ROM, 46 p., 1 plate.
- deGroot-Hedlin, C., and Constable, S.C., 1990, Occam's inversion to generate smooth, two-dimensional models from magnetotelluric data. *Geophysics*, v. 55, p. 1613-1624.
- Denton, J.M., Bell, E.J., and Jodry, R.L., 1980. Geothermal Reservoir Assessment Case Study: Northern Dixie Valley, Nevada. *DOE/ET/27006-1*, 517 p.
- DePolo, D.M., and DePolo, C.M., 1999, Earthquakes in Nevada, 1850-1998. Nevada Bureau of Mines and Geology, Map 119.
- Dickinson, W.R., 1979, Cenozoic plate tectonic setting of the Cordilleran region in the United States in Cenozoic paleogeography of the western United States. in Armentrout, J.M., Cole, M.R., and TerBest, H., ed., *Pacific Coast Paleogeography Symposium*, Pacific Section, Society of Economic Paleontologists and Mineralogists, v. 3, p. 1-13.
- Dickinson, W.R., 2006, Geotectonic evolution of the Great Basin. *Geosphere*, v. 2, no. 7, p. 353-368.
- Dilek, Y., and Eldridge, M.M., 1995, Geology of the Humboldt igneous complex, Nevada, and Tectonic implications for the Jurassic magmatism in the Cordilleran Orogen. *GSA Special Bulletin*, v. 290, p. 229-248.
- Drakos, P., Spielman, P., and Bjournsson, G., 2011, Jersey Valley Exploration and Development. *GRC Trans.*, v. 35, p. 751-759.
- Dixon, E.T., Murrell, M., Goff, F., and Goldstein, S., 2003, Uranium-Series Geochronology of Hydrothermal Deposits, Dixie Valley, Nevada. *EOS, Transactions American Geophysical Union*, Fall Meeting, San Francisco (Dec. 8-12), v.84, no. 46, p. F1613-1614.
- EarthScope Automated Receiver Survey (EARS): <http://ears.iris.washington.edu/Data/Summary/>
- ESRI/ArcGIS World Imagery Service for satellite imagery:  
<http://www.arcgis.com/home/item.html?id=a5fef63517cd4a099b437e55713d3d4>
- Evans, J.R., and Zucca, J.J., 1993, Active source, high-resolution (NeHT) tomography; velocity and Q. in Iyer, J.R., and Hirahara, K., editors, *Seismic Tomography: Theory and Practice*. Chapman and Hall, London.

- Evans, J.R., and Zucca, J.J., 1988, Active high resolution seismic tomography of compressional wave velocity and attenuation structure at Medicine Lake volcano, northern California Cascade range. *Journal of Geophysical Research*, v. 93, p. 15,016-15,036.
- Faulds, J.E., Hinz, N.H., Coolbaugh, M.F., Cashman, P.H., Kratt, C., Dering, G., Edwards, J., Mayhew, B., and McLachlan, H., 2011, Assessment of Favorable Structural Settings of Geothermal Systems in the Great Basin, Western USA. *GRC Trans.*, v. 35, p. 777-783.
- Faulds, J.E., Garside, L., Johnson, G., and Anooshehpour, R., 2003, Geologic and Geophysical Analysis of the Desert Peak-Brady Geothermal Fields: Structural Controls on Geothermal Reservoirs in the Humboldt Structural Zone. IRIS report.
- Fielitz K., 1971. Elastic wave velocities in different rocks at high pressure and temperature up to 750 °C, *Z. Geophys.*, 37, 943-956.
- Foulger, G.R., Grant, C.C., Ross, A. and Julian, B.R., 1997, Industrially induced changes in Earth structure at the Geysers Geothermal Area, California. *Geophysical Research Letters* 24: doi: 10.1029/96GL03152. issn: 0094-8276.
- Forster, C.B., Caine, J.S., Schulz, S., Nielson, D.L., 1997, Fault Zone Architecture and Fluid Flow: An Example from Dixie Valley, Nevada. *Proceedings, 22<sup>nd</sup> Workshop on Geothermal Reservoir Engineering*, Stanford University, California, Jan. 27-29, 8 p.
- Foxall, B., Vasco, D., 2003, Inversion of Synthetic Aperture Radar Interferograms for Sources of Production-Related Subsidence at the Dixie Valley Geothermal Field. *Proceedings, 28<sup>th</sup> Workshop on Geothermal Reservoir Engineering*, Stanford University, California, Jan. 27-29, 7 p.
- Frankel, A., Clayton, R. W., 1986, Finite difference simulations of seismic scattering: Implications for the propagation of short-period seismic waves in the crust and models of crustal heterogeneity, *Journal of Geophysical Research: Solid Earth* (1978-2012), [Volume 91, Issue B6](#), pages 6465-6489, DOI: 10.1029/JB091iB06p06465.
- Garside, L.J., and Schilling, J.H., 1979, Thermal waters of Nevada. *Nevada Bureau of Mines and Geology Bulletin*, v. 91, 163 p.
- Georgsson, L. S., Fridleifsson, G.O., Ólafsson, M., and Flóvenz, O.G., 2000, The geothermal exploration of the Öxarfjörður High-Temperature Area, NE-Iceland. *Proceedings, World Geothermal Congress, Kyushu - Tohoku, Japan, May 28 - June 10*, p. 1157-1162.
- Gibson, B.S. and Levander, A. R., 1988, Lower crustal reflectivity patterns in wide-angle seismic recordings, *Geophysical Research Letters*, 15, 617-620.
- Gilbert, G.K., 1875, Report on the geology of portions of Nevada, California, and Arizona, examined in the years 1871 and 1872. U.S. Geographic and Geological Survey, W. 100th Meridian Rep., 3.
- Gm-System manual, <http://www.geosoft.com>;  
[http://www.geo.wvu.edu/~wilson/gmsys\\_49.pdf](http://www.geo.wvu.edu/~wilson/gmsys_49.pdf)  
[http://www.geo.wvu.edu/~wilson/gmsys\\_49.pdf](http://www.geo.wvu.edu/~wilson/gmsys_49.pdf)
- Goff, F., Bergfeld, D., Janik, C.J., Counce, D., and Murrell, M., 2002, Geochemical data on waters, gases, scales, and rocks from the Dixie Valley region, Nevada (1996-1999). Los Alamos National Laboratory. Report LA-13972-MS, 71 p.
- Goff, F., Janik, C.J., Bergfeld, D., Counce, D., Bruton, C., and Nimz, G., 1998, Geothermal chemistry/exploration investigations at Dixie Valley, Nevada. *US/DOE Geothermal Program Review*, Berkeley, California, April 1-2, 8 p.

- Goff, F., Shevenell, L., Gardner, J., Vuataz, F., and Grigsby, C., 1988, The hydrothermal outflow plume of Valles caldera, New Mexico and a comparison with other outflow plumes. *Journal of Geophysical Research*, v. 93(B6), p. 6041-6058.
- Gourmelen, N., and Amelung, F., 2005, Postseismic mantle relaxation in the Central Nevada Seismic Belt. *Science*, v. 310, p. 1473-1476.
- Grauch, V.J.S., 2002, High-resolution aeromagnetic survey to image shallow faults, Dixie Valley geothermal field, Nevada. U.S. Geological Survey Open-File Report 02-0384, available on-line at <http://pubs.usgs.gov/of/2002/ofr-02-0384/>
- Grauch, V.J.S., 2002, Detailed aeromagnetic studies: Fault interpretations from High-Resolution aeromagnetic data. Great Basin Center for Geothermal Energy and U.S. Department of Energy, Dixie Valley Workshop, June 12-13, Reno, Nevada. <http://www.unr.edu/geothermal/oldermeetings.htm>
- Hammond, W. C., 2005, The ghost of an earthquake. *Science*, v. 310, p. 1440-1442.
- Hauge, T. A., Allmendinger, R.W., Caruso, C., Hauser, E.C., Klemperer, S.L., Opdyke, S., Potter, C.J., Sanford, W., Brown, L., Kaufman, S., and Oliver, J., 1987, Crustal structure of western Nevada from COCORP deep seismic reflection data. *GSA Bulletin*, v. 98, p. 320-329.
- Hauksson, E., and Haase, J.S., 1997, Three-dimensional  $V_p$  and  $V_p$ - $V_s$  velocity models of the Los Angeles basin and central Transverse Ranges, California. *Journal of Geophysical Research*, v. 102, p. 5423-5453.
- Heimgartner, M., Scott, J.B., Thelen, W., Lopez, C.T., and Louie, J.N., 2005, Variable crustal thickness in the western Great Basin: a compilation of old and new refraction data. *GRC Transactions*, v. 29, p. 239-242.
- Hickman, S.H., Zoback, M.D., Barton, C.A., Benoit, R., Svitek, J., and Summers, R., 2000, Stress and Permeability Heterogeneity within the Dixie Valley Geothermal Reservoir: Recent Results from Well 82-5. *Proceedings, 25<sup>th</sup> Workshop on Geothermal Reservoir Engineering*, Stanford University, California, Jan. 24-26, 10 p.
- Hickman, S., Zoback, M., and Benoit, R., 1998, Subsurface Electrical Measurements at Dixie Valley, Nevada, Using Single-Well and Surface-to-Well Induction Logging. *Proceedings, 23<sup>rd</sup> Workshop on Geothermal Reservoir Engineering*, Stanford University, California, Jan. 26-28, 8 p.
- Hickman, S., Zoback, M., and Benoit, R., 1998, Tectonic Controls on Reservoir Permeability in the Dixie Valley, Nevada Geothermal Field. *Proceedings, 23<sup>rd</sup> Workshop on Geothermal Reservoir Engineering*, Stanford University, California, Jan. 26-28, 8 p.
- Hickman, S., and Zoback, M., 1997, In-Situ Stress in a Fault Hosted Geothermal Reservoir at Dixie Valley, Nevada. *Proceedings, 22nd Workshop on Geothermal Reservoir Engineering*, Stanford University, California, Jan. 27-29, 6 p.
- Hittelman, A. M., Dater, D.T., Buhmann, R.W., and Racey, S.D., 1994, Gravity-edition CD-ROM user's manual, NOAA Natl. Geophys. Data Center, Boulder, Colo.
- Holbrook, W.S., Gajewski, D., Krammer, A., and Prodehl, C., 1988, An interpretation of wide-angle compressional and shear wave data in southwest Germany: Poisson's Ratio and petrological implications. *Journal of Geophysical Research*, v. 93, p. 12,081-12,106.

Holliger, K., Levander, A., Carbonell, R. & Hobbs, R., 1994, Some attributes of wavefields scattered from Ivrea-type lower crust, *Tectonophysics*, 232, 267–279.

Hulen, J.B., Hollister, J.W., Johnson, S.D., and Allis, R., 1999, Oils in the Dixie Valley and Kyle hot springs geothermal systems, Nevada — Potentially sensitive indicators of natural and induced reservoir processes. *Proceedings, 24<sup>th</sup> Workshop on Geothermal Reservoir Engineering*, Stanford University, Stanford, California, Jan. 25-27, 15 p.

Iovenitti, J.L., Blackwell, D.D., Sainsbury, J.S., Tibuleac, I.M., Waibel, A.F., Cladouhos, T.T., Karlin, R., Kennedy, B.M., Isaaks, E., Wannamaker P.E., Clyne, M.T., Ibser, F.H., Callahan, O.C., 2012, Towards Developing a Calibrated EGS Exploration Methodology Using the Dixie Valley Geothermal System, Nevada. *Proceedings, 37<sup>th</sup> Workshop on Geothermal Reservoir Engineering* Stanford University, Stanford, California, January 30 - February 1. 15 p.

Iovenitti, J.L., Blackwell, D.D., Sainsbury, J.S., Tibuleac, I.M., Waibel, A.F., Cladouhos, T.T., Karlin, R., Kennedy, B.M., Isaaks, E., Wannamaker P.E., Clyne, M.T., and Callahan, O.C., 2011a, EGS Exploration Methodology Development Using the Dixie Valley Geothermal District as a Calibration Site, A Progress Report. *GRC Transactions*, v. 35, 12 p.

Iovenitti, J.L., Blackwell, D.D., Sainsbury, J.S., Tibuleac, I.M., Waibel, A.F., Cladouhos, T.T., Karlin, R., Kennedy, B.M., Isaaks, E., Wannamaker P.E., Clyne, M.T., and Callahan, O.C., 2011b, EGS Exploration Methodology Development Using the Dixie Valley Geothermal District as a Calibration Site, A Progress Report. Poster Presentation, Annual GRC Meeting in San Diego.

Iovenitti, J.L., Blackwell, D.D., Sainsbury, J.S., Tibuleac, I.M., Cladouhos, T.T., Karlin, R., Kennedy, B.M., Isaaks, E., Wannamaker P.E., Clyne, M.T., and Callahan, O.C., 2011c, EGS Exploration Methodology Development Using the Dixie Valley Geothermal District as a Calibration Site, A Progress Report. Abstract and Poster Presentation, American Geophysical Union (AGU), San Francisco, Paper Number H21E-1173.

Iovenitti, J.L., Blackwell, D.D., Tibuleac, I.M., Cladouhos, T.T., Karlin, R., Kennedy, B.M., Isaaks, E., Wannamaker P.E., Clyne, M.T., and Callahan, O.C., 2010a, EGS Exploration Methodology Development Using the Dixie Valley Geothermal District as a Calibration Site, A Progress Report. Paper and Poster Presentation, Annual GRC Meeting in San Diego.

Iovenitti, J.L., Tibuleac, I.M., Hopkins, D., Cladouhos, T.T., Karlin, R., Wannamaker P.E., Kennedy, B.M., Blackwell, D.D., Clyne, M.T., and Isaaks, E., 2010b, Development of Exploration Methods for Engineered Geothermal Systems through Integrated Geophysical, Geologic and Geochemical Interpretation. Abstract and Poster Presentation, American Geophysical Union (AGU), San Francisco.

**Ito, H., De Vilbiss, J. and Nur, A. (1979).** Compressional and shear waves in saturated rock during water-saturated transition. *Journal of Geophysical Research* 84: doi: 10.1029/OJGREA0000840000B9004731000001. issn: 0148-0227.

ITSI, 2005, Kinematic and Dynamic Studies: Genetic Occurrence Models for Geothermal Prospecting. Geothermal Program Office, Naval Air Weapons Station, 86 p.

Iverson, W. P., Fahmy, B. A., and Smithson, S. B., 1989, Vp/Vs from mode-converted P-SV reflections: *Geophysics*, 54, 843-852.

Iyer, H.M., and Dawson, P.B., 1993, Imaging Volcanoes using Teleseismic Tomography. in Iyer, H.M., Hirahara, K., editors, *Seismic Tomography: Theory and Practice*. Chapman and Hall, London.

- Janik, C., Nimz, G., and Goff, F., 2002, Origin, Age, and Geochemical Evolution of Dixie Valley Geothermal Fluid. Presentation to Dixie Valley Geothermal Workshop, June 12-13, Reno, Nevada.  
<http://www.unr.edu/geothermal/oldermeetings.htm>
- Jaya, M.S., Shapiro, S.A., Kristinsdóttir, L.H., Bruhn, D., Milsch, H., and Spangenberg, E., 2010, Temperature dependence of seismic properties in geothermal rocks at reservoir conditions. *Geothermics*, v. 39, p. 115–123.
- Jekeli, C., K. Erkan, O. Huang, 2010, Gravity vs pseudogravity: A comparison based on magnetic and gravity gradient measurements. *Earth and Environmental Science*, v. 135, Part 1, p. 123-127, DOI: 10.1007/978-3-642-10634-7\_17.
- John, D.A., 1995, Tilted middle Tertiary ash flow calderas and subjacent granitic plutons, southern Stillwater Range, Nevada: Cross sections of an Oligocene igneous center. *Geological Society of America Bulletin*, v. 107, p. 180-200.
- Johnson, R.A., and Loy, K.L., 1992, Seismic reflection evidence for seismogenic low-angle faulting in southeastern Arizona. *Geology*, v. 20, p. 597-600.
- Johnson, S.D. and Hulen, J.B., 2002, Subsurface stratigraphy, structure, and alteration in the Senator thermal area, Northern Dixie Valley geothermal field, NV – Initial results from injection well 38-32, and a new structural scenario for the Stillwater escarpment. *GRC Transactions*, v. 26, p. 533-542.
- Julian, B. R., Ross, A., Foulger, G. R., Evans, J. R., 1996, Three-Dimensional seismic image of a geothermal reservoir: The Geysers, California, *Geophysical Research Letters*, 23, pp. 685–688.
- Kampfmann W., Berckhemer H., 1985, High temperature experiments on the elastic and anelastic behavior of magmatic rocks, *Phys. Earth planet. Int.*, 40, 223–247.
- Kennedy, B.M., T.P. Fischer, and D.L. Shuster, 2000, Heat and helium in geothermal systems. *Proceedings 25<sup>th</sup> Workshop on Geothermal Reservoir Engineering*, Stanford Geothermal Program Report SGP-TR-165, 167–173.
- Kennedy, B.M., van Soest, M.C., 2006, A Helium Isotope Perspective on the Dixie Valley, Nevada, Hydrothermal System. *Geothermics*, v. 35, p. 26-43.
- Kennedy, B.M., Fischer, T.P., and Shuster, D.L., 2000, Heat and helium in geothermal systems. *Proceedings 25<sup>th</sup> Workshop on Geothermal Reservoir Engineering*, Stanford University, California, p. 167–173.
- Kennedy, B.M., Janik, C., Benoit, D., and Shuster, D.L., 1999, Natural geochemical tracers for injectate fluids at Dixie Valley. *Proceedings 24<sup>th</sup> Workshop on Geothermal Reservoir Engineering*, Stanford University, California, p. 108 – 115.
- Kennedy-Bowdoin, T., Silver, E.A., Martini, B.A., and Pickles, W.L., 2004, Geothermal Prospecting using Hyperspectral Imaging and Field Observations, Dixie Meadows, NV. *GRC Transactions*, v. 28, Aug. 29-Sept. 1, 4 p.
- Kennett, B.L.N., Engdahl, E.R., and Buland, R., 1995, Constraints on seismic velocities in the Earth from traveltimes. *Geophysical Journal International*, v. 122, p. 108 -124.

- Kern, H., Popp, T., Gorbatshevich, F., Zharikov, A., Lobanov, K.V., and Smirnov, Y.P., 2001, Pressure and temperature dependence of  $V_p$  and  $V_s$  in rocks from the superdeep well and from surface analogues at Kola and the nature of velocity anisotropy. *Tectonophysics*, v. 338, p. 113-134.
- Kern, H., 1982, Elastic-wave velocity in crustal and mantle rocks at high pressure and temperature: the role of the high—low quartz transition and of dehydration reactions: *Physics of the Earth and Planetary Interiors*, v. 29, p. 12-23.
- Kern, H., Richter, A., 1981, Temperature derivatives of compressional and shear wave velocities in crustal and mantle rocks at 6 kbar confining pressure, *J. Geophys.*, 49, 47–56.
- King, G., Oppenheimer, D., Amelung, F., 1994, Block versus continuum deformation in the Western United States. *Earth and Planetary Science Letters*, v. 128, 55-64.
- Klemperer, S.L., Hauge, T.A., Hauser, E.C., Oliver, J.E., and Potter, C.J., 1986, The Moho in the northern Basin and Range Province, Nevada, along the COCORP 40°N seismic reflection transect. *Geological Society of America Bulletin*, v. 97 (no. 5), p. 603–618.
- Koch, M., 1992, Bootstrap inversion for vertical and lateral variations of the S wave structure and the  $V_p/V_s$ -ratio from shallow earthquakes in the Rhinegraben seismic zone, Germany. *Tectonophysics*, v. 210, p. 91–115.
- Knopoff, L., 1967, Density-velocity relations for rocks. *Journal of Geophysical Research Astron. Soc.*, v. 13, p. 1-8.
- Kreemer, C., and Hammond, W.C., 2008, Geodetic Constraints on the Slip Rate of the Mohawk Valley Fault Zone, California. USGS Final Technical Report, award no. 08HQGR0027. <http://earthquake.usgs.gov/research/external/reports/08HQGR0027.pdf>
- Krishna, A., 1988, Crustal velocity models in the western united states from travel times and amplitudes of seismic refraction data. *Bulletin of the Seismological Society of America*, v. 78, no. 2, p. 816-837.
- Kucks, R.P., P.L. Hill, D.A. Ponce, D.A., 2006, Nevada magnetic and gravity maps and data: A website for distribution of data by USGS. URL: <http://pubs.usgs.gov/ds/2006/234/data/>.
- Lachenbruch, A.H., and J.H. Sass, 1977, Heat flow in the United States and the thermal regime of the crust. Heacock, J.G., editor, *The Nature and Physical Properties of the Earth's Crust*. American Geophysical Union Monograph, v. 20, p.626–675.
- Lawrence, J. F. and Prieto, G. A. Prieto, 2010, Attenuation tomography of the western United States from ambient seismic noise. *Journal of Geophysical Research*, v. 116, B06302, doi:10.1029/2010JB007836, 2011.
- Lawrence, R.L., and Wright, L., 2001, Rule-Based Classification Systems using Classification and Regression (CART) Analysis. *Photogrammetric Engineering & Remote Sensing*, v. 67, no. 10, October, p. 1137-1142.
- Lees, J.M., 2007, Seismic tomography of magmatic systems. *Journal of Volcanology and Geothermal Research*, v. 167, p. 37–56.
- Lees, V., and Wu, H., 2000, Poisson's ratio and porosity at Coso geothermal area, California. *Journal of Volcanology and Geothermal Research*, v. 95, p. 157–173.

- Levander, A. R., Hobbs, R. W., Smith, S. K., England, R. W., Snyder, D. B., and Hollinger, K., 1994, The crust as a heterogeneous 'optical' medium, or 'crocodiles in the mist': *Tectonophysics*, 232, 281–297.
- Lin, J., and Stein, R.S., 2004, Stress triggering in thrust and subduction earthquakes, and stress interaction between the southern San Andreas and nearby thrust and strike-slip faults. *Journal of Geophysical Research*, v. 109, B02303.
- Line, C.E.R., Hobbs, R.W., and Snyder, D.B., 1998, Estimates of upper-crustal heterogeneity in the Baltic Shield from seismic scattering and borehole logs. *Tectonophysics*, v. 286, p. 171 - 183.
- Line, C.E.R., Hobbs, R.W., and Snyder, D.B., 1998, Estimates of upper-crustal heterogeneity in the Baltic Shield from seismic scattering and borehole logs. *Tectonophysics*, v. 286, p. 171 - 183.
- Louie, J.N., Thelen, W., Smith, S.B., Scott, J.B., Clark, M., and Pullammanappallil, S., 2004, The Northern Walker Lane refraction experiment: Pn arrivals and the northern Sierra Nevada root. *Tectonophysics*, v. 388, no. 1-4, p. 253-269.
- Lowell, R.P., and Stephen, R.A., 1991, Heat - flow and lateral seismic velocity heterogeneities near Deep Sea Drilling Project - Ocean Drilling program Site 504. *Geology*, v. 19, p. 1141-1144.
- Lutz, S.J., Caskey, S.J., and Johnson S.D., 2003, Geyserite, faulted sinter terraces, and other fossil hot spring deposits, northern Dixie Valley fault system, Nevada. *Nevada Petroleum Society Field Trip Guide-book*, Aug. 22-24, p. 75-89.
- Lutz, S.J., Moore, J.N., Blamey, N.J.F., and Norman, D.I., 2002, Fluid-Inclusion Chemistry of the Dixie Valley (NV) Geothermal System. *Proceedings, 27<sup>th</sup> Workshop on Geothermal Reservoir Engineering*, Stanford University, California, Jan. 28-30, 11 p.
- Lutz, S.J., Caskey, S.J., Mildenhall, D.D., Browne, P.R.L., and Johnson, S.D., 2002, Dating sinter deposits in northern Dixie Valley, Nevada- the paleoseismic record and implications for the Dixie Valley geothermal system. *Proceedings, 27<sup>th</sup> Workshop on Geothermal Reservoir Engineering*, Stanford University, California, Jan. 28-30. 10 p.
- Lutz, S.J., Moore, J.N., and Benoit, D., 1998, Integrated alteration mineralogy and fluid-inclusion study at the Dixie Valley geothermal field, Nevada. *Proceedings, 23<sup>rd</sup> Workshop on Geothermal Reservoir Engineering*, Stanford University, Stanford, California, January 26-28, p. 315-321.
- Lutz, S.J., Moore, J.N., Benoit, D., 1997, Geologic Framework of Jurassic Reservoir Rocks in the Dixie Valley Geothermal Field, Nevada: Implications from Hydrothermal Alteration and Stratigraphy. *Proceedings, 22<sup>nd</sup> Workshop on Geothermal Reservoir Engineering*, Stanford University, California, Jan. 27-29, 9 pp.
- Majer, E.L. and McEvilly, T.V., 1979, Seismological Investigations at The Geysers Geothermal Field, *Geophysics*, Vol. 44, No. 2, p. 246-269.
- Malin, P.E., and Shalev, E., 1999, Shear-wave splitting crack density maps for the Geysers and Mammoth. *Proceedings, 24<sup>th</sup> Workshop on Geothermal Reservoir Engineering* Stanford University, Stanford, California, January 25-27.
- Mallan, R., and Wilt, M., 2001, Subsurface Electrical Measurements at Dixie Valley, Nevada, Using Single-Well and Surface-Well Induction Logging. *Proceedings, 26<sup>th</sup> Workshop on Geothermal Reservoir Engineering*, Stanford University, California, Jan. 29-31, 6 p.

- Mankhemthong, N., Oppliger, G.L., Aslett, Z., 2008, Structural Localization of Two Temperature Geothermal Systems within the Gravity Defined Linkage between Dixie Valley and Fairview Valley, Nevada, USA. GRC Transactions, v. 32, 5 p.
- Marquardt, D.W., 1963, An algorithm for least-squares estimation of non-linear parameters. Journal SIAM, v. 11, p. 431-441.
- Mavko, G., 2008, Parameters that influence Seismic Velocity. Stanford Rock Physics Laboratory, Presentation, Stanford University, California.
- Mavko, G.M., 1980, Velocity and attenuation in partially molten rocks. J. Geophys. Res., v. 85 (B10), p. 5173-5189.
- McKenna, J.R., Blackwell, D.D., Richards, M.C., 2005, Natural State Modeling, Structure, Preliminary Temperature and Chemical Synthesis of the Dixie Valley, Nevada Geothermal Field. Proceedings, 32<sup>nd</sup> Workshop on Geothermal Reservoir Engineering, Stanford University, California, Jan. 31-Feb. 2, 8 p.
- McKenna, J.R., and Blackwell, D.D., 2004, Numerical modeling of transient Basin and Range extensional geothermal systems. Geothermics, v. 33, p. 457-476.
- McLachlan, G. J., 2004, Discriminant Analysis and Statistical Pattern Recognition. Wiley Interscience, MR1190469. ISBN 0471691151.
- McLin, K.S., Moore, J.N., Park, J., Norman, D.I., 2008, Mineralogy and Fluid Inclusion Gas Chemistry of Production Well Mineral Scale Deposits at the Dixie Valley Geothermal Field, USA. Proceedings, 23<sup>rd</sup> Workshop on Geothermal Reservoir Engineering, Stanford University, California, Jan. 28-30, 4 p.
- Mickey, W.V., 1964, Microearthquake monitoring at the Shoal site. U.S. Coast and Geodetic Survey Report, AFTAC Project No. VELA T/4052/CGS/B31, p. 1-82.
- Mickey, W.V., 1966, Seismic clusters. U.S. Dept. of Comm., ESSA Symposium on Earthquake Prediction, p. 63-68.
- Mooney, W.D., Laske, G., and Masters, T.G., 1998, Crust 5.1: a global crustal model at 5x5 degrees. Journal of Geophysical Research, v. 103, p. 727-747.
- Nakajima, J., and Hasegawa, A., 2003, Tomographic imaging of seismic velocity structure in and around the Onikobe volcanic area, northeastern Japan: implications for fluid distribution. Journal of Volcanology and Geothermal Research, v. 127, p. 1-18.
- Nakajima, J., Matsuzawa, T., and Hasegawa, A., 2001, Three-dimensional structure of and beneath northeastern Japan' Implications for arc magmatism and fluids, Jour. Geophys. Res., v. 106, no. B10, p. 21843 -21 857.
- Nicholson, C., and Simpson, D.W., 1985, Changes in Vp/Vs with depth. Bull. Seis. Soc. Am., v. 75, p. 1105-1123.
- Nimz, G., Janik, C., Goff, F., Dunlap, C., Huebner, M., Counce, D., and Johnson, S., 1999, Regional hydrology of the Dixie Valley geothermal field, Nevada: Preliminary interpretations of chemical and isotopic data. Lawrence Livermore National Laboratory Publication, UCRL-JC-135417, 9 p.
- O'Connell, R.J., Sumner, E.E., and Budiansky, B., 1983, Bulk thermoelastic attenuation of composite materials. J. Geophys. Res., v. 88, p. 10,343-10,348.

- O'Connell, R.J., and Boudianky, B., 1974, Seismic Velocities in dry and saturated cracked solids. *J. Geophys. Res.*, v. 79, p. 5412-5429.
- Okaya, D.A., and Thompson, G.A., 1985, Geometry of Cenozoic extensional faulting: Dixie Valley, Nevada. *Tectonics*, v. 4, no. 1, p. 107-125.
- Oliver, J., Ryall, A., Brune, J. N., and Slemmons, D.B., 1966, Microearthquake activity recorded by portable seismographs of high sensitivity. *Bulletin Seismological Society of America*, v. 56, p. 899-924.
- Page, B.M., 1965, Preliminary Geologic Map of a part of the Stillwater Range, Churchill County, Nevada. Nevada Bureau of Mines, Map 28.
- Peacock, S., Westbrook, G.K., and Graham, D.P., 1997, Seismic velocities in the Northern Barbados Ridge, accretionary complex, site 9491. *Proceedings of the Ocean Drilling Program, Scientific Results*, v. 156.
- Phillips, W.S., and Stead, R.J., 2008, Attenuation of Lg in the western US using the US Array. *Geophysical Research Letters*, v. 35, L07307.
- Pickett, G.R., 1963, Acoustic character logs and their applications in formation evaluation: *J. Petr. Tech.*, June, 659-66.
- Plank, G.R., 1998, Structure, stratigraphy, and tectonics of a part of the Stillwater escarpment and implications for the Dixie Valley geothermal system. unpublished report for Oxbow Geothermal and Master's Thesis for University of Nevada Reno, 153 pp.
- Ponce, D.A., 1997, Gravity data of Nevada. U.S. Geological Survey Digital Data Series DDS-41, 1-27.
- Preston, L.A., 2010, P- and S-body wave tomography of the state of Nevada. SANDIA Report, SAND2010-2205.
- Rasmussen, R., and Pedersen, L. B., 1979, End corrections in potential field modeling: *Geophysical Prospecting*, v. 27, p. 749-760.
- Reed, M.J., 2007, An Investigation of the Dixie Valley Geothermal Field, Nevada, Using Temporal Moment Analysis of Tracer Tests. *Proceedings, 32<sup>nd</sup> Workshop on Geothermal Reservoir Engineering*, Stanford University, California, Jan. 22-24, 8 p.
- Reheis, M., 1999, Extent of Pleistocene lakes in the western Great Basin. U.S. Geological Survey Miscellaneous Field Investigation Map, MF-2323, 1 sheet.
- Reheis, M.C., and Morrison, R.B. Link, P.K., and Kowallis, B.J., 1997, High, old pluvial lakes of western Nevada Proterozoic to recent stratigraphy, tectonics, and volcanology, Utah, Nevada, southern Idaho, and central Mexico. Provo, Brigham Young University Geology Studies, v. 1, p. 459-492.
- Reiter, M., 2008, Geothermal anomalies in the crust and upper mantle along Southern Rocky Mountain transitions. *GSA Bulletin*, March/April, v. 120, no. 3/4; p. 431-441.
- Rial, J.A., Elkibbi, M., Yang, M., 2005, Shear-wave splitting as a tool for the characterization of geothermal fractured reservoirs: lessons learned. *Geothermics*, v. 34, p. 365-385.
- Ritzwoller, M.H., Shapiro, N.M., Barmin, M.P., and Levshin, A.L., 2002, Global surface wave diffraction tomography. *Journal of Geophysical Research*, v. 107(B12), p. 23-35. *Geothermics*, v. 34, p. 365-385.

Rose, P.E., Johnson, S.D., Kilbourn, P., and Kasteler, C., 2002, Tracer testing at Dixie Valley, Nevada, using 1-naphthalene sulfonate and 2,6-naphthalene disulfonate. Proceedings 27<sup>nd</sup> Workshop on Geothermal Reservoir Engineering, Stanford University.

RStudio IDE, User Interface for R. <http://www.rstudio.com>

Rybach, L.G., and Bunterbath, M., 1982, Relationships between the petrophysical properties density, seismic velocity, heat generation and mineralogical constitution. Earth Planet. Seis. Lett., v. 57, p. 367–376, 1982.

Saltus, R. W., 1988, Regional, residual, and derivative gravity maps of Nevada. Nev. Bur. Mines and Geol. Map 94B, 1:1,000,000.

Schmeling, H., 1985, Partial melt below Iceland: A combined interpretation of seismic and conductivity data. J. Geophys. Res., v. 90 (B12), p. 10105-10116.

Shankland, T. J. and Waff, H. S., 1977, Partial melting and electrical conductivity anomalies in the upper mantle, Journal of Geophysical Research [Volume 82, Issue 33](#), p. 5409–5417.

Shapiro, N.M., and Ritzwoller, M.H., 2004, Thermodynamic constraints on seismic inversions. Geophysical Journal International, v. 157, p. 1175-1188.

Sharma, S.R., Sundar, A., Rao, V.K., and Ramana, D.V., 1991, Surface heat flow and pn velocity distribution in peninsular India. Journal of Geodynamics, v. 13, no. 1, p. 67-76.

Sherburn S., Bannister, S., and Bibby, H., 2003, Seismic velocity structure of the central Taupo Volcanic Zone, New Zealand, from local earthquake tomography. Journal of Volcanology and Geothermal Research, v. 122, p. 69-88.

Shevenell, L. and Garside, L.J., 2003, Nevada geothermal resources. Nevada Bureau of Mines and Geology, Map 141, 1 sheet, 1:750;000.

Shevenell, L., Kasameyer, P., Bruton, C., Renner, J.L., and Kennedy, B.M., 2002, The Department of Energy's Workshop: Dixie Valley Geothermal Research, Executive Summary, Group Conclusions and recommendations. PDF available online at (1) and presentations at (2):  
(1)[http://www.unr.edu/geothermal/pdffiles/intro\\_summarydv.pdf](http://www.unr.edu/geothermal/pdffiles/intro_summarydv.pdf)  
(2)[http://www.unr.edu/geothermal/oldermeetings.htm#Dixie\\_Valley\\_Geo\\_2002](http://www.unr.edu/geothermal/oldermeetings.htm#Dixie_Valley_Geo_2002)

Shevenell, L., Garside, L.J., and Hess, R.W., 2000, Nevada Geothermal Resources: Nevada Bureau of Mines and Geology Map 126, scale 1:1,000,000 and Map 141, scale at 1:750,000.

Simiyu, S.M., 1999, Seismic Velocity Analysis in the Olkaria Geothermal Field. Proceedings, 24<sup>th</sup> Workshop on Geothermal Reservoir Engineering Stanford University, Stanford, California, January 25-27.

Smith, R.P., Grauch, V.J.S., and Blackwell, D.D., 2002, Preliminary Results of a High-Resolution Aeromagnetic Survey to Identify Buried Faults at Dixie Valley, Nevada. GRC Transactions, v. 26, p. 543-546.

Smith, R.P. and Grauch, V.J.S., 2002, High-resolution aeromagnetic survey reveals distribution of faults in Dixie Valley, Nevada. Geological Society of America, Annual Meeting, Denver, October 27, - Theme session on New Views of Extensional Basins and Related Volcanic Fields Using Geophysics and Remote Sensing.

Smith, R.P., Wisian, K.W., Blackwell, D.D., 2001, Geologic and Geophysical Evidence for Intra-basin and Footwall Faulting at Dixie Valley, Nevada. GRC Transactions, v. 25, Aug. 26-69. 8 p.

- Smith, R.D., 1979. Geophysical Report: Magnetotellurics, gravity, magnetics in Dixie Valley Nevada, unpublished Geotronics Corp., Austin, TX, 53 p., plus 7 Plates.
- Sonders, L.J., and C.H. Jones, 1999, The western United States: how the west was widened; Annual Reviews of Earth and Planetary Sciences, v. 27, 417-462.
- Southland Royalty Corp., 1979, Bouguer gravity map. Plate 2.1A of Gravity and Magnetic Survey Dixie Valley, Nevada performed by Austin Exploration. Inc. for AMOCO Production Co, unpublished report.
- Speed, R.C., 1976, Geologic Map of the Humboldt Lopolith and surrounding terrane. The Geological Society of America, Inc., Map and Chart Series MC-14, 1:81050, 4 p.
- Stauder, W., and Ryall, A., 1967, Spatial distribution and source mechanism of microearthquakes in Central Nevada. Bulletin of the Seismological Society of America, December 1, v. 57, no.6, p. 1317 -1345.
- Stewart, J.H., 1998, Regional characteristics tilt domains, and extensional history of the late Cenozoic Basin and Range Province, western North America. in Faulds, J.E., and Stewart, J.H., editors, Accommodation zones and transfer zones: The regional segmentation of the Basin and Range Province, Geological Society of America Special Paper 323, Boulder, CO, 47-74.
- Stewart, J.H., and Carlson, J.E., 1978, Geologic map of Nevada. U.S. Geological Survey, 1:500,000 scale.
- Talwani, M., and Heirtzler, J.R., 1964, Computation of magnetic anomalies caused by two-dimensional bodies of arbitrary shape. in Parks, G. A., Editor, Computers in the mineral industries, Part 1: Stanford University Publications, Geological Sciences, v. 9, p. 464-480.
- Talwani, M., Worzel, J.L., and Landisman, M., 1959, Rapid gravity computations for two-dimensional bodies with application to the Mendocino submarine fracture zone. Journal of Geophysical Research, v. 64, p. 49-59.
- Tatham, R. H., 1982, Vp/Vs and lithology, Geophysics, 47, p. 336-344.
- Taylor, R., 1990, Relationships between cognitive test-performance and everyday cognitive difficulties in multiple-sclerosis. British Journal of Clinical Psychology, v. 29, p. 251-252.
- Telford, W.M., Geldart, L. P. and Sheriff, R. E., 1990, Applied Geophysics, 2<sup>nd</sup> ed. Cambridge U. Press, Cambridge, U.K.
- Thompson, G.A., Catchings, R., Goodwin, E., Holbrook, S. Jarchow, C., Mann, C., McCarthy, J, and Okaya, D., 1989, Geophysics of the western Basin and Range Province. in Pakiser, L.C., and Mooney, W.D. editors. Geophysical Framework of the continental United States, Geol. Soc. Of Amer. Memoir 172, p. 117-204.
- Tivey, M. A., Sager, W. W., Lee, S., Tominaga, M., 2006, Origin of the Pacific Jurassic quiet zone, Geology, 34, p. 789-792.
- Toda, S., Stein, R.S., Richards-Dinger, K., and Bozkurt, S., 2005, Forecasting the evolution of seismicity in southern California: Animations built on earthquake stress transfer. Journal of Geophysical Research, v. 110, 17 p.
- Tosdal, R.M., Wooden, J.L., and Kistler, R.W., 2000, Geometry of the neopro- tozoic continental break-up, and implications for location of Nevadan mineral belts, in Cluer, J.K., Price, J.G., Struhsacker, E.M., Hardyman, R.F., and Morris, C.L., editors, Geology and Ore Deposits 2000: The Great Basin and Beyond. Geological Society of Nevada Symposium Proceedings, p. 451-466.

Unruh, J., Pullammanappallil, S., Honjas, W., and Monastero, F., 2001, New seismic imaging of the Coso geothermal Field, Eastern California. Proceedings, 26<sup>th</sup> Workshop on Geothermal Reservoir Engineering, Stanford University, California, 7 p.

UTEP PACES GEONET, Gravity and magnetic data set repository -Gravity and magnetic data base of the United States. <http://irpsrvgis00.utep.edu/repositorywebsite>

Vanorio, T., Virieux, J., Zollo, A., Capuano, P., and Russo, G., 2006, A rock physics and seismic tomography study to characterize the structure of the Campi Flegrei caldera. <http://hdl.handle.net/2122/2171>, p. 25–33.

Vikre, P.C., 1994, Gold mineralization and fault evolution at the Dixie Comstock Mine, Churchill County, Nevada. *Economic Geology*, v. 89, no. 4, p. 707-719.

Vlahovic, G., Elkibbi, M., and Rial, J.A., 2002, Shear-wave splitting and reservoir crack characterization: the Coso geothermal Field. *Journal of Volcanology and Geothermal Research*, v. 120, p. 123-140.

Von Herzen, R.P. and Uyeda, S., 1963, Heat flow through the eastern Pacific Ocean floor; *Journal of Geophysical Research*, v. 68, p. 4219-4250.

Von Seggern, D.H., Tibuleac, I.M. and Louie, J.N., 2009, Computing Green's Functions from ambient noise recorded by narrow-band seismometers, accelerometers, and analog seismometers. Abstract presented at the 2009 Annual Meeting Announcement Seismological Society of America, 8–10 April, Monterey, California.

Yoshikawa, M., and Sudo, Y., 2004, Three Dimensional Seismic Velocity Structure beneath the Otake-Hatchobaru Geothermal Area at Kuju Volcano in Central Kyushu, Japan. *Annuals of Disaster Prevention Research Institute, Kyoto Univ.*, No. 47 B.

Waibel, A.F., 2011, Structural controls on the location of geothermal cells in and adjacent to Dixie Valley, Nevada. *GRC Transactions*, v. 35, 8 p.

Waibel, A.F., 1987, An Overview of the Geology and Secondary Mineralogy of the High Temperature Geothermal Systems in Dixie Valley, Nevada. *GRC Transactions*, v. 11, p. 479-486, and *GRC Bulletin*, v. 16, no. 9, p. 5-13.

Waibel, A.F., 1999, Dixie Valley Geology, Report from Dave Blackwell.

Wallace, R.E., 1984, Fault scarps formed during the earthquake of Oct. 2, 1915, Pleasant Valley, Nevada, and some tectonic implications. *U.S. Geological Survey Professional Paper 1274-A*, p. 1-33.

Wallace, R.E., and Whitney, R.A., 1984, Late Quaternary history of the Stillwater seismic gap, Nevada. *Bulletin of the Seismological Society of America*, v. 74, no. 1, p. 301-314.

Wannamaker, P.E., Doerner, W.M., and Hasterok, D.P., 2007, Integrated Dense Array and Transect MT Surveying at Dixie Valley Geothermal Area, Nevada; Structural Controls, Hydrothermal Alteration and Deep Fluid Sources. Proceedings, 32<sup>nd</sup> Workshop on Geothermal Reservoir Engineering, Stanford University, California, Jan. 22-24, 6 p.

Wannamaker, P.E., Doerner, W.M., and Hasterok, D.P., 2006, Cryptic Faulting and Multi-Scale Geothermal Fluid Connections in the Dixie Valley-Central Nevada Seismic Belt Area: Implications from MT Resistivity Surveying. Proceedings, 31<sup>st</sup> Workshop on Geothermal Reservoir Engineering, Stanford University, California, Jan. 30-Feb. 1, 8 p.

- Waldhauser, F., and Ellsworth, W.L., 2000, A double-difference earthquake location algorithm: Method and application to the northern Hayward fault. *Bulletin Seismological Society of America*, v. 90, p. 1353-1368.
- Wesnousky, S.G., Barron, A.D., Briggs, R.W., Caskey, S.J., Kumar, S., and Owen, L., 2005, Paleoseismic transect across the northern Great Basin. *Journal of Geophysical Research*, v. 110, 26 p.
- Wesnousky, S., Caskey, S.J., and Bell, J.W., 2003, Recency of Faulting and Neotectonic Framework in the Dixie Valley Geothermal Field and Other Geothermal Fields of the Basin and Range. Final Technical Report, University of Nevada, Reno, 26 p.
- Westphal, W.H., and Lange, A.L., 1967, Local seismic monitoring-Fairview Peak Area, Nevada. *Bulletin Seismological Society of America*, p. 1279-1298.
- Willden, R. and Speed, R. C., 1974. Geology and mineral deposit of Churchill County, Nevada. Nevada Bureau of Mines and Geology Bulletin, v. 83, 95 p., 1:250,000.
- Williams, C.F., Sass, J. H., and Grubb, F. V., 1997, Thermal signature of subsurface fluid flow near the Dixie Valley geothermal Filed Nevada., *Proceedings 22<sup>th</sup> Workshop on Geothermal Reservoir Engineering*, Stanford Geothermal Program Report SGP-TR-155, 161–168.
- Wright, P.M., 1991, Exploration for new hydrothermal resources for electrical power generation in the 48 contiguous U.S. states. *GRC Transactions*, v.15, p. 217-228.
- Wisian, K.W., and Blackwell, D.D., 2004, Numerical modeling of Basin and range geothermal systems. *Geothermics*, v. 33, p. 713-741.
- Won, I.J., and Bevis, M., 1987, Computing the gravitational and magnetic anomalies due to a polygon: Algorithms and Fortran subroutines. *Geophysics*, v. 52, p. 232-238.
- Wu, R. S. and Aki, R., 1988, Seismic wave scattering in the three-dimensionally heterogeneous earth, in the special issue "Seismic Wave Scattering and Attenuation" ed. by Wu and Aki, *Pure and Applied Geophys.*, 128, p. 1-6.
- Yoshikawa, M., and Sudo, Y., 2004, Three Dimensional Seismic Velocity Structure beneath the Otake-Hatchobaru Geothermal Area at Kuju Volcano in Central Kyushu, Japan. *Annals of Disaster Prevention Research Institute, Kyoto Univ.*, No. 47 B.
- Zoback, M.L., McKee, E.H., Blakely, R.J., and Thompson, G.A., 1994, The northern Nevada rift: Regional tectono-magmatic relations and middle Miocene stress direction. *Geological Society of America Bulletin*, March, v. 106, p. 371-382.
- Zucca, J., and Evans, J. R., 1989, Seismic imaging for velocity and attenuation structure in geothermal fields. U.S. Geological Survey, Report UCRL--LOO 84 1, DE90 010742.
- Williams, C.F., Sass, J. H., and Grubb, F. V., 1997, Thermal signature of subsurface fluid flow near the Dixie Valley geothermal Filed Nevada., *Proceedings 22<sup>th</sup> Workshop on Geothermal Reservoir Engineering*, Stanford Geothermal Program Report SGP-TR-155, p. 161–168.
- Wright, P.M., 1991, Exploation for new hydrothermal resources for electrical power generation in the 48 contiguous U.S. states. *GRC Transactions*, v.15, p. 217-228.
- Wu, R. S. and Flatté, S. M., 1990, Transmission fluctuations of seismic waves across seismic arrays, in "Seismic Wave Scattering and Attenuation" ed. by Wu and Aki, *Pure and Applied Geophys.*, 132, p. 175-196.